PHD

Ultrasound Tomography for control of Batch Crystallization

Koulountzios, Panos

Award date:
2022

Awarding institution:
University of Bath

Ultrasound Tomography for control of Batch Crystallization

Submitted by

Panagiotis Kouloutzios

For the degree of Doctor of Philosophy

University of Bath

Department of Electronic and Electrical Engineering

Signature of Author... Panagiotis Kouloutzios

Abstract

The main objective of this thesis is to develop a better understanding of materials' interfaces in spatial and temporal domains over dynamical industrial processes via 2D and 3D visualization and quantitative acoustic measurements using Ultrasound Computed Tomography (USCT). USCT is an imaging method that permits the determination of the spatial distribution of materials based on their acoustic properties. Tomographic techniques are usually based on a number of sensors that are located in a meaningful order around the region-of-interest (ROI). In the particular tomographic technique, piezoelectric transducers that emit signals of a standard frequency have been used. The main advantage of this imaging modality is the low-cost development but also its non-destructive and non-invasive behaviour to the process.

The control of industrial processes is becoming crucial as the research and engineering community aims at fully automated solutions. Thus, monitoring and control of tank reactors play a significant role in the overall developments. In general, this thesis focuses on improving the performance of static/dynamical USCT visualization and quantitative measurements for industrial processes. The developed studies aim to investigate in depth the USCT developments and the application in industrial reactors processes and dynamical complex processes involving high mixing. This work aims especially, to investigate USCT functionality in the batch crystallization process, where there is a great need for real-time measurement and integration of imaging and control systems towards the process automation. Detailed applications and further work are suggested. Although USCT is a new imaging technique and lots of issues are still preserved to be solved, it is believed that such research would have contributions to the future development of USCT research.

This thesis includes a number of novel approaches that constitute contributions to the USCT imaging field. At first the quantitative sound-speed imaging was developed, providing good correlation with concentration in concentrated solutions. Then the same concept transmission imaging tested in many crystallization scenarios establishing a thorough investigation of USCT in batch crystallization. In continuation, the developed transmission imaging extended in 3D and finally in 4D imaging using a spatiotemporal Total Variation algorithm. Lastly, a new triple-modality imaging is introduced as a fast and accurate method for industrial imaging proving to be more efficient than the single methods.

I lovingly dedicate this thesis to my family

(Ioannis, Ioanna, Aglaia),

who greatly supported me through all of my academic journey.

Acknowledgements

First and foremost, I would like to thank my supervisor Prof Manuchehr Soleimani for his invaluable support and encouragement throughout my entire PhD study. His enthusiasm in research and abundant knowledge have always inspired and motivated me. Over half of my PhD journey did not happen on campus and I definitely would not have come this far without his consistent motivation and guidance.

Secondly, I need to give a lot of praise to people from “NETRIX S.A.” company, whom I worked closely with. Each person during my time at “NETRIX S.A.” has helped me on the project as well as make the office a fun place to work. A special mention to Dr Tomasz Rymarczyk who was my manager during working with “NETRIX S.A.” as well as my project industrial supervisor. I would also take the opportunity to special thank my friend, Dr. Dana Beiki, for all his reviews on several of my manuscripts through my research journey. I also thank my friend, Mr. Foivos Anastasopoulos for reviewing the introduction part of this thesis.

At last, massive thanks to my parents and my sister for all their support and love. Most of my academic years have been entirely supported by my parents and I would never have been where I am without them. So truly thank you for being there through my ups and downs and always believing in me. Last but not least, I would like to express my sincere gratitude for Sonia's supportive and encouraging spirit throughout all the uncertainties, especially when reaching the end.

List of figures

List of tables

Contents

Chapter 1 General overview and motivation

1.1. Ultrasound tomography

Tomography is the technique that produces images of objects' internal structure, based on the interactions between the object and the emitted energy by the radiating devices. The word "tomography" is derived from the Greek words "tomos" which mean "a slice" and "graphein" which means "to draw". As it is priorly developed in a 2D technique, it was addressing to cross-sectional slices of the scanned objects. Nowadays the research and development of such tomographic systems turned into 3D applications. Tomography comprises of many different disciplines such as X-ray tomography (CT), electrical resistance tomography, magnetic induction tomography (MIT), ultrasound tomography (UST), neutron tomography, positron emission tomography, quantum tomography etc., all characterised by the different choices of energy radiation used in probing medium. Therefore, tomography methods have been widely used for many decades in medicine, geophysics, archaeology, oceanography, non-destructive testing and other industrial processes.

Ultrasound Computed Tomography (USCT) is the imaging modality which uses ultrasounds to scan a region of interest (ROI). It is non-destructive and non-invasive to the whole process as ultrasounds are emitted in high frequencies, and by traveling within different media it provides quality information of them. USCT is also a non-ionizing technology, thus it is a challenging alternative in medical imaging. Lastly, it is less costly in terms of setup than other tomographic modalities such as CT or MRI. Ultrasonic systems monitor the internal process by detecting objects with different acoustical properties. Thereafter, USCT has a great potential on various imaging applications.

Ultrasound tomographic reconstruction methods are based on several propagation behaviours of ultrasounds such as reflection, transmission, diffraction or on the full-wave propagation (which includes all the behaviours of propagating ultrasound). Current research classifies the acoustical tomography in two main approaches, the wave-based and the ray-based methods. The “wave-based” methods solve the actual wave equation numerically. They are computationally costly, and their workload grows rapidly as a function of the frequency [1]. However, these methods offer high accuracy in spatial resolution. Wave-based methods usually are solved by finite elements of finite difference methods. Time reversal methods and full-waveform inversion methods belong to wave-based methods. Complex computations are essential for executing these methods. A full-wave model of continuous ultrasound wave fields may offer several attractive features over widely used partial-wave approximations. For example, many full-wave techniques can be easily adjusted for complex geometries, and multiple reflections (back-scattering) of sound can be considered and modelled. Therefore, despite the computational complexity of full-wave modelling, it can provide high-accuracy in spatial resolution that is not achievable by the ray-based methods. Thereafter, it is a perfect candidate for off-line imaging where the spatial resolution is crucial and the temporal resolution is not important. Wave-based methods have been extensively researched in medical breast imaging [2]–[7], [8]–[10], medical imaging for bones assessment [11]–[15], geophysical imaging and seismic tomography [16]–[22] and in under-water acoustic tomography [23]–[26]. These methods are not in need of in-situ monitoring as data are acquired at first and then the processing for imaging takes place.

The other approach is based on geometrical acoustics in which sound is supposed to propagate in conceptional rays and the wavelength of excited sound is neglected, as it is a high-frequency approximation. These methods are also called “ray-based”, due to the concept of ray propagation, and they account for direct signal propagations. The multiple-scattered pulses are not taken into account, whereas in the wave-based methods they are modelled inherently. Transmission and reflection reconstructions can be based on geometric acoustics. Geometric acoustics model the propagation of the first arrival pulse by ray tracing methods. Thus, the reconstructions use the time-of-flight or acoustic decay of the first arrival pulse, instead of the acquired full-waveform. The first arrival pulse can be the transmitted or a direct reflected pulse, depending on the functionality (transmission or reflection mode). Subsequently, reconstructions can be performed with less computational complexity and with higher temporal resolution as the amount of processed data is drastically decreased. Many works utilise these reconstruction methods in industrial process imaging where there is significant need for on-line monitoring. Industrial processes consist of high temporal dynamic effects that need a high signal acquisition rate. On the other hand, most industrial reactor processes incorporate liquid elaborations, dispersed liquid media or liquid/gas and liquid/particles flow, which are scenarios that engage dynamic distributions rather than stable, well-defined structures. In this case, an industrial tomographic system could focus more on the acquisition rate and less on the reconstructed image resolution. Thereafter, the UST systems for industrial problems of interest in most cases prioritise the temporal over the spatial resolution. Straight-rays transmission and reflection imaging methods have been researched in a variety of industrial application such as multiphase flow [27]–[31], non-destructive testing [32]–[35] and hydro-cyclone monitoring [36].

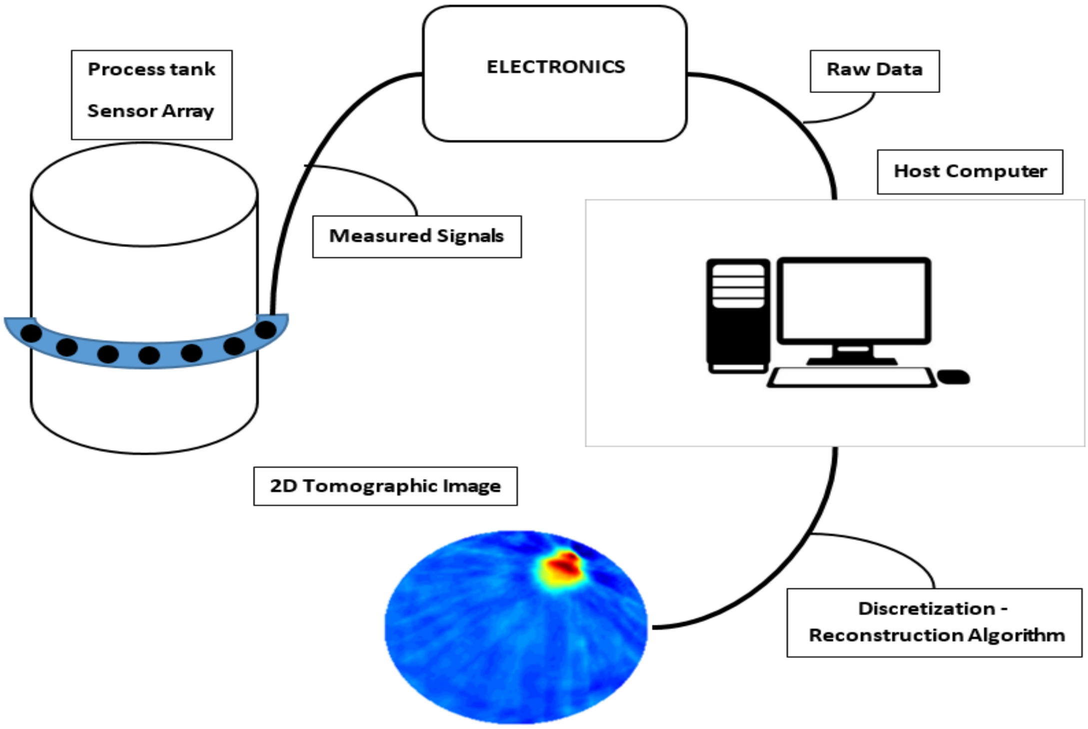

Figure 1.1 Ultrasound Tomography technique for process reactor monitoring.

A typical USCT system can be divided into three basic components: a multi- piezoelectric sensors array, a sensing electronics setup for data acquisition and a computer system for image reconstruction, as shown in Figure 1.1. Usually, a computer controls the system hardware and implements image reconstruction based on acquired full-waveform or post-processed data. The sensors measurements end up to the host computer unit. Between the sensors' array and the host computer unit there is an electronic hardware setup which usually consists of a data acquisition board. The received signals, at many times, need to pass through multiple stages of amplification and filtering by amplifier circuitries. Subsequently, the analogue signals are converted to digital data using analogue-to-digital converters. Finally, the collected raw data are processed by tomographic algorithms to generate images.

1.2.**Crystallization**

Crystallization is the process of forming a crystalline material from a liquid, gas or amorphous solid. It is widely used in intermediate unit operations in the chemical industry such as purification, separation and in final production steps of the production of sugars and pharmaceuticals. Worldwide production rates of basic crystalline products, such as sucrose, salt, fertilizers, and other bulk chemicals exceed 1 Mt/year and the demand is constantly increasing. In modern chemical engineering, crystallization is considered as the simultaneous heat and mass transfer process with a strong dependence on fluid and particle mechanics. Nowadays, the state-of-the-art research on crystallization is focused on process' measurements and control. Various sensing methods have been researched in process monitoring and feature extraction towards the process automation. Crystallization can be carried out from a vapor, melt or a solution. Below, the district crystallization methods are listed.

- Melt crystallization: in which the melt is cooled below its melting point.
- Solution Crystallization:
    - Evaporative: Solvent evaporation, increase the concentration.
    - Colling: Temperature decrease, decreases solubility.
    - Anti-solvent: The solute is well-soluble in the original solvent but is slightly soluble in the solvent/anti-solvent mixture.
    - Precipitation: Mix two well-soluble reactants to give a poorly soluble product.
- Membrane assisted Crystallization: Extracting the solvent, increase the concentration.

Crystallization is driven by the excess concentration in solution above the solubility limit, which in solution equates to supersaturation. Hence it is necessary to know the solubility of a crystallising material in the solvent used [37].

Solubility & supersaturation

The amount of solute that can be dissolved at equilibrium in the solvent, making a solution saturated at fixed conditions of temperature, pressure and PH is defined as solubility, C*. Supersaturation is a significant parameter in the crystallization process, as it is considered as the driving force for the nucleation and crystal growth. A supersaturated solution has non-equilibrium conditions and tends to approach equilibrium state; Thereafter, it creates solids in form of nuclei [38], [39]. The supersaturation is defined as difference in the chemical potentials between the equilibrium composition and the actual composition. A supersaturated solution occurs when a dissolved solute reaches a concentration that exceeds the equilibrium level of solubility. The relationship between supersaturation and crystallization is represented as a solubility diagram and defines the phase diagram of the process. Phase diagram is a map that represents the material phase as a function of ambient conditions such as temperature, concentrations etc. A solubility diagram can be of different forms depending on the crystallization type that is to be performed.

Figure 1.2 presents four different solubility curves based on different crystallization procedures and also the relation between concentration, solubility and supersaturation. Figure 1.2a shows a diagram based on evaporative crystallization. In this case, the solvent is removed by evaporation, which is very useful when the solvent is non-aqueous and has a relatively high vapour pressure. Figure 1.2b presents the solubility curve of cooling crystallization, in which temperature defines the solubility change. Figure 1.2c shows a solubility curve of antisolvent crystallization. Adding a salt, acid/base or any other anti-solvent changes the properties of the solvent. Lastly, Figure 1.2d shows the solubility curve for a precipitation procedure. The crystallization takes place almost immediately as when the two soluble compounds are mixed in a solution that reacts quickly to form a product of low solubility.

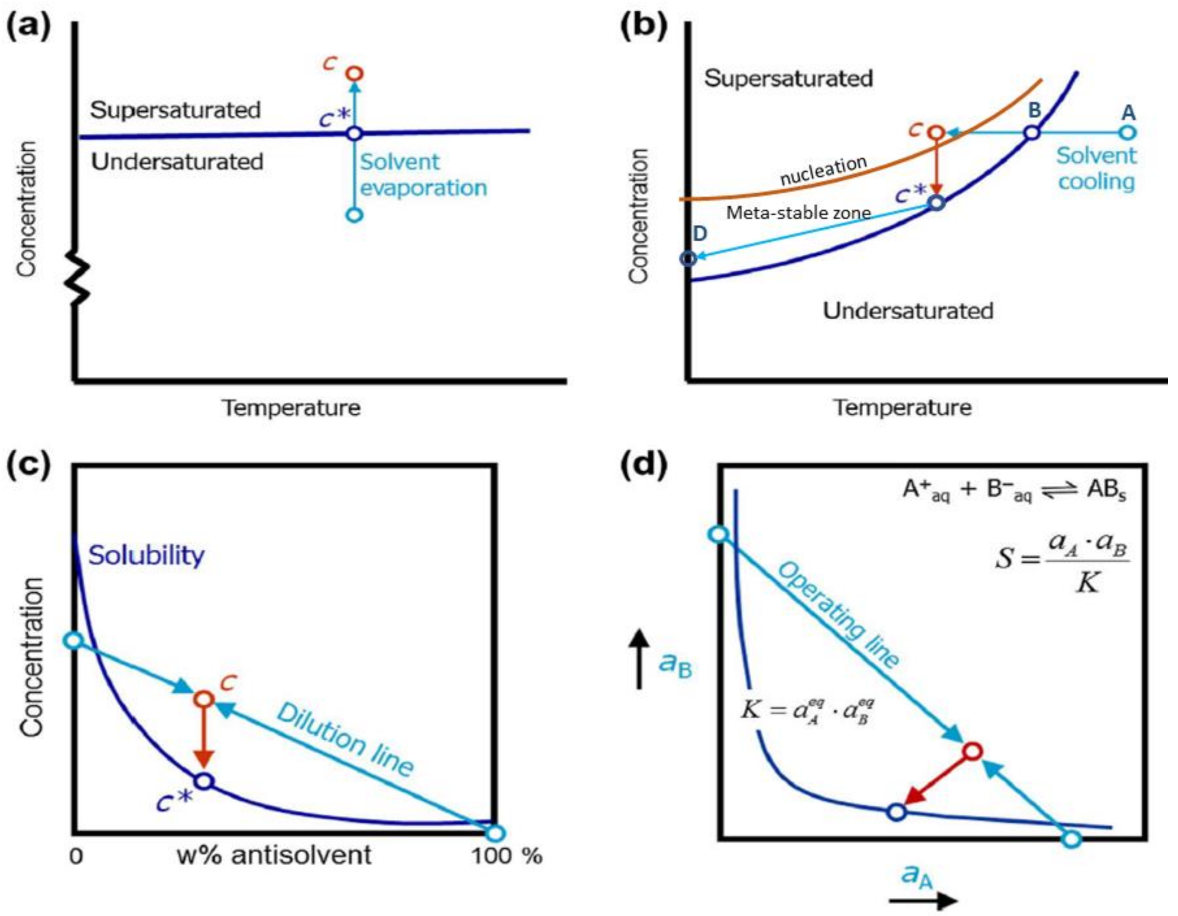

Figure 1.2 The phase diagrams, solubility lines and operating points for different crystallization techniques including (a) evaporative, (b) cooling, (c) anti-solvent, (d) precipitations, [40].

Figure 1.2b illustrates the solubility graph of cooling crystallization. This time, the metastable zone and a trajectory from state A-D are indicated. For most substances, the solubility increases with increasing temperature. The trajectory simulates the relation of concentration and temperature in a cooling crystallization experiment. The experiment starts from point A, which is an undersaturated state. Crystals that may be added to the solution at this point, would dissolve. Cooling the system helps to move towards point C, as the solution gradually enters the meta-stable zone at point B. At this point, existed crystals will grow, but no new crystals are formed. Reaching point C, spontaneous formation of new crystals occurs, i.e. nucleation. This dramatically decreases the concentration and point C* will be reached. Cooling further, the crystals form and grow between C and C* and subsequently the solution concentration is decreased. The system will never reach beyond the metastable zone (unstable zone) due to the immediate nucleation. Finally, the end of the experiment is at point D [41].

The metastable zone defines the operating window of the crystallization process [42]. Slow growth rates have been identified when operating close to the saturation curve, with the optimal level to be defined approximately in the half of the meta-stable zone regarding to industrial crystallizers functionality [43].

Nucleation

Prior to the crystal formation, nuclei must exist in a supersaturated solution. Nucleation is the first stage of nuclei formation. It can be primary (homogeneous or heterogeneous) or secondary. Primary nucleation can be achieved if non-existence of prior crystals in the solution occurs. Primary homogeneous nucleation takes place when the solution is free of impurities and disturbances mainly caused by mechanical effects. In the exact opposite case, the nucleation would be disturbed turning into a primary heterogenous. When a solution owns crystals, nuclei may form in the vicinity of crystals even at very low levels of supersaturation; this behaviour is referred to as secondary nucleation. The secondary nucleation occurs only in the presence of crystals of the substance that should be crystallized. Secondary nucleation occurs at much lower supersaturations than primary nucleation. The different known mechanisms for secondary nucleation are initial breeding (result from dust of the seed crystals added into the supersaturated solution), collision breeding (result from the breakage of existed crystals due to crystal – crystal, crystal – wall or crystal – impeller collisions) and fluid shear (result from shear forces outcomes from the liquid motion). Among these mechanisms, the collision breeding is most frequently observed in crystallization processes [44], [45].

Crystal formation

Once stable nuclei are formed, continuous size enlargement of crystals occurs which is defined as crystal growth. Mass and heat transfer are the main processes which define the growth. The three main steps for a crystal growth process include [39]:

- Mass transfer of solute molecules from the bulk solution to the proximity of the crystal surface (diffusion).

- Transmission of the adsorbed solute molecules at the crystal surface into the crystal lattice (surface integration).
- Release of the heat of the crystallization process at the point of growth.

During crystal growth, nucleated crystals in supersaturated solution start growing to a discrete size. According to literature [44], crystals can be categorised to seven general morphologies as cubic, octahedral, tetragonal, orthorhombic, monoclinic, triclinic, trigonal and hexagonal. However, there can be more classifications as the relative crystals' face sizes can vary significantly. The later classifications can be recognised in the literature as different habits of a crystal. Factors that can affect the habit of crystals are the possible existence of impurities or even the degree of supersaturation and nucleation resulting from different solvents.

During crystal growth, crystals can reach dimensions of a few μm to mm in size. Crystal size plays a significant role in the pharmaceutical and chemical industry. The distribution of different crystal sizes is measured by crystal size distribution (CSD) analysis. The CSD can be represented by the cumulative distribution function, in which the total of all sizes "retained" for a range of sizes, is displayed. The crystal size distribution (CSD) associates to the number of crystals, volume or mass of crystals concerning a certain size range which refers to a density distribution. A narrow CSD curve indicates a uniform crystal size distribution while a broad or multimodal curve indicates higher tendency to result in a slow filtration rate, a poor flow ability or a variable dissolution rate [46]. Crystal growth is seriously affected by the distributions of the supersaturation within a crystallizer. Moreover, crystals own a higher density than the liquid solution and thereafter tend to settle. Mixing process is in need for achieving uniform supersaturated distributions and for keeping the crystals well-suspended. Nowadays, crystallizers are equipped with stirrers or pump impellers or even air bubbles streams (airlift crystallizer) [47].

Characterization methods in solution crystallization

Many failures can occur due to poor understanding and control of crystallization processes. Measurement techniques aid significantly the control of the process by providing useful insights in case of off-line or in-line measurements. Process Analytical Technology (PAT), introduced in 2004 by the FDA Guidance “PAT- a framework for innovative pharmaceutical development, manufacturing and quality assurance” [48]. PAT tools obtained significant attention in academic and industrial research as novel technologies to analyse and control processes. These tools enable process understanding for scientific purposes, risk management, quality assurance of products and a reduction of risk strategies especially in pharmaceutical industry [49]. PAT tools aim to provide insights on the yield’s physical (dissolution rate, solubility) and chemical (reactivity) properties. Further advantages of PAT utility are the improvements of the process understanding and the reduction of process failure, quality assurance through continuous monitoring and feedback control and lastly, the minimization of cycle time to wards manufacturing efficiency.

PAT monitoring tools can be categorised as off-line, on-line and in-line depending on whether they are attached on the process, or they are separated. In off-line scenario, a sample is taken out from the process to be analysed by a PAT tool, avoiding the typical time delay and sampling errors. In on-line scenario, the samples are not removed from the process stream but temporarily separated, for example via a by-pass system which transports the sample directly through the on-line measurement device where the samples are analysed in close proximity to the process stream and afterwards the sample returns to the process stream.

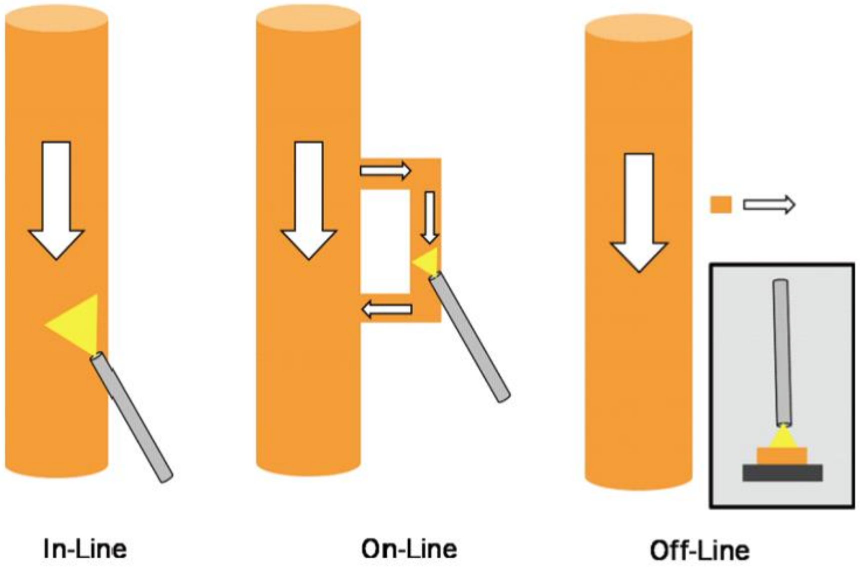

Figure 1.3 Different operations of the PAT tools [48].

Finally, in in-line scenario the PAT tools are immersed in the process and no sample is taken. Figure 1.3 shows a scheme of the different measurement methods. Both on-line and in-line methods allow instant measurements, aiming at in-situ analysis and control.

Various single-point measurement methods have been used to measure whether the liquid solution phase, or the solid phase by measuring crystal growth or the crystal forms (polymorphic or solvate). Liquid phase concentration is a very important factor to be measured over a crystallization process. In pharmaceutical industry, the integrity of the active pharmaceutical ingredients depends on solubility. If a product has high solubility, it could produce side effects or if it has low solubility, it could be ineffective. Therefore, liquid phase measurements allowing to monitor the solubility and supersaturation phase are critical. Liquid phase concentration has been measured via various methods in crystallization processes. Liquid phase monitoring includes spectroscopic methods, densitometry, electrical conductivity measurements and ultrasonic technique with single frequency [50]. Spectroscopic methods are from the most common methods for the determination of concentration. Beer-Lamber law explains the physical behaviour of the spectral data in dispersed media. The spectroscopic techniques that have been applied to measure the liquid phase of a crystal slurry include Attenuated Total Reflectance (ATR), Attenuated Total Reflectance- Fourier transform infrared (ATR-FIR), Ultraviolet/Visible (ATR-UV/Vis) and Raman spectroscopy [51], [52]. For example, the ATR-FIR spectroscopy has been tested in measuring the solubility as a function of temperature or solvent composition [53]. Regarding Raman spectroscopy, it has been successfully used to measure the liquid concentration [54], [55], however it comes with a few disadvantages such as the sample heating produced by the probe that can degrade the sample [56]. Except of the spectroscopic methods, the use of densitometry is an alternative in measuring the solute concentration. However its usage is limited as it is not able to operate in high density slurries [38], [57]. The electrical conductivity of a solution is proportional to the volume fraction of the particles [44]. Thus, electrical conductivity measurements can determine the supersaturation level during crystallization [58]. Finally, the ultrasonic technique (single frequency) is proven to be a simple and robust method in monitoring crystallization. It is used for the determination of the metastable zone and supersaturation by measuring the concentration of the solution [59], [43].

Additional attention has been gained by the abilities of single-point measurement methods in solid phase monitoring. Crystal growth rates have been determined by various of off-line and in-line sizing techniques. They are able to provide with information on the crystals' particle size, the crystals size distribution (CSD) and the crystal form and purity. These methods include coulter counter, cascade sieving and laser diffraction, which all of them require sampling and can only be applied on off-line analysis. Moreover, in-line particle size measuring methods involve optical reflectance measurements (ORM) technique [60], ultrasound spectroscopy (UAS) [61], ultrasound technique (single-frequency) [62], Raman Spectroscopy [53], Near Infrared spectroscopy and turbidimetry method [38]. The in-line solid phase monitoring methods are categorised in direct and indirect methods. Direct methods are those based on the measurement of change in the crystals' size or mass, while indirect methods are based on change in solution concentration over time. It has been demonstrated that ultrasonic technique is an indirect method due to lack of ability carrying measurement on crystals' dimensions, it can monitor the crystal growth kinetics by measuring of the de-supersaturation curve. Growth rate of organic and inorganic compounds have been measured from the de-supersaturation curve by ultrasonic technique [63]. Various other methods aim to measure the crystal growth such as spectroscopic methods, ultrasonic method (single frequency) and optical reflectance measurement (ORM) method and in-situ. However, there are some limitations in using in-line particle analysers. For example, in line optical microscopy struggles to offer efficiency in high density solutions, as low-quality images result from opaque crystal suspensions. In this specific case, ORM and UAS are more suitable, as they characterised as quality measurement methods for a wide range of the suspension densities (ORM: up to 80 vol%, UAS: up to 70 vol%). A disadvantage of UAS is that due to the lengthy of the measuring time (60s), this device is not suitable for very rapidly changing dynamic systems [60]. Also, UAS is limited regarding the complexity in analysing the obtained data. Because of being an indirect analysis method, the analysis of the attenuation spectra is done by means of mathematical models to calculate the crystal size distribution (CSD). Correlation models are developed which finally estimate the mean crystal size by approximation and not by direct measurements.

1.3. **Aims and objectives**

There is a great need for on-line monitoring in many industrial operations [64], [65], [66]. The state-of-the-art industrial control research is focused on the integration of on-line monitoring and system control theory, which gives great potential to the automation of processes [67], [68], [69]. Ultrasounds are commonly used for monitoring industrial processes. Ultrasonic single-frequency and spectroscopic methods are highly distributed in process control, as mentioned in section 1.2. They have proven to offer solutions in fermentation, solidification and crystallization processes in the food or pharmaceutical industry [70]–[72]. Using the acoustical properties of slurry mixtures, they are able to in-situ characterize the process [73], [74], [75], [76]. Contrary to the above-mentioned crystallization monitoring based on ultrasound single-point measurement methods, tomographic methods have not yet been applied to the field in a wide extent. However, a few recent studies have presented other tomographic modalities potential in the monitoring of crystallization and stirred tanks' functionality [77]–[84]. Tomographic imaging systems and their recent development have proven to be an alternative and trustworthy method of on-line monitoring offering significant advantages to large-scale processes. Tomography could add useful information regarding the topology and the material phase distributions in mixtures. It can also offer the opportunity to quantify the degree of homogeneity of particulate suspensions and other multiphase mixtures. Even though tomographic techniques cannot compete against the microscopy methods in CSD measurements, they can add useful spatial information and can be used as a fault detection or quality assurance tool for the complex mixing processes. They can also be used as complementary alternative measurements to the PSD single-point measurements aiming at multiple measurements integration.

Thereafter, there are significant indications that USCT could be used to characterize the density of the materials during such continuous processes and monitor the distribution of the first stage crystals, optimizing the yield. This study aims to investigate the utility and feasibility and of ultrasound tomography in the batch crystallization process occurring in chemical and pharmaceutical industry.

1.4. Thesis Organisation & Contributions

Contributions of this thesis are discussed in this chapter by a chapter-based arrangement in the following contents:

Chapter 2 introduces the industrial tomography applications and especially the basic concept of USCT and related applications. In this chapter, the batch crystallization with the established measurement techniques and the risen challenges are also discussed.

Chapter 3 introduces the USCT principles, while it is presenting in depth-introduction of USCT function and specification of the developed systems including hardware design and data acquisition methods. The chapter also introduces the forward and inverse problem of USCT and various reconstruction methods. The two USCT systems presented, were developed by “NETRIX S.A.” company (Description of the systems have been shared by “NETRIX S.A.”).

Chapter 4 demonstrates the effectiveness of a newly developed in-line sound speed travel-time USCT system to inspect distributions of different density liquid mixtures. The study presents for the first-time, sound-speed tomographic imaging of liquid elaboration processes. The proposed USCT sensitivity matrix based on “straight-ray” approximation was applied. A comparison between Tikhonov and Total Variation regularization method indicates the superiority of the second method. Finally, the efficiency of the integrated USCT system with a 40KHz centre frequency was tested in concentrated solution. This study, for the first time, presents meaningful quantitative industrial USCT imaging and also provides a clear relation between sound-speed imaging and density characterization of liquid solutions. Moreover, specific analysis has been conducted based on the system’s technical features such as choosing an appropriate system’s design, software development and results analysis that can lead to significant results regarding spatial and temporal resolution over the industrial reactor monitoring.

Chapter 5 investigates the capability of the proposed travel-time ultrasound tomography system in dispersed two-phase media, by testing applicability in monitoring processes consisting of crystalline suspensions in a nonstationary setting. It also investigates the system’s response in the crystallization process, by analysing the ultrasonic signals interaction with different material phases, such as liquid solutions and crystalline liquid suspensions.

Chapter 6 investigates the performance of an ultrasound transmission tomography system that can exploit both time-of-flight and amplitude information on a batch crystallization process aligned with industrial standards. High stirring has been utilised in the tests including particles suspensions, and real-time calcium carbonate reactive crystallization. Finally, analysis of the experimental results can provide the potential and limitations of the system in this complex industrial process.

Chapter 7 presents an extension to 3D and 4D travel-time transmission tomography. This chapter investigates the expansion of 2D-imaging margins by applying 3D model to experimental stationary data. Dynamical experiments were conducted as well, by implementing a 4D spatio-temporal TV regularization. Finally, the dynamical algorithm was tested in crystallization experiments.

Chapter 8 introduces an optimal method of ultrasound triple-modality reconstruction based on full-waveform signals. The proposed method combines the time-of-flight, acoustic attenuation and reflection reconstructions to a final result. All the individual methods are based on geometrical acoustic techniques and thus the complexity of the triple-modality reconstruction is assumed to be still in low levels even though it is a combination of multiple methods. Static experiments showed good system performance in distinguishing objects of different sizes and shapes in single and multiple objects. The solutions used in the experiments showed that the triple-modality imaging could also use the TOF scale to characterise small changes in the density of biphasic media, which is a significant addition to the system.

Chapter 9 is a conclusion chapter with two sections. Section 1 summarize contents that involved in each chapter, including conclusions of novel ideas, what has been conducted, results and novel finding of the research. Section 2 proposes the future developments.

1.5. List of publications

A number of publications have been made which are directly and indirectly related to some of the Chapters as part of the project. The publications are original research papers on ultrasound tomography application in batch crystallization quality testing. The research ideas from the publications have arisen on discussions between the author and the co-authors during the years 2018-2021. The original articles have been reproduced with permission of the copyright holders. The thesis also includes additional unpublished work.

- *"Ultrasonic Tomography for automated material inspection in liquid masses"*, [85] was presented at 2018 World Congress of Industrial Process Tomography 9 (WCIPT9) in Bath, UK. Some results of this work are displayed i*n Chapter 4.*

- *"A Quantitative Ultrasonic Travel-Time Tomography to Investigate Liquid Elaborations in Industrial Processes"*, [86], was published in Sensors (MDPI).It follows up the first conference paper and forms a major part of the work in Chapter 4.

- *"Ultrasonic time-of-flight computed tomography for investigation of batch crystallization processes"*, [87], was published in Sensors(MDPI) and this publication's content constitutes Chapter 5.

- *"Handwriting with sound-speed imaging using ultrasound computed tomography."*, [88], was published in IEEE Sensors Letters and it is a presentation of handwriting with an object with USCT, testing the tank in dynamical phenomena. Some results of this work are displayed in Chapter 4.

- *"An ultrasound tomography method for monitoring CO2 capture process involving stirring and CaCO3 precipitation."*, [89], was published in MDPI Sensors and this publications content constitutes Chapter 6.

- *“Four-dimensional ultrasound computed tomography for industrial applications”,* [90], was published in IEEE Transaction on Instrumentation and Measurement Society Journal. The content of this work forms Chapter 7.

- *“A triple-modality ultrasound computed tomography based on full-waveform data for industrial processes.”,* [91], was published in IEEE Sensors journal and this publication’s content constitutes Chapter 8.

- *“Towards Real-Time Control of a Semibatch Crystallization Process by Electrical and Ultrasound Tomographic Techniques.”,* [92].

- *“Dual modality EIT-UTT for water dominate three-phase material imaging.”,* [93].

Chapter 2 USCT industrial applications

2.1.Industrial process tomography

Measurements of the flow and phase of vigorous stirred industrial and chemical mixtures are very important due to the materials' safety and control. The tomographic imaging offers great potential in detecting and visualising profiles of such processes without being invasive and destructive. Nowadays, there are significant advances in industrial process tomography (IPT) that leads IPT to be a mainstream industrial deployable technique. Tomographic approaches aim to derive data taken from multiple sensors observing different attributes of a process; and obtain a rich dataset of measurements that detail the particular properties of the mixture within the process.

IPT plays an important role in many sectors of the industry such as manufacturing as well as in food and pharmaceutical operations. Table 2.1 presents the recent reported application of IPT. The growing necessity to monitor process plant activities leads to the further improvement of on-line procedures, making tomography an appealing technology. Nowadays, industrial reactors such as chemical reactors, crystallizers, complex stirrers are in a great need of on-line monitoring and automatic control, with the state-of-the-art research focusing on tomographic monitoring for process automation. IPT has been applied to imaging of mixing processes, separators, chemical reactors, stirred tanks, and industrial pipelines and vessels [94]. More specifically, IPT found use in either industrial, field or laboratory tests in many applications. The goal of IPT has been to sense and interpret complex data in order to extract qualitative and quantitative information of the behaviour of fluids moving within processes, or the generated yield coming from a mixing batch process. In all applications, there is a trade-off between the spatial and temporal resolution. There are two main broad types of tomography:

- Hard-field Tomography: Hard-field means that regardless of the type of material or medium, the direction of travel of the energy waves from the power source is constant. Examples of Hard Field Tomography, Magnetic Resonance Imaging (MRI) and Positron emission tomography (PET), X-ray tomography (CT). USCT can be assumed as hard-field in high frequencies [95].

- Soft-field Tomography: Soft-field means that the transmitting field does not follow the straight line pattern anymore, and the signal distribution depends on the type of the excitation source. The nature of soft field is much more complex than hard field, and requires considerably more computer analysis and algorithms to reconstruct the image. The examples of such tomographic systems include Electrical Impedance Tomography (EIT), Electrical Capacitance Tomography (ECT), Magnetic Induction Tomography (MIT).

Table 2.1 Recent reported applications of process tomography.

Process	**Modality**	**Status**
Hydrocyclone monitoring [96] Monitoring pressure filtration [97]	EIT	Industrial tests
Nylon polymerization [98] Nuclear waste site characterization Waste storage ponds Subsurface resistivity [99] Leaks in underground pipes		Field tests
Bubble column dynamics Foam density distribution [100] Mixing in stirred vessel [80] Slurry transport [101] Blast furnace – hearth wall thickness		Laboratory tests
Bead milling [102] Pneumatic conveying [103]	ECT	Industrial tests

Density flowmeter [104]		
Flame monitoring [105] Fluidized beds Powder flow in dipleg [106] Solid rocket propellant Imaging wet gas		Laboratory tests
Onset of crystallization in steel production Flow of molten steel	MIT	Industrial tests
Metal solidification [107]		Laboratory tests
Non-destructive Testing [108] Metrology [108] Quality inspection in food industry [109]	CT	Industrial tests
Non-Destructive Testing [110] Two-phase gas/liquid flow [93] Hydrocyclone monitoring [36] Air temperature fields monitoring [111] Bubble column dynamics [27]	USCT	Laboratory tests

2.2. USCT applications

Ultrasound tomography starts gaining interest in overall tomographic studies as it is non-ionizing, it can be cheaper compared to CT, MRI and other complicated tomographic setups and it is data-rich technology providing multiple reconstruction methods. Ultrasound tomography is widely used in medical imaging as well as in industrial imaging.

In medical imaging the most of the state-of-the-art work is focused on early breast cancer diagnosis [112], [113], [114], [115]. Sound-speed USCT (SS-USCT) also is a great method for breast cancer imaging because of the distinguishing sound-speed of tumors to surrounding tissue [116]. This method is based on the time-of-flight of the transmitted ultrasonic signals. Another ultrasonic reconstruction, which is also used in the breast imaging field, is the acoustical-attenuation (AA-USCT) [7]. AA reconstructions are based on the amplitude decay of the transmitted signals, and they tend to provide more contrast enhanced images than SS methods. Remarkable progress has taken place on the computational acoustics and the applications of them in breast imaging, which is the main area of medical USCT progress. Regarding the complexity of human tissues' structure, computational models directly solve the wave equations and provide better ability for detection, resolution and artefact control [117], [7].

On the other hand, USCT offers several usages in industrial sector such as in non-invasive, non-destructive evaluation techniques for visualizing the internal structure of a number of different media [118], [119], [120]. Non-destructive testing (NDT) is the process of inspecting or evaluating materials and components for discontinuities, or differences in characteristics without destroying the serviceability of them. UST industrial applications are vastly focused on the liquid transportation pipelines and multiphase flow monitoring [95], [121], [122], [123]–[125]. USCT also finds great need in conducting pipes and liquid/ gas flow imaging, which is a process widespread in the chemical, oil and gas, pharmaceutical and energy industries [126], [31], [127].

Comparing the industrial and medical USCT systems, the big difference is the thorough study of more effective computational models such as the full waveform reconstructions in medical applications due to the complex formation of the biological structures. These models are not suitable for in-situ imaging and therefore they have not applied widely in industrial applications. However, the study of the hardware systems that can execute the heavy computations of these models in parallel with the industrial processes like crystallization would be of a great interest.

2.3. Tomography in process tanks & reactors

Industrial reactors are broadly used in different unit operations, making the tomographic studies on their functionality a hot topic for the research communities [69], [77], [128]–[133]. Slurry transportation processes can also be found in many process reactors, for example, dredging, food processing, and nuclear waste management. Slurry flow usually involves moving high-density material through a carrier liquid (e.g., water), with few tomographic studies being focused on slurry mixtures [36], [101], [133], [134]. Mixing in industrial reactors is critical and challenging, especially in the case of complex fluid rheology. There are different types of mixing processes: liquid–liquid mixing, gas–liquid mixing, solid–liquid mixing, and the mixing of multiphase non-Newtonian fluids. Furthermore, the challenges can be further increased when the product has high-quality requirements for the degree of homogenization, and the end-product has limited tolerance to variations in the hydrodynamics conditions in the reactor. As the mixing phenomena can significantly affect the quality of the end products, it is of significant importance to utilize monitoring instrumentation for detailed analysis and to perform an efficient operation in terms of final yield.

2.4. Batch Crystallization & measurement techniques

There are two main different crystallization processes. Batch crystallization and continuous crystallization are different in their function, as batch systems' production of crystals is made only once at the end of the batch run. There are several advantages of batch crystallization. The equipment is relatively simple and flexible and requires a relatively low level of maintenance. Batch crystallization is considered as a relatively slow process, comparing to continuous crystallization, and it could be used to examine many operational variables in a short time. Thereafter, a batch process can be controlled more easily. In addition, batch crystallizers can produce a narrower crystal size distribution (CSD) than the continuous well-mixed crystallizers, which is a great advantage to a lot of industrial and pharmaceutical processes. Thus, this specific process can offer significant advantages in producing monodisperse crystals. One of the first lab-scale batch reactors for crystallization is presented in Figure 2.1 [41].

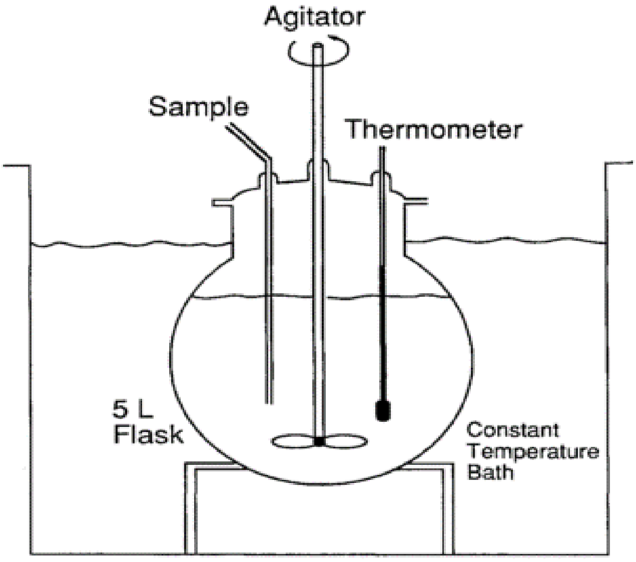

Figure 2.1 Laboratory batch crystallizer schematic [41].

In this draw the basic parameters of the process are presented, which are the flow rate of the sample's injection, the speed of the impeller and the temperature of the mixture inside the reactor.

Required quality targets for the batch crystallization process are the yield and the purity, morphology, and size distribution of the crystals. Different products can result from variations in the crystallization operation such as mixing, temperature profile, and solute concentration. In other words, changes in the operating conditions determine variations in the growth, nucleation, and agglomeration of crystals. So, these operating conditions could be parameters of the process control. Improving the monitoring of industrial crystallizers is therefore a major current industrial concern as it is clearly in strong connection with the need for mastering the properties of solid Active Pharmaceutical Ingredients (APIs).

Normally, yield and quality targets for batch crystallization are given in terms of solute concentration and crystal size distribution (CSD). Several multipurpose and reliable methods measuring content characteristics such as uniformity, dissolution and absorption rates were developed. They are mainly based on the use of in situ spectroscopic techniques. Such techniques include mid- and near-infrared, Raman, UV-visible, and ultrasound spectroscopy [135], [76], [136], [137], [61]. Non-spectroscopic ultrasound methods have been studied in the form of single-frequency acoustic emission with promising results, leading to less complex measurement setups [135], [138]. Ultrasound single-point measurement techniques have been already proposed as a promising method to determine the density of slurry mixtures, which is important in characterizing the extent of crystallization [75], [61], [76], [139], [140], [141]. Moreover, several studies suggest the use of ultrasounds in relation to the density and compressibility of binary mixtures. Among the most commonly used are the equations of Urick et al. [142]. Early tomographic applications in monitoring in-situ crystallization processes include X-ray microtomography [143], [144], X-Ray diffraction tomography (XCT) [65], Electrical Impedance Tomography (EIT) [79], Electrical Capacitance Tomography (ECT) [145] and Electrical Resistance Tomography (ERT) [130]. Figure 2.2 shows a study using EIT for the detection and analysis of the injection point in a batch-crystallizer.

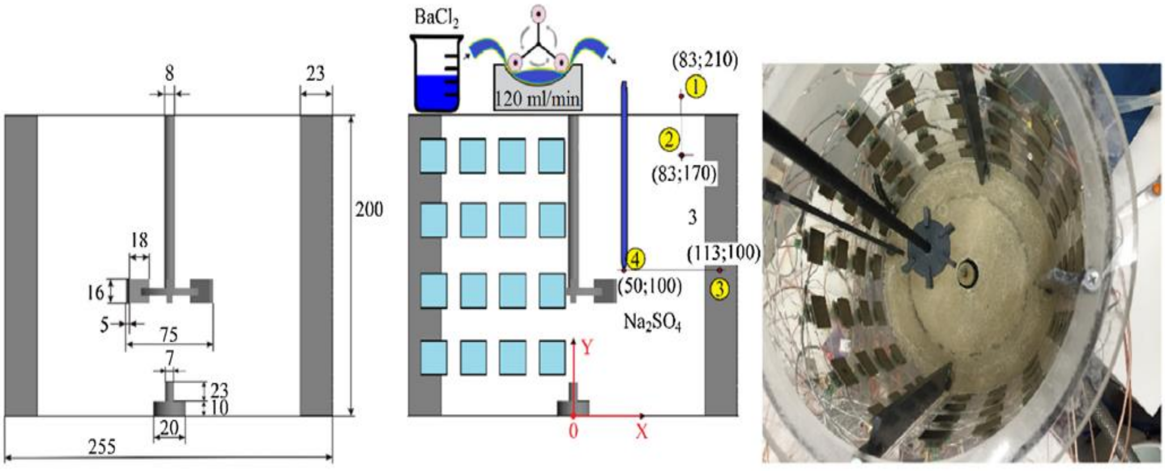

(a) **(b)** **(c)**

Figure 2.2 (a) Schematic representation of batch reactor. (b) Experimental set-up including injection point schematic. (c) Photo of reactor equipped with an EIT system for in-situ monitoring [79].

Chapter 3 USCT principles

In this chapter, the main definitions and concepts of acoustics and ultrasonic tomographic imaging, that will be used in the rest of the thesis, will be introduced. First, a review of the theoretical acoustics and the sound propagation theory in moving inhomogeneous medium is presented. Further, we briefly discuss different inversion formulas and methods, based on the geometrical acoustics principles.

3.1.Ultrasound Physics

Acoustics is the science of sound and overall describes the propagation and attenuation of waves in different media constituting the environment. Sound in general, is a propagating oscillating motion of particles.

3.1.1. Acoustic wave properties

Waves can be defined by two main ways as longitudinal and transverse. Longitudinal waves propagate in parallel to the particles' oscillation, while the transverse (or shear) waves propagate perpendicular to the directions of particles' oscillation, as depicted in Figure 3.1. Also, other wave types, e.g. torsional, surface and plane waves, may occur. Usually in acoustic applications the motion common occurring waves are the longitudinal and the transverse waves. However, in gases and fluids the transverse waves do not occur.

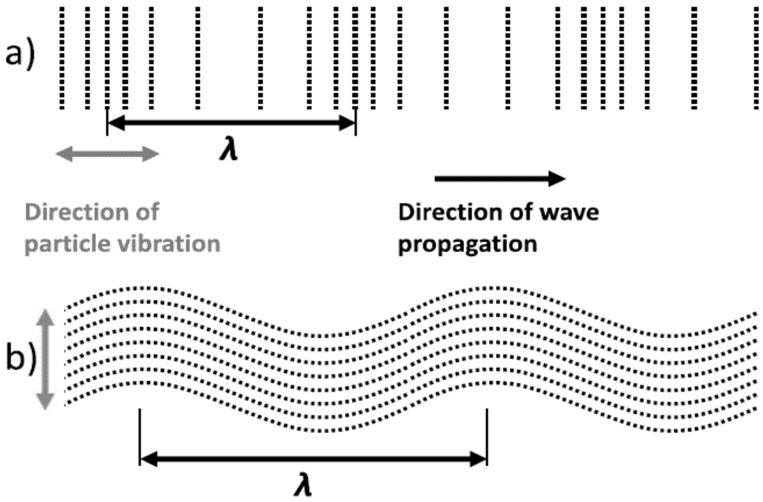

Figure 3.1 (a) Longitudinal and (b) transverse wave. The wavelength λ and the direction of the particle vibrations are indicated [146].

The most basic definition of a wave is a disturbance that propagates through a medium. Waves are generally described by the pressure variations in the medium due to an exciting source. A one-dimensional sound wave equation for pressure p moving in a direction x, at instant time t with a medium's sound-speed c is denoted as:

$$\frac{\partial^2 p}{\partial x^2} = \frac{1}{c^2}\frac{\partial^2 p}{\partial t^2} \tag{3.1}$$

The total pressure in the medium is given in location x and time t by eq. (3.2):

$$p_T(x,t) = p_0(x,t) + p_1(x,t) \tag{3.2}$$

where p_0 represents the ambient pressure of the medium and p_1, the fluctuations caused in the acoustic field. Pressure level is defined by a large dynamic range, therefore it is convenient to work with relative continuous scale rather than an absolute one. The sound pressure level is expressed by:

$$SPL_{dB} = 20\log_{10}\frac{p}{p_{ref}} \tag{3.3}$$

where p_{ref} is the reference pressure, e.g. 20 μPa (the floor pressure level, as it is the smallest that an human ear can sense). One of the solutions that satisfy the one-dimensional wave equation, eq. (3.2), is the periodic function of eq. (3.4). Periodic function is one that repeats itself exactly after certain intervals of time. The simplest case of a periodic function is sinusoidal that can be defined mathematically by a sine or cosine function:

$$p(x,t) = p_0 cos2\pi f(\frac{x}{\lambda} - \frac{t}{T}) \tag{3.4}$$

where p is the pressure level, x, and t, are the coordinates in space and time, respectively; c is the speed of sound in the medium and f is the frequency with the $2\pi f$ indicating the angular frequency. T is the period of the signal, defining the time between two identical oscillations. The inverse of period is frequency f. λ indicates the wavelength, $\lambda = c/f$.

3.1.2. Medium's acoustical properties

The propagation of acoustic waves will be influenced by, and also can cause changes, in the acoustical properties of the medium. In this section some of the main acoustic properties of the mediums are discussed.

Density

Wave propagation is seriously affected by the density d of a medium. Density is defined as the mass of a substance divided into its volume, shown in eq. (3.5)

$$d = \frac{m}{V} \tag{3.5}$$

Generally, in denser substances the sound is moving faster, due to the molecular structure.

Speed of sound

The elapsed time Δt for the wave travelling the distance Δx between two points, e.g. locations of the sending and the receiving transducer, give relation for the speed of sound

$$c = \frac{\Delta x}{\Delta t} \tag{3.6}$$

The transmission of the wave and the speed c are dependent on the medium properties, e.g. density and elasticity. Acoustic wave with different frequencies travel at the same speed of sound in a given medium. The sound speed can also be affected by the medium's temperature. Nevertheless, a temperature variation around the few degrees causes very small deviations in the sound speed [147].

Absorption

When an acoustic wave propagates through a medium, it experiences a loss of kinetic energy by a phenomenon called absorption. Absorption is the property which describes the transformation of acoustic energy into thermal energy. The extent of absorption however is dependent of different variables like frequency of the beam, viscosity of the medium and the relaxation time of the medium. Viscosity is the property that describes the measure of the frictional forces between particles of the medium as they move past one another. The amount of heat generated by the vibrating particles would increase with increase in the frictional forces. Hence, the absorption of ultrasound increases with the increasing viscosity. Viscosity dependence on frequency is given by f^2, being more significant at higher frequencies:

$$a_{vis} \approx \frac{f^2}{2\rho c^3}(\frac{2\eta}{3} + \eta_B) \tag{3.7}$$

where η is the coefficient of shear viscosity (due to molecules colliding between regions of different particle velocity) and η_B is the coefficient of bulk viscosity (refers to losses during compression, when some of the energy is not stored as elastic potential energy but is converted into heat).

The frequency of the beam also plays a key role in determining the absorption of the ultrasound. Higher frequencies lead to frictional heat and subsequently to energy absorption. Therefore, the absorption ultrasound increases with the increase in the excitation frequency. The absorption of acoustic waves in a wide variety of lossy media can be characterized by an empirical power law function of frequency:

$$a = a_0 f^y \tag{3.8}$$

In Eq. (3.8), a is the absorption coefficient in units of Npm^{-1}, a_0 is the power law pre-factor in $Np\left(\frac{rad}{s}\right)^{-y} m^{-1}$ and y is the power law exponent. The reported values of absorption coefficient can be also found with units $dB/(MHz^y cm)$.

The time taken by the medium particles to revert to their original mean positions within the medium due to the displacement caused by an ultrasound pulse is known as the “relaxation time”. Its value is dependent on medium’s properties and excitation. When the relaxation time is short, vibrating particles revert faster to their original positions. When the relaxation time is long, the particles would tend to get to their original positions slower. The absorption of ultrasound would be increasing with increase in the length of the relaxation time. Longer the relaxation time, higher the absorption of ultrasound. The relation between the absorption per wavelength, a_{rel} and the relaxation time T, is given by eq. (3.9), where f is the frequency in Hz.

$$a_{rel} = \frac{Tf}{1 + (Tf)^2} \tag{3.9}$$

Impedance

Every material has a characteristic property to transport the energy of a mechanical wave. Acoustic impedance is the acoustical property that represents the ability to resist to the mechanical energy transportation. It is defined as the product of the sound-speed and the density of the material, as shown in eq. (3.10). It expresses the resistance of the medium to the acoustic wave propagation through the interface of different media.

$$z = pc \tag{3.10}$$

where p is the density and c is the sound speed of the medium. The changes of impedance

3.1.3.Ultrasound propagation in inhomogeneous media

To describe the ultrasound propagation model, we use the theoretical background of ray theory of sound propagation in inhomogeneous media from [148].

Attenuation

In an ideal isotropic material, the acoustic pressure of a travelling sound wave remains constant and, hence, the energy is conserved. However, if the material has more continuity inside, the attenuation phenomenon takes place within the material. The attenuation can be occur by means of absorption, scattering and beam spreading. It can be represented by a decaying exponential and is always dependent on the signal's frequency. Every acoustic propagation in a homogeneous or non-homogeneous media can be characterized by an attenuation coefficient, expressed by:

$$a(f) = \frac{8.686}{h}\, ln \frac{A_{ref}(f)}{A(f)} \tag{3.11}$$

where h is the thickness of a material specimen, $A(f)$ is the transmission amplitude and $A_{ref}(f)$ is the amplitude of the measured reference on frequency.

Transmission & Reflection

When a wave is transmitted through the interface of two media, the physical properties of the materials surrounding the interface determine how much of the energy is transmitted through this junction. Figure 3.2 shows the possible trajectories of an incidence pulse propagating in inhomogeneous media. The efficiency of the energy transfer from one medium to the next is given by the ration of the two impedances. The transmission coefficient T is determined as:

$$T = \frac{2Z_2 cos\theta_i}{Z_2 cos\theta_i + Z_1 cos\theta_t} \tag{3.12}$$

The relative amplitude of the wave that is reflected back and its magnitude can be expresses as reflection coefficient R:

$$R = \frac{Z_2 cos\theta_i - Z_1 cos\theta_t}{Z_2 cos\theta_i + Z_1 cos\theta_t} \tag{3.13}$$

where θ_i and θ_t are the incidence and refraction angles, respectively. Z_1 and Z_2 are the acoustic impedances of the two materials.

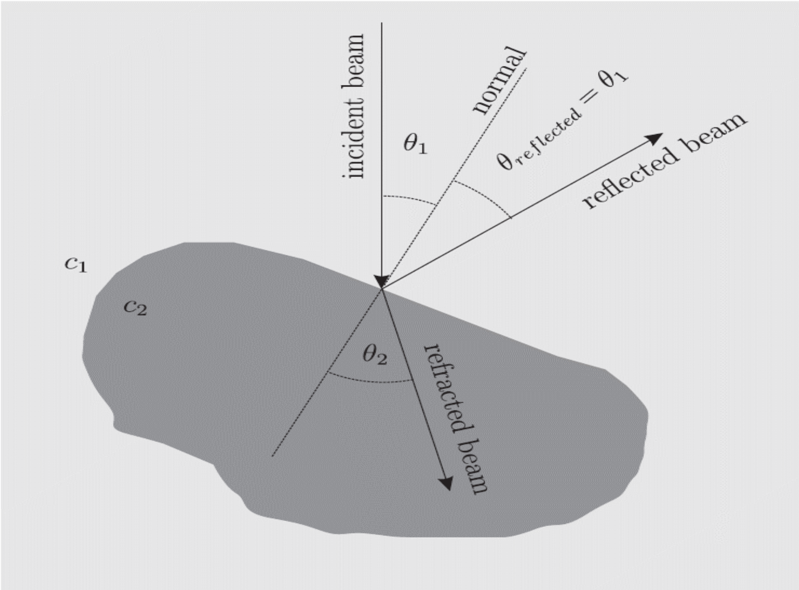

Figure 3.2 Transmission, reflection, and refraction of the acoustic wave [149].

Scattering

Scattering is produced when an acoustic wave travels through an inhomogeneous medium. Regions with different acoustic impedance (also known as scatterers) produce scattering. In those cases, part of the wave energy is diverted. The amount of scatter produced depends basically on two main factors [150]:

- The ratio between the acoustic wavelength and the size of the scatterers of the medium.
- The impedance differences between the background medium and the scatterers.
- The density of scatterers in the medium.

Depending on the ratio between the wavelength and the scatterer’s size, three types of scattering can be defined:

Case 1 (Wavelength « scatterer’s size): Specular scattering takes place when the surface of interaction is smooth. As a result, a considerable amount of acoustic energy will be reflected away or back (the later occurs in the case of normal incidence) to the transducer.

Case 2 (Wavelength > scatterer’s size): Diffuse scattering originates when the wave interacts with a rough interface and the details that causes roughness are smaller than the given wavelength. The wave’s energy will be diverted in many different directions and a minimum portion will be reflected back in the same propagating trajectory of the original wave.

Case 3 (Wavelength ≈ scatterer’s size): Diffractive scattering occurs by the scattered signal’s emission in several directions. As a result of the spatial variations, interference patterns are produced leading to reinforcement or cancellation of the wave.

Diffraction

When the incident acoustic wave interacts with an infinite or practically infinite interface between two different media, as we mentioned, only reflection and refraction occur because. In those cases, the interface acts as an acoustic barrier. The region beyond the frontier is called acoustic shadow zone, as it becomes acoustically obscured due to the interface’s presence. However, when an incident wave’s wavelength is finite in comparison with the sizes of the frontier, the wave will spread out and bend around the interface’s edges. A similar phenomenon is observed when that frontier presents small openings.

This phenomenon causes the wave paths’ bending. Consequently, regions that would have been shadowed otherwise will experience the presence of the wave as well. The amount of diffraction depends on the size of that interface or size of the opening, the distance to the source and the acoustic wavelength (or frequency f). Diffraction is enhanced at low frequencies, i.e., for wavelengths that are long when compared to the interface. On the other hand, if the wavelength is negligible compared to the size of the interface, diffraction is minimal. In addition, the closer the source is located to the barrier, the larger becomes the shadow zone on the other side of the interface.

Refraction

When an ultrasonic wave passes through an interface between two materials with different acoustic impedances both reflected and refracted waves are produced. Snell's law describes the relationship between the angles of the refracted, reflected and transmitted waves with the speeds of the propagation media, shown in Figure 3.2. The angle of the transmitted wave will vary according to the expression, where θ and c are indicated in Figure 3.2:

$$\frac{\sin\theta_1}{sin\theta_2} = \frac{c_1}{c_2} \tag{3.14}$$

3.2. **USCT hardware system**

Two systems have been used in experimental procedures in this thesis. The two USCT systems are developed by "NETRIX S.A." company and offered for the purpose of mutual collaboration and research.

3.2.1. USCT 1.0

USCT.1.0 is a travel-time tomograph as it provides with raw time-of-flight measurements. Figure 3.3 shows the tomograph and its separate parts, as well as the design of the system. The system consists of 32 active measurement probes which are attached with the sensors and a measurement device which is the main tomograph. All the active probes are connected to the tomograph.

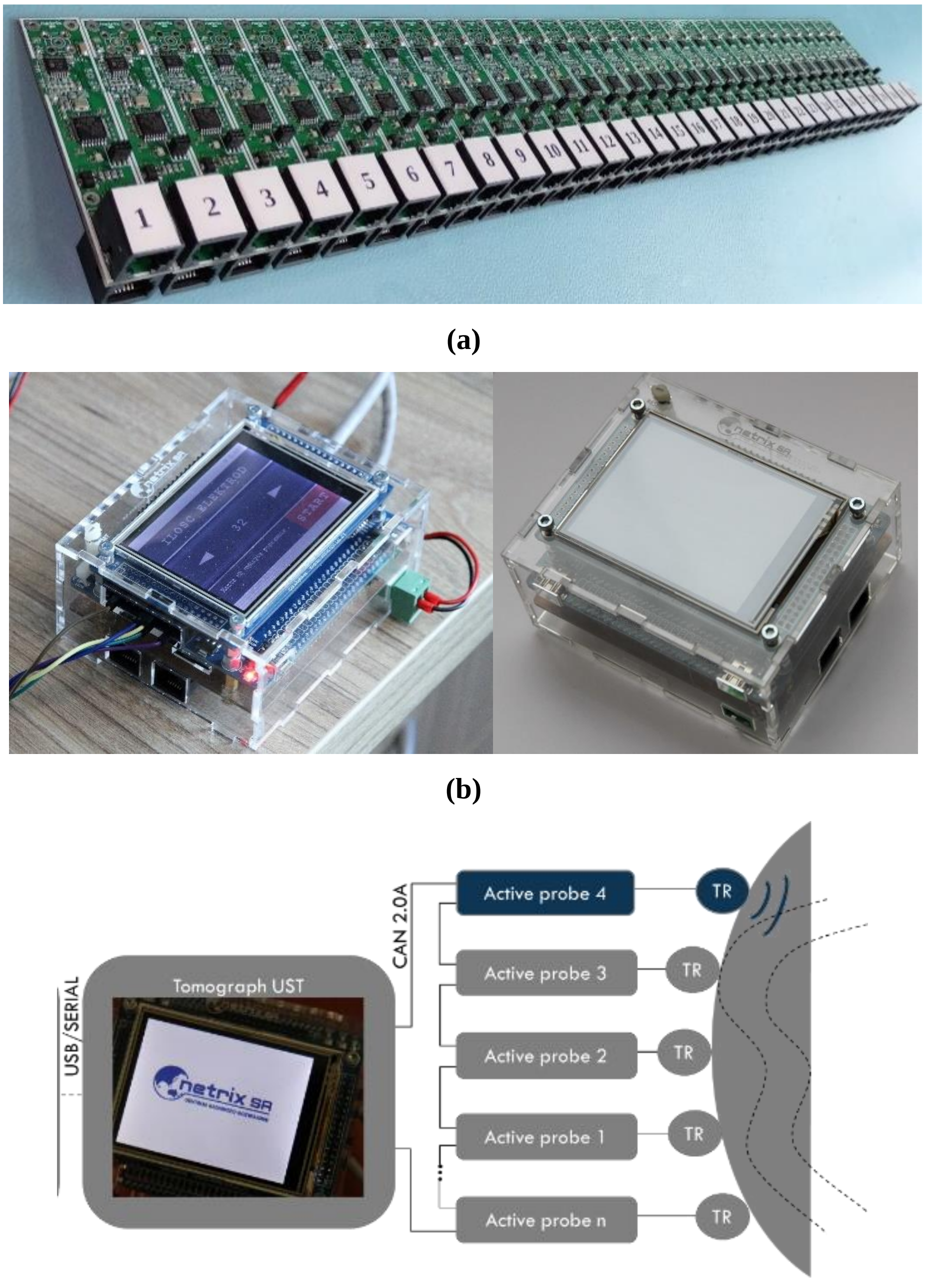

(a)

(b)

(c)

Figure 3.3 Ultrasound tomography device “USCT 1.0”: a) view of composite 32 PCBs of ultrasound probes, b) measurement device, (c) design of the system.

The concept of the developed ultrasound tomograph is based on a parallel data transferring architecture. Its main attribute is the active measurement probes, controlled by, an external module, a CAN bus, as shown in Figure 3.4a.

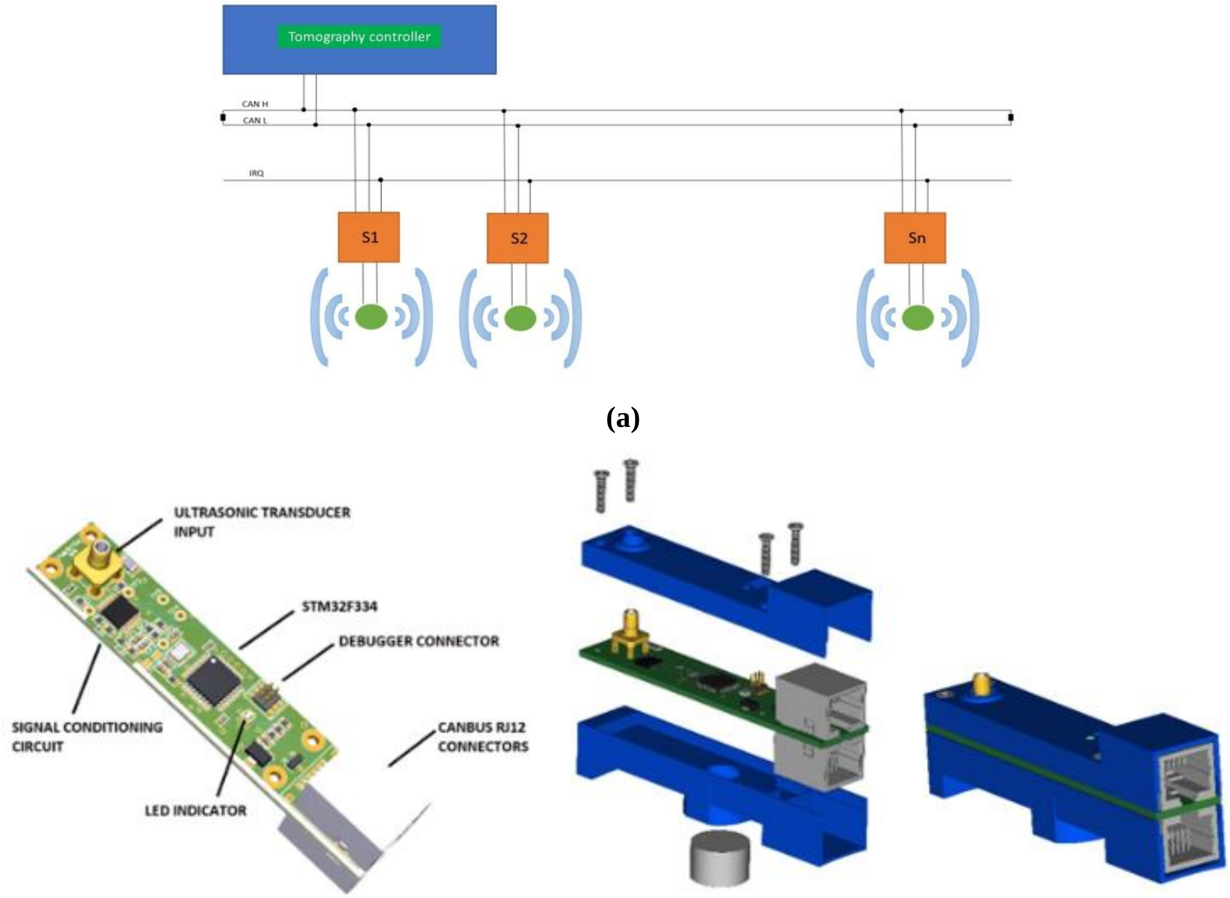

(a)

(b)

Figure 3.4 (a) Block diagram of the ultrasound tomograph. (b) Design of active ultrasonic probe.

This is a less time-consuming transferring and receiving data method. This design can exclude a switching part from the system, while the receivers should be in the "receiving mode". Subsequently, a multiplexer introducing additional delays is neglected. Active measuring probes have been designed and used which are divided into digital and analogue parts. Active probes measure the time individually from the moment the signal is sent until it is picked up by individual transducers. We assume that this is the time in which the pulse overcome the distance between the probes. Note that the time recorded is the time that the propagating pulse needs to surpass the ROI. This system measures the time of the first arrival pulse, as it focuses on transmitted signals. The digital part is responsible for sending measurement data to the tomography controller, via the bus. The analogue part has been adapted to work with a piezoelectric transducer operating at 40 kHz, as shown in Figure 3.4b.

Transducers of MHz of excitation frequency are inappropriate for the tomographic application in which we are aiming, because of their narrow directivity. Tomographs equipped with a high number of sensors can use high frequencies of MHz, but this is not an option for a system that aims to optimize the image reconstruction time. Usually in-line tomographs aim for a minimum possible quantity of sensors, as other than that could lead to extensive data handling, transferring and computation time. Sensors of few hundred kHz can have a better angular coverage. In this work, piezoelectric transducers of 40 kHz are used. The active probe can work both as a receiver of an ultrasonic signal and as a transmitter. The main controller of the tomograph is responsible for managing the measurement sequence, setting the active probes in the transmit/ receive mode as well as storing collected results from the other probes. The probes are designed so that they can be placed very close to each other. Power lines, communication buses and break lines were carried out using RJ-12 cables [151].

Reverberation time is the time required for the sound to completely decay in a closed space. In a tomographic concept of consecutive excitations, the long reverberation time would introduce problems as remaining vibrations would convolute with excited pulses. The time of one measuring frame depends on the reverberation time. Consecutive sensor actuations could be undertaken if pulses are not completely attenuated. Thus, the reflections caused even by the tank's wall can extend the time of a single measurement. For example, these times are of hundreds of microseconds order, while the reflections/backscatters of ultrasonic waves last several milliseconds. Depending on the number of measuring probes, the time required to create one image will be manifold the time of a single measurement. In the case of the test container with 32 measurement probes, obtaining data for one image take about 240 msec. In this way, the temporal resolution of the system is about 4 frames per second (fps), which does not account for reconstruction algorithms time to be performed. For inline monitoring purposes, the image reconstruction also needs to be fast. By using a precalculated sensitivity matrix, following a single-step reconstruction like filtered LBP and also using a not very dense discretization grid, the imaging software's temporal resolution is at 5 fps on a good CPU, namely faster than the data collection. In this case, the system's overall temporal would remain at 4fps. In the case of an iterative algorithm like SBTV a GPU or FPGA implementation would be crucial for tackling computational delays. Moreover, optimizing the SBTV's code for on-line monitoring would be advantageous.

While an active probe sends an ultrasonic signal of 5 cycles (tone burst), the rest of the probes are in receiving mode. Active probes measure the time from the moment the signal is sent to when it is picked up by individual transducers (TOF). The sequence repeats until every probe produces a signal, and therefore, their respective times are collected. Figure 3.5a shows the signal waveform of one pair of transducers and 3.5b shows the trajectory of the transmitted and reflected recorded signals.

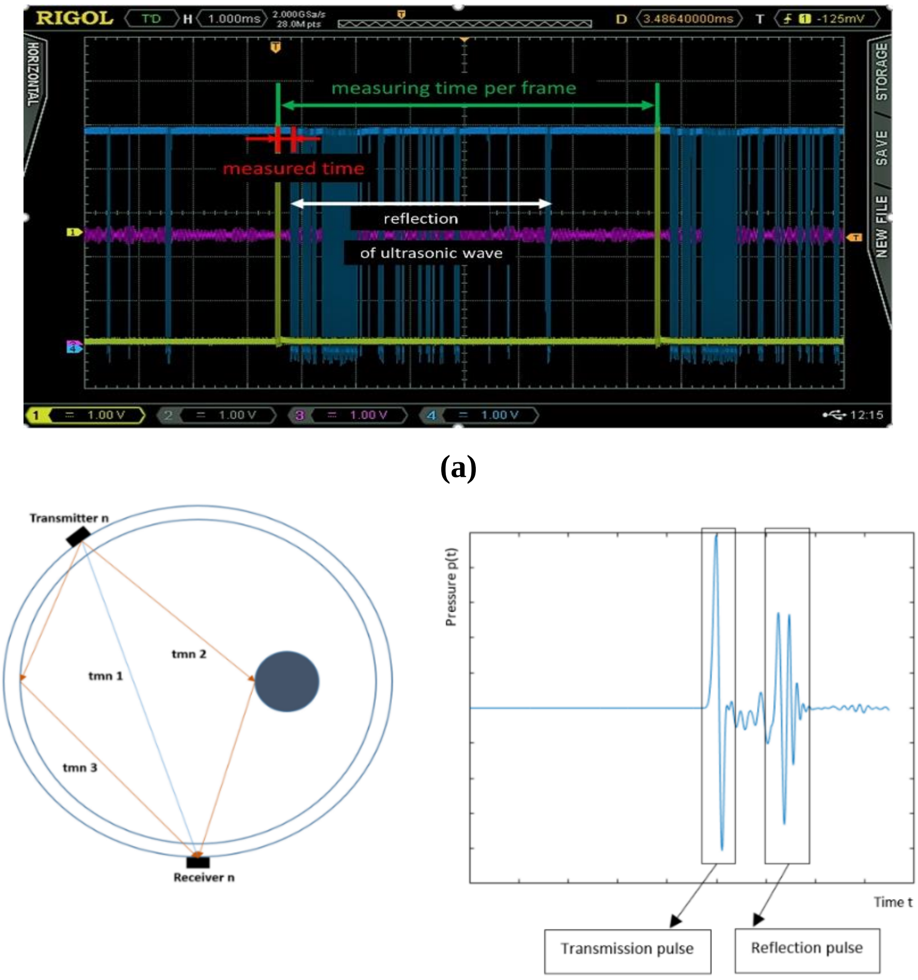

(a)

(b)

Figure 3.5 (a) Display via digital oscilloscope measurements of the excited, acquired and filtered signal. (b) Schematic of generated pulse's three different propagating paths. The circular perimeter displays the tank and the dark blue circle inside it displays the object. The lines represent the three different paths as transmission 1,2 and 3 ("tmn1", "tmn2", "tmn3"). The form of a received waveform is also presented, at right.

A rectangular signal is fed to the ultrasound transducer to force transmission. The obtained signal is also transformed into a rectangular signal (processed signal) so that it can be read and sent to the microcontroller. The red segment is the measured delay caused by transmission to the control unit. Thanks to the active measuring probes, transfer of analogue signal is reduced to a minimum, and interferences reduced. The probes communicate with the main unit via the digital CAN bus. The concept of an active probe enables the switching system to work independently from the rest of the system. This type of tomography is suitable for processes that use substances in the same material phase, adapted for ultrasonic transmitted signal.

3.2.2. USCT 3.0

The USCT 3.0 ultrasonic tomograph is a full-waveform and it has a configurable range of settings. It can provide raw full-waveform data (full-waveform mode) or processed TOF and amplitude values of the travel-time pulse (transmission mode). It also offers adjustable features on the acquisition's wavelength range. These settings are adapted to the needs of the specific process as they significantly affect the data acquisition time. For example, the transmission mode is a lot less time-consuming than the full-waveform mode due to the size of the processed data. Transmission mode can offer a data acquisition frequency of 4fps, while full-waveform mode offers 0.08 fps. Therefore, the settings adjustment depends on the investigation process and the range of measured data. Regarding real-time monitoring, the tomograph is preferably set to transmission mode.

The tomograph in transmission mode measures signal' travel-time and signal amplitude. The device automatically finds the minimum and maximum values of the signal, based on which it converts the percentage value to the numerical value of the ADC converter. The comparator threshold works only in the signal area beyond the value specified by the following parameter. The moment the signal exceeds the comparator threshold, the measurement window opens. The most considerable amplitude value from this area is stored and processed to compute its time-of-flight. The tomograph in full-waveform mode provides the full-waveform offering adjustable sampling frequency option.

The hardware design provides 84 measurement channels for possible use. The system consists of eight four-channel measurement cards connected by an FD CAN bus with a measuring module, which is a bridge between the microprocessor measuring system and the panel. The measurement module is a bridge between a microprocessor measuring system and a touch panel or external control application, as shown in Figure 3.6. It monitors the course of the measurement, stores parameters, controls the high-voltage converter, and switches the bus.

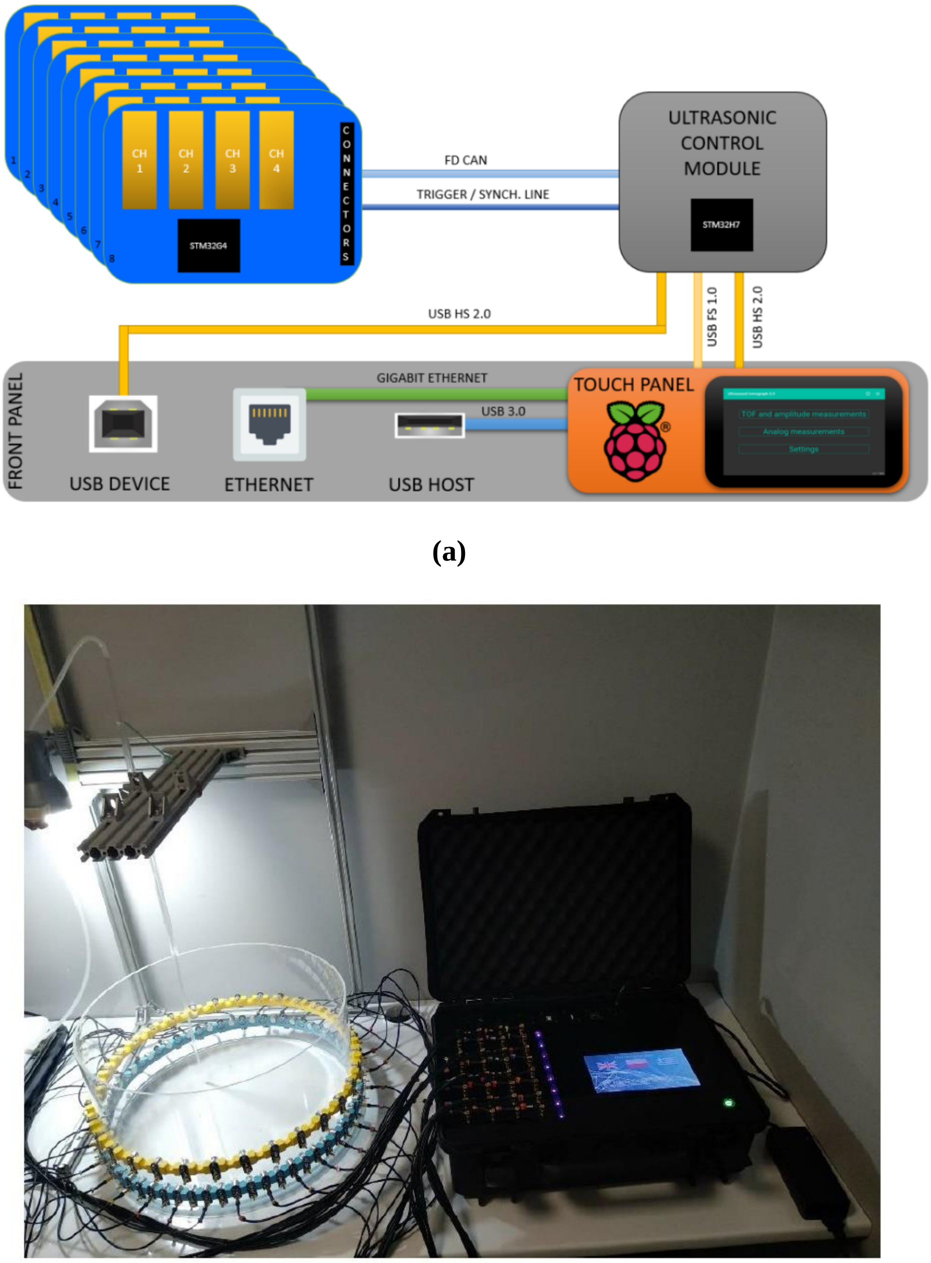

(a)

(b)

Figure 3.6 (a) Ultrasonic tomograph block diagram. (b) Ultrasound tomographic USCT 3.0 system attached in tank.

The touch panel was made using a Raspberry Pi 4B 2GB RAM board and a 7-inch capacitive touch screen. The most crucial data buses have been led to the front panel of the device. The four-channel measurement card was made in a modular manner.

Each sensor has its signal conditioning and measurement circuit, so all measurements for each excitation can be done simultaneously. The designed measuring cards have a maximum sampling rate of 4MBPS per channel. Each channel is equipped with a separate generator of AC rectangular waveforms with amplitude up to 144Vp-p and an instantaneous current capacity of 3A. It is possible to sample the analogue signal on all channels simultaneously. Three eight-order filters are built into each channel for effective harmonic filtering, triggered by analogue keys: a 40kHz band-pass filter with 40kHz centre frequency and 50kHz bandwidth for 40kHz ultrasonic transducers, a 350kHz band-pass filter with 200kHz centre frequency and 200kHz bandwidth for 300kHz and 400kHz transducers, and a 1MHz high-pass filter with 1MHz cut-off frequency for 1MHz transducers. A circuit has also been designed to convert the alternating analogue acoustic signal to a parameter with switchable configurations for three frequency ranges suitable for 40kHz, 300kHz, 400kHz and 1MHz transducers. The unit has two-stage gain control on each channel. The first stage from +7.5dB to +55.5dB (AD8331), while the second stage from +6dB to +36dB (6 settings - STM32's built-in PGA). Each channel is shielded, so the channels are very well isolated from each other. The device’s implemented signal filtering is particularly important. Built-in filters allow to get rid of harmonics of other frequencies, but they also affect the signal strength.

The sections of amplifying and filtering analogue signals were made on small separate PCBs. For better isolation of individual channels, it is possible to mount a shielding housing on each module. In addition, a four-channel high-rectangular-voltage generator was designed at the bottom of the plate. The generator circuit consists of four four-channel MOSFET drivers connected to double H bridges (TC8220). A single section can generate a three-stage square wave signal (Vpp–GND–Vnn). Depending on the power source, the circuit can generate voltages from +100 V to −100 V. In the presented prototype, the generator circuit is powered by a symmetrical voltage of +/−24 V. Therefore, the maximum instantaneous current efficiency of MOSFET keys is 3 A. The converters were synchronized with a built-in counter in the STM32G474 microcontroller. The generation of appropriate waveforms controlling the MOSFET keys of the four-channel high-voltage generator was carried out by cascading three meters. The microcontroller generates 4 square waveforms (for a positive key, for a negative key, and for two keys connected to the device’s ground). The control signals travel directly to all four generator sections. Each section has an input that activates or deactivates a given section. Thanks to that, it is not necessary to generate control signals separately for each section. The analogue module is a system that amplifies the ultrasonic transmitting signal. The proposed design has an integrated AD8331 amplifier with gain control using an external DAC converter and a system converting the AC signal to ADL5511 envelopes and two THS4521 differential amplifiers. Due to the distance between the modules and the microcontroller and the presence of a high-voltage generator on the same PCB, the final output signal from the module is a symmetrical differential signal, which reduces the amount of noise. The sampling frequency is 0.25 samples per micro-second, which results directly from the ADC converter speed. A Built-in envelope converter was used for converting an analogue acoustic signal to the envelope.

3.3. **Data acquisition & pre-processing**

Typical data acquisition method for USCT systems is the full-waveform method. Full-wave algorithms use these data. On the other hand, geometrical acoustic methods are based on single TOF and amplitude values which has been derived by the full-waveform. The two methods have significant differences on execution time and on image quality, as it is stated below at section 3.4. Figure 3.7 a full-waveform signal from a tone-burst excitation of 400 kHz. The sensors are positioned in a distance of 10cm of each other. For each pair emitter-receiver, a signal similar to the one depicted in the figure is obtained. As result, a total of N emitters- N receivers signals are recorded for all the possible pairs employed, where N emitters is the number of sources that will emit in turn and N receivers is the number of receivers employed per emitter. Each individual signal contains information of the scanned medium due to its interaction with structures with different SS and AA. Every signal can be characterized by two main parameters, its time of flight (TOF) and its amplitude. This will, of course, reduce the information of the signal, which typically could contain hundreds or thousands non-zero values. The use of only two parameters of the wave, is an important simplification. There are approaches for image reconstruction for which this is enough information (geometrical acoustic methods). Nevertheless, other approaches consider all the wave signal (full-wave algorithms).

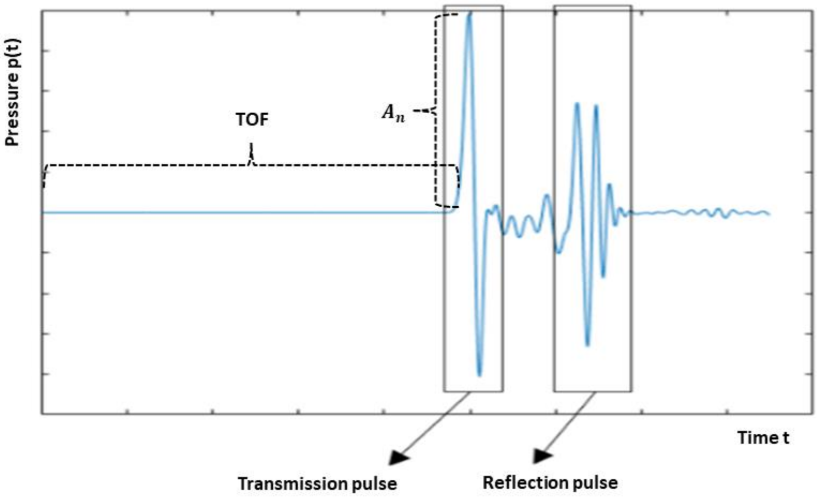

Figure 3.7 Schematic representation of the received signals for a pair of transducers. Time-of-flight and amplitude of the first arrival pulse are indicated on the waveform.

The measurement data for transmission tomography include time-of-flight (TOF) data and Amplitude Attenuation (AA) data. TOF measurement data come from the subtraction of background data from the full data, and they define the travel-time delays in microseconds (μs).

$$TOF = TOF_{full} - TOF_{back} \tag{3.15}$$

AA measurement data [7] are computed by

$$AA = \frac{1}{f_c} \ln\left(\frac{AA_{full}}{AA_{back}}\right) \tag{3.16}$$

Where AA_{back} is the reference amplitude data and AA_{full} is the data when the domain changes from background, namely the data that come during the process and describe the changes in the acoustic field. f_c is the center frequency of the excitation pulse. A_{back} is the amplitude of the signal of reference (background) measurements (e.g. when there is only water in the field of view) and A_{full} is the amplitude at the same receiver from the experimental measurements (e.g. with the phantom located in the FOV).

3.4. Reconstruction algorithms for USCT

In this section, the main algorithms of reconstruction employed in USCT are described. The main algorithms for USCT reconstruction are based on transmission, diffraction and reflection features. This thesis investigates analytic single-step reconstructions like filtered LBP, regularization methods like Hybrid Tikhonov and Total Variation algorithms and finally an iterative multimodality USCT algorithm (proposed in chapter 8). The main reason for this, is the need of quick and accurate reconstructions of the measured area, as the scope of this thesis is the development of methods that could be applied to in-line/ on-line measurement concepts.

Geometrical acoustics

Geometrical acoustics is the most employed approach for recovering real and synthetic USCT data, either for industrial or clinical applications [152]–[156]. These methods offer high computational efficiency providing fast image reconstructions. The simplified numerical approximation obtained by these methods, makes them computationally high-efficient. High temporal resolution is crucial in all fields of imaging, especially in dynamic industrial processes, turning geometrical acoustic into a standard for on-line USCT industrial monitoring methods. These numerical methods use only a part of the full-waveform information (i.e. TOF to obtain the sound-speed maps, or AA to obtain the acoustic absorption maps) instead of using the full-waveform, instead of using the full-waveform. Thereafter, geometrical acoustics have been defined with a supremacy in time-execution but with also the lack of resolution comparing with other computationally intensive methods like full-wave reconstruction or full-waveform inversion (FWI) methods [3].

Geometrical acoustics consists of straight-rays approximation method and bent-rays method. Straight-rays approximation method describes the energy propagation of the wave along rectilinear paths. The use of straight-rays is based on inverse Radon transform [157].

These straight-rays algorithms exhibit very fast performance and present real time imaging capabilities. If variations of density and sound-speed are negligible, the first-arrival pulse trajectory between a transmitter and a receiver will be a straight line. Making this assumption, refraction, diffraction and interference are not taking into account and the sound travel path considered as a straight line. Thus, the straight-ray approximation is considered as a very simplified model for sound propagation that will be on the other hand, extremely efficient from a computational point of view. On the other hand, bent-rays method takes into account the medium's physical processes. They account for refraction and diffraction effect. A comparison between straight and bent algorithms was established in [158]. It is concluded that in two-dimensional reconstructions, bent rays can present a fast performance but, they are around 40, in average, times slower than straight-rays. Regarding three-dimensional reconstruction, the optimization in image quality does not compensate the computational complexity. Therefore, majority of the algorithms employed for industrial applications use straight-rays to account for direct transmitted signals.

USCT images produced by a geometrical acoustic algorithm can be significantly affected by an inaccurate estimation of the first-arrival pulse's TOF and amplitude. These estimations depend on two main factors.

- The mechanical precision of the experimental setup used for data acquisition.
- The efficiency of the methods used to characterize the first arrival signal.

The estimated features of the first-arrival pulse are used as an input in a geometrical acoustics reconstruction algorithm.

Straight-rays approximation

Transmission reconstruction would take place via measuring either travel-time or the amplitude decay of the first-arrival pulse [159]. The most used approximation for transmission USCT is the ray-based methods. It is fundamental in most tomographic schemes, as the line integral defines the path of a high frequency propagating pulse between an emitter and a receiver. It is a simplified approach, which does not account for the diffraction effect caused by non-homogeneous medium. Considering a homogeneous medium with no absorption and density variations, the changes produced by the wave's propagation can be described by eq. (3.17).

$$\frac{1}{c^2}\frac{\partial^2 p(r,t)}{\partial t^2} - \nabla^2 p(r,t) = 0 \tag{3.17}$$

where p is the pressure and c is the sound-speed of the medium. Eq. (3.18) had a simple periodic solution:

$$p(r,t) = A(r)e^{-if(\theta(r)+t)} \tag{3.18}$$

where $A(r)$ and $\theta(r)$ are the wave amplitude and phase at position r respectively. When eq. (3.18) is introduced in eq. (3.17), the following relation can be obtained:

$$|\nabla^2\theta(r)| - \frac{1}{c^2} = \frac{\nabla^2 A}{Af^2} \tag{3.19}$$

The Eikonal equation can be obtained by taking a high frequency approximation of eq. (3.19). In that case, the Laplacian of the wave's amplitude can be less relevant than the square of the frequency. Subsequently, eq. (3.20) is formed:

$$|\nabla^2\theta(r)| = \frac{1}{c^2} = S(r)^2 \tag{3.20}$$

where S describes the slowness of the field, which is the inverse of the sound-speed ($S = 1/c$). Eq. (3.20) describes the wavefront of the pulse and its propagation. Wavefront is the imaginary surface that represents the corresponding points of a wave with equal phase. $\theta(r)$ is the wave's time-of-flight required for it to reach domain's point r.According to Fermat's principle, the sound travels along the path that takes the shortest time. Eq. (3.20) describes the time that is needed by the wavefront to reach any point r.

3.4.1. Transmission Reconstruction

When diffractions and reflections can be ignored, USCT can work on transmission mode which is very similar to x-ray CT. In both cases, a transmitter illuminates the object and a line integral of the attenuation can be estimated by measuring the energy on the far side of the object. Although, a remarkable difference between ultrasounds and x-rays is the capability in ultrasounds to measure the exact pressure of the wave as a function of time or the TOF of the signal, because the propagation speed is much lower than in the x-rays [160].

In mathematical aspect, ultrasound transmission tomography (UTT) image reconstruction could be handled as a linear inverse problem. Acoustic transmitters and receivers surround the region of interest (ROI). UTT is used to reconstruct a cross-sectional image of an object from projections consisting of line integrals. The acquisition pulses considered as attenuated or delayed signals by the existing inclusion during their pathway inside the region of interest. The pathways of the pulses, expressed as line integrals inside the region-of-interest (ROI), combined either with the TOF or amplitude measurements to generate images.

Traditionally, the propagation of ultrasonic wave is considered as a straight line from transmitter to receiver in the UTT mode. Thus, spherical wave (cone-beam) could be considered as an infinite sum of plane waves (fan-beam). Each spherical wave can be approximated by a cone of rays and subsequently, every plane wave by a fan of rays. We consider the 2D tomographic setup illustrated in Figure 3.8.

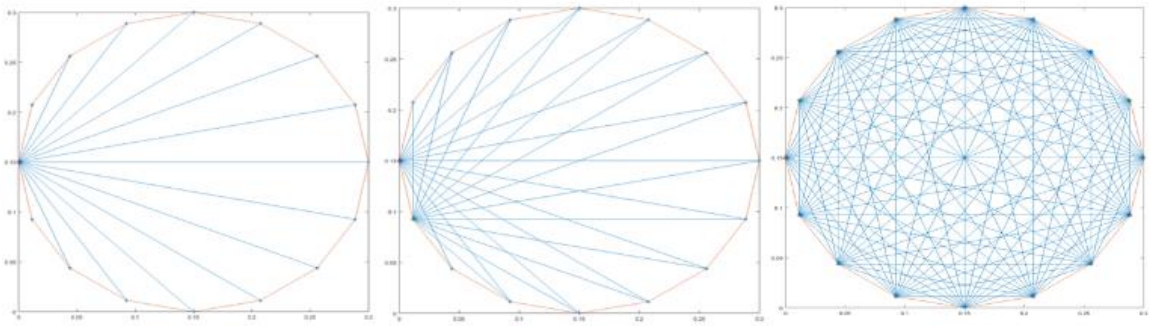

(a) **(b)** **(c)**

Figure 3.8 A simulation of the tomographic excitations with ray propagation. There are 16 sensors circle-wise. (a), (b) First and second sensors emissions, respectively. (c) All the ray paths between the 16 sensors are depicted.

At left, an image of single excitation is displayed, a double excitation is displayed in the centre and at right a full excitation with all the pulses’ trajectories is displayed indicating the full scanning of the ROI. All the excitation used a beam of 1800 angle degrees.

The necessity of efficient and fast forward and back-projection algorithms was recognised immediately after the establishment of the CT and other tomographic methods. A few different approached have been employed in the subject, called as “ray-driven” methods (ray casting). In these methods the source and the detector are connected with lines according to the acquisition sequence. The projection value is calculated as a weighted sum of all the pixels that line intersects. The exact type of the weighting varies with the different methods, but mainly intersection methods consider the intersection length (e.g. the portion on the line that goes through the pixel is assigned as a weighted value) [161]. Siddon’s and Josheph’s method are the two classical approaches [162], [163]. A variant of this approach is a strip-integral based method, assuming a widder ray equally sizes to the transducers’ dimension. The authors proposed to use a triangle’s subtraction method for the calculation of the weighted value [164]. Interpolated methods are ray-driven methods applying a fixed length sampling to the ray as they consider a continuous plane instead of a discretised grid. A simple algorithm is obtained if the interpolation is chosen to be tri-linear and the integration through the continuous volume is approximated by summing values at equidistant points along the ray [165]. Figure 3.9b depicts the interpolated ray-driven methods [166].

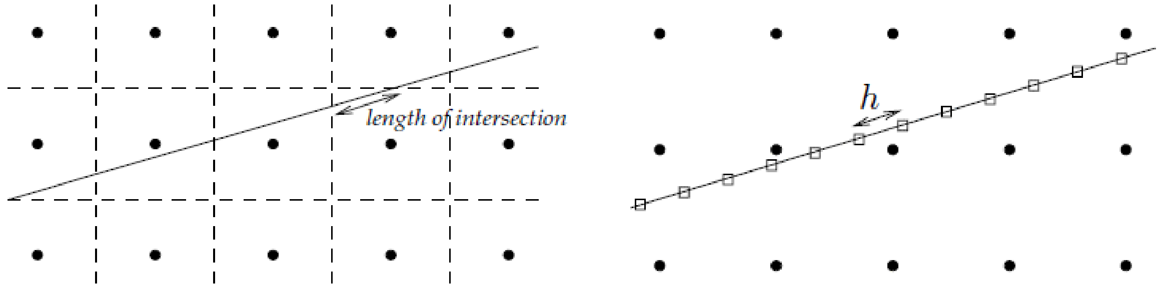

(a) **(b)**

Figure 3.9 Two methods of ray-pixel intersection. Triangles indicate bi-linear and squares tri-linear interpolation. Models of tomographic projections. (a) Siddon’s method, (b) sampling methods[165].

Sound-speed mapping

Sound-speed transmission tomography methods have been popular in research and development of USCT. The tomographic system measures the time-of-flight of transmitted pulses. TOF values are calculated by measuring the arrival time of the first transmitted pulse of the captured waveform. The most used approximation for USCT is the ray-based method. The ray trajectories are calculated by solving the following vector equation and accounting for very high emission frequencies [167]. The below equation is an alternative to eq. (3.1).

$$\frac{d}{ds}\left(\frac{1}{c}\frac{d\boldsymbol{x}}{ds}\right) = \frac{1}{c^2}\nabla c \tag{3.21}$$

where s is the arc length along the ray trajectory, $\boldsymbol{x}$ is the position vector, and the c is the speed of sound. This, together with the source position and the initial take-off angle, fully specifies the ray. Once the reference and experimental data are compared, it is necessary to account with a method to use the observed differences to recover the characteristics of the medium. An analytical solution to the reconstruction problem was originally proposed by Radon's theorem. The theorem proved that any two-dimensional object can be reconstructed uniquely from an infinite set of its projections. A projection, using the Radon formulation, is the line-integral, along a given direction in the object. In the case of a uniform sound speed model that only depends on the depth, one can use a convenient parameterisation for the rays which is based on the ray-approximation approach.

$$T = \int_{ray} s(x)\, dl \tag{3.22}$$

where, the above integral is based on a single ray path, s denotes the slowness domain $s = c^{-1}$ and finally T gives the time of flight of the pulse. Assuming that the ray-path is intensive to a small slowness perturbation, the perturbation in travel-time is given by the path integral of the slowness perturbation along the ray.

$$\delta T = \int_{ray} \delta s(x)\, dl \tag{3.23}$$

Since travel-time perturbations given by eq. (3.23) are insensitive to slowness perturbations anywhere off the geometric ray-path, the sensitivity kernel is identically zero everywhere in space except along the ray-path where it is constant. The implication for ray-based travel-time tomography is that travel-time perturbations should be back-projected purely along the ray-path. A tomographic approach consists of many of these rays, whose amount depends on the angle of the emission beam. All these equations of rays form a system of linear equations, the so-called forward problem. The measurement data formed from subtraction between reference, TOF_{back}, and experimental data, TOF_{full}, and they define the travel-time delays in microseconds, eq. (3.15). For a generalised tomographic problem, the above eq. (3.23) can be expressed as:

$$\Delta T_m = \sum_{n=1}^{N} A_{m,n}\ \Delta s_n \tag{3.24}$$

where ΔS is the slowness perturbation, A is the modelling operator which describes the sensitivity distribution and ΔT is the travel-time distributions. Modelling operator is assigned by the weighting values of ray-pixel intersection described above multiplied by the ray's length value. The multiplication of modelling operator (expressed in length values) with the measurements (expressed in TOF values) results to the approximated sound-speed values distribution.

Travel-time mapping

In the case of a travel-time delays model, one can use a convenient parameterisation for the rays which is based on the ray-approximation approach.

$$\Delta T = \int_{ray} \Delta t(x)\, dl \tag{3.25}$$

where, the above integral is based on a single ray path, ΔT denotes the travel-time delay measurements (e.g. difference measurements resulting from the subtraction of reference from real experimental data) and $\Delta t(x)$ represents the travel-time delay distributions. The linearised expression of the above problem is given by equation below:

$$\Delta T_m = \sum_{n=1}^{N} A_{m,n}\ \Delta t_n \tag{3.26}$$

where ΔT_m is the travel-time delays produced by the n_{th} _cell, 1<n<N and $A_{m,n}$ is the weighted value that describes how much each specific wave-ray affects every pixel (ray-pixel intersection). $A_{m,n}$ is normalised in the range of [0 1] by the sum value in every pixel of the domain and it is described below in eq. (4.9). Finally, t_n defines the domain of travel-time delays distribution. This model is simpler than the sound-speed model as it avoids to account for the length of the rays and subsequently do the transformation the sound-speed domain.

Acoustic attenuation mapping

The amplitude decay method is employed to reconstruct the acoustic attenuation distribution using geometrical acoustics, [112], [168], [169]. Acoustic attenuation mapping can be achieved following an alternative method of sound speed mapping. As it was explained in section 3.1, when the acoustic wave propagates through the medium, it will experience a loss of the initial amplitude by geometrical spreading and by the absorption characteristics of the medium, eq. (3.8). The last statement constitutes the base of the method. Acoustic attenuation can be expressed as a linear function of the excitation frequency.

$$a(f) = a_0 f \tag{3.27}$$

where f is the central frequency, a_0 is the attenuation coefficient and $a(f)$ is the attenuation distribution. In our work the attenuation in water is neglected, as measurements in water considered as reference measurements. Using the former assumptions, a simple expression to formulate the inversion problem for the attenuation reconstruction can be obtained:

$$\Delta M = \int_{ray} \Delta a_0(x)\ dl \tag{3.28}$$

$$\Delta M_m = \sum_{n=1}^{n} A_{m,n} \Delta a_{0n} \tag{3.29}$$

where n represents the scanned pixel, m identifies the receiving transducer, Δa_{0n} expresses the absorption coefficient distribution and $A_{m,n}$ is the sensitivity matrix assigned with weighted values of ray-pixel intersection method. ΔM_m is the measured data and come from the comparison of the arrival pulse's peak of reference (background) and experimental (full) data.

3.4.2. Diffraction Reconstruction

Using a finite frequency (band limited) approximation to the wave equation leads to a sensitivity kernel where the sensitivity of the travel time delay also appears in a zone around the fastest ray path. A number of works have defined sensitivity kernels based on geometrical rules assigning sensitivity within the first Fresnel zone. Forward models based on these types of kernels will be referred to as fat ray-based [19], [170].

Fréchet sensitivity kernels are based on the first Fresnel zone [171]. Fresnel volume or 'fat ray' tomography is an appealing compromise between the efficient ray theory tomography and the computationally intensive full waveform tomography [172]. Using a finite frequency approximation to the wave equation leads to a sensitivity kernel where the sensitivity of the travel time delay also appears in a zone around the fastest ray path. This model assumes that the wave propagation between the source and the receiver has finite high frequency. The travel time is sensitive to an area around the ray-path, typically defined using the first Fresnel zone. The smaller the frequency, the 'fatter' the ray kernel. A weighting function based on the travel-time delay dictates that more sensitivity is attributed to pixels nearer the axis of the Fresnel volume, which is the infinite frequency ray path. The sensitivity then decreases linearly from the axis to zero at the edge of the Fresnel volume. For a regular model grid, the Fresnel zone is defined as the region containing all pixels with sensitivity computed based on the transmitter to receiver distance, the signal frequency, and the background velocity [172]. Figure 3.10 shows the sensitivity maps in our 32-channel system.

The first Fresnel zone is that part of the refracting medium through which energy is transmitted from the source to the receiver within less than a quarter of a period of the ray arrival; thus, this energy interferes more or less constructively. In this approach, a weighting function based on the travel-time delay dictates that more sensitivity is attributed to pixels nearer the axis of the Fresnel volume, which is the infinite frequency ray path.

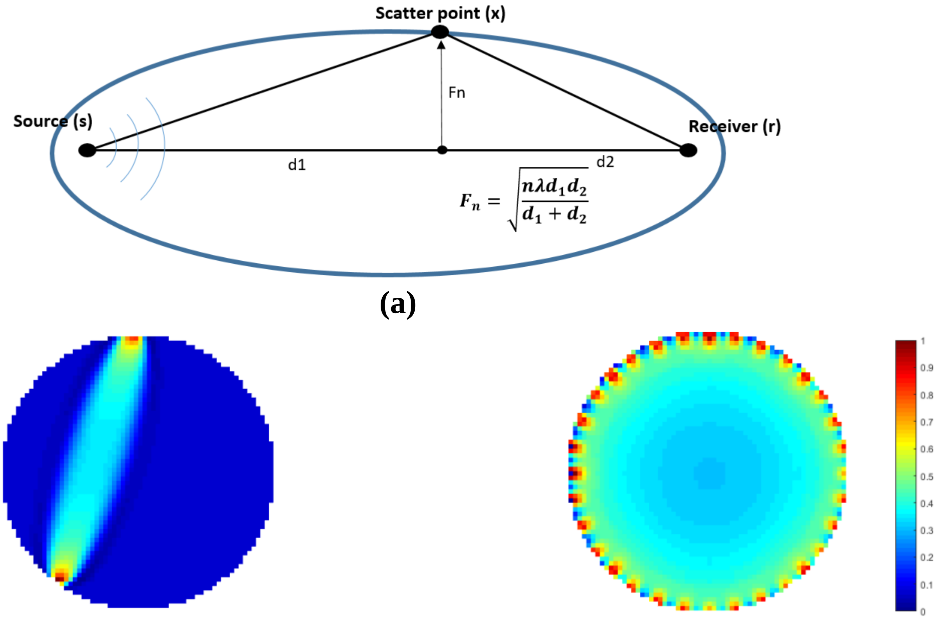

(a)

(b) **(c)**

Figure 3.10 (a) Fresnel zone geometry including the calculation of the radius. (b) Fréchet sensitivity kernel with a centre frequency of 40 kHz. (c) Overall sensitivity matrix plot (sum of all kernels), displaying the sensitivity distribution of the modelled matrix.

To find the first Fresnel zone, we calculate the delay time, Δt, between the first arrival and the arrival of waves that have been scattered at x. The delay time is given in eq. (3.30).

$$\Delta t(x) = t(s,x) + t(x,r) - t_0(s,r) \tag{3.30}$$

Here $t(s,x)$ and $t(x,r)$ are the travel time from the source (s) to x and from x to the receiver (r) and $t_0(s,r)$ is the travel time along the ray path from source to receiver. One can evaluate the times of traveling using ray tracing method. A point x is always within the first Fresnel zone if the corresponding travel-time satisfies the following equation, in which T defines the emitted wave's period:

$$|\Delta t(x)| < \frac{T}{4} \tag{3.31}$$

The following function defines the sensitivity of a Fréchet kernel based on the first Fresnel zone:

$$S(\boldsymbol{x}) = K\ \mathrm{V}(s, \boldsymbol{x})\ \mathrm{V}(\boldsymbol{x}, r)\ \cos\left(2\pi \frac{\Delta t(\boldsymbol{x})}{T}\right)\ exp(-\left(\frac{a\Delta t(\boldsymbol{x})}{\frac{T}{4}}\right)^2) \tag{3.32}$$

In this case S(x) is the sensitivity at x, $V(s, \boldsymbol{x})$ is the amplitude of the wave field at point x propagating from point s (source), $V(\boldsymbol{x}, r)$ is the amplitude at point r propagating from point x (scattered wave) and K the normalisation factor. The sensitivity formula has been developed on the Fresnel zones method [173]. SIPPI MATLAB software (Hansen, Copenhagen, Denmark) has been used to generate these sensitivity kernels [174]. In this work we used Fréchet sensitivity maps described by Buursink et al. [172].

3.4.3. Inverse problem

To explain the inverse problem in ultrasound tomography we use the sound-speed mapping, by using as measurement data the time-of-flight data ΔT. Amplitude data can be always used with the same way to provide an acoustic attenuation mapping. The linear inverse problem in travel-time ultrasound tomography can be defined as the retrieval of the change in time of traveling of the pulse ΔT from a change in the measured boundary acoustic velocity Δs. Eq. (3.33) is a linear equation that describes the forward problem principal concept. System matrix A is computed by the foundations of rays propagation in space, as described in the previous section.

$$\Delta T = \mathrm{A}\, \Delta s + e \tag{3.33}$$

where A is the forward operator and e is the noise in the measurements. Δs is defined as the acoustic velocity profile of the scanned region in different discrete times and Δm as the TOF measurements. If the inverse of A existed, then eq. (3.33) could be solved directly; The inverse problem could be formed as:

$$\varDelta s \approx A^{-1} \varDelta T \tag{3.34}$$

However, traditionally, acoustic tomography presents much smaller number of measurements than the number of reconstructed image pixels. Subsequently, the sensitivity matrix A is not a square matrix and not invertible. Therefore, the problem turns to be ill-posed and non-linear and a common technique to solve it, is to use the transpose matrix of A. This is the so-called “linear back-projection” reconstruction [175].

$$\varDelta s \approx A^{T} \varDelta T \tag{3.35}$$

To reconstruct the image, each sensitivity matrix transpose is multiplied by its corresponding sensor loss value, back-projecting to the image plane individually. Then, these matrices are summed to provide the back projected acoustic velocity or travel-time or attenuation distributions [176].

The inverse problem attempts to determine the acoustic distributions, $\varDelta s$, from a finite number of measurements, $\varDelta T$, shown in eq. (3.35). A mathematical model of a physical model is well posed if:

- For all admissible data, a solution exists;
- For all admissible data, the solution is unique;
- The solution depends continuously on the data.

However, due to the limitation of sensors size and placement restrictions, the number of independent measurements is always less than the number of image elements to be estimated. Thus, the problem to be solved turns to a rank-deficient problem. This makes the unique solutions of such systems non-exist. Furthermore, small changes in measurements could result in extremely large amount of changes in the model estimation, which fails the third condition. Hence, the USCT inverse problem is considered as inherently an ill-posed problem. To overcome such situations, regularization methods are introduced to impose additional information or constrain for stabilization.

3.4.3.1. Hybrid Tikhonov regularization

It is well known that the standard Tikhonov regularization is an effective method to deal with ill-posed problems utilising the conventional L^2 norm. The essence of the method is to transform the solving of eq. (3.35) into an optimization problem [177]. Tikhonov regularization imposes additional information, which is known as a prior, and hence the least square minimization problem incorporating regularization term can be formulated. as below

$$minA(\Delta s) = ||A\Delta s - \Delta T||^2 + a\ ||\Delta s||^2 \tag{3.36}$$

Where $a > 0$, is called the regularization parameter; $||\Delta v||^2$ is a stabilizing item [177].

Usually, the quality of reconstructed image is far from perfect when the standard Tikhonov regularization method is applied. The disadvantage is its excessive smoothness. The effect will remove the detailed information from the reconstructed image and decrease spatial resolution [178]. Most of improvements focus on the design of stabilizing items. Improvement on standard Tikhonov Regularization can be achieved by adding the NOSER regularization [179]. Tikhonov method performs very well with ill-posed problems by reducing noise but it tends to over-smooth the output image as it assumes the solution to be smooth. The NOSER method is very good at position reconstruction but performs worse with noise, which affects the solution more when the object is at larger distances. However, the combination of Tikhonov and NOSER perform well. This leads to a ‘Hybrid Tikhonov’ (HT), which is defined by eq. (3.37):

$$\Delta s = ((A^T \mathrm{A}) + a\,\Gamma + b\ diag(A^T \mathrm{A}))^{-1}\ A^T\ \Delta T \tag{3.37}$$

where A is the sensitivity matrix, Δs and ΔT are the measurement data and acoustic parameter distribution respectively; Γ, the regularization matrix, is the identity and α and b are the scaling parameters of Tikhonov and NOSER respectively [179].

3.4.3.2. Split Bregman Total Variation regularization

Split Bregman Total Variation regularization (SBTV) was introduced by Rudin, Osher, and Fatemi [180]. It is an iterative regularization algorithm. TV de-noising is an effective filtering method for recovering and reconstructing piecewise-constant signals, all while being a deterministic technique, which safeguards discontinuities in image processing tasks [181], [182]. The unconstrained formulation for the linearized model of UST problem as following:

$$minA(\varDelta s) = \left|\left|(\mathrm{A}\,\varDelta s + e) - \varDelta T\right|\right|_2^2 + \ a\left|\left|\nabla\varDelta s\right|\right|_1 \tag{3.38}$$

where a, the regularisation parameter, ∇ is the gradient, $\left|\left|.\right|\right|_1$ is the l_1–norm and, $\left|\left|.\right|\right|_2$ is the l_2–norm.

Previous research has demonstrated the superiority of traditional TV regularization for image quality improvements. However, the penalty term of TV is non-differentiable, and due to this a computational cost and slow computational rate may be caused. The SBTV proposes a good solution to this problem. The split Bregman algorithm, that combines the Bregman distance with splitting technique, was proposed in [183]. SBTV replace the traditional TV term with the Bregman distance, it's consequently able to provide the highly accurate denoised images with a fast convergence rate. Using a constrain as a penalty term, the unconstrained problem is given below:

$$\varDelta s = argmin_{\varDelta s,d}\left\{\frac{\mu}{2}\left|\left|A\varDelta s - \varDelta T\right|\right|_2^2 + a\left|\left|d\right|\right|_1 + \frac{\beta}{2}\left|\left|d - \nabla\varDelta s\right|\right|_2^2\right\} \tag{3.39}$$

Then applying the split Bregman iteration, the method can be formulated as:

$$(\varDelta s^{k+1}, d^{k+1}) = argmin_{\varDelta s,d}\ \{\tfrac{\mu}{2}\left|\left|A\varDelta s - \varDelta T\right|\right|_2^2 a\left|\left|d\right|\right|_1 + \tfrac{\lambda}{2}\left|\left|d - \nabla\varDelta s - b^{\kappa}\right|\right|_2^2\} \tag{3.40}$$

$$b^{k+1} = b^k + \nabla\varDelta s^{k+1} - d^{k+1} \tag{3.41}$$

3.4.3.3. Spatiotemporal Total Variation regularization

Instead of calculating an image based on the sequence of past frames, we propose a temporal image reconstruction algorithm which uses a set of data frames nearby in time. When proceeding the inverse calculation, the common practice is to conduct the inverse algorithm calculations for each frame independently, this approach is not optimal as the redundant information from the previous calculation will be repeatedly used. In order to avoid the redundant information, the Spatial Temporal TV (STTV) algorithm was applied in this thesis to improve the inverse solving process, as such method can use the redundant information over the consecutive frames to accelerate the convergence rate. We chose spatiotemporal total variation, as UST images can be well approximated by a piecewise constant function and consecutives frames are expected to be similar. Figure 3.11 describes graphically the method.

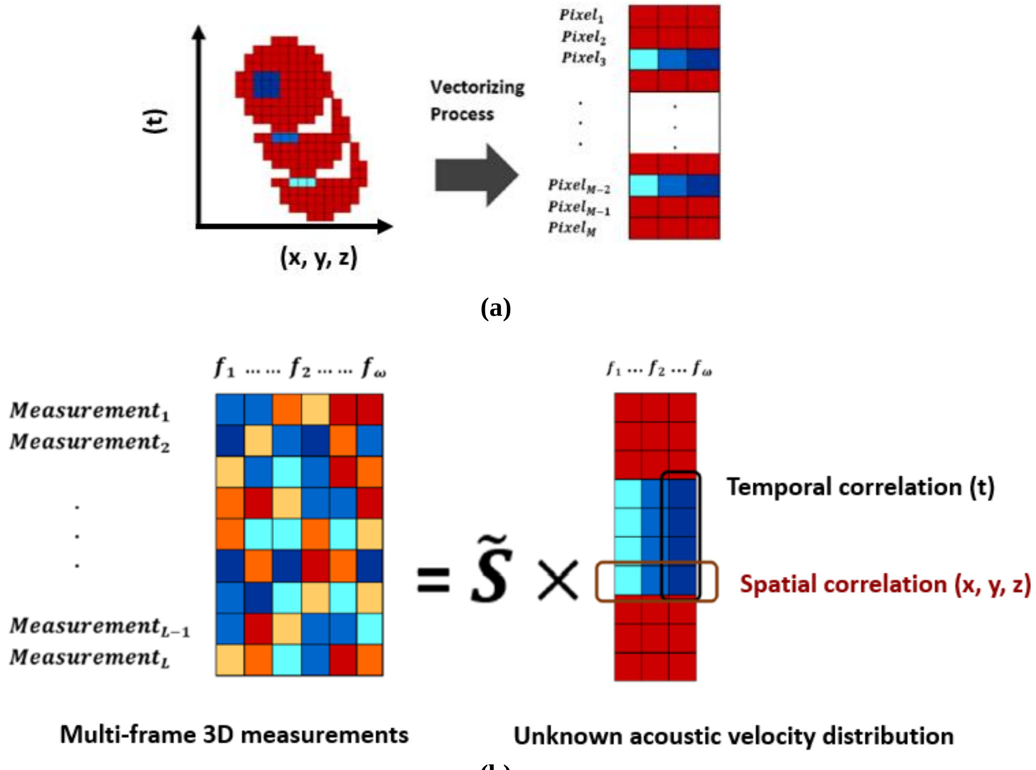

Figure 3.11 Spatial-temporal correlation reconstruction model is presented (the diagram is adopted from [184]). (a) The reconstructed pixels for every frame are stored in one row and so a matrix instead of a vector is formed. (b) The forward problem for the spatial-temporal regularization was drawn, highlighting the regularization between spatial and temporal data.

This allows to exploit redundant information across consecutive frames. The spatiotemporal total variation problem can be written as follows [185]:

$$arg\min_{\Delta \mathrm{s}}\left\|\nabla_{x,y,z}\Delta \mathrm{s}\right\|_1 + \|\nabla_t \Delta \mathrm{s}\|_1 \quad \mathrm{s.t.} \quad \left\|\widetilde{\mathrm{A}}\Delta \mathrm{s} - \Delta \mathrm{T}\right\|_2^2 \le \delta \tag{3.42}$$

where first and second terms correspond to isotropic spatial TV and temporal TV functional, respectively, and where Δs represents a 4D travel-time delays distribution and $\widetilde{\mathrm{A}}$ is the augmented sensitivity matrix on a frame-by- frame basis.

The constrained optimization problem (3.58) can be solved using the split Bregman formulation, which efficiently handled constrained optimization and L1-regularization [158], [186]. Using the Bregman iteration, the constrained problem is converted to an iterative scheme:

$$\Delta \mathrm{s}^{k+1} = arg\min_{\Delta \mathrm{s}}\left\|\nabla_{x,y,z}\Delta \mathrm{s}\right\|_1 + \|\nabla_t \Delta \mathrm{s}\|_1 + \sum_{i=1}^{I}\frac{\mu}{2}\left\|\widetilde{\mathrm{A}}\Delta \mathrm{s} - \Delta \mathrm{T}^k\right\|_2^2 \tag{3.43}$$

$$\Delta \mathrm{T}^{k+1} = \Delta \mathrm{T}^k - \widetilde{\mathrm{A}}\Delta \mathrm{s}^{k+1} + \Delta \mathrm{T}, \tag{3.44}$$

where (3.59) is an unconstrained optimization problem and (3.60) is a Bregman iteration that imposes the constraint iteratively. The cost function in (3.59) is still hard to minimize given the non-differentiability of the TV functional, but this can be easily done with a splitting technique. Including auxiliary variables allow splitting L1- and L2-functional in such a way that they can be solved in separate steps in an easy manner. Images Δs are given analytically by solving a linear system and L1-functional are solved using shrinkage formula. To perform the split, we include $\mathrm{d}_x = \nabla_x, \mathrm{d}_y = \nabla_{y,}\ \mathrm{d}_z = \nabla_z, \mathrm{d}_t = \nabla_t$, so eq. (3.59) becomes:

$$\begin{gathered}\left(\Delta \mathrm{s}^{k+1}, \mathrm{d}_x, \mathrm{d}_y, \mathrm{d}_z, \mathrm{d}_t\right) = \\ arg\min_{\Delta \mathrm{s}, \mathrm{d}_x, \mathrm{d}_{y,} \mathrm{d}_z, \mathrm{d}_t}\left\|\left(\mathrm{d}_x, \mathrm{d}_y, \mathrm{d}_z\right)\right\|_1 + \|\mathrm{d}_t\|_1 + \frac{\mu}{2}\left\|\tilde{A}\Delta \mathrm{s} - \Delta \mathrm{T}^k\right\|_2^2 \quad \text{st.} \quad \mathrm{d}_i = \nabla_i \Delta \mathrm{s}\end{gathered} \tag{3.45}$$

3.4.4. Reflection Reconstruction

This section presents the basic theoretical background of reflection tomography. Ultrasound tomography reflection mode system operates by determining the first reflections (echoes) of ultrasound waves at the boundaries or interfaces between medium’s different material phases. The system emits an ultrasound pressure wave into the fluid and measures the time taken for the transmitted and reflected waves to reach the receiving transducers. The TOF information is a function of the position of the interfaces within the process, the angle between the transmitting and receiving sensor, the velocity of sound in the continuous phase and the temperature and density of the medium. The sensitivity of the sensor is a function of the diameter of the tank and the position of the interface [187].

An ellipse algorithm was applied to reconstruct all the useful ellipses, which finally produce the shape of the inclusion. The most commonly used method for reconstructing images from projection measurements in industrial ultrasound tomography is back-projection, as we stated before. The aim for reflection tomography is to restore all these pulses using the geometric acoustics technique and especially the scattered pulses from the object’s surface that reaches a particular receiver. It is worth clarifying that the reconstruction of only these back-projections will clearly depict the objects surface.

Forward model

The objective of the time-of-flight ultrasound reflection forward model is to simulate the reflected pulses propagation over a scattered medium. Figure 3.12a displays a panoramic representation of the sensors and a nonhomogeneous medium. A circular object has been displayed to be included in the tank. Tx1 sensor excites a tone burst pulse while Rx1, Rx2, Rx14, and Rx15 record the reflection signals from the objects surface. The trajectory of the reflected pulses is shown, as well. Blues curves represents the wave-front that reaches the object and a portion of it reflects back. In this case, a relevant algorithm is developed to connect every Tx with its four Rx points. For instance, in Tx1-Rx1, the algorithm connects the two points, finds the mid-point P of the line, then connects P to the centre of the circle (centre of the circular object); the intersection point C is the estimated reflection point.

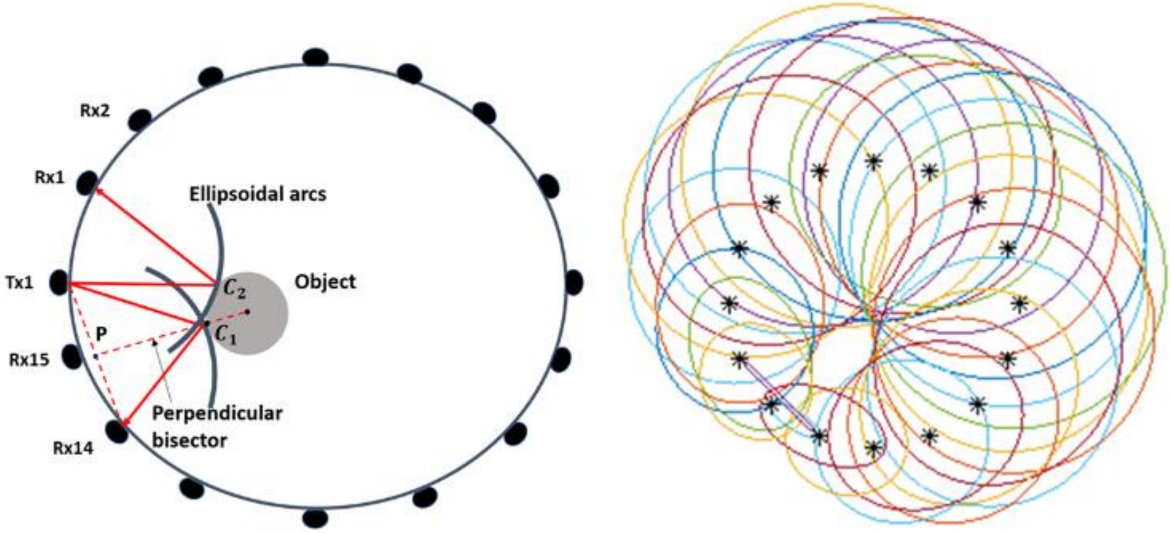

(a) **(b)**

Figure 3.12**. (a)** The schematic represents the reflection tomography functionality and geometrical representation of ultrasound reflection path for the pairs Tx1-Rx1 and Tx1-Rx14. The reflection points C_1 and C_2 are also indicated. **(b)** The corresponding reflection image by superimposing all the ellipses.

Using the coordinates of C, one can compute the travelling distance of the pulse and subsequently the reflected TOF data. This method comprises the reflection forward problem and can be used to calculate simulated reflection TOF data.

Therefore, according to Figure 3.12a, a line is computed from the middle point of sensors to the region’s centre of mass. The intersection of this line with the region’s boundaries forms the intersection point C. Given that the wave’s overall travelled distance d, which is depicted by the red solid lines in the figure 3.12 can be calculated, the simulated reflected data, TOF_{rf}^{sim}, are generated by eq. (3.69).

$$TOF_{rf}^{sim} = \frac{s_0}{d} \tag{3.46}$$

Inversion

To reconstruct the acoustic profile of the medium using captured reflected TOF data, a reflection reconstruction model based on an ellipse intersecting algorithm was used [188], [189], [190], [191], [125]. If transmitter and receiver are different, the back-projection is an ellipsoidal locus with the ellipse's foci at transducer positions. The image is reconstructed by drawing arcs of an ellipse along the reflection path. Input TOF values are translated to the pulse's travelled distance by using the prior information of the sensors' coordinates, as shown in eq. (3.47).

$$d = s_0 TOF_{refl} \tag{3.47}$$

$$where\ d = d_{\mathrm{Tx1-C}} + d_{\mathrm{Rx1-C}}$$

where $d_{\mathrm{Rx1-C}}$ and $d_{\mathrm{Tx1-C}}$ denote the axial distance between the reflection point and the receiver and between the reflection point and the transmitter, respectively. TOF_{refl} represents the time of flight and s_0 is the sound speed in the water. Superimposing the arcs of ellipses generate an image where the intersection of these ellipses highlights the boundary of the circular object. From the definition of the ellipse, the below equation is formed:

$$AC + CB = 2a = d \tag{3.48}$$

A and B are two foci of the ellipse, and C is a point located in the ellipse curve, a stands for the long axis length of the ellipse. We see these symbols and the geometrical meaning of them in figure 3.13. A and B represent the transmitter and receiver; respectively, C stands for a particular point of the target surface, reflecting the ultrasound wave. The point C can be calculated by eq. (3.48).

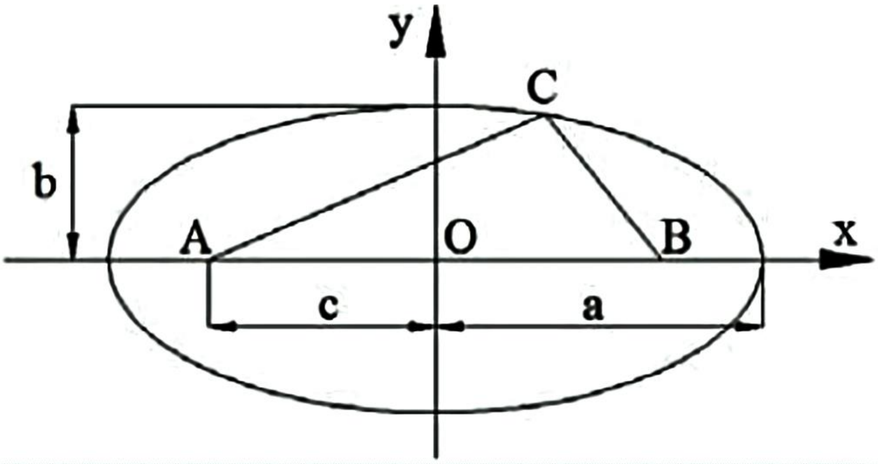

Figure 3.13. Geometric coordinate and parameters of an ellipse A and B represent the transmitter and receiver respectively, C stands for a certain point of the target surface which would reflect the ultrasound wave [192].

Since the reflection point, C, is calculated, the value of a can be easily calculated, using also the ellipse eccentricity equation of eq. (3.49).

$$a^2 = b^2 + c^2 \tag{3.49}$$

The value of b and c can also be easily obtained where b is the short axis length of the ellipse and c is the distance between focus and the ellipse centre. The distance can be calculated by the equation:

$$c = \frac{1}{2}\sqrt{(x_r - x_R)^2 + (y_r - y_R)^2} \tag{3.50}$$

where x_r, x_R, y_r, y_R are the transducer coordinates, their subscripts indicate the transducer mode. When all ellipse parameters are obtained, a particular ellipse can be drawn in a determined position and dimension by eq. (3.51).

$$\frac{x^2}{a^2} + \frac{y^2}{b^2} = 1 \tag{3.51}$$

At last, the target image can be found by many ellipses that are mutually intersected. Figure 3.12b presents ellipses generated by the developed reflection reconstruction program.

3.5. **Summary**

This chapter introduces the details of USCT, including an introduction to ultrasound physics, the used systems' description and the applied reconstruction methods. At first, the ultrasound physics with a special focus on ultrasound propagation in inhomogeneous media were discussed. The energy propagation in the region-of-interest is a significant feature to be modelled for accurate reconstructions. Then, a detailed description of the two tomographic systems provided by “NETRIX S.A.”, “USCT 1.0” and “USTC 3.0”, followed. In continuation, the applied reconstruction algorithms for USCT were presented including the forward problem for different modes of USCT but also the popular regularization methods for image reconstruction. In general, this chapter covers basic theory, and all experimental studies discussed in the following chapters are based on the contents introduced in this chapter.

Chapter 4 Quantitative sound-speed USCT

This work presents an ultrasound tomography imaging system and method for quantitative mapping of the sound speed in liquid masses. It is highly desirable to be able to inspect vessel fluid mass distribution, notably in the chemical and food industrial operations. Optimization of industrial reactors has been crucial to the improvement of industrial processes. There is a great need to investigate how and if tomographic imaging sensors could aid the automatic control of these process tanks. Single-measurement ultrasound techniques and especially spectrometric methods have been a subject of study in industrial applications. Tomographic systems provide key multi-dimensional and spatial information when compared to the well-established single-channel measurement system. Recently, ultrasound tomography has attracted remarkable interest in a wide spectrum of industrial applications. The system has been designed as 32 piezoelectric ring-array positioned in a 30 cm tank, with an excitation frequency of 40 kHz. 2-D transmission travel-time tomography was developed to reconstruct the fluid mass distributions. Early experiments use inclusions of a few centimetres and on a liquid solution of different concentrations. These experiments were conducted to test the spatial and quantitative resolution of the ultrasound imaging device. Analysing the reconstructed images, it is possible to provide accurate spatial resolution with low position errors. The system also was demonstrated in a dynamical scenario using inclusion movement, applying a data acquisition temporal resolution of 4 frames per second (fps). 2-D sound velocity quantitative imaging was developed for the investigation of ultrasonic propagation in different liquids' concentrations. This work, for the first time, shows how quantitative sound velocity imaging using transmission mode time of flight data could be used to characterize liquid density distribution of industrial reactors. The results suggest that ultrasound tomography can be used to quantitatively monitor important process parameters.

4.1. **Introduction**

Semi-batchwise tank precipitators are often used in crystallization, fermentation and in other processes of chemical and food industry. Crystals or food solid parts are being produced by mixing miscible liquids. The quality of the solid products is based on particle size, morphology and purity. Fluid interaction is critical to result in good yield. Therefore, controlling the stirring and injection rate during the process is very important, since suspension uniformity has been always a crucial factor for crystallization yield. Tomographic solutions tend to be a reliable method of inspecting the distributions of suspension during injection and mixing process. Earlier works explored the benefits of Electrical Resistance Tomography (ERT) in a process reactor setup [129], [193], which presented good performance. USCT could be extremely useful to characterize the density of different solutions during prior stages of the process (before nucleation), but can also aid the latter stages by monitoring the distribution of crystalline suspensions. Therefore, USCT process reactors monitoring is currently under great attention by the research and engineering community, especially in crystallization and fermentation processes [194], [128].

This chapter presents an in-line monitoring, sound–speed transmission USCT system, for industrial tanks, based on the first propagating pulse's arrival time (TOF). The main purpose of this work is to investigate ultrasonic wave propagation in liquids inside industrial reactors. The innovative approach of the sound-speed imaging has the potential to be of great advantage to processes that want to distinguish real-time between liquids of different densities or even liquid/solid particle formations within an industrial tank. Such slurries can easily be found in fermentation and crystallization processes.

The chapter is organised as follows. Section 4.2 presents the main functionality of the tomographic system and details its specifications, as well as the applied methods for reconstructions. Section 4.3 describes the experimental apparatus, presents the results and the experimental analysis. Finally, in section 4.4, the conclusions for the developed instrumental design are drawn; its potential and limitations are presented.

4.2. **Methods**

4.2.1. System design & Measurement data

The developed USCT 1.0 system is divided into three basic components: a multi-piezoelectric sensor, a sensing electronic setup for data acquisition and a computer system for image reconstruction. The proposed set up consists of a big tank of 350 mm with a ring of 32 piezoelectric transducers aligned in circle, located in a layer of 330 mm inner area diameter, as depicted in Figure 4.1. The used tank is made from polypropylene profax plastic, due to its low acoustic impedance. The acoustic attenuation of the plastic tank is 5.2 dB/cm with a thickness of 1 cm. The sensors are attached on the outer surface, being non-destructive, pulses travel through the thickness of the tank. It is important for the tank to be composed of "friendly" acoustic materials, so pulses travel without being attenuated. Sensors use a centre frequency of 40 kHz, with a sound pressure level close to 97 dB (30cm/10V rms). The reason to choose such a frequency is quite important, relating to the directivity of the emitting sensors. Piezoelectric transducers have a specific pattern of emission, related to their design. While the frequency is going higher, the directivity of sensors becomes narrower. Narrow emission patterns would lead to a sparsely scanned ROI. Circular pipeline-based sensors measure an entire cross-sectional volume.

Figure 4.1. The developed ultrasonic system. A ring of 32 piezoelectric transducers mounted to the black bucket.

In the case of the test container with 32 measurement probes, obtaining data for one image take about 240 msec. In this way, the temporal resolution of the system is about 4 frames per second, which does not account for reconstruction algorithms time to be performed. This type of tomography is suitable for processes that use substances in the same material phase, adapted for ultrasonic transmitted signal. Ultrasounds as a mechanical wave, while interacting in a domain, could be transmitted, refracted, diffracted, and reflected. All these ultrasounds' properties are based on the ROI characteristics and materials. When an incident wave passes through two different materials, its energy transforms to transmitted, refracted, diffracted, and reflected energy according to materials acoustic impedance and the geometry of the event, according to Schnell law. The transmission travel-time tomography is based on the time that the transmitted pulse needs to pass through the scanned area. To compute the sound-speed distribution the system must record the transmitted pulse in each emission frame. When there are big divergences in densities of the ROI, namely, when the materials inside the ROI are in a different phase (liquid/solid), the transmitted mechanical waves lose a lot of their energy due to the great difference in the acoustic impedance of materials under test. Therefore, in such cases, the picked signal is not the transmitted one and subsequently, the sound-speed imaging is not accurate. In conclusion, the proposed sound-speed method can work on cases in which the acoustic impedance does not dramatically change.

TOF data acquisition

Figure 4.2 describes the effect of difference imaging to the TOF data. This is the concept behind the tomographic technique which can compute sound speed velocities of materials. By knowing the exact distance, time and the properties of the region that the wave travels one can compute the sound speed profile of this particular path. Difference imaging is a relative imaging method. If only one material would intervene to the path of ultrasound we could define a sound-speed value directly by not measuring anything else. This is called absolute imaging and to be achieved, one has to put the sensors in close contact with the material which want to measure. Moreover, subtraction of data, imposed by difference imaging, aid to stabilize any other abnormalities that may be caused by experimental setup and added in the measurement as noise. For instance, as the transducers have been attached in the outer surface of the tank's wall their excitation is affected by the transmission through the walls.

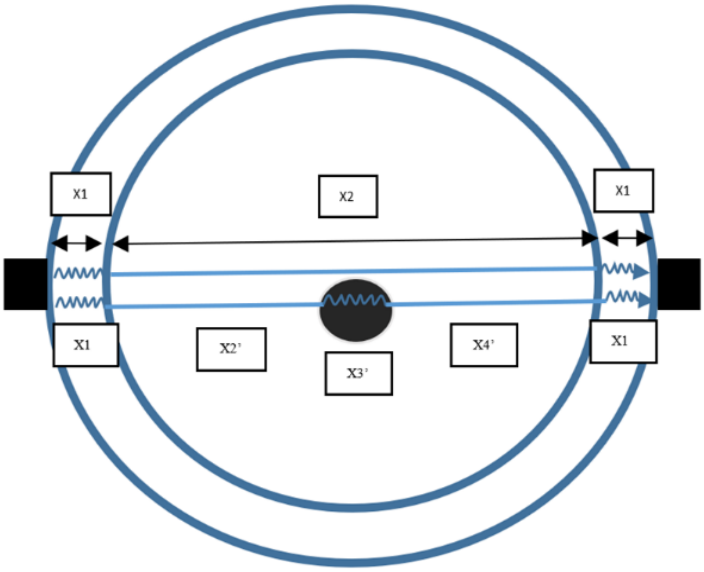

Figure 4.2. Panoramic view of a tank and pulses propagation rays. The black lines are distance symbols, while the blue lines stand for a signal propagating in the tank with and without an inclusion (background and full measurements). The curved lines display the signal’s transmission through objects like the tank walls and the object.

The below equations describe the TOF values of the first arrival pulse in background and full measurements. The elimination of features added by the signal’s propagation through the tanks’ wall by the difference imaging is also presented, eq. (4.1), (4.2), (4.3):

$$T_{back} = 2\mathrm{t}_{x_1} + t_{x_2} \tag{4.1}$$

$$T_{full} = 2\mathrm{t}_{x_1} + t_{x_{2'}} + t_{x_{3'}} + t_{x_{4'}} \tag{4.2}$$

$$\Delta T = T_{full} - T_{back} = -t_{x_2} + t_{x_{2'}} + t_{x_{3'}} + t_{x_{4'}} \tag{4.3}$$

USCT devices usually include a significant level of noise and unwanted signals whether coming from electronics or from physical disturbances of the setup. The goal is to analyse physical phenomena, characterizing its noise factor in order to finally cut the unwanted signals off the system. Devices are each unique, thus they intrinsically bear different types or volumes of noise. The “Deleting Outliers” statistical, filtering method was used to handle this noise for all the dataset [195]. D.M. Hawkins describes the notion of an outlier, as an observation that deviates so much from the other observations as to arouse suspicions, considerably, generated by a different mechanism [196]. In our case, “outlier” TOF values usually are generated from back-scattering or reflected signals. An iterative implementation of the Grubbs Test which checks one value at a time, was used to identify the outlier signals. In any given iteration, the tested value is either the highest value, or the lowest, and is the value that is furthest from the sample mean [195].

In Figure 4.3, the uniform pattern describing the background data, drives us to the conclusion that the developed system provides a high signal-to-noise ratio (SNR). However, unexpected higher values, found in full data. This exposes the system for collection of back-scattered, and reflection pulses. These back-scattered pulses may occur from the surfaces of inclusion(s). This is considered as noise in the transmission tomography data acquisition. In Figure 4.3a, one can also notice the tremendous effect of the “outlier method”. The blue part of the curves is the part of the curve that has been deleted. This filtering method has been applied to all background, full and, also, difference data before the reconstruction performs. Also, reconstructions, using a single-step algorithm like Linear Back-projection (LBP), are depicted in Figure 4.3b. The reconstructions from left to right are using unfiltered data and filtered data, respectively.

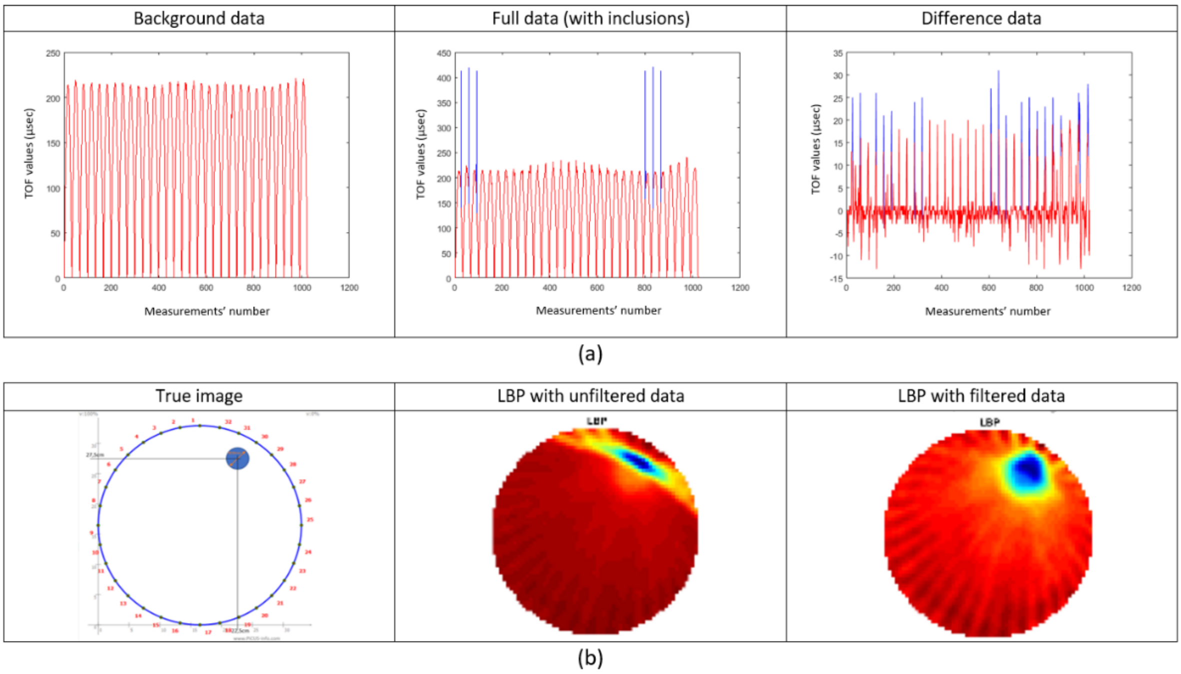

(a)

(b)

Figure 4.3. (a) Filtering the raw TOF data with the statistical method of “deleting outliers” introduced by F. E. Grubbs [195]. (b) Reconstruction using LBP algorithm with and without filtering the data.

4.2.2.Transmission reconstruction

The applied reconstruction method is based on the transmission of actuated pulses. Recorded waveforms, emitted from the sensors allow to reconstruct sound-velocity profiles, using the TOF of the first arrival pulse. Figure 4.4a depicts the experimental tank with the tomographic sensor array attached. On Figure 4.4b, there is a 2D scheme describing the main functionality of transmission tomography. Black squares, positioned in a circular formation, present the transducers. They work as both transmitter and receiver, mounted at the outer boundary of the phantom. Figure 4.4b presents also the modelled wavefront propagation with the blue lines. Each spherical wave can be approximated by a cone of rays and subsequently, every plane wave by a fan of rays.

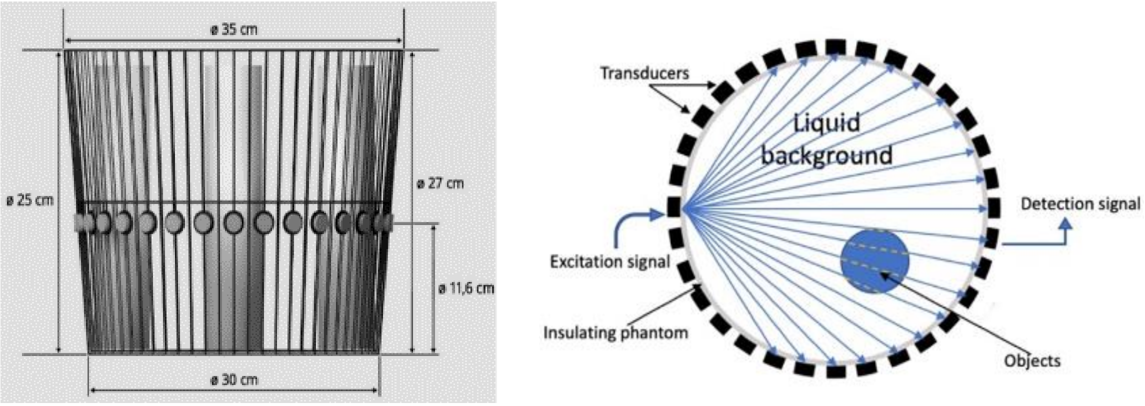

(a) **(b)**

Figure 4.4. (a) A graph with dimensions of a propylene tank with a 32-ultrasonic transducer ring-array hard-mounted on it. (b) Measurement principle of a 32-electrode UTT system (panoramic view).

This work utilises a different method for sound-speed mapping as the commonly used method described in section 3.4.1. The necessity of the proposed method lies to the need of significant temporal resolution by industrial imaging, as it is proved to be faster than the traditional methods. The sensitivity matrix was computed by an algorithm which checks the distance of the ultrasound propagating ray to the centre of the pixel. A thin line approach leading to sparse interaction between image pixels and rays was considered, at first. We called this “sparse” method, according to the analysis on the system matrix sensitivity distribution that follows at the next section (“Refined ray-pixel intersection method”).

Using the recorded time-of-flight data and knowing the exact distance between the sensors, one can compute sound-speed data, which represents the average sound velocity of each one of the waves-rays' path:

$$S = \frac{D}{\Delta T} \tag{4.4}$$

where D is the distance of the travel-path of each ray, S is the computed average sound velocity of a ray and ΔT is the TOF data. The average sound speed of an acoustic wave that travels through the path l, between an emitter and a receiver is represented by s_m (1<m<M) and it can be expressed by the following path of a line, where M is total number of paths in multisensory array measurements. This line is expressed by the integral of the spatial distribution of the sound-speed of the domain (sound velocity distribution):

$$s_m = \int_l V(l)\, dl \tag{4.5}$$

A tomographic inspection consists of many of these rays, whose amount depends on the angle of emission beam. All these ray equations form a system of linear equations, the so-called forward problem (described in detail in section 3.4.1).

$$V_n = \sum_{n=1}^{N} \sum_{m=1}^{M} w_{m,n}\ S_m \tag{4.6}$$

where $S = [S_1, S_2, \dots, S_M]$ is the vector of calculated sound-speed values from the measured TOF values, $V = [V_1, V_2, \dots, V_N]$ is the vector that contains the discretized values of the sound-speed spatial-distribution, and w is an M×N sensitivity matrix, containing the weighted values of ray-pixel intersection. These weighted values describe how much each specific wave-ray affects the domain, namely the pixels. This is the main difference between the proposed method and the traditional sound-speed imaging methods, as the value of the ray's length passing through the pixel needs to be estimated in the latter.

The sensitivity matrix's weighting values have been computed by an algorithm that treats the pixels as circles to make use of the radius. Treating the pixel as a circle can significantly reduce the computation costs [197], [198], [85], [199]. As Rymarczyck et al. noted in their works, the attempt of circle-shaped pixels contains some advantages and disadvantages. A significant advantage of the process is the ability to be executed significantly faster as the single task of the "calculation of distance between a point and a line" needs to be executed. On the contrary, the traditional approach needs the actual distance of the ray travelled through the pixel and therefore needs to perform four times the "calculation of the intersection points of two line segments". The schematic presented in Figure 4.5a depicts the traditional computation of ray's length passing through a pixel, where the intersection points were highlighted with green marks. However, the proposed method contains a few drawbacks. A disadvantage is that the simplification of a circular pixel introduces some sparsity in the matrix's sensitivity distribution. In the case of a regular pixel grid, the whole volume can be covered because any pixel is perfectly attached to another pixel. In the case of a circle-pixel grid, any circle touches the other only at one point, leaving some empty on the top and bottom of the intersection area [198].

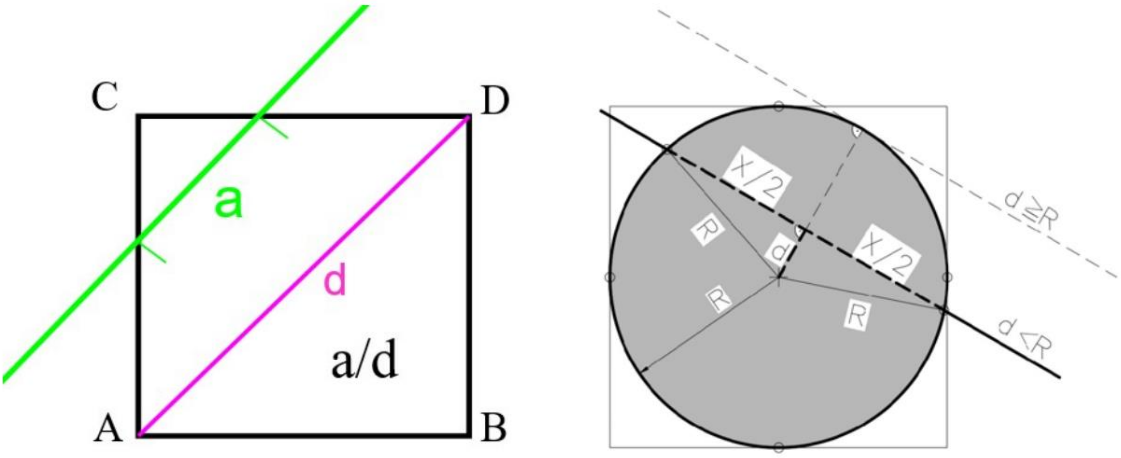

(a) **(b)**

Figure 4.5. (a) The basic principle of determining the length of ray passing through a pixel using the calculation of two intersection points. (b) The proposed circular pixel principle using the circle's centre to calculate the distance to the ray [198].

Subsequently, any rays passing through these small areas would be considered as none-intersection, as indicated in figure 4.5a (the grey dotted ray). The methods presented in the

"Refined pixel intersection method" aim at tackling that. The algorithm uses the pixel's inscribed circle. Then it calculates the Euclidian distance from the centre of each specific pixel to the ray, as shown in eq. (4.7).

$$d = \frac{\|(v_1 - v_2) \times (pt - v_2)\|}{\|v_1 - v_2\|} \tag{4.7}$$

where pt, v_1 and v_2 are the three-dimensional coordinates of the point, one vertex of the line, and a second vertex of the line, respectively. The symbol × defines the cross-product equation. Then the distance, d, is compared to a fixed value, which usually is the radius, R, of pixel's inscribed circle [199]. Four classifications are compared at these divergent values from 1 to 4. Value of 0 is used for all these pixels that are not being intersected with the ray.

$$w_{i,j} = \begin{cases} 0, & d > R \\ 1, & R \leq d < \frac{3R}{4} \\ 2, & \frac{3R}{4} \leq d < \frac{R}{2} \\ 3, & \frac{R}{2} \leq d < \frac{3R}{4} \\ 4, & \frac{3R}{4} \leq d \end{cases} \tag{4.8}$$

Finally, a prior sensitivity matrix is established which simulates our transmission approach to the acoustic physical problem that exists in our experimental data. The algorithm uses as inputs, numbers and topology of sensors and resolution of the reconstructed image and applies the above-mentioned methodology for every pixel and every propagating ultrasound ray. Figure 4.6b presents the pseudocode and 4.2a presents a schematic covering the weights assigning method.

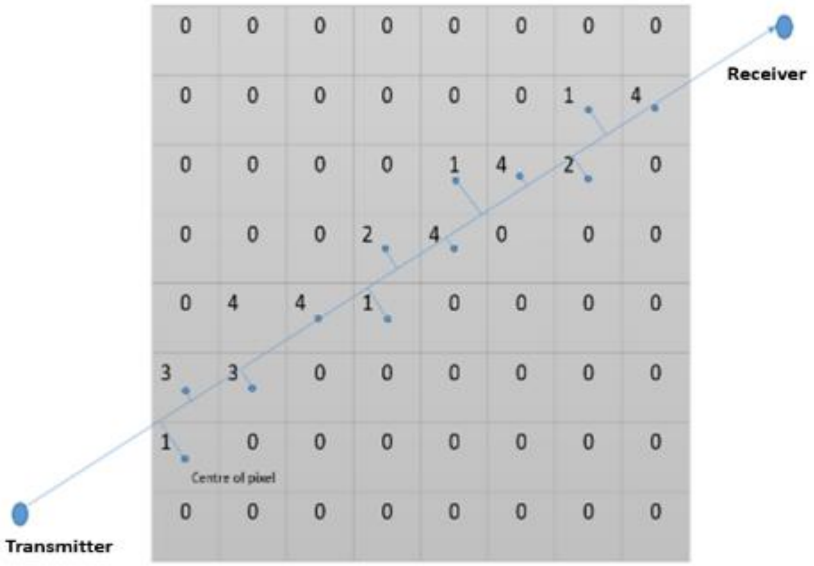

0	0	0	0	0	0	0	0
0	0	0	0	0	0	1	4
0	0	0	0	1	4	2	0
0	0	0	2	4	0	0	0
0	4	4	1	0	0	0	0
3	3	0	0	0	0	0	0
1	0	0	0	0	0	0	0
0	0	0	0	0	0	0	0

Figure 4.6. (a) The method of ray-pixel intersection and the value assignment on system matrix.

A Normalisation method is essential to ensure an accurate sound-speed mapping. The method is based on the wave rays, as described in eq. (4.9). This step is essential to provide a correct sound-speed mapping that agrees with the measurements. Simplifying the concept of this normalisation, it aims to project the actual measurement value along the area of interest and so divides every pixel's value with the summed value of the same pixel along all sensitivity kernels. The normalised weighted values produced by this division are assigned to the sensitivity matrix. As rays superimposed into a unified image, during reconstruction, the sound-speed map of the ROI is being formed. Below lies the normalisation formula:

$$A_{i,j} = \frac{w_{i,j}}{\sum_{i_1=1}^{m} \sum_{j_1=j} w_{i_1,j_1}} \tag{4.9}$$

where $w_{i,j}$ is the sensitivity matrix based on ray-pixel intersection method and $A_{i,j}$ is the normalized matrix, used for reconstructions, and for m measured data and n pixels, $\mathrm{i} = [1, \dots \mathrm{m}]$ and $\mathrm{j} = [1, \dots, \mathrm{n}]$. A single frame of matrix A_1 is depicted in Figure 4.7 in "Sparse" section.

Refined ray-pixel intersection method

The previous “sparse” method for ray-pixel intersection faces few important limitations and drawbacks. This straight-ray model have been demonstrated to be inappropriate for obtaining accurate USCT images [150], [200], lacking a good uniform distribution of values, an innate problem of tomographic coverage. Despite being a computational efficient solution, it introduces sparsity in the sensitivity matrix. Another problem is that while the resolution of reconstruction increases, more “ray artefacts” show up in the results. However, regularization techniques could sometimes overcome these artefacts, but they cannot always do so [85]. Therefore, an alternate approach of ultrasound transmission tomography sensitivity kernels was applied. This is the “Thick Lines” method [201], whose single-frame plot is depicted in Figure 4.7. Regarding this model, the sensitivity map for any two transducers is a straight line with a certain width, equal to the width of the transducer. From experience, the number of transducers as well as the size of pipeline are determining the width of the ray [200].

Upon evaluation of the “Thick Lines” full frame plots, as depicted in Figure 4.7, many discontinuities could be noticed. Despite the fact that, the “Thick Lines” method is more efficient that the “straight line” approach, because of providing better coverage of the ROI, it seems that our sensitivity matrices needs further improvement. The main drawback of “thick lines” method is that the sensitivity matrix only consists of 0 and 1. Thereafter, exists a big values’ divergence in the sensitivity maps, which often give a rough, high-contrast reconstruction. Producing sensitivity matrices with bigger range of values will give more uniform results. Due to this lack of uniformity, another model needs to be considered. The proposed model is based on the “Thick Lines” approach. We call this model “Smoothed Thick Lines”, and it has been constructed by smoothing every single map of sensitivity matrix using a Gaussian filter with standard deviation. The smoothing had to account for a specific direction in order to produce a thick line with higher sensitivity in the central region, and gradually decreased sensitivity layers on its left and right. This approach is presented at the bottom of Figure 4.7. This new sensitivity matrix calculation method provides smoother results, overcoming previously seen discontinuities, as depicted in Figure 4.7. In this way, its sensitivity full frame is also smoother than in the previous method. This smoothing introduces uniformity in values of distribution, and subsequently, slightly better results even when using single step reconstruction algorithms.

	Sensitivity Map	**Frames**	**Sensitivity Matrix – 150 degrees**
"Sparse"	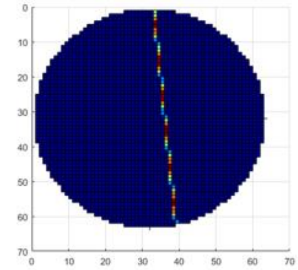	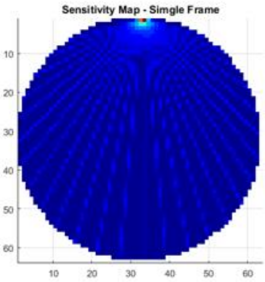	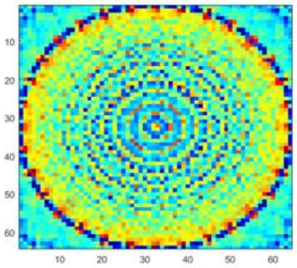
"Thick Lines"	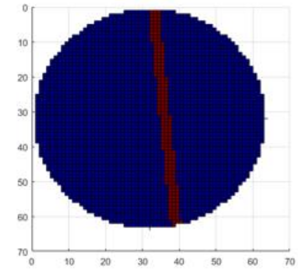	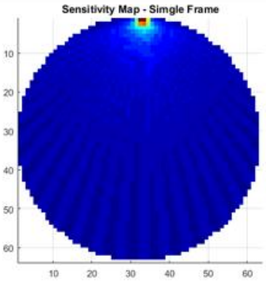	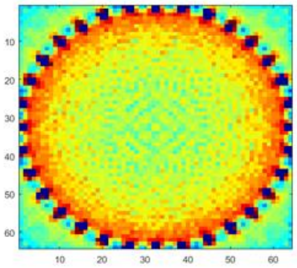
"Smoothed"	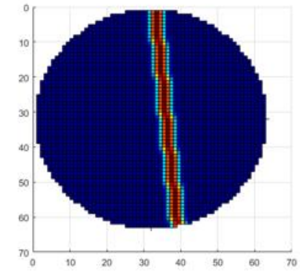	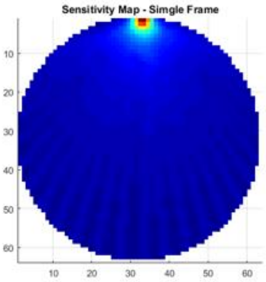	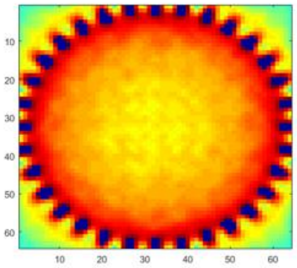

Figure 4.7. Left: Sensitivity maps depicting the different form of ray in each method. Middle: Sensitivity map's frame of the first transmission Right: Sensitivity matrix for each method. The used resolution is (64x64) for a system with 32 sensors in a circle-wise setup of 330 mm.

Sensitivity Matrix Analysis

In this section we perform an evaluation approach to validate the correctness and efficiency of the applied system matrix. Therefore, we will compare the values of the experimental background measurement data with the synthetic data that has been produced using each time one of the three different system matrices (produced above).. To evaluate the performance of each of these approaches to the forward and inverse problem in USCT, an evaluation of forward model and ill-posedness of the inverse problem is considered. Singular Values Decomposition (SVD) provide the means to study the ill-posedness of an inverse problem, by decomposing the sensitivity matrix A. SVD of A is:

$$A = U\Sigma V^T = \sum_{i=1}^{n} u_i \sigma_\iota v_i^T \tag{4.10}$$

where $U = (u_1, u_2, \dots, u_n) \epsilon R^{mxn}$ and $V = (v_1, v_2, \dots, v_n) \epsilon R^{mxn}$ are matrices with orthonormal columns called singular vectors, $U^T U = V^T V = I_n$ and the diagonals of Σ includes the singular values, which are positive numbers $(\sigma_1, \sigma_2, \dots, \sigma_n)$ sorting in non-decreasing order. The plot of singular values decomposition (SVD) of different sensitivity matrices help to understand the level of ill-posedness.

Figure 4.8a displays SVD values of different sensitivity matrices. It is clear that the “Smoothed Thick Lines” approach is more ill-posed when compared to the other two methods. According to this curve, the “Sparse” method is giving us the least ill-posed solution, and on the other hand, the “Smoothed Thick Lines” is giving us the most ill-posed problem. In terms of reconstruction, the best result can be achieved with the “Smoothed Thick lines” method, due to its inherent regularisation. The “Sparse” and “Smoothed Thick Lines” techniques are assumed as hard-field and soft-field methods, respectively. The “Thick Lines” technique goes in between. TOF raw measurements could not be well described by a hard-field tomography model as the “Sparse” method, due to wave characteristics and nature. Other reasons for the low spatial resolution could be caused by dimensions of sensors (not being a point source for example), total count and technical issues. In this case, a system matrix with a slight soft-field approach matches our need. As both “Thick Lines” and “Smoothed Thick Lines” overcome the “Sparse” method. In conclusion, smoothed rays aid the spatial resolution as they tackle sparsity in reconstructions, making regularization sometimes inessential. However, the smoothing factor is always important to match the tomographic problem’s setup (number of sensors and region-of-interest) as at many times smoothed rays could lead to a blurred result.

To evaluate sensitivity matrices further, the values of the experimental background measurement data (without any inclusions to the medium) is compared with the synthetic background data produced, using all the different sensitivity matrices. Figure 4.8b presents experimental data with the blue coloured curve and all synthetic data, from different sensitivity matrices, in other colours. These values are TOF data, and always have a repeatable pattern, due to the circular shape of the tomographic set up. Synthetic data have been produced by solving the forward problem, using a uniform sound speed distribution in the ROI. The closer these data get to the experimental data; more efficient our sensitivity matrix is. Upon observation of signal-forms of four different sensitivity matrices, it is noticeable that “Thick-lines” approach produce better data than the “Sparse” one, and consequently “Smoothed Thick Lines” seems to produce the closest data to the real experimental values.

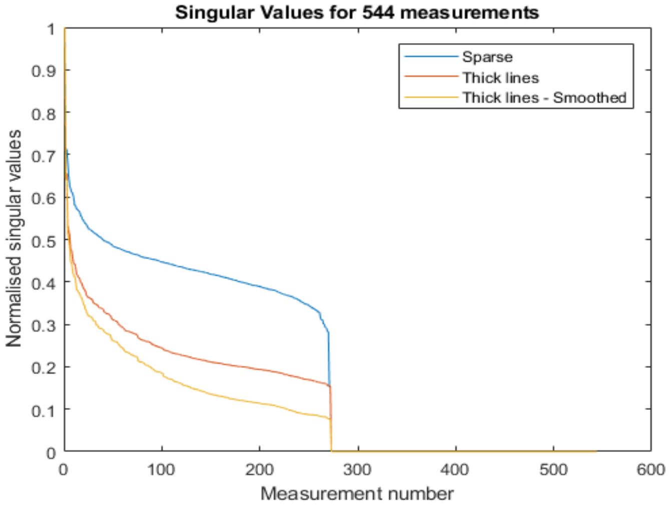

(a)

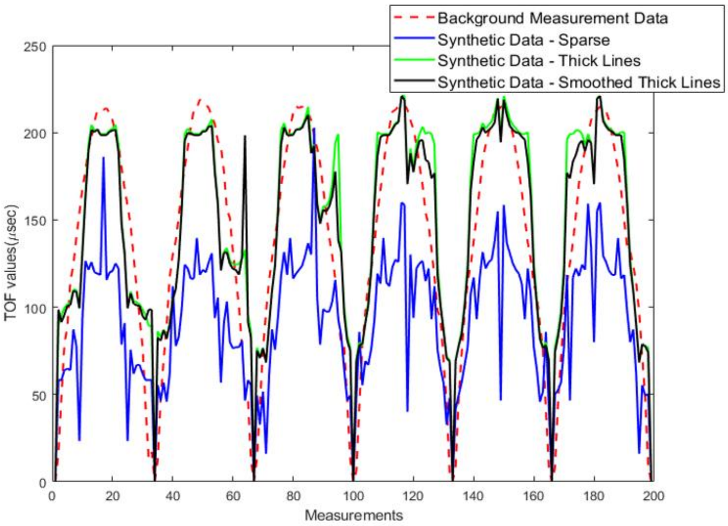

(b)

Figure 4.8. (a) Singular Values of all the different methods of the sensitivity matrices. It helps to characterize inverse problems according to their ill-posedness. (b) Plots of synthetic data produced by all the different methods of sensitivity matrices against the background measurement.

Setup configuration

A very important factor for our reconstruction methods is the spatial resolution. Spatial resolution describes the efficiency of the tomographic system to measure the most and the smaller parts of the ROI. Subsequently, only a tomographic system with high spatial resolution is able to monitor and detect the details and smaller parts of a particular ROI. Factors that affect the spatial resolution in USCT are size and number of sensors elements according always to the dimensions of the ROI, but also the uniform topology of them around the ROI. By experience, the number of transducers, and the size of pipeline usually determine the selection of the width of the ray or the smoothing factor (standard deviation) of it. Factors also are the angle of beam that these sensors emit. In different words, as more uniform and compete is the "scanning" of a ROI, the higher the spatial resolution is [202],[203].

Choosing the most uniform sensitivity matrix method for our reconstruction problem, we need to go on by choosing a suitable tomographic setup. In figure 4.9 we chose to create few sensitivity matrices with different setup to examine the coverage of scanning. We used the third method of sensitivity matrix computation, "smoothed thick lines" in a 32/ 16 ring transducers array with different beam of angles (90 - 150) and different resolution. We need to state that we used a ROI of 33cm diameter and a discretised domain of [64x64] pixels. As we notice in Figure 4.9, the 16 circle-wise setup for a ROI of 33 cm drives to non-uniform coverage of ROI. This could drive to low-quality blurred reconstructed images.

Because of the circularity of our ROI when we are using a wide angle of beam the intersection of rays in the region close to the walls (edges) are more than in the middle. This is why, we get a higher sensitivity value in the edges side by side of the tank's wall. On the other hand, when we are using 90 degrees angle of beam we see that the higher sensitivity values lies on the middle and the area next to the tank's wall has a bit lower values. The sensitivity values affect significantly the outcome. Finally, it seems that a 90 degrees angle fits better to our problem.

Producing a reliable sensitivity matrix, the angle beam of emission plays a significant role. Having to decide between a case of a full angle of 150 degrees and a half angle of 90 degrees, their full frame plots have been presented in Figure 4.9.

	32 sensors	**16 sensors**
90 degrees	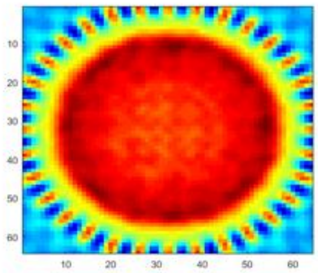	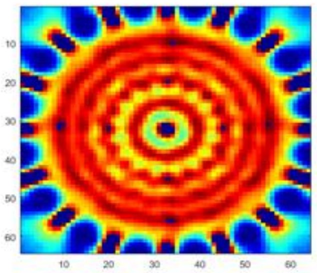
120 degrees	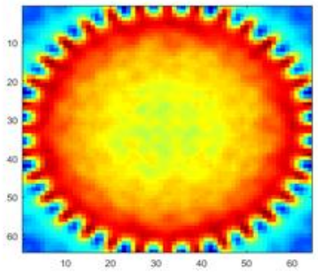	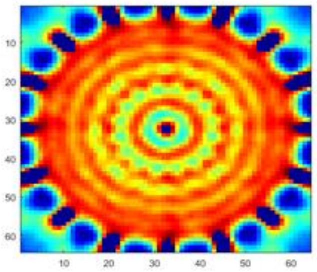
150 degrees	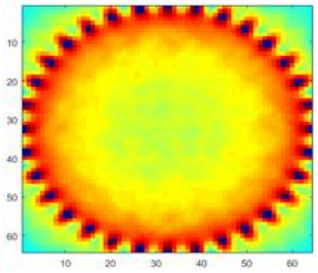	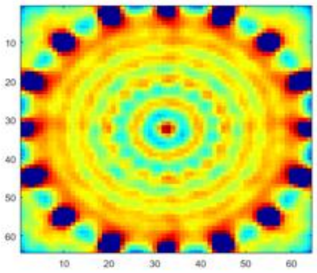

Figure 4.9. Different tomographic setups with 16 and 32 sensors circle-wise emitting in three different excitation angle beams of 90, 120, 150 degrees.

From these plots one can easily notice that the 90 degrees angle of beam provides higher sensitivity in the centre and lower in the edges, which is a fact that describes the physical operation of the system. Eventually, as the more uniform is the sensitivity distribution in the region of interest (ROI), the higher the spatial resolution gets [202], [203]. We consider the tomographic setup that we concluded to be optimal, namely the “smoothed thick lines” method with a resolution of [64x64] and a transmission angle beam of 90 degrees.

4.3. **Results & Analysis**

This section shows the experimental processes and results. Experiments, which are presented in section 4.3.1, named as "Qualitative resolution experiments", aim to study the behaviour of the wave propagation in liquid masses using static inclusions of different shapes and setups. Experiments in this section were categorized as static and dynamical cases. The purpose of static experiments is to test the system's spatial resolution. Therefore, an evaluation of different models and set-ups was applied. Factors that affect spatial resolution in USCT are the size and number of sensor elements, according to the dimensions of the ROI and the sensitivity models and regularization algorithms. Also, a comparison between “Hybrid Tikhonov” and isotropic SBTV methods takes place, with the SBTV method showing supremacy. The section’s dynamic experiments aimed to test the system’s temporal resolution and tolerance on dynamic disturbances. Simple tests by manually shifting objects were applied. The experiments that are presented in section 4.3.2, are focused on the quantitative information of sound-speed imaging. The conducted experiments aim at the relation between sound-speed calculated values and liquid density. The “Smoothed Thick Lines” sensitivity matrix method with 90 degrees angle of beam was used for the reconstructions. An image resolution of [64x64] pixels, with pixel spacing to 5.15 mm, was used for visualizing the reconstructions. The SBTV reconstruction algorithm was used in this work.

4.3.1.Qualitative resolution experiments

Static experiments

Figure 4.10 includes results of four static experiments with single and multiple inclusions. HT and SBTV regularization were applied.

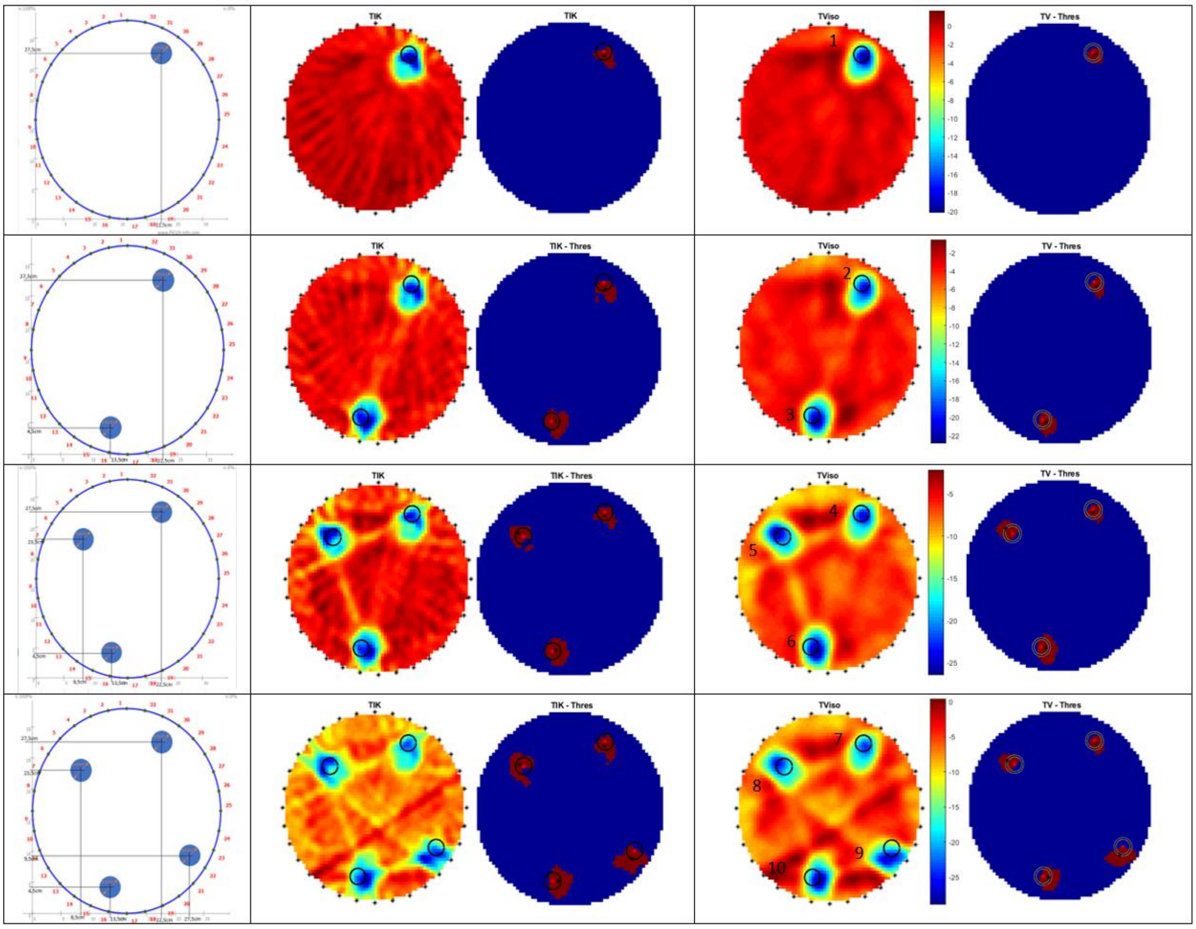

Figure 4.10. Left: True positions of inclusions. Middle: Hybrid Tikhonov and filtered reconstructions. Right: Split-Bregman Total Variation and filtered reconstructions.

We present at left column the geometry of the experiments, at middle the HT reconstructions and at right the SBTV one. The colorbar, presented in the SBTV method it is the same in HT and presents the difference in μs of the first arrival TOF signal. For each of the two methods an image was generated with a threshold value of 20 %. Black circles represent the true position of the inclusions, while the red dots represent the centres of them. Black dots represent the centres of mass of the images. In this figure, one can clearly notice the correlation between the true and the reconstructed locations.

Figure 4.11 represents all the spatial deviations between the location of the reconstructed objects and their true location. In total four experiments have been taken place with a number of 10 reconstructed objects. The Euclidian distance between the centre of the mass of the thresholded image and the true circle has been calculated. Red and green dots depict the SBTV and HT reconstructions, respectively. The minimum value of these distances is 3.8 mm, the maximum is 15.9 mm and the average value of all the distances is 8.6 mm. So, in a

ROI with a 330mm length having an average error by 8.6 mm drives to the fact of 2.61% error percentage, which is relatively small. Comparing the two regularization methods, they provide with relatively close values of position errors. However, SBTV offers better results in terms of shape detection, depending on the supremacy of distinguishing edges.

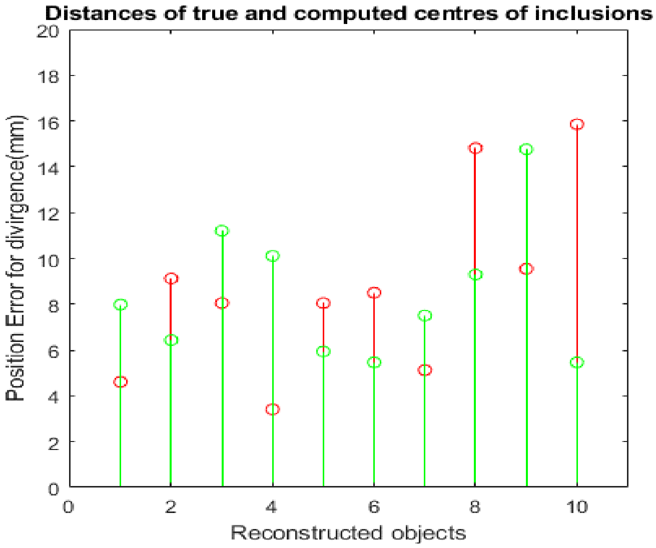

Figure 4.11. Position error divergence for HT and SBTV reconstructions. Red and green dots depict the SBTV and HT reconstructions, respectively.

A significantly low percentage of position error in our reconstructions is a very good indicator for the efficiency of our methods. Our reconstruction method seems that outperforms in topological sense but not in terms of shape or boundary detection, which is a more complicated fact. Despite the accuracy of object detection and topological identification of the proposed method, it is noticeable the lack of good performance in shape detection. An interesting fact that arises and needs comprehensive examination is that as more inclusions we are using the more displaced is the reconstructions we face. This happens due to the multiple back-scattering that is introduced by the multiple inclusions. In USCT and especially in the transmission imaging the back-scattering effect can significantly affect the outcomes.

More static experiments have been conducted using the SBTV method and reported in this section. The inclusions consist of cylindrical objects of 2.8cm (pipe) and 5.8cm (bottle) diameter. The objects are empty (filled with air). Figure 4.12a displays the tank with the inclusion's mechanism and the inclusion objects as well. Several disparate positions of the inclusions and some other positions of multiple inclusions are applied to evaluate the reconstruction accuracy of our system, as depicted in Figure 4.12b.

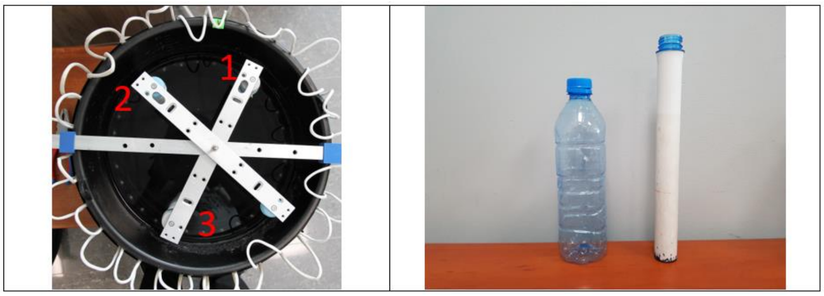

(a)

True	Reconstruction	Position error	True	Reconstruction	Position error
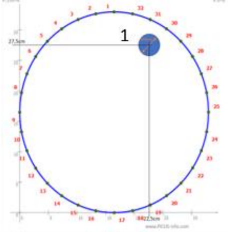	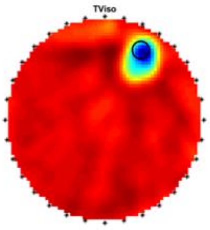	1)7.72 mm	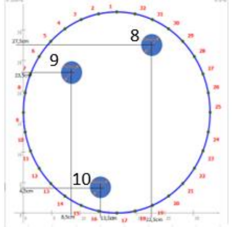	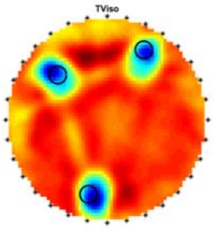	8) 10.6 mm 9) 8.2 mm 10) 8.2 mm
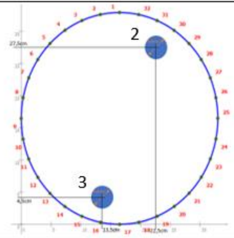	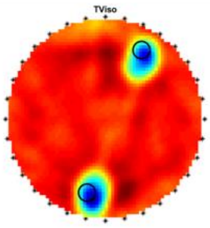	2) 10.8 mm 3) 6.7 mm	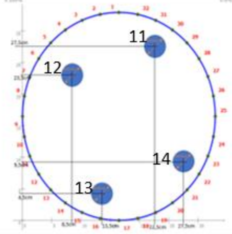	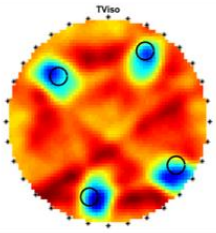	11) 12.8 mm 12) 6.5 mm 13) 14.9 mm 14) 8.7 mm
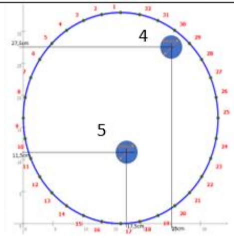	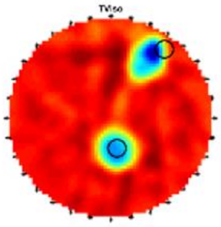	4) 28.84 mm 5) 4.6 mm	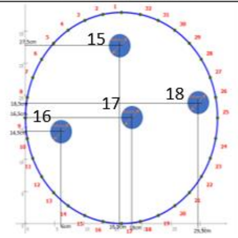	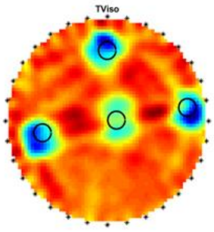	15) 7.2 mm 16) 10.5 mm 17) 20.3 mm 18) 8.2 mm
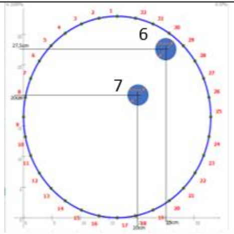	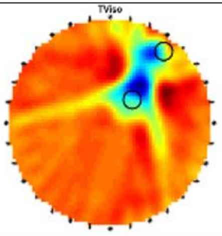	6) 24.2 mm 7) 13.9 mm	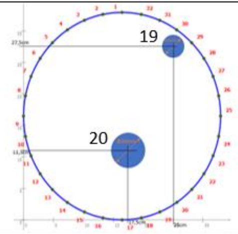	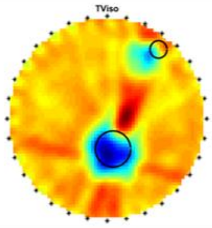	19) 30.1 mm 20) 5.6 mm

(b)

Figure 4.12. (a) Objects used as inclusions in the experiments. (b)Left: True positions of inclusions. Middle: SBTV reconstructions. Right: Position error in mm.

Moreover, to thoroughly test the accuracy of algorithms, two objects were placed in different positions, focused on three specific separating distances. The left column presents the geometry of the experiments, the middle column the SBTV reconstruction and the right one the position error. Black circles represent the true position of the inclusions, while the red dots represent their centres. Black dots represent the centre of mass of the images. The Euclidian distance between the image centre of mass and true circle has been calculated. The minimum distance value is 4.6 mm, the maximum is 30.1 mm and the average value of all the distances is 12.4 mm. Air inclusions experiments show a significant low percentage of position error. This is a very good indicator of the system accuracy. However, in USCT and especially in travel-time imaging, reflections and back-scattering are always an issue. The more back-scattering effect takes place, the more noise is included in our measurements. Back-scattering is most intense, when objects are placed closed to one another. Making reconstruction a more challenging task.

Applying many different topologies of multiple inclusions, our method has proved efficient, providing relatively good results. The above experimental results show that our proposed reconstruction methods work well in challenging cases of inclusions, as good quality images could be produced, with a significant low position error.

Dynamical experiments

Furthermore, the 32-channel USCT system is tested under a dynamical scenario. Processes occurring in industrial reactors are mostly dynamical, in which stirring is taking place, and therefore, inserting significant disturbances on the pressure field inside tank. While ultrasound is completely dependent of pressure fields, an important amount of error could arise from measurements. Therefore, an online monitoring system should always overcome this dynamical error factor. To test the response of the system regarding the dynamical error factor, an inclusion was placed in the tank and continuously moved, all while capturing frames. This movement changed the dynamics of the tank and added a significant amount of disturbance to the pressure field. The movement started from the centre to a corner, and then continued around the boundary area in three cycles. Figure 4.13 displays a dynamic experimental process. A time-variant version of the above SBTV algorithm was used [204]. The figure shows the reconstruction of a single inclusion moved in 100 locations, within the region of imaging. In this case, data acquisition was performed in-situ, while the inclusion was moving. The results are meaningful, in filtering the noise by the moving factor. Moreover, an algorithm of motion tracking was developed, as covered in latter stage. By post-processing the data captured from the device, the algorithm, is able to reconstruct the trajectory of movement of the inclusion over the time, as shown in Figure 4.13.

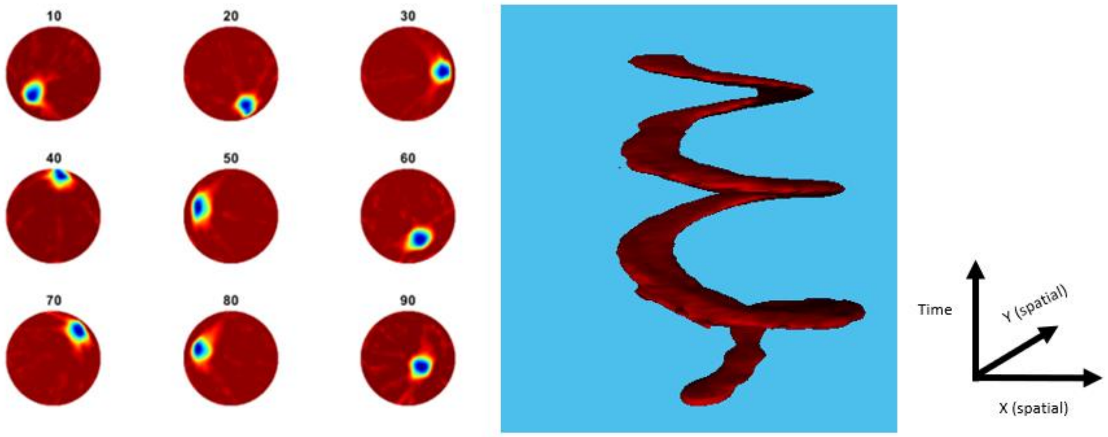

(a) **(b)**

Figure 4.13. Left: Reconstruction of a moving object in 99 location within the region of imaging in every 10 frames. Right: Trajectory of the movement of the sample with shape reconstructed with time (Z axis is time).

In continuation of the previous experiments, we tested the use of ultrasound computed tomography (USCT) for handwriting by imaging changes in sound speed in a medium caused by a manually shifted rod of 20-mm diameter [88]. The rod was used as a writing object and the tomographic instrument was able to acquire and process data over time with a temporal frequency of 4 fps. The imaging was carried out with all letters in the English alphabet. Subsequently, tests are carried in writing various words using USCT data and automatic writing software. The work shows the functional imaging capability offered by USCT combining qualitative and temporal imaging features. The USCT based handwriting is implemented by the combination of a sequence of 2D images creating letter using points on the path of the trajectory of the plastic bar. All the individual images are synthesized to produce letters. Figure 4.14 presents the consecutive reconstructed frames, a volumetric reconstruction and the synthesized image of a letter “S”. Additionally, the normalized values of the difference data, were plotted. A total of 31 informative frames have been recorded for this case. Filter algorithm excludes frames that do not contain substantial information, resulting in 23 processed frames. Finally, 12 frames were presented for the total number of processed frames using step two. The displayed frames start from the 8th frame. Earlier frames have been excluded by the filter. Each frame acts as a point in the letter “S”.

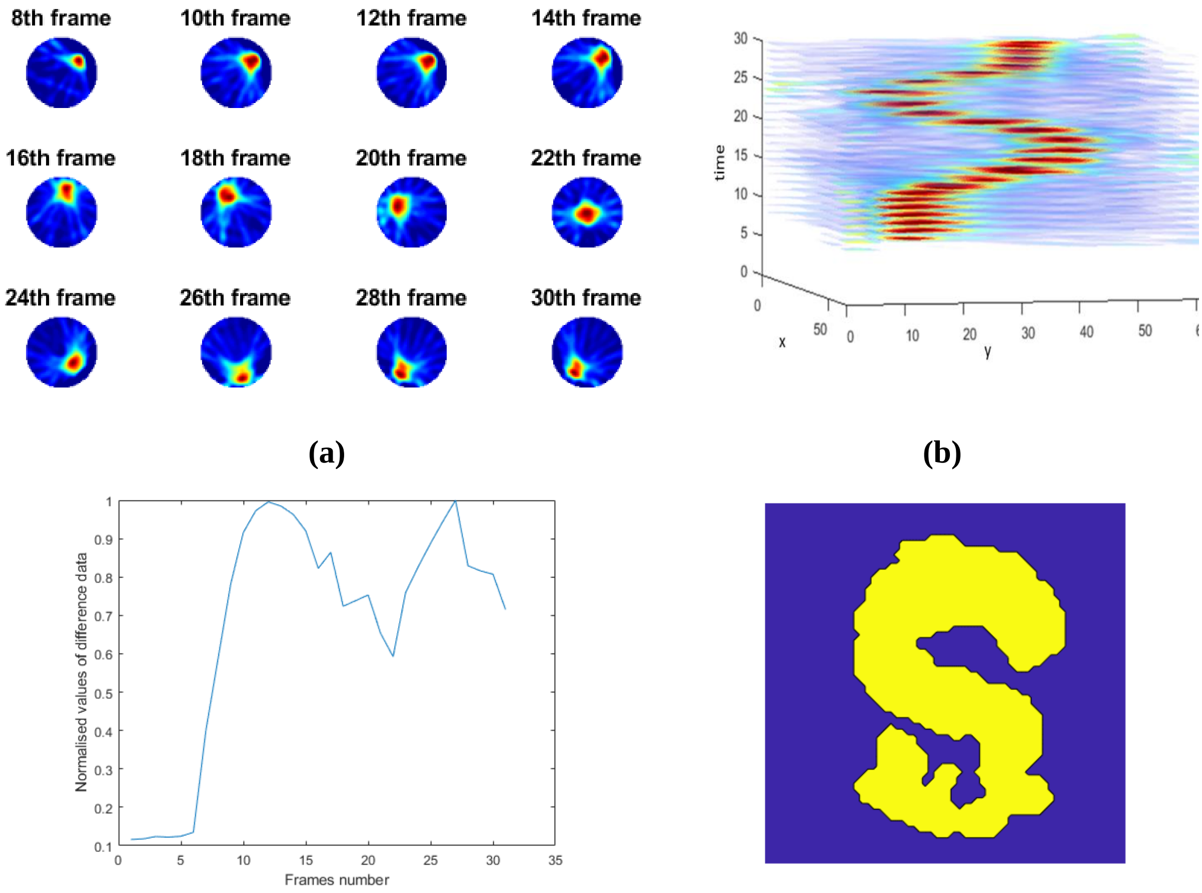

(a) (b)

(c) (d)

Figure 4.14. (a) Frames of USCT images used to construct letter “S”. (b) Plot of reconstructed 3D volumetric dataset. (c) Norm of differences between background and inclusion data. (d) Reconstructed image of letter “S”.

Furthermore, this work presents more challenging cases of multiple letter recognition and word formation. Figure 4.15 shows the reconstructed words “UST”, “DAN”, “HAN”, “manuch”, “netrix”, “Soleimani” and “tomography”. In most cases, the system was able to distinguish between different letters of the alphabet and offer the real genuine hand-writing style without losing the quality features of reconstructions.

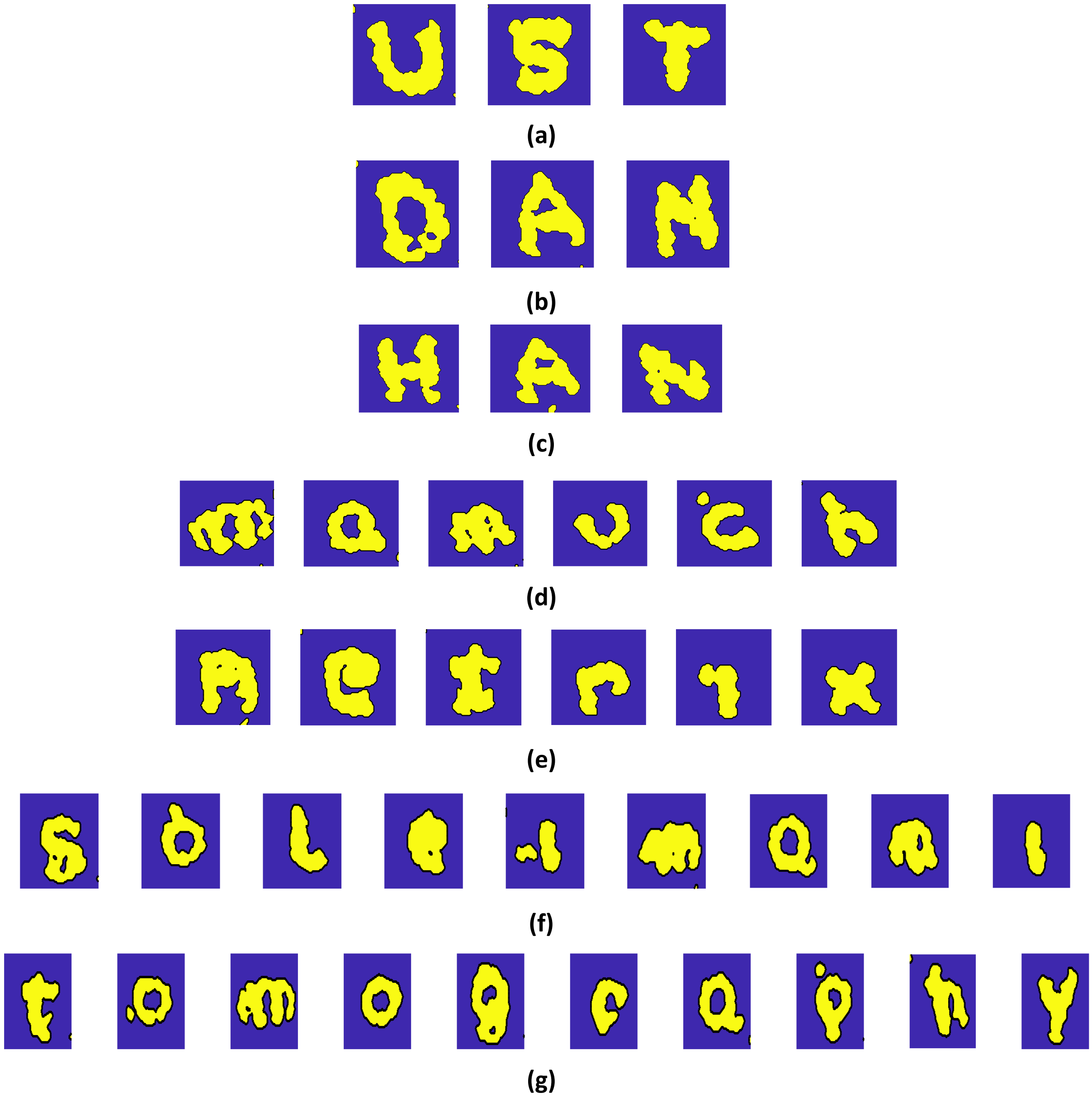

(a)

(b)

(c)

(d)

(e)

(f)

(g)

Figure 4.15. Reconstruction of word (a) UST, (b) DAN, (c) HAN, (d) manuch, (e) netrix, (f) soleimani, (g) tomography.

In the example of the word ‘UST’, a total of 94 frames of USCT images were considered and the norm difference is plotted in Figure 4.16. Given the “between words” specific movement of slightly getting the rod outside of the field-of-view (lifting of the rod), the norm difference data tend to decrease into a minimum level and subsequently can be used to create spaces between letters. When the norm is smaller than 0.1, it indicates that the rod is out of sight of the sensor array, and this allows space between letters. Hence, one can see the distinct frame window of each letter in the word. Moreover, the number of close-to-zero regions in the function of norms over frames can indicate the number of word's characters.

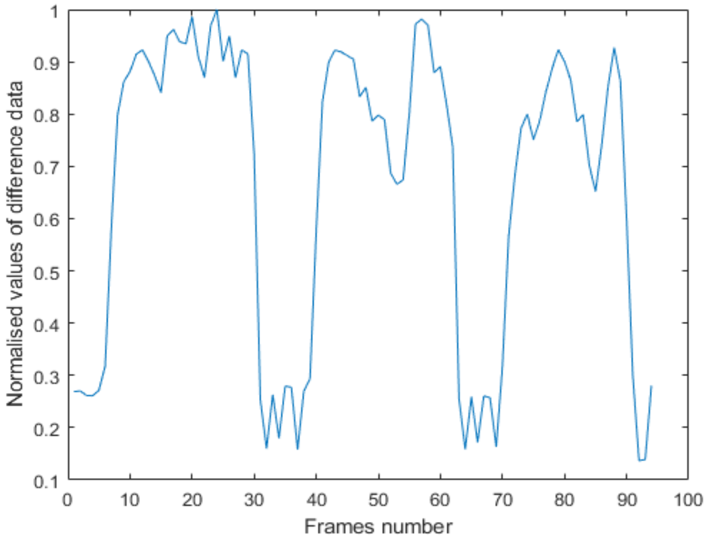

Figure 4.16. Normalised values of difference data in the "UST" word test.

Few unclear results came from cases of small characters within a word formation. In those cases, the rod's motion could follow a more complex way, moreover, the iterative motions in the medium during a word formation could add higher disturbances into it inserting noise to the final images. Thus, the reconstructions of few bigger words might include a few unclear character's reconstructions like in Figure 4.15 (d), (f). Using machine learning one can enhance letter and word recognition, but this can be studied in the future.

4.3.2.Quantitative resolution experiments

Experiments were carried out to test the response of developed sound-speed imaging algorithms, which could be used in industrial reactors inspecting tool in liquid-mixing processes. This is a preliminary study, based on static experiments of different density liquid characterizations. Density factor is important in many industrial reactors. For example, in a crystallization process, suspension density is increase as crystal yields. Inversely, in a grape fermentation scenario, liquid suspension density is lowered as sugar turns to alcohol. Liquid density monitoring could positively impact these processes. Moreover, a sound-speed imaging tomographic system would help characterize the uniformity of several binary or ternary mixtures inside industrial tanks. In this way, the stirring process could start as soon as liquid mixture non-uniformity is detected. The stirring in industrial tanks mostly is to make the liquid mixtures be in a uniform state as changes usually occur regionally.

Figure 4.17 depicts the experiments that have been carried out aiming in the sound velocity characterization of liquid solutions with different densities. Sucrose/ water solutions were used in different unsaturated concentrations. These solutions proved to be a difficult case for characterization because of the small density changes between them. This fact proves the accuracy of the developed TOF sensors and the good quantitative resolution of the tomographic device. Plastic cups filled with a different particle concentration solution each time used for this process. The receiving tank was filled with tap water in the room temperature. Background data have been taken using a plastic cup filled with tap water. Full data have been taken using a plastic cup with the sucrose/water binary mixture. Using subtraction imaging, one can achieve to neglect all the cup thin, plastic surface effect in the capturing signals. Figure 4.17a displays the experimental process while 4.16b displays the quantitative imaging results. Six unsaturated solutions of 20%, 33%, 42.86%, 50%, 56.52% and 60.78% mass/volume concentration (m/vol %) of white granulated sugar (sucrose) and tap water at 20°C were created, while the saturation point of this mixture is 66.7% m/vol. These solutions were used as inclusions in the tank, which was filled with a medium of tap water at 20°C. The concentration points were matched with density values, according to the study of Resa et al. [205]. Three consecutive measurement frames have been taken each time and the average value of them is stored. Figure 4.17b displays, at left, the subtracted filtered TOF data in μs units including the cutting outlier values (blue peaks) and at right the sound velocity reconstruction in m/sec units, for every experiment. An adaptive filtering method was applied for the subtracted data. Every value that can be characterized as an outlier and, at the same time, exists fewer times than the ¼ of the total sensor number, is deleted from the dataset. This filtering technique proves to be a consistent and accurate noise removal method. The sound velocity of inclusion calculated using the mean value of the segmented circular area.

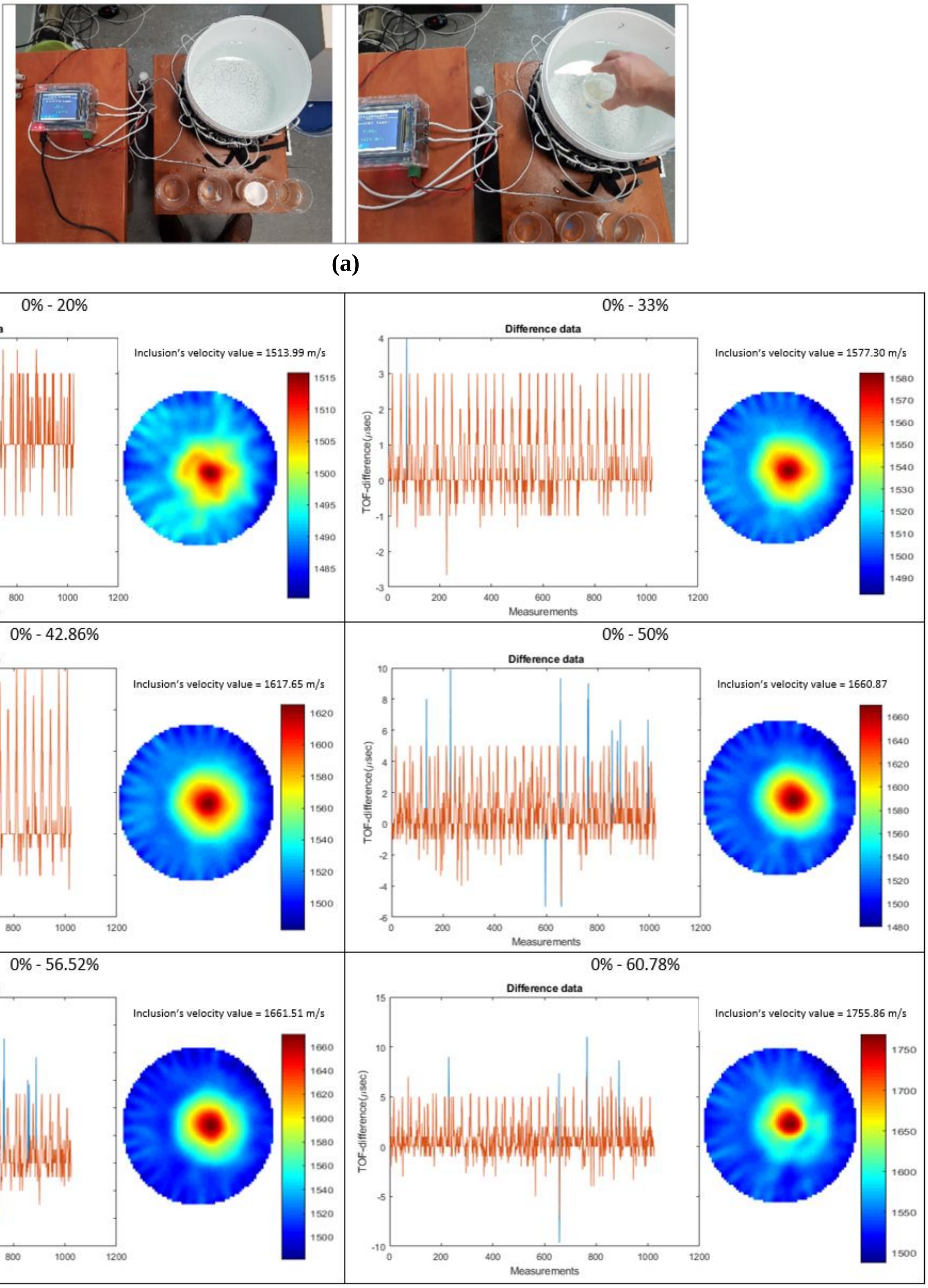

(a)

(b)

Figure 4.17. (a) Experimental setup. (b) Six different water/sucroze solution concentration cases were presented. In every case, the TOF difference data and reconstruction are presented. The scale of reconstructions is in sound-speed units(m/s). The "inclusion's velocity value" represents the mean intensity value of the inclusion's region.

Table 4.1 provides with the numerical values of the experimental process. The table displays density values related to the binary mixture concentrations, single TOF measurements provided by the tomographic device and calculated sound-speed value provided by the sound-speed imaging software. Density values assigned to different concentrations of sucrose/ water binary mixtures based on Resa et al. studies[205]. In this work, Resa et al. calculated a function between density and sucrose concentration in binary unsaturated solutions of sucrose/ water.

Table 4.1 Sound velocity results from experimental work.

Numerical table of experiments			
Mass concentration (m/vol)	**Density** (kg/m³)	**Single TOF measurements** (μs)	**Scale of reconstruction** (m/s)
0%	995.3 (kg/m³)	162	-
20%	1075 (kg/m³)	161	1480 – 1513.93
33%	1134 (kg/m³)	159	1480 – 1577.31
42.86%	1184 (kg/m³)	158	1480 – 1617.65
50%	1224 (kg/m³)	157	1480 – 1660.87
56.52%	1259 (kg/m³)	157	1480 – 1661.51
60.78%	1284 (kg/m³)	156	1480 – 1755.86

They conducted a single-measurement ultrasonic study on sucrose/ water binary mixtures in 30°C using piezoelectric sensors of 2.5 MHz centre frequency. They evaluated their experimental work by mathematical relations described by Urick’s [142] and Natta-Baccaredda’s [206] prior works.

These works present formulas that mainly describe the relationship between changes in the chemical composition of solutions and changes in propagation velocity of sound. Urick’s study of liquid mixtures is based on the linearity of the adiabatic compressibility and density with the volume concentration eq. (4.11) and eq. (4.12). The sound velocity formula arises in (4.13):

$$p = \sum_i \varphi_i p_i \tag{4.11}$$

$$k = \sum\nolimits_{i} \varphi_{i} k_{i} \tag{4.12}$$

$$c = \frac{1}{\sqrt{(\sum_{i} \varphi_{i} p_{i})(\sum_{i} \varphi_{i} k_{i})}} \tag{4.13}$$

where c is the sound velocity, k is the adiabatic compressibility, p is the density and φ is the volume fraction. Based on this study density values were assigned to the specific concentrations of liquid solutions used in our experimental process. Eventually, Resa's work is used as a gold standard to evaluate our experimental work. Third column of table 1 presents the single measurements, which come from the 1st and 16th sensors, accounting for the existence of inclusion in the trajectory of the emitted pulse. The TOF data slightly decreases while the concentration of sucrose becomes higher. The fourth column displays the sound speed scales of all the reconstructions.

Figure 4.18 displays with black dots the results related to the experimental work and with the blue dots, results extracted by the work of P. Resa et al. [205]. A linear interpolation has been applied to the literature values and a polynomial regression method to the experimental ones. As expected, the results follow an increasing function as the concentration of sucrose increases in the binary mixture. The tomographic graph (black colour) and the "gold standard" graph (red colour) are following the same ascending trend, which is very optimistic. The relatively lower values arise from the fact that the experiments have been occurred in lower temperature close to 20°C, while the experimental process of Resa et al. occurred at 30°C. The system provides good absolute values. Translating the concentration values of the sucrose/ water solutions to density values, important concepts can be extracted by this work. The developed sound-speed imaging has been proven having a accurate quantitative resolution. The most challenging reconstruction is the one with the liquid solution of 20% m/vol concentration which leads to a difference in density of 80(kg/m3) between the inclusion and the medium. The fact that the developed system can response so accurately to such challenging changes is very optimistic. Moreover, multiple reconstructions with different concentrations proved a great efficiency of the system to distinguish liquids of density differences up to 40 (kg/m3), which is assured by the different results between the 50% and 42.86% solutions.

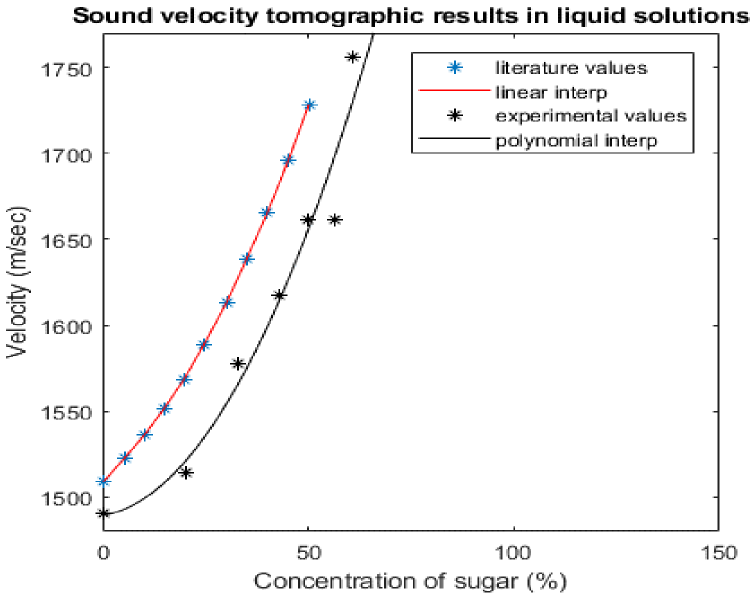

Figure 4.18. Graph of concentrations values. Experimental values are represented with black dots and single measurements values form literature studies represented with blue dots. Literature values extracted from Resa et al. study [205].

In lower than 10% concentration change, which means density change of 35 (kg/m3), like in the case of 56.52% concentration, the calculated sound velocity value is not perfectly matching the expected one, according to the trajectory of the relative graph. These quantitative results prove great feasibility and efficiency of USCT in characterizing different densities of liquid solutions.

Furthermore, additional experiments on different temperature of specific material have been conducted and presented below. The aim of these tests was to highlight the relation between sound-speed and temperature. For the needs of these experiments, tomographic data from the Engineering Tomography Lab's (ETL) USCT have been used. We made two basic experiments. In both we used plastic bottles filled with different liquid material each time. Using subtraction imaging we achieve to neglect the most of the inclusion's effect in the capturing signals. While the speed of sound varies in different temperatures of materials, we choose to do some experiments testing the efficiency of our system to measure materials' speed of sound and subsequently to characterize them. In the first experiment, we used water of different temperatures inside the bottle. In Figure 4.19, we present reconstructions in different temperatures of water. The background data was from a scanning using as inclusion the bottle filled with water in 20°C (medium). On the other hand, the full data comes from a scanning using the bottle filled with water of 10°C and 40°C each time.

Temperature		
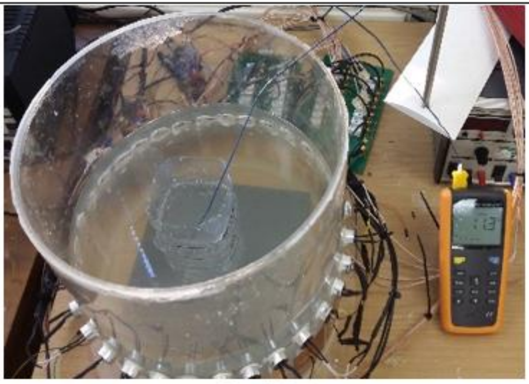 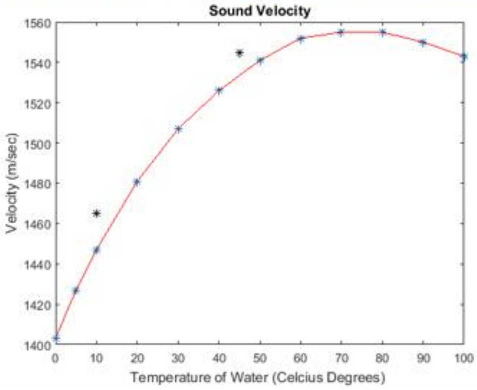 	10-20 Celsius degrees	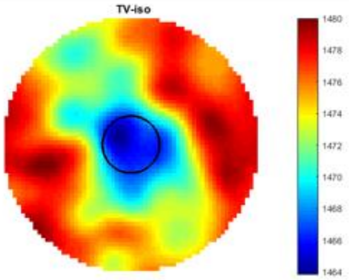 Mean value: 1465 m/s
	40-20 Celsius degrees	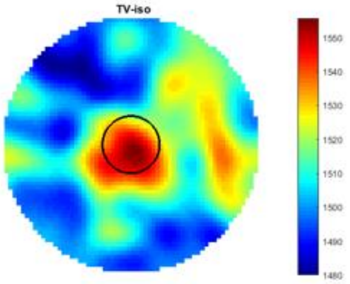 Mean value: 1545 m/s

Figure 4.19. Experiment with different Celsius degrees of water. The scale of reconstructions is in sound-speed (m/s). In both cases the tank's water is at 20°C and the inclusion is at 10°C and 40°C each time. The "mean value" represents the mean intensity value of the inclusion's region (black circle).

The images' scalebar indicates the temperature differences. In order to compute inclusion's speed of sound we are using the mean value of the pixels included to the true shape which is depicted by the black circle. The graph of the Figure 4.19 depicts a function of sound speed of ultrasounds in the different temperatures of water. The indications values were close to the relative function. Even though the temperature experiments in this study are not of a very high resolution, the reconstructed quantitative maps are consistent with the literature values. Here, is remarkable to mention that the quality of reconstruction may not be so good because of the quick propagation of temperature inside the medium. However, the methods seem that can provide with relatively good values. Concluding that the developed algorithms could work well in different cases of higher or lower temperatures inclusions from the medium and reconstruct meaningful images.

4.4. Conclusion

This study demonstrated the effectiveness of a newly developed on-line sound speed travel-time USCT system to inspect liquid mixtures of different densities. The study shows for the first time, a sound-speed tomographic imaging that monitors liquid elaboration processes. The system is based on two-dimensional travel-time ultrasound tomography with a central excitation frequency of 40 kHz. Three types of experiments were applied to test the spatial, quantitative resolution and the system response to a dynamical scenario. The system provides satisfactory results regarding the spatial resolution, being able to detect the position of objects of a few centimetres size. A dynamical experiment, using a moving object and capturing continuous data, showed the dynamical imaging ability of a bit more than 4 frame per second, not accounting for the image reconstruction delays. Such a temporal resolution is suitable for several industrial processes. Furthermore, the sound-speed imaging provides reliable results for characterization of liquid solutions based on distribution of sound velocity distributions. This work provides good performance for sound speed imaging for solutions with different. For the first time, meaningful quantitative data have been presented in the industrial USCT field, providing a clear relation between sound-speed imaging and density characterization of liquid solutions. The advantages lie in material distinguishing for liquid mixing-cases, in characterizing uniformity of mixtures and finally in calculating approximate sound-speed and subsequently density distributions of liquid mixtures.

Chapter 5 TOF USCT for investigation of crystallization processes

Crystallization is a crucial step in many industrial processes, being used as a separation and purification technique. Many sensor technologies constantly are being investigated for monitoring crystallization and other chemical reactor processes. Ultrasound techniques have been used for particle size characterization of liquid suspensions, in crystallization process. An ultrasound tomography system can provide spatial information inside the process when compared to single-measurement systems. Thereafter, the ultrasound tomography investigation on crystallization process is considered of a significant importance. In this study, real-time ultrasound tomography, equipped with a contactless sensor array, is conducted on a lab-scale (20cm) batch reactor which facilitated a calcium carbonate reactive crystallization process. Real-time ultrasound tomographic imaging is done via a contactless ultrasound tomography sensor array. The effect of the injection rate and the stirring speed was considered as two control parameters in these crystallization functions. Transmission mode ultrasound tomography, comprising of 32 piezoelectric transducers with a central frequency of 40 kHz, has been used. The process-based experimental investigation shows the capability of the proposed ultrasound tomography system for crystallization process monitoring. Information on process dynamics, as well as process malfunction, can be obtained via the ultrasound tomography system.

5.1. Introduction

Basic industrial crystallization setups consist of the batch, semi batch and continuous crystallisers [207]. Batch crystallisers are extensively used for the manufacturing of a wide range of high-value fine chemicals. They are generally useful in small-scale operations, especially when working with highly viscous or toxic chemical systems. The yield, purity, morphology, and size distribution of the crystals comprise the quality targets of the process.

Changes in the operating conditions such as mixing, temperature profile and solute concentration, determine variations in the growth, nucleation and agglomeration of crystals. In precipitation systems, mixing at meso- and microscale combined with the additional rate of the reagent are the two key factors that directly control the quality of a reactive crystallization reaction [208], [209]. Subsequently, the control of industrial crystallisers is a major current industrial concern as it is clearly a very important step of process engineering [210] and tomographic imaging is a potential methodology that can offer significant solutions noninvasively via in-line monitoring.

Ultrasonic measurement techniques have been proven efficient to characterise slurry mixtures during crystallization processes [63], [195], [106], [211], [212]. State of the art scientific research presents that ultrasound measurements can differentiate between a region containing well-dispersed crystals and a region containing networks of associated crystals. Ultrasonic compression wave absorption and phase velocity spectra data were found to be sensitive to this difference in suspension structure [67]. Thus, both the commencement of the crystallization and the nature of the final product could be detected by ultrasound. In that sense, USCT has the potential to be an appealing candidate for process monitoring, since being combined with automatic control can offer automation to large-scale productions.

The aim of this research is to examine the USCT capabilities in providing useful information on the distribution of phases within flowing mixtures by distinguishing between different suspension particle concentrations or even between differences in compounds' structural phase. Two sections with experimental processes are presented in this chapter. The first section consists of experimental processes using fine sugar particles and water/sugar suspensions focusing on the ultrasonic imaging in liquid slurry mixture of sucrose/water particles. The second section focuses on reactive crystallization experiments, such as calcium carbonate crystallization.

The chapter is organised as follows. Section 5.2 presents the main functionality of the tomographic system and details its specifications and reconstruction method used. Section 5.3 presents the experimental results and evaluation of them. Finally, in section 5.4, the conclusions and discussion are presented.

5.2. **Methods**

The developed USCT.1 system was used. The setup consists of a ring of piezoelectric transducers array, a sensing electronics setup, and a computer system for image reconstruction. These sensors are mounted to the outer surface of the tank using an ultrasonic coupling gel and a belt, keeping the system in place. Figure 5.1a displays the basic concept of an USCT system for the control of batch crystallization and generally for stirred tanks environment. The sensor array is connected to the main computer unit, processing signal information and providing tomographic evidence, which leads to the characterisation of the process. The computer unit can also control the parameters involved in the process, namely stirring and injection rate, by utilising a PID (proportional-integral-derivative) controller. The automation of the process can be achieved by aligning the tomographic information to the control of these parameters. This figure explains the motivation of the current work. Therefore, there is a necessity to distinguish the different phases involved in the crystallization process. As shown in Figure 5.1b, the sensors are positioned in a ring-array, scanning the cross-sectional plane located 5 cm above the bottom of the tank. The measurement device collects data at the arrival time of the first transmitted pulse allowing travel time imaging. The tomographic data collection is carried out in a parallel fashion, where each transducer has its own transmitting/receiving circuit [86].

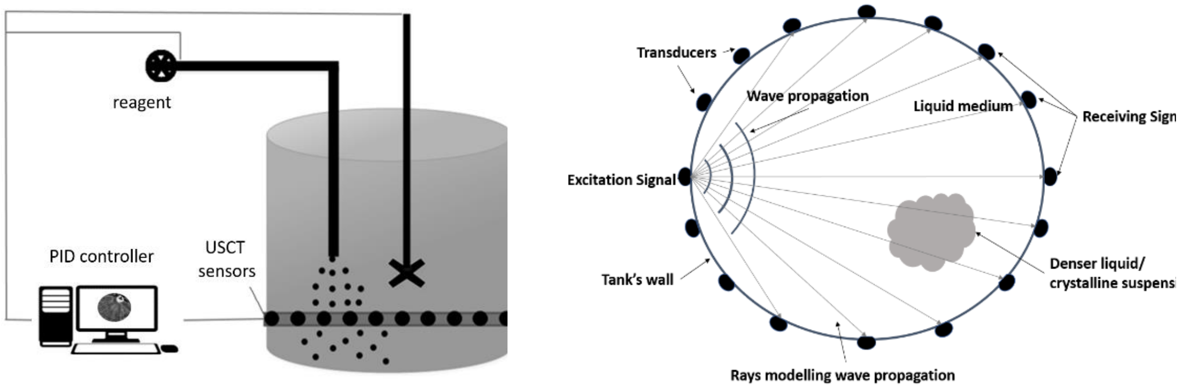

(a) **(b)**

Figure 5.1. Schematics depict (a) USCT applied in an automatic control of batch crystallization scenario and (b) travel-time tomography functionality (panoramic view).

The ultrasonic transducers use a centre frequency of 40 kHz, with a sound pressure level close to 97 dB (30 cm/10 V rms). The temporal resolution of the data acquisition is 4 f/s, which is sufficient for this process.

Figure 5.2a presents the first stirred tank, which is made of acrylic material and Figure 5.2b shows the second tank, which is made from polypropylene pro-fax plastic, due to its low acoustic impedance. The thickness of both tanks is about 1 cm. The acrylic tank's diameter is 20 cm while the plastic tank is 32 cm. The sensors are attached to the outer surface, being non-destructive, and the pulses travel through the wall of the tank. As the sensors are attached in the outer surface of the tank's wall, reconstruction software accounts for the pulses' penetration of the tank's wall, to better calculate the time-of-flight (TOF) values providing more accurate raw values describing mainly the medium material's characteristics.

(a) **(b)**

Figure 5.2. (a) USCT ring array integrated to a 20 cm-diameter acrylic tank. (b) USCT ring array integrated to a 32 cm-diameter polypropylene tank.

A travel-time diffraction tomography method was developed and applied to this work, as described in section 3.4.2. The tomographic system measures the time-of-flight of transmitted pulses. The raw data are used by reconstruction software enriched with Split-Bergman Total Variation regularization method, described in section 3.4.3.2. To analyse the experiments related to crystalline particle imaging and crystallization we use some quantitative information from data and the image. We calculate the average values of TOF delays, namely of the subtraction of background from full data, for every recorded frame.

$$x_k = \frac{1}{M}\sum_{i=1}^{M} \text{Full}_{n,m} - \text{Back}_{n,m} \ , k = [1, \ldots, K], n = [1, \ldots, N], m = [1, \ldots, M] \qquad (5.1)$$

where M is the 256 receiving data coming from the tomographic device and N is the number of captured frames.

5.3.Results & analysis

Results have been distinguished in two sections as “Crystalline particle imaging”, 5.3.1, and “Reactive crystallization imaging”, 5.3.2. Section 5.3.1 presents primary experimental work on test scenarios for crystallization case. In these experiments, mostly the interest is focused on forming localised suspensions detection, temporal sensitivity over changes on the process, external physical disturbances, discontinuities in feeding, tracking of movement of injection point and suspension propagation monitoring. All these aim to test system’s efficiency in live malfunction scenario and suspension concentration monitoring. Section 5.3.2 aims to test the system's efficiency in actual crystallization. No-stirring experiments, which actually comprises a prior test in the crystallization conditions, were conducted to test the USCT's response in crystalline suspension detection and movement tracking of manually shifted injection point. These experiments also tested the quantitative response of USCT over different injection cases. In this way quantitative information over the forming time and concentration of localised suspensions aimed to be analysed. Finally, the stirring crystallization experiments aim to investigate for first time the USCT function on batch crystallization including a medium range mixing conditions utilising a magnetic stirrer.

5.3.1.Crystalline Particle Imaging

This section presents experiments for USCT on the combination of fluid and solid particles. Specifically, its main purpose is to analyse the TOF responses in inhomogeneous two-phase media. In the first two experiments fine sugar particles were used as the adding substance to the liquid medium, without any stirring being applied. In the third experiment a water/sugar suspension was injected, while stirring has been applied using a magnetic stirrer.

In all three experiments, a temporal resolution of 4 fps was applied (without accounting for reconstruction time for fps). An acrylic circular tank of 20 cm diameter, filled with tap water, and a ring of 16 ultrasonic transducers were used in all experimental setups of this section.

5.3.1.1. Continuous Sucrose Particles Pouring

In the first experiment, fine sugar particles were thrown in the medium, at a steady, continuous pace. The experiment aims to test the system's sensitivity on localised forming suspensions over the addition point and also addition point's movement tracking. The addition in this experiment is continuous. Figure 5.3a shows a schematic of a planar and cross-sectional view of the tank, including the injection positions and the circular ring of ultrasonic transducers. Figure 5.3b shows a photo of the actual experiments. The recording happened in-line with the process, and it started before and finished after the pouring of the solid sugars. Pouring was continuous and lasted for 55 s. The injection started from position A and after 29 s started moving to position B. This movement lasted for 15 s. Then stayed at B until the end. The injection stopped 5 secs before the end of capturing frames' sequence. Figure 5.3c presents the results in frame data with the recorded time as a reference. The results are being presented in a travel-time mapping thus, the scale presents delays of the first arrived pulses. Note that as the sugar particles poured into the water, some time was needed before they started precipitating to the bottom. Thus, one can notice the existence of lower difference TOF values, at first, then higher and then lower again. This fact was due to the sedimentation of the sugar particles, as no stirring was used. The scale bar of the reconstructions show TOF delays that goes up to 155 μs, which are considered high values and occurred due to the abrupt changes in homogeneity of the medium, due to the continuous high pouring rate.

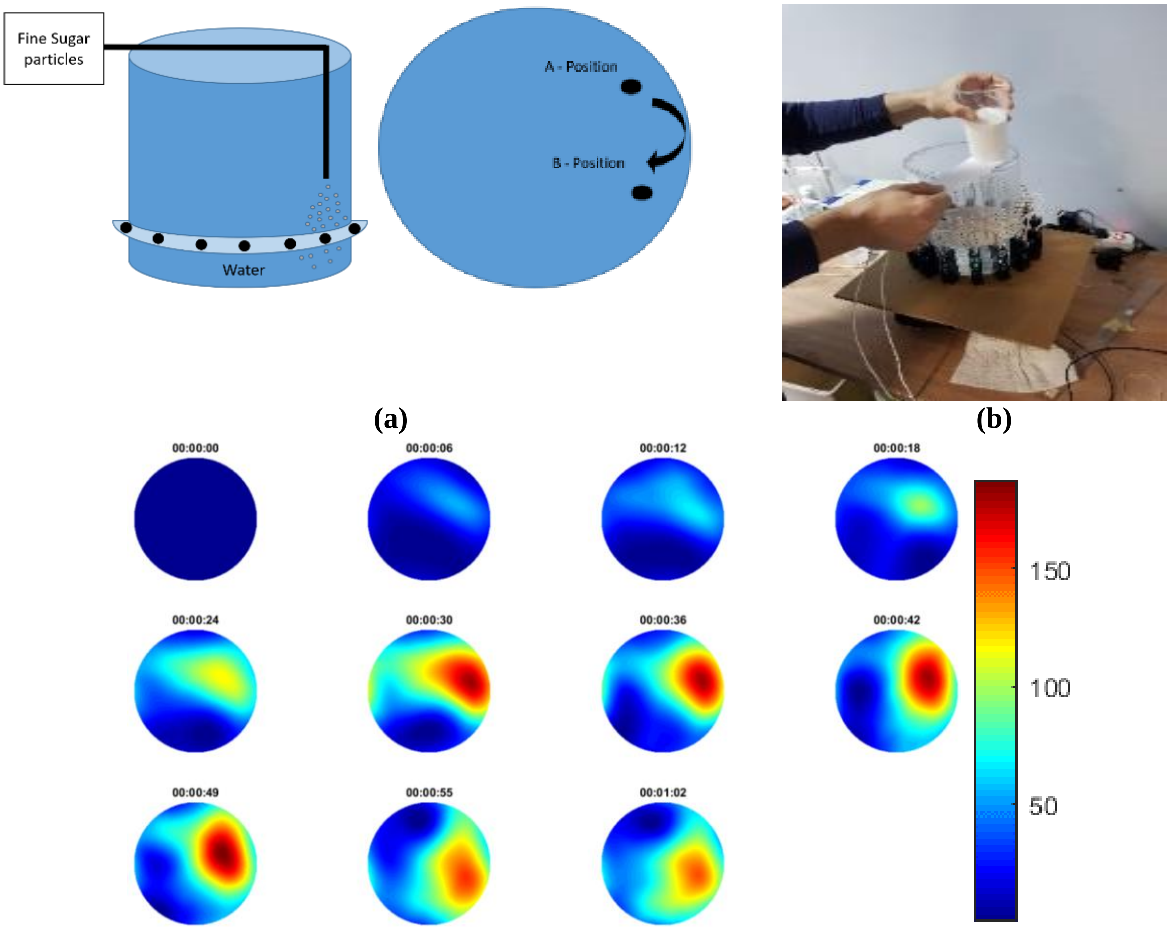

(a) **(b)**

(c)

Figure 5.3. (a) Schematic of the experiment with panoramic view of the injection points. The transition from A to B occurred 29–44 s from the starting time. (b) Photo of the experiment. (c) Reconstruction with the specific capture time. Scale bar describes pulses' travel-time delays.

5.3.1.2. Noncontinuous Sucrose Particles Pouring Using a Mechanical Rotator

This experiment aimed at ascertaining the efficiency of the USCT device in real-time measurements and in a continuous change of the injection point. Furthermore, a noncontinuous addition of sucrose particles utilised to test the system's sensitivity on concentration changes in specific region (addition point) over time. Sugar particles were fed into the medium (contaminated water) as shown in Figure 5.4a. A mechanism was used to apply noncontinuous pouring. The mechanism rotated the plastic layer that consisted of four holes. The holes let a specific amount of sugar be released into the water each time.

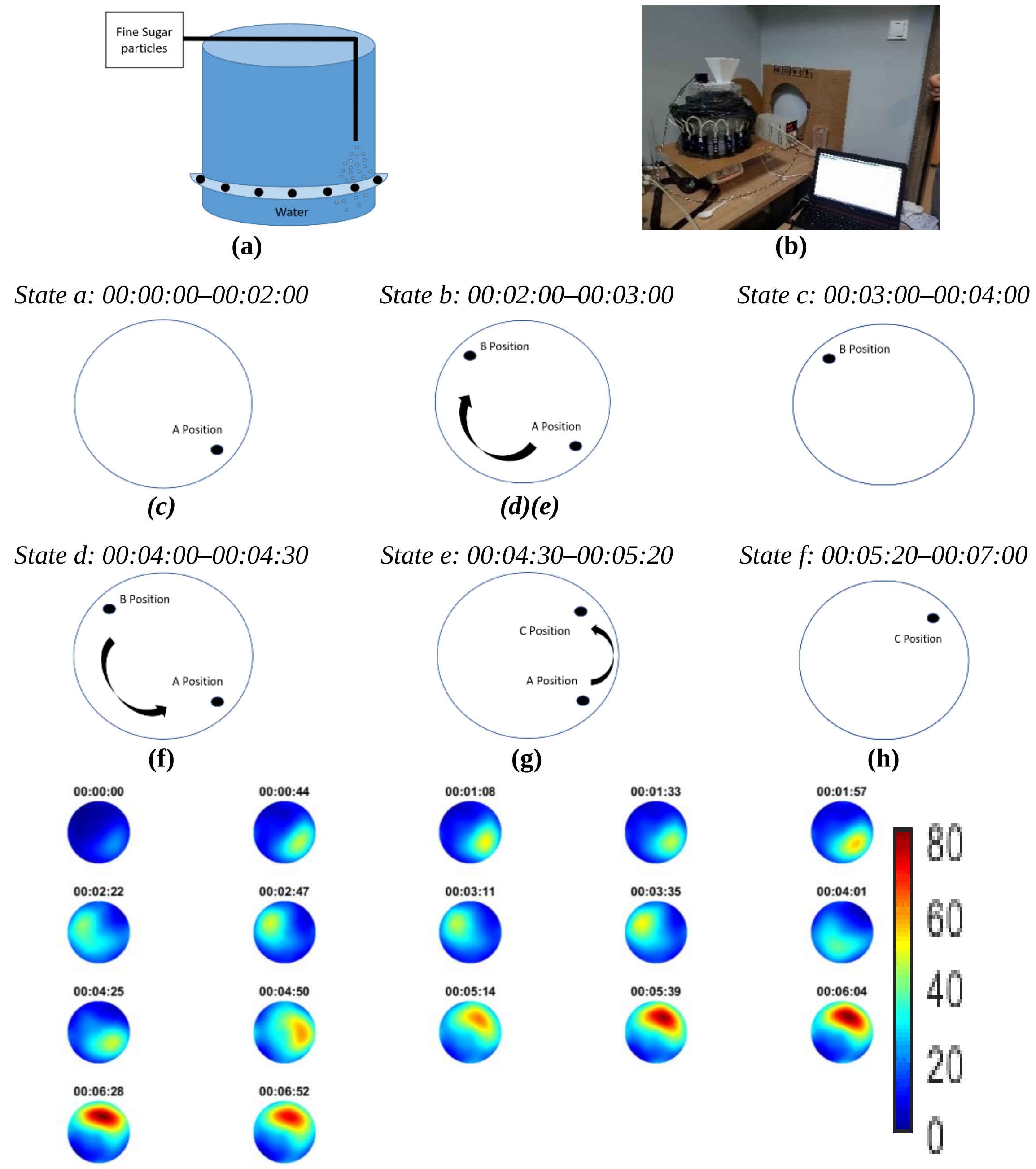

(a) **(b)**

State a: 00:00:00–00:02:00 *State b: 00:02:00–00:03:00* *State c: 00:03:00–00:04:00*

(c) ***(d)(e)***

State d: 00:04:00–00:04:30 *State e: 00:04:30–00:05:20* *State f: 00:05:20–00:07:00*

(f) **(g)** **(h)**

(i)

Figure 5.4. (a) Schematic of the tank. (b) Experimental apparatus photo. (c)–(h) Graph explaining the shifting of injection position. (i) Reconstruction of time-of-flight (TOF) delays with the specific capture time. Scale bar describes pulses’ travel-time delays of the first pulse.

Furthermore, the point of injection constantly changed during the process. Figure 5.4a,b depicts a schematic and a photo of the experimental setup, respectively. Figure 5.4c–h presents the six stages of the experimental process with the corresponding time reference, which describes the movement of injection point. The whole process lasted for 7 min. As the sugar particles needed some time to start sedimentation and the layer of the sensor's ring was a few centimetres below the surface of the water, the first denser regions started becoming obvious a few frames after the beginning, as the reconstructed frames show in Figure 5.4g.

The reconstructions agree with the injection's shifting position. The intermittent injection led to a continuous change of particles' concentration over time, being at a high then lower and then higher level, again. This change of the particles' concentration within the field of view translated into higher then lower and then higher again delays of TOF signals. After 4:30 min from the start of the process, the injection point passed through position A again, which drove of sugars in the region to higher concentration. Therefore, one can notice a significant increase of TOF delays in the last reconstructed frames. Moreover, the injection stayed a bit longer between position A and C and, subsequently, as the experiment approached the end, bigger TOF delays could be noticed.

5.3.1.3. Injection of 75% (kg/mol) Sucrose/Water Suspension

In this experiment, a sucrose/water suspension of 75% kg/mL was used as a tracer. The purpose is to test the system's temporal response over the process and track the suspension's propagation. Automatic injection by using an electronic pump was applied. The feed rate speed was 35 mL/min. During the process, which lasted for 7 min, mixing occurred. Stirring speed was at 40 rpm. This rate was assumed to be moderate as no swirl effect [213] was depicted. The first higher concentrated regions started forming in the position of injection, driving the first TOF delays. The tank's dynamics allowed the propagation of the suspension in the medium. As the medium turned more inhomogeneous, so bigger delays of the first arrival pulse could be noticed. Figure 5.5a–c depicts the experimental process and the different stages of the suspension's propagation with the corresponding time reference.

Experimental photos and schematics are displayed to clearly present the experimental setup. Figure 5.5g depict the reconstructed images over time. High TOF delays up to 155 μs at the end of the process show the high-concentrated regions with the sucrose suspension. Within the frames one can notice the propagation rate as well.

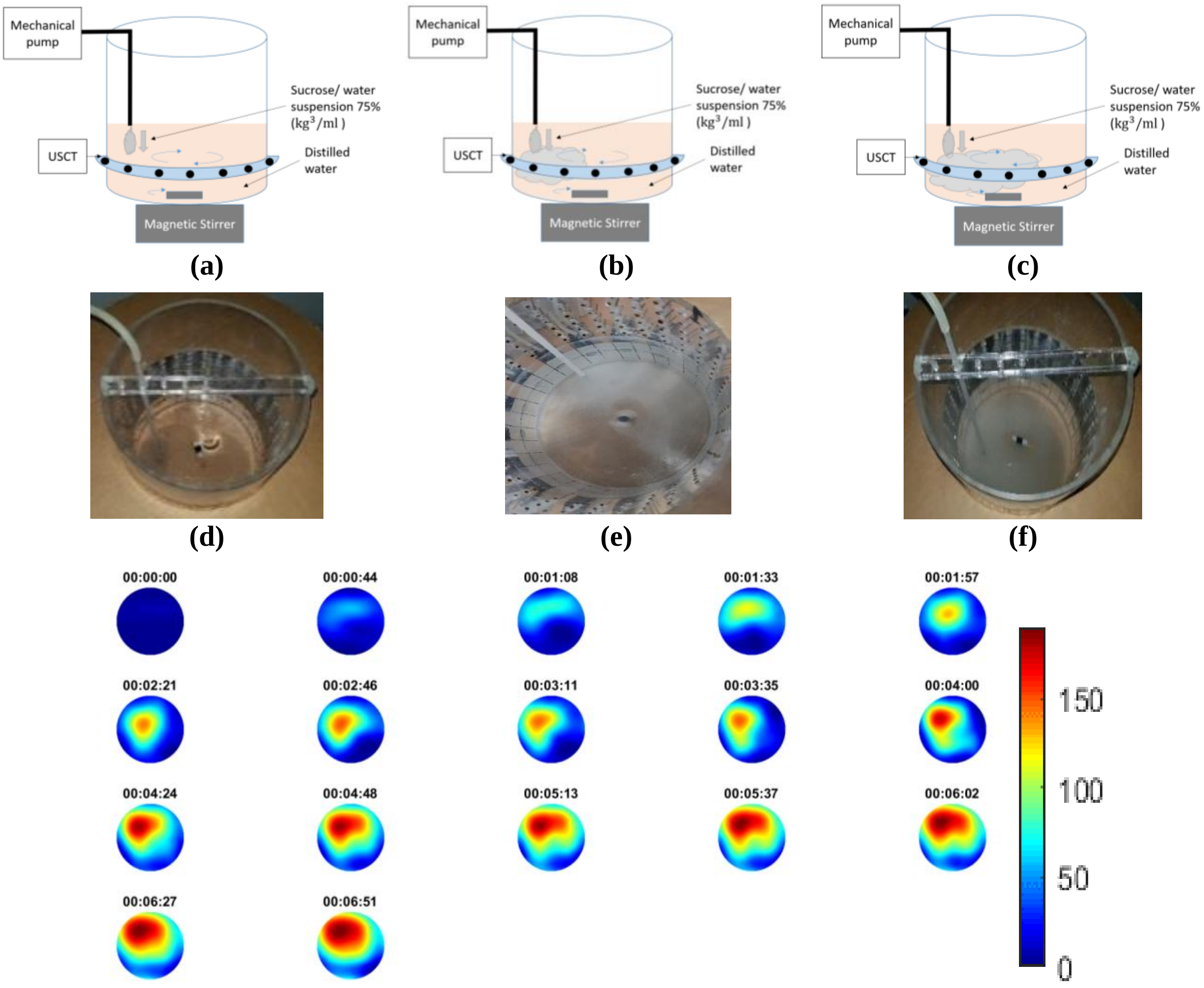

(a) (b) (c)

(d) (e) (f)

(g)

Figure 5.5. (a)–(c) Schematic of the experiment with corresponding photos. (d)–(f) Experimental photos of the start, the middle and the end of the process, respectively. (g) Reconstruction with the specific capture time. Scale bar describes pulses' travel-time delays.

5.3.1.4. Analysis of Experimental Results

Figure 5.6 presents a graph of the mean value of all the recorded measured data of the first, second and third experiment, respectively. These values depict travel-time delays over frame. For every recorded frame, there were 256 values from 16 sensors each time. These values were the TOF delays, coming from the subtraction of the background from the full measurement data, using eq. (5.1). The blue graph presents the first experiment of that section. This function is described by an ascending trend with a significantly high slope, due to the abrupt pouring of the fine sugar. The function became smaller over time, as the corresponding experiment lasted for a shorter period. The red graph, which comes from the second experiment, has an ascending trend as well. The major difference between the two functions is that the slope of the one related to the first experiment is bigger than the one related to the second one. Moreover, the blue graph consists of higher TOF values. These facts come from the different method of pouring. In the first experiment, the pouring rate was abrupt and continuous, while, in the second case, the pouring was periodical. The black graph is related to the experiment of sucrose/water suspension injection. Comparing the black and the red graphs, one can notice the higher values of the black graph, despite that the two experiments lasting for the same amount of time (8 min). According to the use of solid particles in the first experiment, one could expect higher TOF values. The stirring process helped to create a uniform material distribution and reduced the sedimentation effects. This drove the higher delays of the signal as the rate of disturbances were also high. Furthermore, some additional TOF delays were introduced due to the stirring itself.

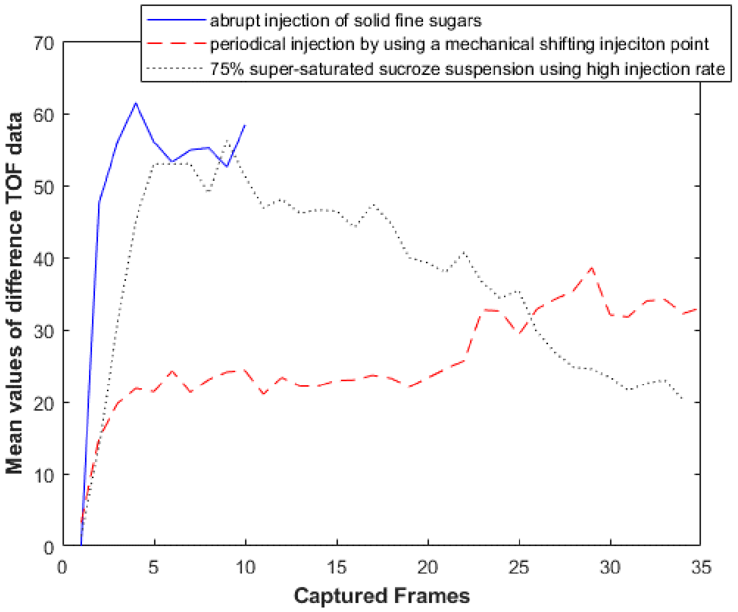

Figure 5.6. Plot of all frames' mean value of difference data. The ascending trend of the graph reveals the gradually increasing delay that was introduced to the raw TOF data. The first experiment with the pouring of solid particles of fine sugars lasted for a lot less than the others, according to its nature.

5.3.2. Reactive crystallization imaging

In this section, lab-scale batch crystallization experiments were conducted. The experimental apparatuses were designed to be aligned to industrial framework. The current study focuses on stirred crystallization tanks [214]. Calcium carbonate reactive crystallization was performed [215]. Nonstirring experiments were previously conducted to test the response of the system in the actual crystal formation. Full scale crystallization experiments (using stirring) were conducted at the end. In a batch concept, the stirring process is necessary, although the nonstirring experiments can give important indications of TOF responses on crystalline slurries without accounting for tank dynamics. Figure 5.1 shows the experimental setup by naming all the used equipment. A 32 cm propylene and a 20 cm acrylic tank with the integrated ultrasonic tomographic device were used among the experiments. An electronic peristaltic pump and an IKA Midi 1 (IKA, Cologne, Germany) digital magnetic stirrer were fitted to the stirred tank. The basis of the crystallization process is the reaction of a sodium carbonate solution (reagent) with a calcium chloride solution. The chemical reaction is described in eq. (5.2).

Figure 5.7. Photo of the batch crystallization experimental apparatus. (a) Carbon dioxide tube for gas injection, (b) reagent vessel filled with sodium carbonate solution (reagent), (c) electronic peristaltic pump, (d) receiving tank filled with calcium chloride solution, (e) IKA Midi 1 digital magnetic stirrer, (f) tomographic device developed by NETRIX company, (g) power supply, (h) computer unit used for running MATLAB code and providing tomographic results.

$$CaCl_2^{aq} + Na_2CO_3^{aq} \rightarrow CaCO_3 + 2NaCl^{aq} \tag{5.2}$$

The first step of the experimental procedure was the preparation of the reagent. Three hundred grams of sodium hydroxide was dissolved in a vessel filled with 1 L of demineralised water. A carbon dioxide dosing tube and pH meter probe were used to control the pH of the sodium hydroxide. The sodium hydroxide solution was gassed with carbon dioxide to reach and maintain a pH of about 11, resulting to an 1 M $\mathrm{Na_2CO_3}$ (sodium carbonate) solution was prepared in the reagent's vessel. The solution remained stable for 48 h because of the large amount of heat released by the reaction and the presence of gases. The reagent solution was injected into the receiving tank using a peristaltic pump. A silicone tube was introduced into the sodium carbonate reagent and passed through the pump, the other end of which was on the surface of the liquid in the receiving tank. The receiving tank was filled with two litres of 1 M $CaCl_2$ (calcium chloride) aqueous solution. The tank with the installed ultrasonic tomograph was placed on the digital stirrer. The crystallization reaction took place while pumping the aqueous solution of $Na_2CO_3^{aq}$ into calcium chloride at a fixed speed. During the experiment, mixing started in the tank with the $CaCl_2$ solution.

5.3.2.1.No-stirring Crystallization

Figures 5.8 and 5.9 present the nonstirring calcium carbonate crystallization experiments. Due to the lack of dynamics, immediate crystalline suspensions were formed at the location where the injection point was. Crystallization occurred regionally and at a faster pace. In the first nonstirring experiment, which is presented in Figure 5.8, the injection point was shifted manually. Therefore, the formation of crystalline suspensions followed the movement of injection. For this experiment, the 32 cm propylene tank was used. The reagent's feed rate was 20 mL/min. Denser suspensions were immediately created, during the injection of the reagent. The denser suspensions started sedimenting. While the suspensions went down, they passed through the FOV (field-of-view) of the sensors. Figure 5.8a–d shows photos from the experiments in different moments. The reconstructed results agree with the shape of the forming crystalline suspensions, presented in Figure 5.8e.

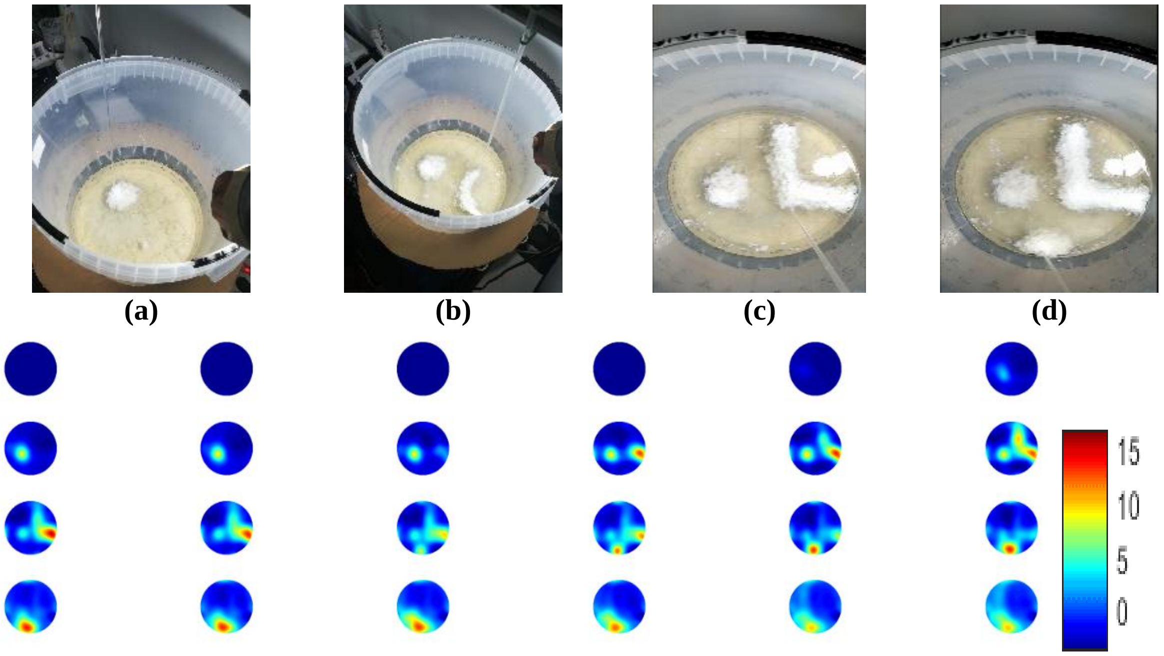

(a) (b) (c) (d)

(e)

Figure 5.8. (a)–(d) Photos of the experiment capturing the shift of injection point and subsequently the localised forming suspensions. (e) Reconstructed frames with the specific capture time.

An interesting point is that regions with a constant injection over a point reached high TOF delays values, and when the injection point moved, the region went to lower values again. This was due to the immediate crystal formation, especially in this type of reactive crystallization. However, when the injection point moved, the crystallization in the region stopped and subsequently already created crystalline suspensions whether start dissolving or start sedimenting. Therefore, one can notice this decay of TOF delays values after the moving of the injection in the reconstructed frames.

Figure 5.9 presents a sequence of nonstirring calcium carbonate crystallization using four different injection rates of 9, 18, 27 and 36 mL/min. The injection point was the same in every case. As no stirring was happening, the crystalline suspensions tended to form in a specific location while the medium got denser, as shown in the experimental photos in Figure 5.9. Photos were taken at two specific points describing the middle and ending experimental phase, in every case. Two litres of calcium chloride solution was used as reagent in all processes. Different injection rates can be translated to a faster experimental process. Recording took place from the beginning, until the end of injection process.

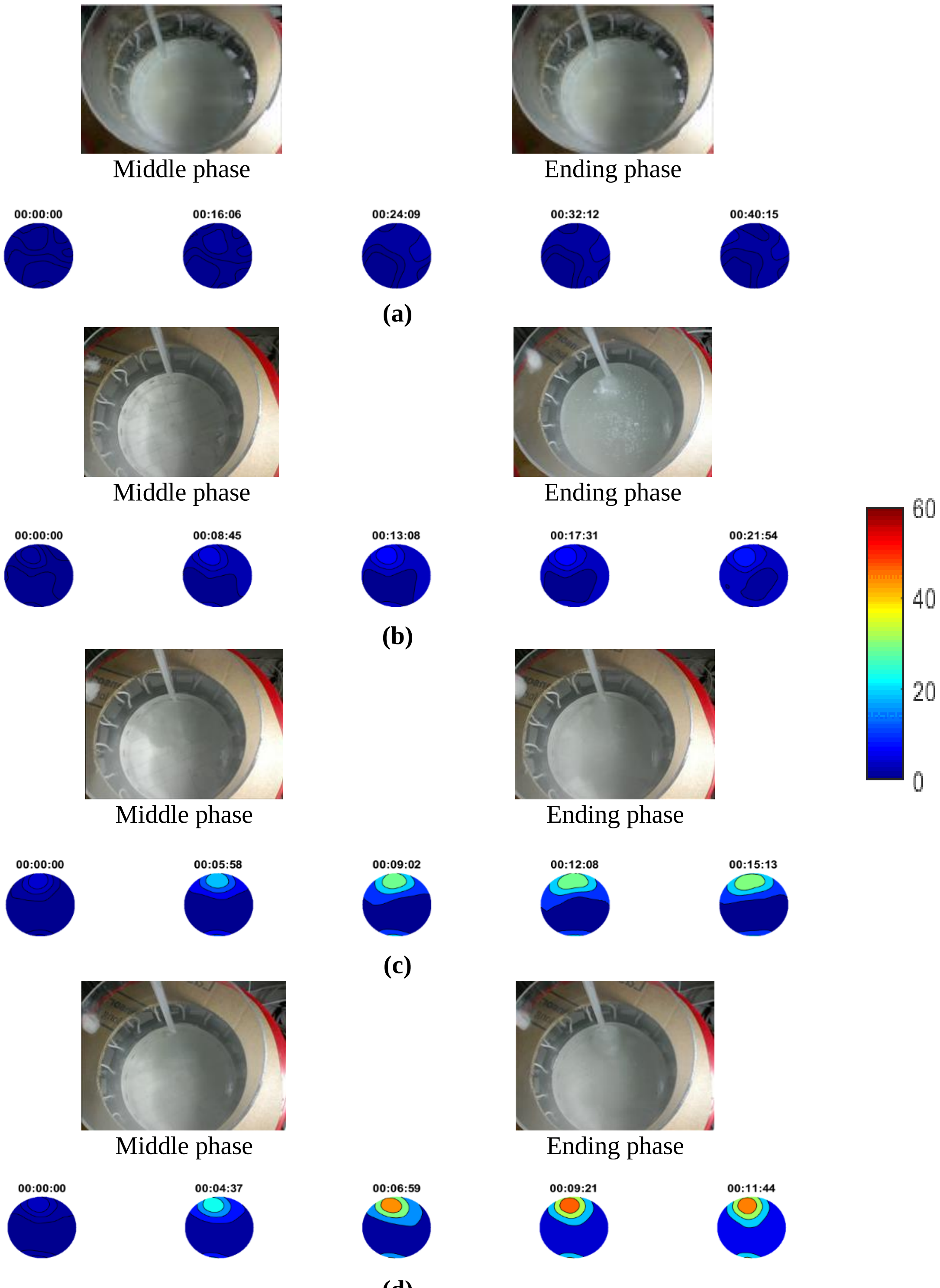

Figure 5.9. Reconstructions of nonstirring calcium carbonate crystallization experiments. (a) 9 mL/min, (b) 18 mL/min, (c) 27 mL/min and (d) 36 mL/min injection rate. Note that a uniform image scale bar is used for all four sets of experiments to provide comparative evaluation. Scale bar describes pulses' travel-time delays.

Therefore, the number of reconstructions was related to the rate of injection. An averaging method over 100 frames was applied, to eliminate the existed noise coming from stirring conditions.

Reconstructions provide clear depictions of the localised forming suspensions in almost all of the cases, as a gradual increase of TOF values over time. In the first case of 9 mL/min, no localised suspension was noticed due to the nature of the low injection rate. Comparing all the cases, the results show a quantitative relation between the travel-time imaging and the concentrations of the forming suspensions, since the increase of the injection rate turns the suspensions more concentrated. A common scale is used for the presentation of results to point out this fact. Contours were applied to clearly distinguish the higher concentrated regions of the tank. The tomographic system proves accuracy by monitoring efficiently almost all the experimental cases and providing a quantitative scale of TOF values related to the concentration of crystalline particle in the forming suspensions.

5.3.2.2.Stirring Crystallization

Four experiments with stirring calcium carbonate crystallization were conducted aligned to industrial standards. Four different reagent injection rates of 9, 18, 27 and 36 mL/min were applied. The injection point was the same in every case. Two litres of calcium chloride solution used as reagent in all the processes. Experiments lasted different amounts of time related to the rate of injection. Recording took place from the beginning until the end of the injection process and an averaging method over 100 frames was applied.

The stirring process created significant changes in the forming suspensions and the aim of these tests was to inspect and analyse the system’s responses in stirred tanks and crystallisers. A good combination of the mixing factor and the tank’s kinetics led to a uniform distribution of crystalline suspensions across the whole medium. This fact significantly affected the crystal yield. The optimal agitation is the minimum stirring rate needed to keep all crystal particles suspended from the bottom. Therefore, the size distribution and concentration of particles vary within an agitated suspension according to the dynamical state of the medium [216]. Stirring rate can affect seriously the tomographic signals by creating disturbances in the medium. Usually swirls are created which affects the signals and subsequently the reconstructions [213], [217], [218]. Assessing the stirring rate of the 20 cm tank, a few different rates of stirring were applied while recording. Figure 5.10 shows recorded data from the tank filled with calcium chloride solution in rates of 45, 100 and 270 rpm. The graphs clearly show the increasing noise factor as we go to higher stirring rates. However, we noticed that when the stirring speed reached 100 rpm, the noise was not significant. Therefore, this rate was picked leading to an eliminated noise effect.

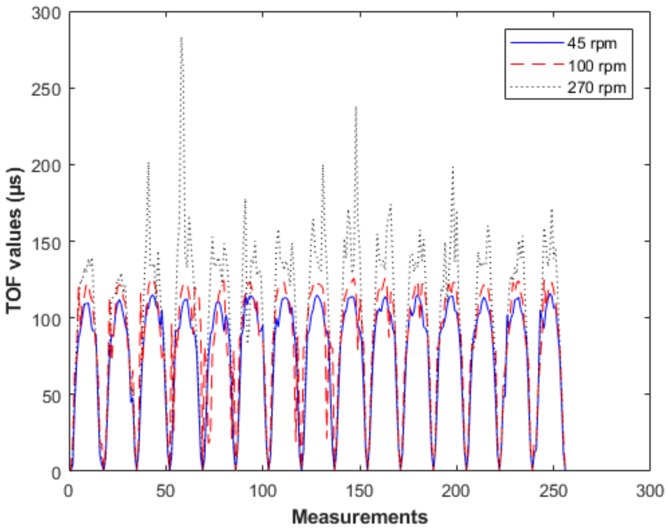

Figure 5.10. Plots of time-of-flight (TOF) data from background measurements using three different stirring rates of 45, 100, 270 rpm. The tank was filled with calcium chloride.

Figure 5.11 presents experimental photos and the results from stirring reactive crystallization. Experimental photos describe the middle and ending phase in every case. In all the cases, the tomographic system was capable of reconstructing regions with higher concentrations of crystalline particles, as shown by the contours reconstructions. As regards the reconstructions' scale, the system showed capability in distinguishing between cases of different injection rates, as higher concentration suspensions tended to be formed by higher injection rates. In the 18, 27 and 36 mL/min cases, the injection rate seemed to be high enough comparing to the tank's dynamical state since the system detected constant localised forming suspensions. Nevertheless, in the 18 mL/min case, suspensions seemed to start dissolving at some point and thereafter because of the dynamics. In the last two higher-injection-rate cases, stirring couldn't affect the propagation of suspensions at all. On the other hand, the first case of 9 mL/min seems to consist of a good combination of injection and stirring rate, as reconstructions did not detect localised forming suspensions.

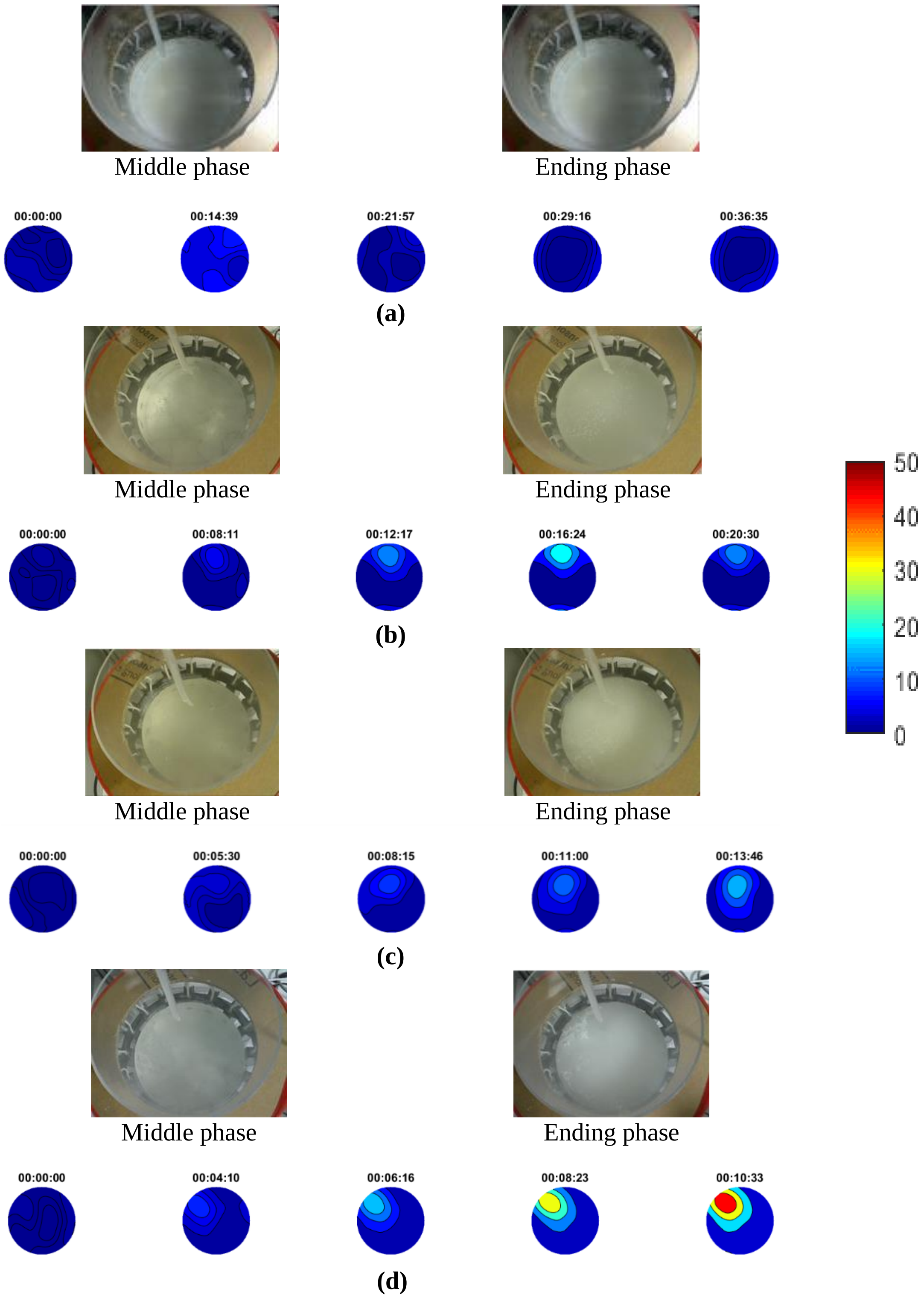

Figure 5.11. Reconstructions of stirring calcium carbonate crystallization experiments with (a) 9 mL/min, (b) 18 mL/min, (c) 27 mL/min and (d) 36 mL/min injection rate. Stirring rate was at 100 rpm using magnetic stirrer. Note a uniform image scale bar is used for all four sets of experiments to provide comparative evaluation. Scale bar describes pulses' travel-time delays.

Higher TOF values could be noticed in the beginning of the experiment, close to the injection point, but they lowered quickly as stirring turned the medium more homogeneous. This fact led to a better crystal yield. Regarding the three higher injection cases, the more concentrated regions reveal bad conditions of the experimental procedure and subsequently rougher crystals should be expected.

5.3.2.3.Analysis of Experimental Results

Figure 5.12a depicts the difference data mean values of the four nonstirring experiments of this section. These graphs were computed by eq. (5.1). One can expect higher medium inhomogeneities in nonstirring cases rather than in stirring cases, thus, comparing the graphs between Figure 15.12a, b, one can notice a higher rate of change. Stirring always made the medium more homogeneous avoiding supersaturation. In addition, the most significant conclusion is the ascending trend of the mean value in almost all the cases over time, which assures the efficient detection of higher concentrated mixtures by the device.

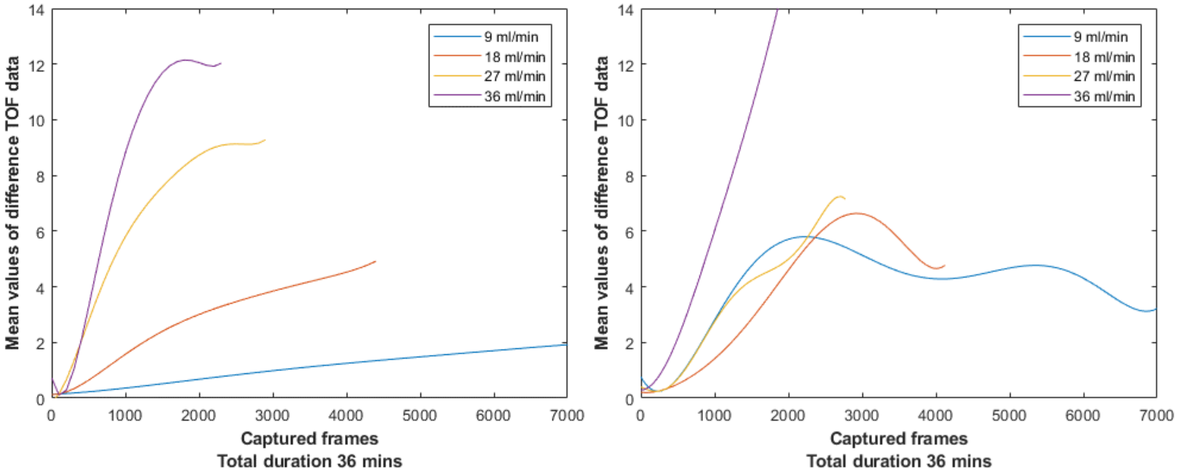

(a) **(b)**

Figure 5.12. (a) Plot of all frame's mean value of difference data for nonstirring cases. (b) Plot of all frame's mean value of difference data for stirring cases using a IKA Midi 1 digital magnetic stirrer at 100 rpm.

A quantitative relationship between the TOF delays and the localised forming suspensions can be noticed in nonstirring cases. The quantitative relationship is an ascending trend of the maximum TOF values while the injection rate increases, as shown in Figure 5.12a. Figure 5.12b presents the mean values of difference data from stirring experiments. Because of the amount of noise introduced by stirring and the different means of suspension formation, the system was unable to provide a clear relationship of the TOF delays of these experiments, in comparison to the nonstirring cases. For instance, graphs of 18 and 27 mL/min become really close after the 1500th frame. Moreover, in 9 mL/min case, one can notice a high slope of the graph at the beginning of the experiment, which could be a result of the stirring noise factor. However, after the 1800th frame, it starts to stabilise and then slightly reduces over time, due to the gradual dissolving of the suspensions in the medium.

Examining the stirring experiments, one can realise the importance of the different combinations of stirring and injection rates. In the 9 and 18 mL/min cases, a dissolution of the forming suspensions can be noticed after a point, which caused slightly decreased TOF values. On the other hand, this could not be seen in the two higher injection stirring cases (27, 36 mL/min), since 100 rpm was not enough to dissolve formations of such a high injection rate. Subsequently, an efficient combination of stirring and injection should assure the nonforming of localised suspensions, or even the direct dissolution of them.

These results display a promising potential of travel-time ultrasound tomography not only for monitoring the process by detecting and reconstructing regions with higher crystalline particle concentration but also for quantifying different formations of crystalline suspensions by utilising the scale of the travel-time delays.

5.4. **Conclusions & Remarks**

This chapter presented a USCT application on monitoring batch crystallization processes. The system was first demonstrated in monitoring processes consisting of crystalline suspensions in a nonstationary setting. This followed the monitoring of the calcium carbonate crystallization reaction. The study examined the combination of injection and stirring factor to the process through the results of the ultrasound tomography system.

The travel-time ultrasound tomographic system provided satisfactory responses in almost all the cases. This has been shown based on a gradual increase of TOF differences due to the gradual crystalline suspension formation over time. The device also shows a good response to distinguishing between different material phases, such as liquid solutions and crystalline liquid suspensions. Experimental results in Section 3 display the distinction between suspensions of various crystalline concentrations.

A calcium carbonate crystallization reaction aligned with industrial standards is shown in Section 4. The device provided good results in the nonstirring experiments. The experiment of shifting the injection point, showed accuracy in tracking the crystalline formation, following the injective disruption, over time. Analysing the other nonstirring experiments showed a promising potential of travel-time ultrasound tomography not only for monitoring the process by detecting and reconstructing regions with higher crystalline particle concentration but also for quantifying the different forms of crystalline suspensions by utilising the scale of the travel-time delays. The results agreed with the theoretical approach that sound propagates slower in high-concentration suspensions. Our approach showed good potential for distinguishing between material phases and monitoring high-material-phase-contrast processes. As regards the stirring experiments, verifications were applied in the adding component, namely different feed and stirring rates have been applied. Both factors affect significant process outcomes. The stirring factor was found to be extremely important for ultrasonic monitoring since it affects the propagation of the excitation pulses. Through these tests, significant conclusions about the process itself have been made, such as the definition of the adequate stirring rate that this specific process needs to avoid aeration of the liquid compounds, and the optimal combination of stirring and feeding.

For low-feed rates, there is a more uniform image showing that the process of crystallization occurred without any localised issues. With higher rate of injection, the USCT device showed the localised changes in TOF images, which could lead to localised crystallization. This demonstrated the application of a proposed tomographic device for quality assurance in batch crystallization process. The process of dynamic information could be extracted both from measured USCT data and images providing key insight on process efficiency and process safety.

This study presented a feasibility investigation of ultrasound tomography’s functionality in batch crystallisers. Results are promising for the on-line monitoring and the characterisation of the forming of the suspensions by sound propagation principles. Injection rate and stirring speeds were used as control parameters. The aim was to identify the capabilities of travel-time USCT in the gradually increasing suspension concentration. Results from the experiments were satisfying, showing good potential in distinguishing between phases of different concentrations of particles in suspension. Important conclusions of this study are the determination of:

- Reaction progress by the mean TOF delays values;
- Homogeneity of the medium during injection process by the reconstructions;
- Unwanted by-product formation by the reconstructions.

Even though such a device cannot measure the particle’s size directly, it seems that it could be of great aid in crystallization processes. It can be used as monitoring of homogeneity or detecting malfunctions and faults. It could work as a quality assurance figure to protect from process malfunctions that could lead to a nonuniform crystal yield. By in-line monitoring, unexpectedly higher formed suspensions can be detected and, with that, one can control the stirring and injection factors, which are significant adjustable parameters of the process.

On-going research will focus on investigating the effect of a full-waveform ultrasound tomography instrument, utilising attenuation, and back-scattering information. Moreover, higher excitation frequencies will be tested to investigate the penetration depth of the ultrasounds in the process, as it is a crucial adjustment for wave propagation and interaction with particles and slurries.

Chapter 6 Real-time inspection of reactive crystallization and mixing process

In this work, an USCT system was employed to investigate the fast-kinetic reactive crystallization process of calcium carbonate. USCT measurements and reconstruction provided key insights into the bulk particle distribution inside the stirred tank reactor and could be used to estimate the settling rate and settling time of the particles. To establish the utility of the USCT system for dynamical crystallization processes, first, the experimental imaging tasks were carried out with the stirred solid beads, as well as the feeding and stirring of the CaCO3 crystals. The feeding region, the mixing process, and the particles settling time could be detected from USCT data. Reactive crystallization experiments for CO2 capture were then conducted. Moreover, there was further potential for quantitative characterization of the suspension density in this process. USCT-based reconstructions were investigated for several experimental scenarios and operating conditions. This study demonstrates a real-time monitoring and fault detection application of USCT for reactive crystallization processes. A diverse range of experimental studies shown here demonstrate the versatility of the USCT system in process application, hoping to unlock the commercial and industrial utility of the USCT devices.

6.1. Introduction

Among several types of crystallization processes, the industrial demand for reactive crystallization (also known as precipitation) has been increasing in recent years [219]. The growth is mostly due to the energy efficiency of these processes in comparison to, for instance, cooling or evaporative crystallization. In reactive crystallization, the formation of solid particles from solution is very fast and reactions are instantaneous, which causes local variations in density and supersaturation gradient. In these processes, efficient mixing at different scales (i.e., micro-, meso-, and macro-mixing) becomes a critical factor and has a significant impact on process characteristics such as crystal size distribution and shape [209]. Coupling the fast reaction kinetics with the complex nature of the fluid flow hydrodynamics renders the monitoring and control of the unit operations challenging. The real-time characterization and control of fast kinetic crystallization systems have profound importance in ensuring end-product quality in these mixing sensitive processes. The influence of mixing speed on crystal size distribution (CSD) has been studied widely [139], [220], [208]. However, due to the abovementioned complexities, the development of functional monitoring and control schemes for these fast kinetic processes is still an ongoing research topic [221].

The reconstructed tomograms can help to identify the reaction endpoint and ensure the chemical reactions are controlled precisely. In reactor processes - particularly in crystallization - integrated tomographic visualization, data fusion, and machine learning have the potential to be utilized as a complementary method to the conventional point-based measurement techniques, aiming at fault detection, suspension density and spatial distributions characterization, and PSD indications. The USCT can be used in a contactless fashion as it was in this study, offering an advantage over other tomographic modalities such as EIT that requires direct contact with the medium. Furthermore, the sensitivity of EIT is reduced in the central area of the reactor tank, while USCT can offer a good and uniform resolution over all regions. More commercial availability of the EIT devices could be a reason for their use in various processes. This work aims to demonstrate that the USCT is a very versatile IPT tool and deserves further commercial development for deployment in real-life applications.

In the present work, an ultrasound computed tomography system was utilized to investigate the reactive crystallization process of calcium carbonate. USCT offers some major advantages over other tomographic methods, offering a low-cost alternative that could reach suitable outcomes in spatial and temporal resolution. The calcium carbonate production is integrated with a carbon capture process where CO_2 gas is absorbed into sodium hydroxide solutions. The idea presents real-world applicability for carbon dioxide utilization and valorisation to an economically attractive chemical [222]. USCT measurements and reconstruction provided insights into the bulk particle distribution inside the stirred reactor and were used to estimate the settling velocity of the particles. The study provides insights into the crystallization system and aimed to link the online tomographic measurements to fault detection and malfunction identification when out-of-specification events occur throughout the process.

It is worth noticing that the USCT technology has reached remarkable image resolution that is comparable to MRI and XCT for various medical applications, as well as geophysical applications [16], [223], [224]. The medical applications of the USCT for brain and breast imaging can be considered as static-type imaging, so a very large number of (smaller size) transducers could be used. The same could be carried out in industrial process applications. However, the limiting factor is the dynamical nature of most of the process monitoring applications. Deployment of a very large number of sensors leads to extensive measurement time and extensive computational time.

The chapter is organised as follows. Section II presents the main functionality of the tomographic system and details its specifications. Moreover, the methods undertaken for transmitted and reflected TOF and AA picking are further characterised. Section III describes the reconstruction formulas for transmission and reflection tomography, while section IV presents the proposed algorithm for reflected TOF picking, which helps optimising the recordings. Section V presents the developed fusion method. Finally, in section VI, the experimental results are presented and evaluated, and in section VII, the conclusions and discussion occur.

6.2. **Methods**

6.2.1. Experimental setup

The USCT system in this study is based on transmission-mode USCT data. Recorded waveforms are used to reconstruct travel-time delays and acoustic attenuation (AA) profiles using the time-of-flight (TOF) of the first arrival pulse and its amplitude, respectively. Figure 6.1 depicts the tomographic setup focused on a tank reactor. The tomographic setup consists of the sensor’s ring array, the electronic hardware/controller, and the host computer, which is responsible for the tomographic software and displaying the results. The reactor tank is made of acrylic material and is equipped with a feeding pump and a stirrer. The sensor's array is defined by 16 piezoelectric transducers. They work as both transmitter and receiver, mounted at the outer boundary of the tank, using an ultrasonic glue. The instrument can provide TOF and amplitude data as it filters the full-waveform signal and shares the data with the host computer. For this pre-processing step, the electronic hardware is responsible as the filtering occurs in analogue form. Therefore, the system's temporal resolution is optimized, as a significant amount of data are cut off before the data transfer stage. The tomographic instrument measures the time needed for a wave to overcome the medium but also the energy that is being lost by absorption or back-scattering.

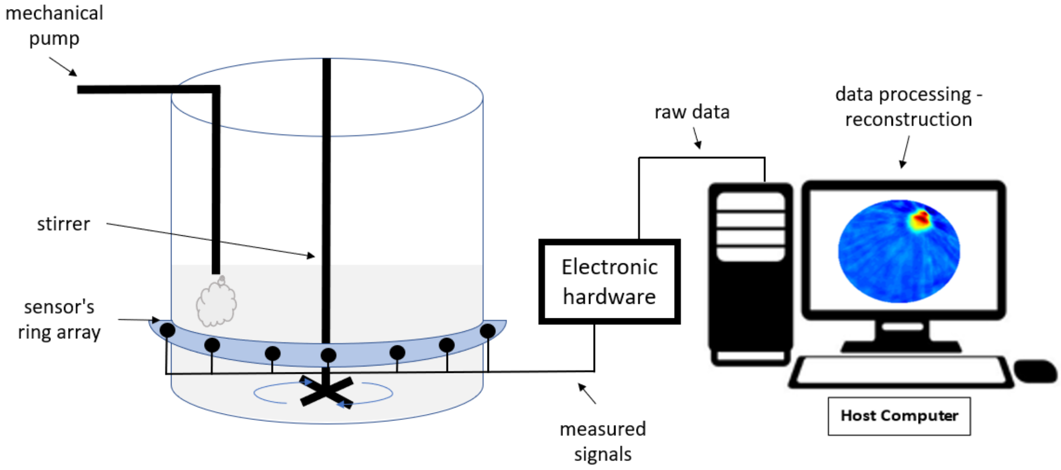

Figure 6.1 A tank reactor with the integrated USCT system.

Table 6.1 UT system's settings.

Parameter	Value
Transducers' frequency	400 kHz
Number of pulses	6
Supply voltage	+72/−72 V
Pull to the ground after extortion	ENABLE
GAIN first stage	45.2 dB
GAIN the second stage	1 v/v
Analog filter	Band-pass, fc=350 kHz (center freq.), fb=200kHz (bandwidth)
Parameter filtering	HI
Number of channels	32
Functionality mode	Transmission
Comparator threshold	5.11%

UST3.0 with 400 kHz operation was used in this work, as described in section 3.2.2. The system was used in transmission mode, providing the approximated TOF/ AA data. The USCT hardware system consists of a circular ring of 16 transducers, an electronic hardware setup for emitting and recording TOF and AA data of the first arrival pulse, and computer software for analysis and reconstructions. Each recording comprises 256 measurements, accounting for 16 recordings for every one of the 16 emissions that take place. The system provides 4 frames of computed TOF/AA values each second. The USCT system's design features are presented in Table 6.1. Figure 6.2 shows the full waveform signal used for the selection of TOF and AA values. A minimum threshold of 10% was used to cut down the minor pulses caused by back-scattering or equipment-related noise. The threshold's level is presented in Figure 6.2 by the black horizontal line. The TOF value is determined by the projection of the first signal's point after the threshold to the x-axis (time step axis), shown by the red point in the corresponding graph. The biggest y-value (the y-axis is a measurement value that represents the amplitude of the receiving wave) within a 20% signal's window in the transmitted pulse "region" indicates the recorded pulse's amplitude, depicted by the black point in the graph. A more detailed method for signal picking can be seen in [91], where the hardware is also briefly described. In both TOF and amplitude data, the "Deleting Outliers" statistical filtering method was used to handle the noise coming from multi-backscattering. An iterative implementation of the Grubbs Test, which checks one value at a time, was used to identify the outlier signals [195]. The MCUSD11A400B11RS transducer (ultrasonic sensor, frequency 400 kHz +/−16 kHz, diameter 11 mm, material made of aluminium, input voltage 300 Vp-p, directivity (−3 dB) 7° +/− 2°, operating temperature −20 °C to 80 °C. Manufacturer: MULTICOMP) was used for the sensor array.

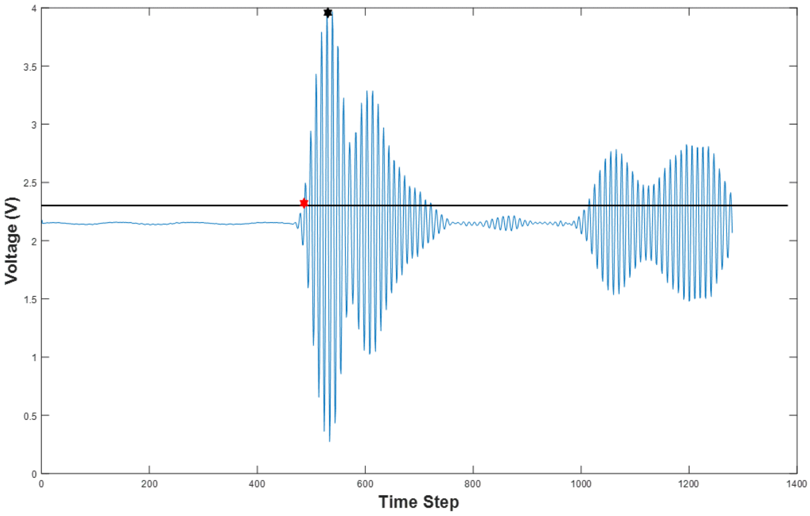

Figure 6.2 Recorded full-waveform signal from 1st transmitter-6th receiver pair.

The proposed tomographic approach uses the diffraction sensitivity matrix (section 3.4.2) which simulates the propagation of the measured energy from sensors. To generate the propagation model of the emitting energy, a computational model based on diffraction on the 1st Fresnel zone is utilized [87]. Fresnel volume or 'fat ray' tomography is an appealing compromise between the efficient ray theory tomography and the computationally intensive full waveform tomograph [172]. Furthermore, Total Variation regularization method was applied in the reconstruction, as described in section 3.4.4.2. The measurement data for diffraction tomography includes TOF data and Amplitude Attenuation (AA) data. TOF and AA measurement data were computed according to the description in section 3.3

6.2.2. $CaCO_3$ Crystallization Setup

Ultrasonic measurements have a proven efficiency in the characterization of suspension densities and slurry mixtures. Prior studies have shown the relation between phase velocity and acoustic attenuation on growing suspensions and different frequency excitations [225], [226]. These studies were based on single measurements, providing an indication of the average changes in the entire domain. The USCT method can extend these to provide local and regional information. In crystallization cases, the regions of well-dispersed crystals and regions of associated crystal networks could exist together. Moreover, accounting for the vigorous stirring process and the aeration that could be introduced to the mixture, a three-phase flow would occur by a region of dispersed gas/solid/liquid phase (liquid solution-crystalline particles-bubbles). Acoustic attenuation can be reduced further as sound propagates through the dispersed phase, due to multiple back-scattering. Regarding time-of-flight, delays are noticeable in the propagating signals over frames due to the forming dispersed phase and the low-frequency excitation of 400 kHz.

The micron-sized crystallization process of the present work is part of the carbon capture and utilization scheme where process monitoring with the USCT system is presented. Carbon dioxide is scarcely soluble in water under the standard temperature and pressure conditions. $\mathrm{CO_2}$ absorption is improved by increasing the pH of water so that the resultant chemical reaction becomes very fast at higher pH values. Sodium hydroxide–water with pH 14.10 ± 0.1 was used to prepare the reagent solution for the crystallization process. A small-scale $\mathrm{CO_2}$ bottle (purity > 99.99%) was employed to demonstrate the carbon capture process and to inject the gas into the solutions. The operation was performed by first collecting the CO2-loaded solutions, and later using them for calcium carbonate crystallization. In the process under investigation, the semi-batch feed to the stirred tank reactor contained dissociated $\mathrm{CO_{3(aq)}^{2-}}$, $\mathrm{OH_{(aq)}^{-}}$, and $\mathrm{Na_{(aq)}^{+}}$ ionic solution at a pH range of 12 ± 0.1. The governing chemical reaction is presented in eq. (6.1) where aqueous $\mathrm{CO_{3(aq)}^{2-}}$ flows through an inlet pipe (diameter: 2 mm) into the crystallizer containing a known concentration of calcium chloride ($\mathrm{CaCl_2}$, purity > 98%, Merck). A detailed description of the CO2 capture process and its integration with the calcium carbonate crystallization is given in [227].

$$\mathrm{CO_3^{2-}}_{\mathrm{(aq)}} + 2\ \mathrm{Na^+}_{\mathrm{(aq)}} + \mathrm{CaCl_2}_{\mathrm{(aq)}} \rightarrow \mathrm{CaCO_3}_{\mathrm{(s)}} \downarrow + 2\ \mathrm{NaCl}_{\mathrm{(aq)}} \qquad (6.1)$$

The feed addition rate to the receiving reactor was constant at $40\ \mathrm{mL\ min^{-1}}$ during the whole experiment. All the experimental runs were carried out at a temperature of 20 ± 2 °C. Figure 6.3 shows the schematics of the utilized crystallization reactor.

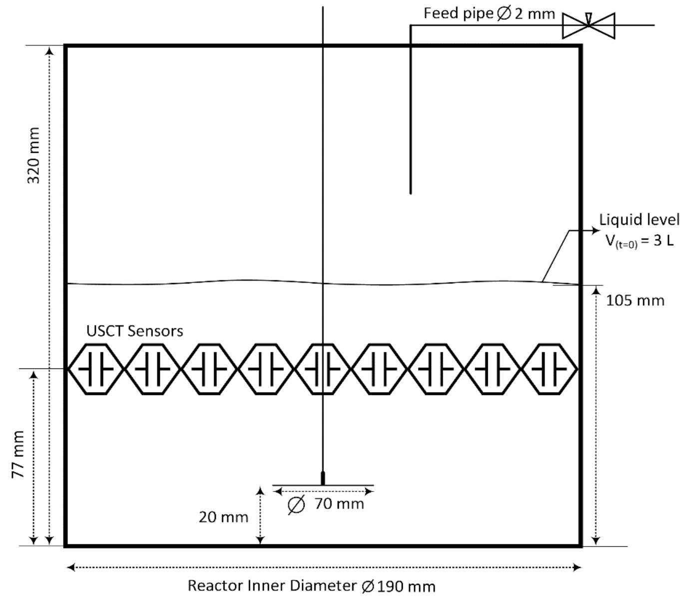

Figure 6.3. Schematics of the experimental setup. Dimensions of the plexiglass reactor and position of the USCT sensors. The initial solution volume in the tank is 3 L.

Figure 6.4 shows photographs of the entire experimental setup in which the USCT system was utilized to conduct process monitoring. The crystallization reactor was made of plexiglass with an inner diameter of 190 mm, and a plastic-made, flat-blade Rushton impeller was used for agitation.

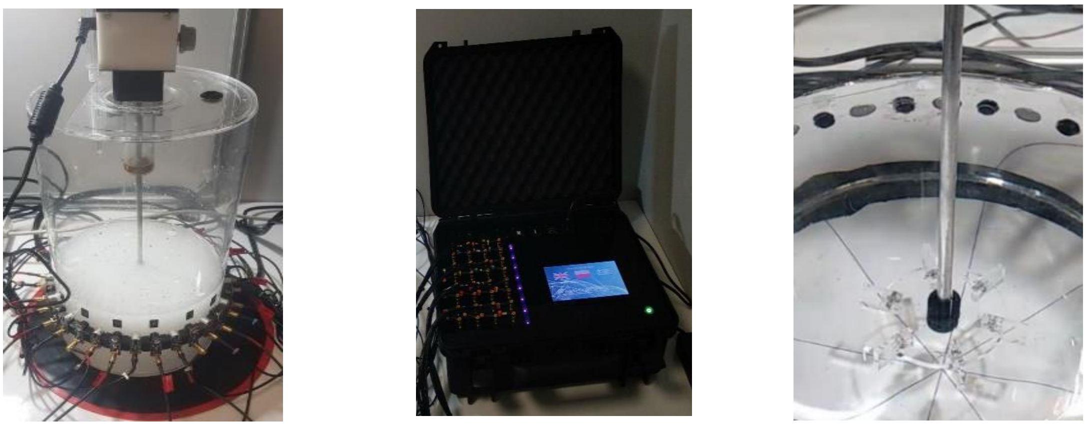

(a) **(b)** **(c)**

Figure 6.4. Ultrasound experimental setup. (a) Reactor tank, (b) measurement unit, (c) mixer.

6.3. **Results & Analysis**

Several dynamical experiments were specifically designed to evaluate the USCT response to various process events. The effects of certain operator-induced malfunctions including switching on/off the stirrer and the feed pump, particle addition, and phase changes were investigated. The section includes three main parts which present a variety of experiments. At first, section 6.3.1 presents experimental work that aims to investigate particle beads insertion in a process tank with high mixing conditions. These early cases are considered as a proof of concept on particle-fluid slurries and high-mixing. Furthermore, multiple tests with a variety of beads' concentration have been conducted and data have been acquired and analysed. Then, section 6.3.2 aim to investigate the USCT's efficiency in solid CaCO3 particles addition to the tank combining high-mixing conditions, as well. The purpose of this experiment is to investigate USCT imaging in CaCO3 particles addition over high-dynamical conditions (quantification/ settling time). At last, section 6.2.3 present two crystallization experiments using high mixing. The purpose of these experiments was to investigate USCT's functionality over the high mixing crystallization and also the USCT's response to process' malfunctions.

6.3.1. Particle beads detection

To establish the dynamical imaging based on particle concentration, circular particle beads of 4 mm in diameter were poured into the stirred tank reactor containing 3 L of water. The idea of the proposed experiment was to investigate the effects of mixing and the real-time changes in the dynamical states of the reactor by using USCT. A description of the experimental procedures is presented in Table 6.2.

Table 6.2 Particle beads detection experimental procedure

Steps	**Task**
1	*T+0 min: Reactor filled with 3 L of water*
2	*T+0 min: USCT measurements start*
3	*T+1 min: Addition of 100 g of particle beads at 1 min*
4	*T+2 min: Mixer starts at 200 RPM at 2 min*
5	*T+3 min: Stop mixer at 3 min*
6	*T+4 min: End of USCT measurements at 4 min*

Figure 6.5 shows experimental photos and tomographic reconstructions over time during the experiment with 100 g of particle beads. Figure 6.5a–c present three distinguished states of the experiments during the first 2 min: (a) the beginning, (b) the middle, and (c) the end of particle addition. The sedimentation process of solid particle beads is clear in the presented experimental photographs. The 2D reconstructions show the gradually increasing values of the injection point as the particles were poured into the tank. Acoustic field inhomogeneities were introduced both due to the existence of particles within the sensors' field-of-view (FOV) and the disturbances that occurred due to pouring. Figure 6.5d presents the reconstructed frames during the particles' pouring, showing an increasing trend of TOF delays. Figure 6.5e displays the tank's state immediately after the pouring and provides insights into the particle's settling over time, as it is described by a decreasing trend of TOF delays.

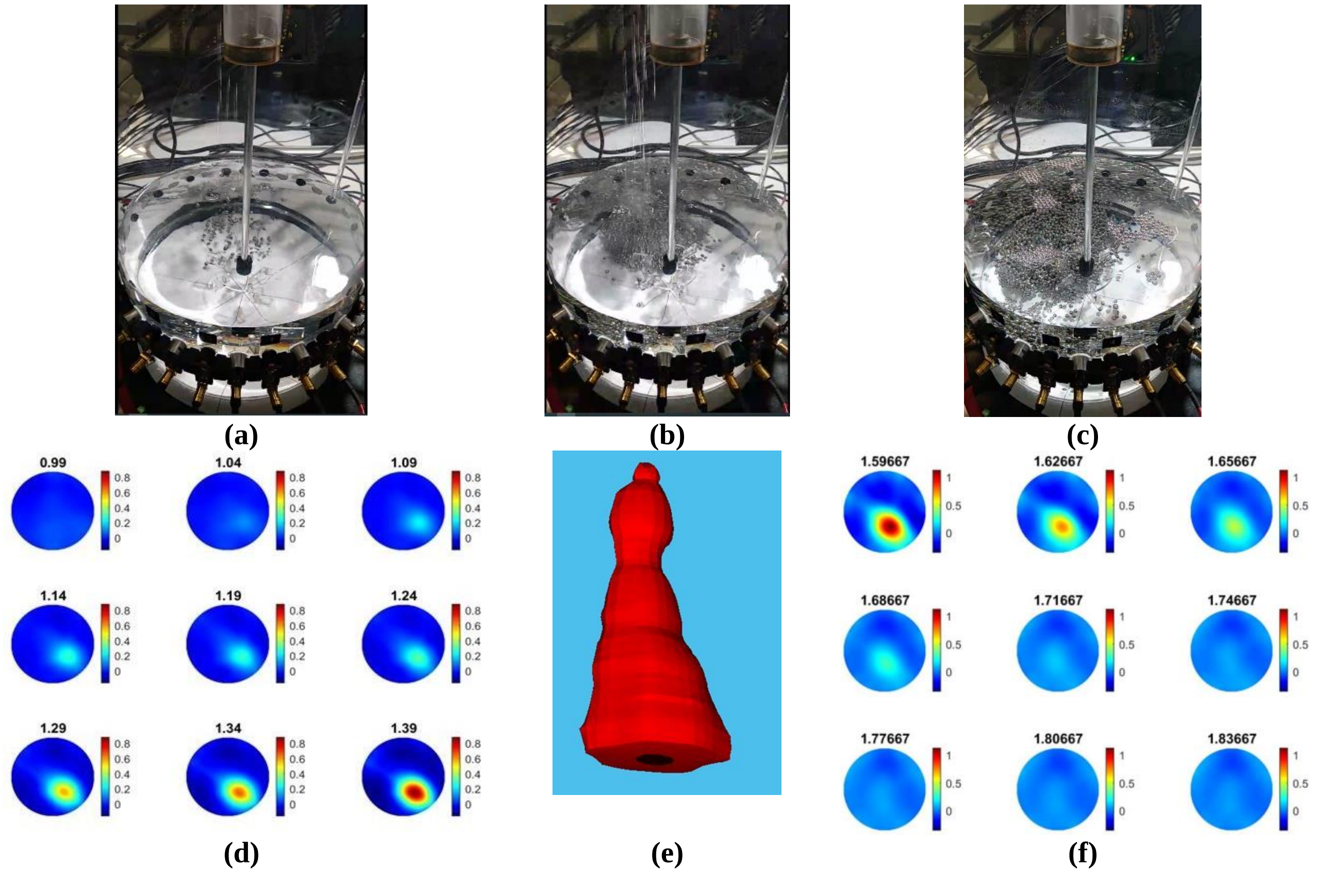

Figure 6.5. Addition of 100 g of particle beads in 3 L of water: **(a), (b), (c)** Photos from particle beads experiments demonstrating feeding and mixing (200 RPM) during the experiment. **(d)** Reconstructions between 0.99 min and 1.39 min, **(e)** Volumetric distribution of particle beads in the period of the start of feeding balls. **(f)** Reconstructions between 1.6 min and 1.84 min, balls feeding will gradually stop.

As tabulated in Table 6.2, mixing at 200 RPM was switched on at approximately T+2 min into the experiment. Due to the mixing, the whole medium turned into a dispersed liquid-solid state, as displayed by the experimental photo in Figure 6.6a. Tomographic reconstruction addresses the mixing-induced inhomogeneities by compromising the higher intensity values across the entire region-of-interest (ROI), as shown in Figure 6.6c. According to Figure 6.6b, the particles tended to assemble in the tank's central area (where the stirring took place), which is due to the central vortex formation and the centripetal force induced by the stirrer rotation. The reconstructions in Figure 6.6d were in good agreement with the experimental observations where higher inhomogeneities were formed at the central location after the start of the stirrer.

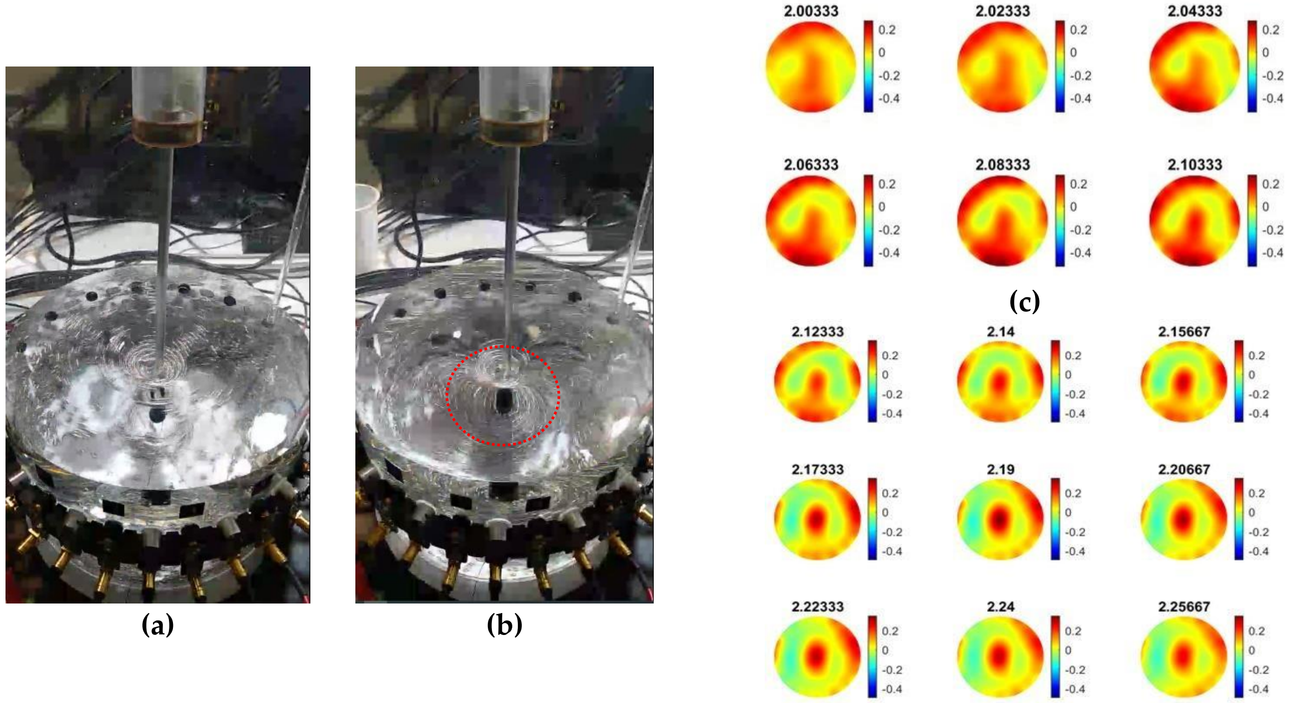

(a) **(b)** **(c)** **(d)**

Figure 6.6. (a), (b) Images from particle beads experiments demonstrating feeding and mixing (200 RPM) during the experiment. (c), (d) Images between 2:00 min and 2:56 min, showing the process of mixing. Amount of particles: 100 g, water volume: 3 L.

The exact experimental procedures as discussed above (Section 4.1) were conducted two more times, each time adding 100 g of additional particle beads to 3 L of water and recording the measurements. Figure 6.7 shows the dynamical analysis of the experiment using the mean value of the 256 measurements. All the three curves are described by a small prior bump that corresponds to the pouring and the disturbances that are caused and a latter one that corresponds to the concentration of the mixture, as it comes after the stirring starts. Comparing the three curves, quantification can be achieved with TOF imaging as the delays are related to the concentration of the two/phase mixture. For these experimental cases, AA data were analysed, offering the same responses as the TOF data.

The experiment with the plastic beads offers insights into the system's functionality in high-dynamical scenarios. First, efficiency was proven in detecting malfunction cases coming from localized higher concentrations and generated disturbances in the medium (by pouring). Then, quantification was achieved in different concentration tests. Finally, the specific flat blade turbine impeller introduced the specific pattern of gathering the plastic beads close to the stirring area (tank's centre).

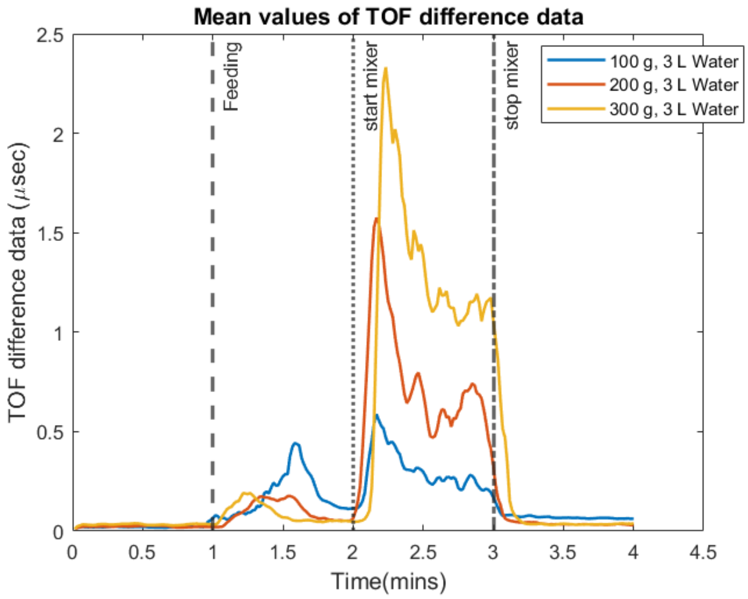

Procedures & Events
Timeline (min):

T+1: Beads addition
T+2: Mixer ON (200 RPM)

T+3: Mixer OFF
T+4: System OFF

Figure 6.7. Mean values of the time-of-flight delay for the three experiments with different bead concentrations. The volume of water inside the reactor is constant at 3 L and 3 different amounts of particles are tested each time. The peaks of the curves is ralated particle concentration.

6.3.2. *Characterizing CaCO3 solid particles distribution*

Four different concentrations of solid calcium carbonate suspensions were used to investigate the sound propagation. Samples of commercial calcite (provided by VWR, purity>99%) were added by hand from the top of the reactor containing 3 L of water. Figure 6.8a presents the experimental procedure in sequence.

Procedures & Events Timeline (min):

T+1: Mixer ON | T+4–4.5: Mixer OFF & Solid Addition | T+5: Mixer ON | T+8: Mixer OFF

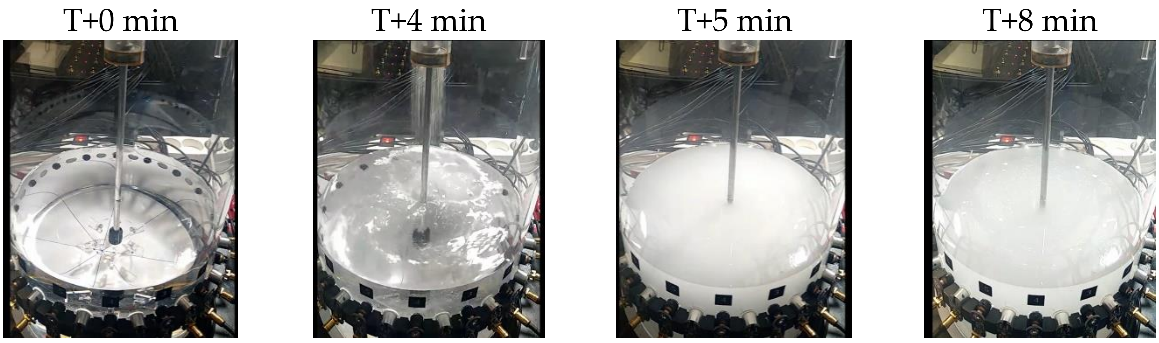

(a)

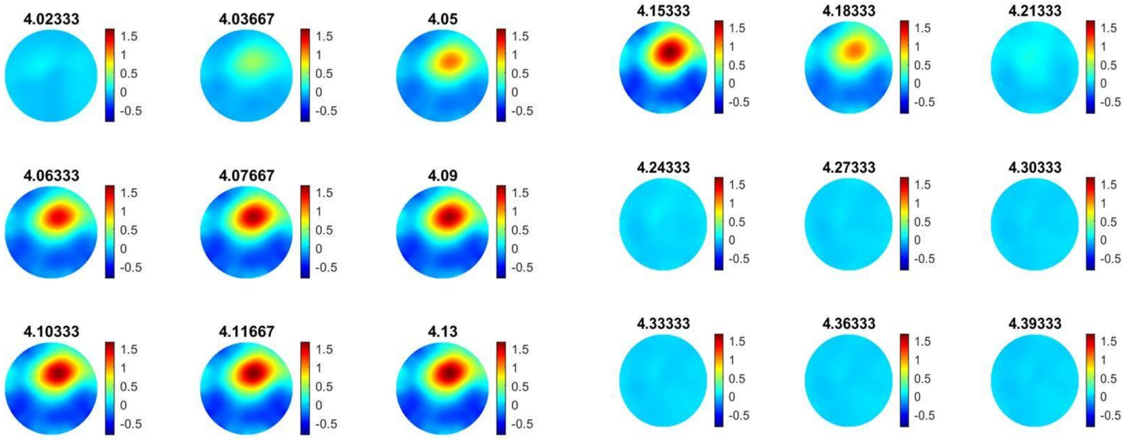

(b)

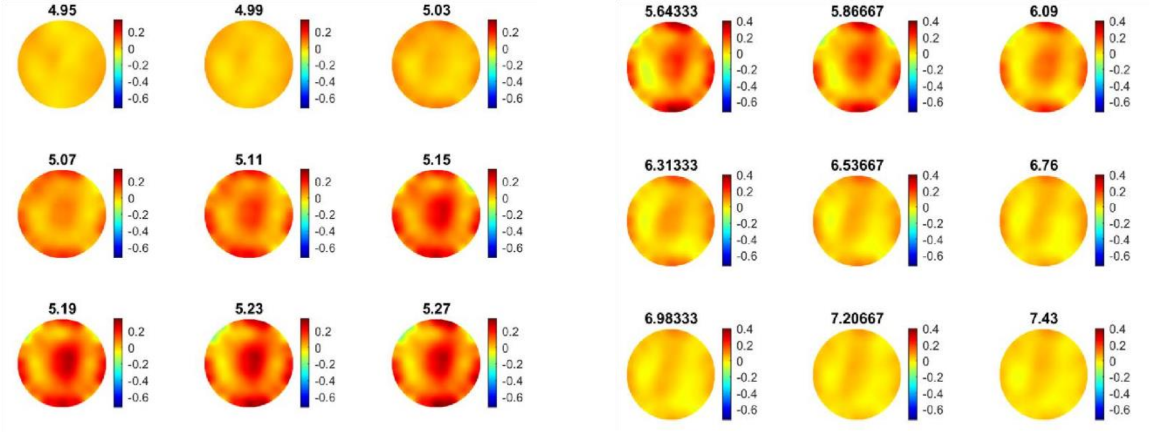

(c)

Figure 6.8. Images on shown time step images of feeding (b) Reconstruction between time 4.02 min to 4.39 min, describing feeding. (c) Reconstruction between time 4.95 min to 7.43 min during the mixing process.

Figures 6.8b,c display the reconstructions over the pouring process of the calcium carbonate particles, while Figure 6.8d shows the reconstruction over the mixing process and provides insights into the mixture’s homogeneity. The tomographic images were obtained for the concentration of 25 g L^{-1} at several key events and show the particle addition and also the effect of mixing that leads the medium to a homogeneous state.

As presented in Figure 6.9, all the conducted experiments’ mean TOF data are defined in a similar graph. In T+1 min, stirring starts in the reference medium (water) having almost zero impact on the mean TOF data.

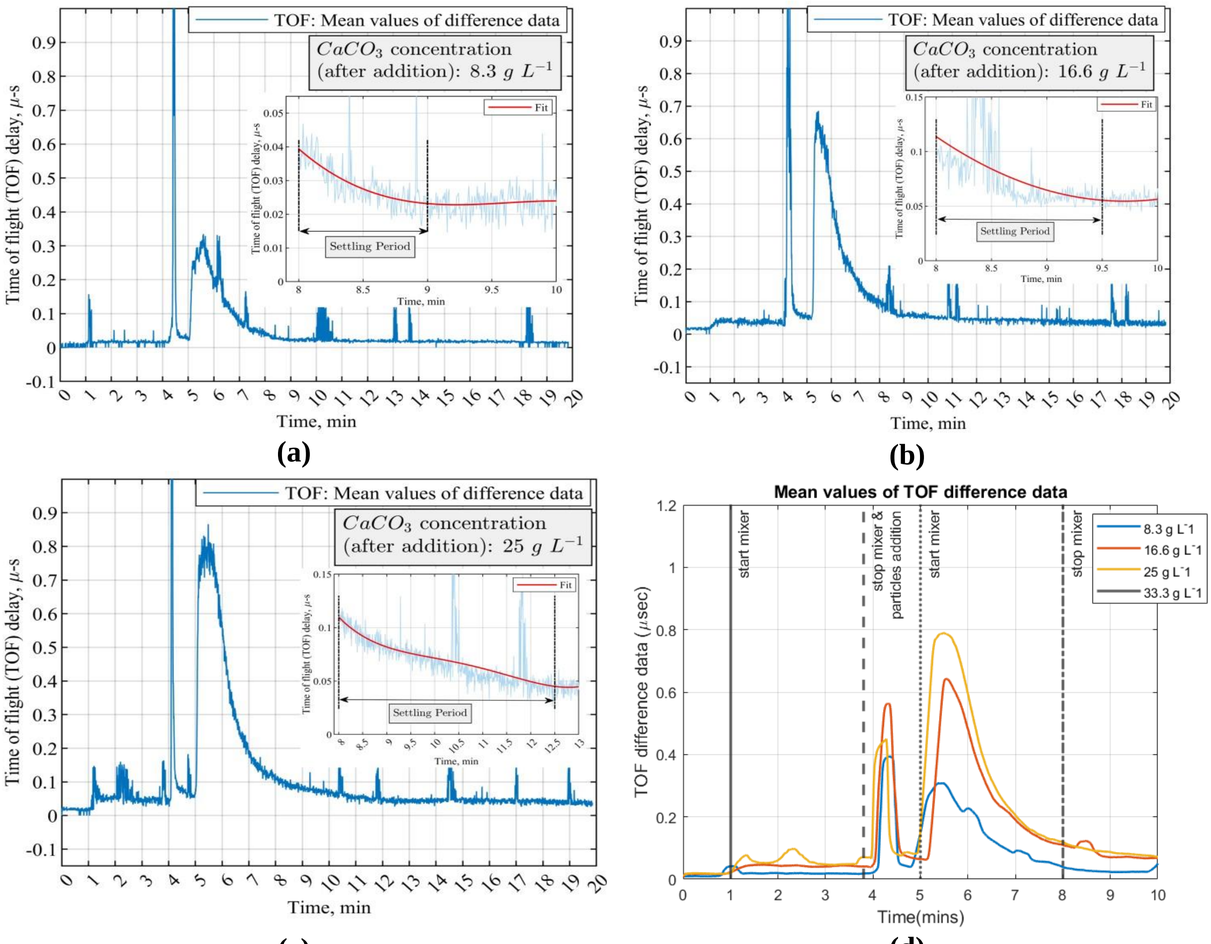

(a) (b) (c) (d)

Figure 6.9. Mean values of the time-of-flight difference data in four concentrations of CaCO3 suspensions. Experimental procedures are the same for all the concentrations. The initial volume of water is 3 L. Settling period is defined to calculate the settling velocity of particles. (a–c) Plot for 8.3 g, 16.6 g, and 25 g; (d) all the mean values from (a–c) in one plot.

The highest peak at T+4 min in the mean values graph is due to an abrupt change and disturbance in the reactor caused by the pouring of CaCO3 particles. Switching on the mixer at T+5 min distributes the micron-sized particles in the suspension and causes a rapid increase in the TOF. The increase in the TOF delays agrees with the concentration increase. The TOF has a descending trend after reaching the maximum peak (ca. from T+5.5 min afterward), which characterizes a relatively homogenous medium that facilitates sound propagation, concluding in the sound speed propagation decrease at higher concentrations of solid calcium carbonate in the reactor, resulting in higher TOF delays. For the corresponding experiments, AA data were analysed, offering the same responses as the TOF data.

Quantification of particle settling time

The settling velocity of particles is a function of the free settling velocity (terminal velocity): it decreases as solid particle concentration increases in the fluid domain. The free settling velocity of particles for the Stokes' regime, V_t, is determined based on the following expression:

$$V_t = \frac{g d_p^2 (\rho_\sigma - \rho_f)}{18\mu} \tag{6.2}$$

where, ρ_f and ρ_s are fluid and solid density, respectively, d_p represents particle diameter, g is the gravitational acceleration and μ denotes the dynamic viscosity of the fluid (0.0089 Pa s for water). The value of free settling velocity is strongly dependent on higher volumetric concentrations of solids (ϕ); when a cloud of solid particles is settling in a quiescent liquid, additional interactions and hindering effects (i.e., increased drag caused by the proximity of particles) influence its settling velocity. A typical semiempirical approach known as Richardson-Zaki is based on the power-law function of volume fraction,

$$V_{HS} = V_t (1 - \varphi)^n \tag{6.3}$$

where V_{HS} denotes the hindered settling velocity, and n is the function of particle Reynolds number and dilution degree of the suspension: n = 6.5 for $Re_p < 0.2$.

In the present work, the settling period was approximated based on the ultrasound tomographic measurements of the most diluted suspension (i.e., $8.3\ \mathrm{g\,L^{-1}}\ \mathrm{CaCO_3}$ concentration). The settling period is defined as the time interval for a cloud of solid particles to reach from the suspension surface to the plane of the sensors after the mixer is switched off—the distance from the suspension surface to the plane of the sensor is ca. 33 mm. A plateau in the measured mean value of the sound speed is obtained after the stirrer is switched off, as shown in Figure 6.9. The initial point of the plateau in the measurement is attributed to the time that solid particles are passing the plane of sensors.

As calculated based on eq. (6.2) and (6.3) for the abovementioned particle size, the average settling period is approximately 1 min for the solid volumetric concentration of 0.31% (8.3 $\mathrm{g\,L^{-1}}$). The calculated value of 1 min is in good agreement with the estimated settling period from the USCT measurement (Figure 6.9a). However, in denser particle suspensions, the estimated settling periods based on USCT are higher up to 5 min for the case of 33.3 $\mathrm{g\,L^{-1}}$ solids ($\varphi = 1.22\,\%$). According to eq. (6.3), the particle hindered settling velocity does not explain the estimated settling times by the USCT. Apparently, the denser suspensions of size-distributed particles tend to discharge from the measurement zone (plane of sensors). Moreover, considering that the tank is without any baffles, the fluid motion continues in the tangential direction after stopping the mixer. The effects of particle motion, travel path of particles, and settling times can be further investigated by Computational Fluid Dynamics (CFD) simulations and the Lagrangian particle tracking method alongside the USCT experiments.

6.3.3. Reactive crystallization monitoring

Ultrasound-based tomographic measurement was used to detect localized crystalline suspensions and monitor the reactive crystallization of the calcium carbonate process according to the chemical reaction in eq. (6.1). In all the cases, the initial concentration of calcium chloride was $1.6\ \mathrm{g\,L^{-1}}$. The operating parameters of the experiments are listed in Table 6.3. The entire experimental procedure was repeated two times to ensure the repeatability of the measurements.

Table 6.3 Main operating parameters for the CaCO3 crystallization experiments.

Parameter	Unit	Value
$CaCl_2$ concentrations	$g\ L^{-1}$	0, 1.6
NaOH concentration at the feed	$mol\ L^{-1}$	12.1 ± 0.1
$CO_{3(aq)}^{2-}$ concentration at the feed	$mol\ L^{-1}$	0.15 ± 0.5
Feed addition rate	$mL\ min^{-1}$	40
Impeller diameter	m	0.07
Stirring rate	rpm	100
Impeller tip speed	$m\ s^{-1}$	0.37

Two instances of the mean value of sound speed are presented in Figure 6.10. Due to the fast kinetic nature of the particulate system, the nucleation phenomena are instantaneous, which results in the formation of micron-sized particles. The mean value of sound speed obtained from averaging the ultrasound signals is not sensitive enough to react significantly to the onset of inherently stochastic nucleation, which begins at approximately T+5 min into the process. The formation of amorphous calcium carbonate (ACC) after initiating the feed solution could be an alternative cause of the measurement delay.

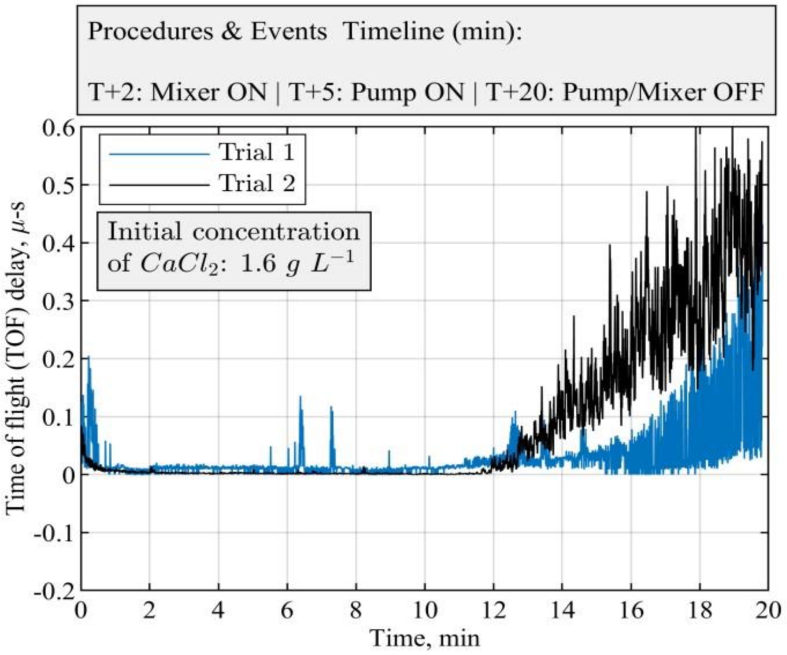

Figure 6.10. USCT measurement of the reactive crystallization process: mixing speed of 100 RPM and feed addition rate of 40 ml min−1. Mean value of sound speed measured for two identical crystallization experiments.

The formed ACC in the precipitation system will dissolve first and, then, transform within minutes to produce crystalline forms of vaterite and calcite, depending on the pH of the solution and the mixing conditions [228].

Nucleation determines the main properties of the crystal population, including the crystal polymorph, the number of crystals, and their size distribution. In the current precipitation system, there is a possibility for the following succession of mechanisms to occur [229], [230]: (i) the formation and growth of ACC; (ii) the simultaneous creation of ACC surface complexation sites from which calcite starts to precipitate; (iii) the calcite growth from ACC; (iv) the creation of further calcite surface complexation sites and competitive precipitation of calcite. Hence, the observed delay between the times of 5 and 10 min in the USCT measurement could be attributed to the nature of the precipitation system. More investigations can be conducted to improve the overall operational performance of the measurement and the chemical process.

Furthermore, ultrasound tomographic reconstructions provide deeper insight into the precipitation process of calcium carbonate. Data of Trial 1, in Figure 6.11, were used to reconstruct the tomographic images, which shows the feeding points and the phase change throughout the process. The injection point is encircled by the black circle in the first reconstructed frame presented.

As demonstrated in the experiments with particle beads (Section 4.1), USCT measurement proved to be effective in recognizing and characterizing the bulk particle distribution in the reactor. Figure 6.12 shows the final stages of the calcium carbonate crystallization (based on Table 6.3), where the concentration of the suspension increases, and the particles are primarily accumulated in the central vortex region where a three-phase composition is formed regarding liquid solution, solid particles, and bubbles.

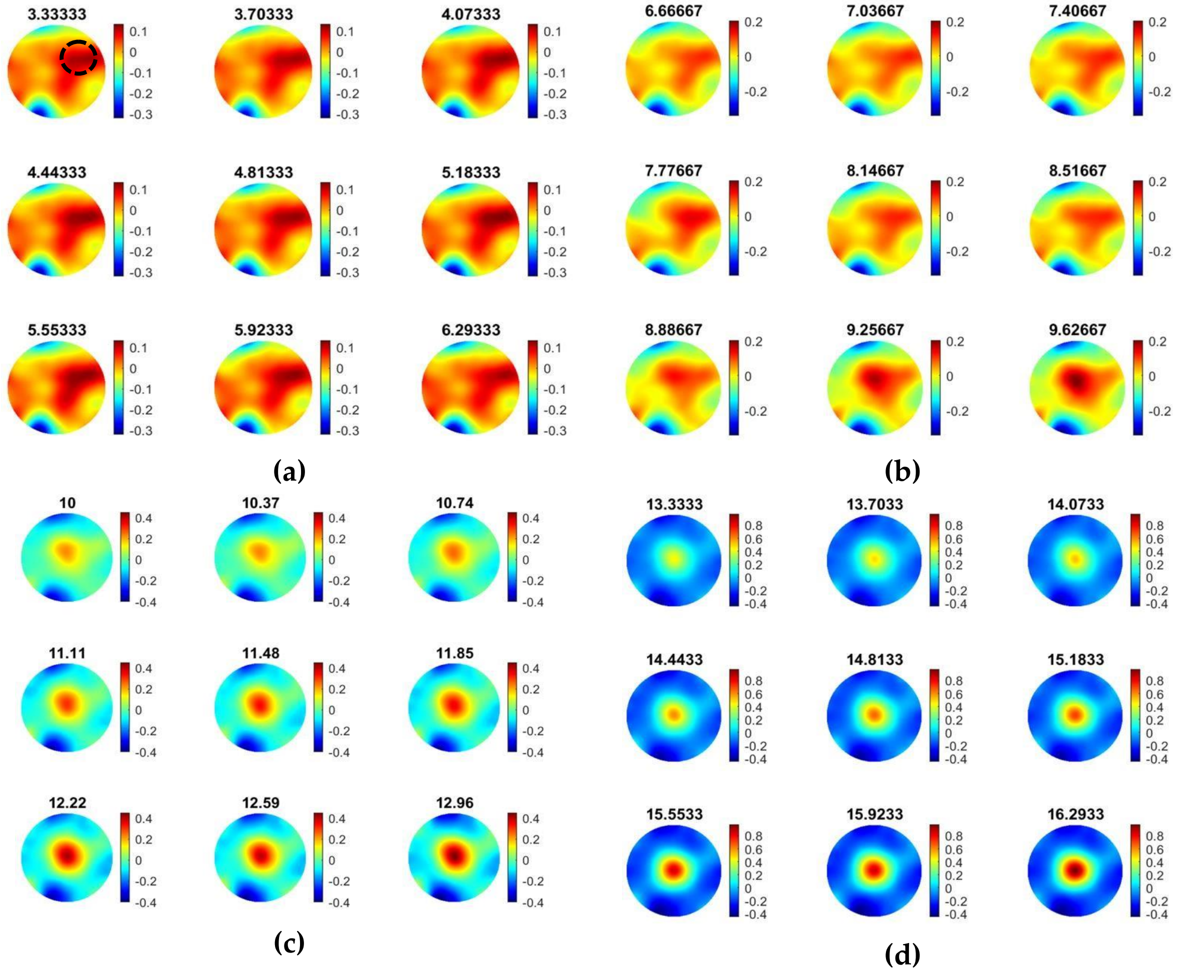

Figure 6.11. Ultrasound reconstructions during the calcium carbonate crystallization process (Trial 1 in Fig. 8). Mixing speed of 100 RPM and feed addition rate of 40 $mL\ min^{-1}$. Parts (a) and (b) show the feeding points and (c) and (d) are representing the crystal formation. (a) USCT reconstruction during experiments; from T+ (b) USCT reconstruction during experiments: (a) from T + 3.3 min to T + 6.29 min, (b) from T + 6.6 min to T + 9.6 min, (c) from T + 10 min to T + 12.9 min., (d) from T + 13.3 min to T + 16.29 min.

In reactive crystallization, the time-of-flight USCT provides useful information on feeding points and the later stage of the material phase change and crystal growth. Referring to the mean value plot of TOF data in Figure 6.10, it is less clear to see the start and stop of the mixer and the start and stop of the pump. This may lead to some limitations for the TOF data to be used in malfunction identification (e.g., failure of the pump or mixer) and the process control implementation. In [91], we developed a full waveform USCT algorithm taking into account the acoustic attenuation, as well as the TOF data. Indeed, for the amplitude attenuation, the image reconstruction process follows a similar procedure as the transmission time-of-flight-mode USCT.

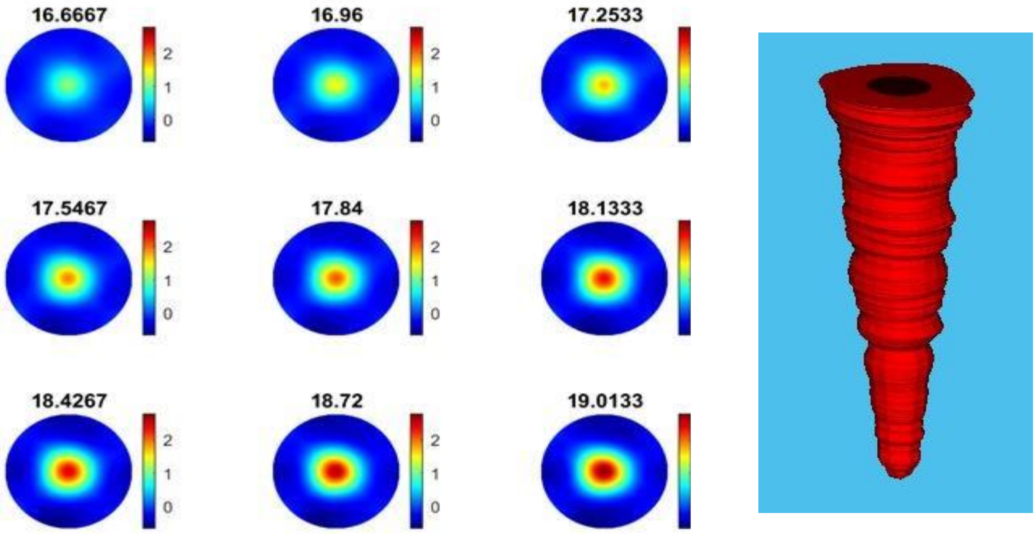

(a) **(b)**

Figure 6.12. Calcium carbonate crystallization monitoring: evolution of the particle concentration and formation of a central vortex toward the end of the process (time: 16.6 min to 19 min). Experiments are related to trial 1 in Figure 10; operating parameters are listed in Table 3. (a) The TOF images frames, (b) growth of dispersed phase.

Figure 6.13 presents AA reconstructions for the same period as Figure 6.12. Comparing the two figures, one can conclude that time-of-flight and acoustic attenuation provide similar results, as even the trend of increase is similar. Hence, amplitude attenuation imaging has not been presented in this work.

Figure 6.12b shows the mean value of acoustic attenuation for a central excitation frequency of fc = 400 kHz. However, as one can see from Figure 6.14b below, the mean value plot for amplitude attenuation shows several clearer points of interest, such as the points where the mixer is switched on (2 min) and the pump is switched on (5 min), the stop of the stirrer (7.5 min), and the start of the stirrer (8 min). This suggests that the amplitude attenuation may provide complementary information for future control and malfunction analysis in crystallization processes. Figure 6.14 shows the mean of time-of-flight and amplitude attenuation data for similar time steps as Figure 6.10. However, plots in Figure 6.14 generated by smoothing the original data with a step of 10 frames. Similar imaging results can be seen between the TOF images and the AA images.

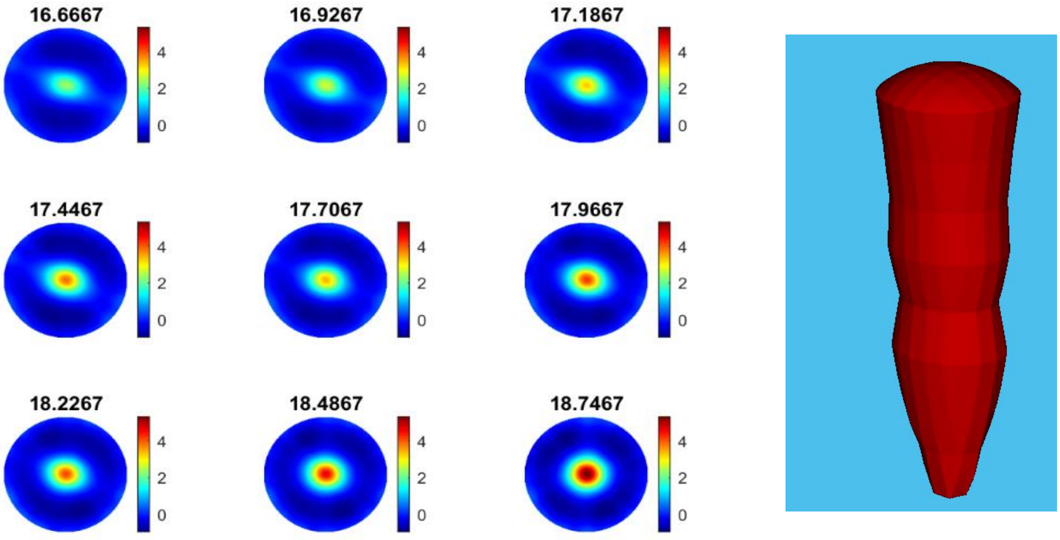

(**a**) (**b**)

Figure 6.13. (a) Image reconstruction for amplitude attenuation for the same time windows as Figure 6.12. (b) Reconstructed volume depicting the growth of dispersed phase.

Regarding TOF data, only the positive TOF delays were considered for this study as diffraction of the ultrasound is expected from the dispersed phase, especially at the low excitation frequency of 400 kHz. A multi-modality USCT, as developed in [91], and further information fusion from TOF and AA could be investigated in future studies.

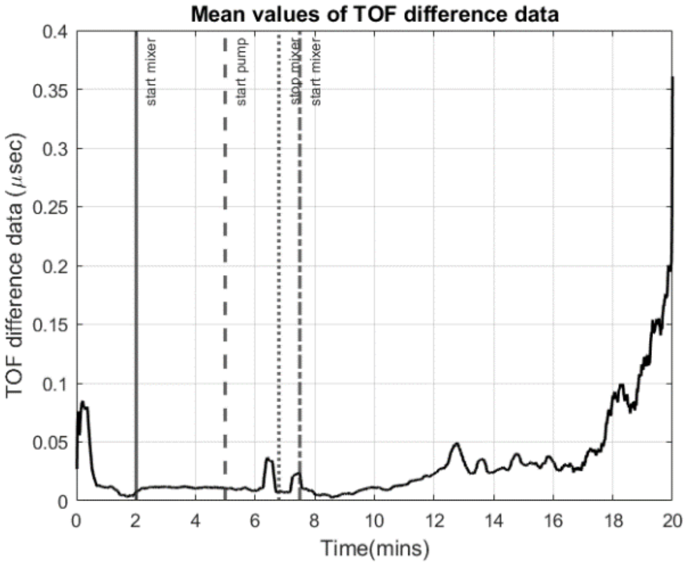

(a)

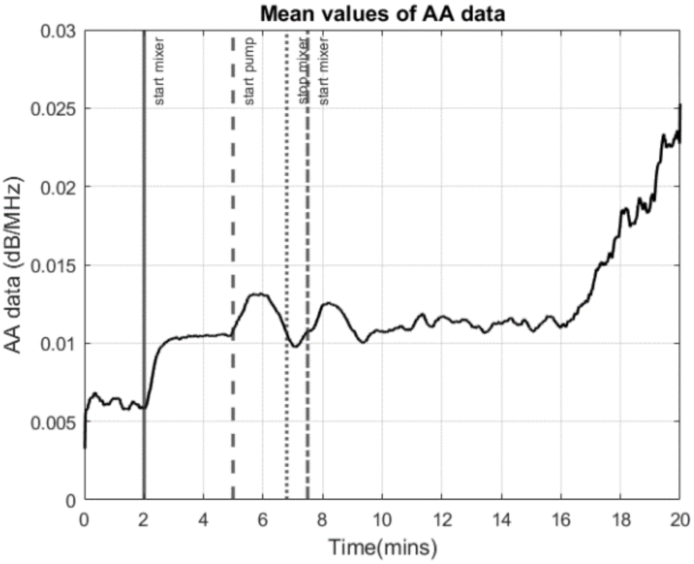

(b)

Figure 6.14. (a) Mean value of TOF data. (b) Mean value of acoustic attenuation data (in dB/MHz). In both cases: mixer on at 2 min and pump on at 5 min, stop of stirrer at 7.5 min, and stirrer starts again at 8 min.

6.4. **Conclusion**

6.4.1. Discussions

The presented work displays the potential applications of the USCT in chemical reactor processes and especially in batch crystallization. First the experimental tests focussed on particles' concentration and dynamical status characterization in mixing scenarios. As mixing highly affects the dynamical state of the tanks, it introduces noise to the system which disturbs the ultrasonic measurements. Noise always is apparent in the measurements when the dynamics of the tank abruptly change. The main challenge, regarding ultrasonic online measurements in mixing environments is the elimination of the "stirring noise" and the use of the quantitative information, without the measured data being seriously distorted.

Experiment with the plastic beads offers insights into the system's functionality in high-dynamical scenarios. First proved efficiency in detecting malfunction cases coming from localised higher concentrations and generated disturbances in the medium (by pouring). Then quantification was achieved in different concentration tests. Finally, the flat blade turbine impeller introduced the specific pattern of gathering the plastic beads close to the stirring area (tank's centre). The experiment with the CaCO3 particles proved a good quantification response to the particles’ concentration in a higher depth of resolution proving a good potential for crystallization and precipitation processes. Moreover, conclusions have been drawn regarding the particles’ settling time. Finally, the reactive crystallization experiment was a full-scale test on live-process challenges. In the specific process, the system showed capability in detecting the injection point, as a prior localised suspension in the form of ACC. Moreover, providing real-time measurements of travel-time delays’ mean values aims at the inhomogeneities’ characterisation over time and subsequently dispersion state of the mixture. Finally acoustic attenuation data proved to be more sensitive comparing to the time-of-flight responses, as their response was significantly better in the malfunction analysis.

Concluding, the mean value data for each experiment of USCT were plotted to show a global picture of the process’ progress and dynamics in all cases. Distributed sensing measurement systems such as process tomography provide the capability to measure spatiotemporal field information from within the process. Therefore, the reconstructed images aided in the injection point and in the mixture’s homogeneity characterization. The USCT images showed the feeding process, the mixing process, and material phase changes during the crystallization process. Moreover, USCT data were further analysed to estimate the settling velocity and settling time of particles in the suspension.

6.4.2. Conclusions

Transmission-mode USCT was examined for industrial process monitoring. The experiments were designed in such a way that enables critical evaluation of the USCT and its usability for process monitoring and potentially for process control. For transmission USCT, we implemented both time-of-flight, allowing speed-of-sound imaging, and amplitude attenuation imaging. Although we mostly showed the time-of-flight data, the amplitude attenuation was also examined and provided similar or, in some cases, complementary information on the state of the process. The major events on the process, such as feeding, and switching on and off the pumps and the stirrer, could be seen in the data. These indicators could be integrated into the process and be used for process malfunction. CO2 capturing via reactive crystallization is becoming a new tool to reduce the negative environmental impact of CO2, helping in net-zero targets. There is clear indication that the USCT tool can be used to monitor such a process noninvasively and could then become a practical tool to process design that can maximize the overall process yield contributing to affordable carbon capture and carbon reduction. To develop a complete understanding of a complex industrial process, such as carbon capture experiments, it is likely that a multi-modality sensing and imaging approach will be required. In such a multimodality imaging setup, the data-rich USCT is likely to play a vital role. The work of this paper demonstrates that USCT is a very attractive and proven tool to many industrial applications. Hopefully, this work will stimulate further commercial exploitation of the USCT technology.

Chapter 7 3D & 4D transmission imaging

A volumetric USCT method is established for industrial process applications. A two-plane array USCT system is developed for 3D imaging of the process under test. Such a 3D system allows capturing axial variations, which is not possible in 2D or 2.5D imaging. For the specific purpose of in-line chemical reactors monitoring, a transmission method was applied which provided high temporal resolution. A sensitivity matrix base on cone-beam excitation was built. Dynamical volumetric image is then generated using a time correlative total variation (TV) algorithm leading to a 4D process monitoring. An efficient 3D sensitivity matrix computation based on an optimised ray-voxel intersection method is presented. In combination with the advanced 4D TV algorithm, high-quality information is gained from time and space. At first, the 3D imaging methodology was tested and verified using static objects. Secondly, 4D imaging was investigated by using a moving rod in an experimental tank. The system was then implanted to carry out a dynamical process monitoring imaging 4D crystallization process. Finally, the results are evaluated using quantitative image evaluation in 3D mode and process dynamics in 4D imaging mode.

7.1. Introduction

USCT has been studied and developed in 2D and 3D setups for various medical and industrial process imaging applications. Volumetric (3D) industrial tomography is more informative than the 2D setups, as it provides full information from the three-dimensional region-of-interest (ROI) using modalities such as EIT, ECT, XCT and others [143], [186], [231]–[233]. Volumetric imaging in all the above modalities provides a more detailed understanding of the industrial process under investigation. Considering full geometrical conditions allows producing high-quality images with more information. The benefits of 3D imaging were displayed on industrial process tomography against traditional 2D and 2.5D imaging in [145]. The 2.5D imaging is a prior to 3D technique and is conducted by interpolating independent 2D images into a 3D volume, being considered as an approximation method.

USCT has been studied in 3D fashion in transmission and multi-modality techniques, mainly for medical applications [234]–[237]. Medical applications of the USCT [238]–[240] have been very promising in breast cancer imaging, where the advanced 3D full-waveform inversion (FWI) or other computationally complex algorithms [169], [241], [242] can provide images reaching the quality standards of XCT or to Magnetic Resonance Imaging (MRI). Aiming at high spatial resolution, medical systems require not only heavy computational reconstruction algorithms but also many sensors (for example, 1000 transducers). This leads to time-consuming data collection and eventually, imaging is too slow and not suitable for agile industrial applications. On the other hand, almost all newly developed USCT systems for industrial applications are based on 2D imaging [187], [243]–[245]. However, the significant need for volumetric monitoring in industrial process imaging leads to new incorporated 3D developments. Regarding the high temporal changes of the live industrial processes, developing a fast-imaging system is crucial. Therefore, the number of sensors and the form of the acquired data are designed optimally for high temporal imaging, satisfying the spatial resolution requirements.

Early tomographic developments have been focused on enhancing the spatial resolution of single-frame data. Conventional single-step reconstruction algorithms are based on single frame data. However, in a real-time environment, multiple data-frames needs to be processed. In that case, dynamic regularization algorithms, accounting for temporal resolution, needs to be addressed. First attempts of such algorithms were made in 2D tomographic problems [246], [247]. Nevertheless, the need for established 3D systems drove to the development of temporal 4D regularization algorithms [186], [248]–[251].

This work provides a method for USCT 3D and 4D imaging that fulfils the needs of industrial process tomography. A 3D transmission USCT was developed, using the first-arrival pulse's time-of-flight and incorporating multiple ring arrays. USCT in transmission mode can be considered as a hard-field tomography, thereafter an improved ray-voxel intersection adjustment is proposed similar to those implemented in XCT. Ultrasound transmission tomography involves some ill-condition inverse problem, requiring a regularization-based image reconstruction method. The work contributes to the field of USCT as it is the first deployment of a 3D USCT system for process reactors monitoring. Moreover, this work's additional contribution is the application of the 4D regularization algorithm in 3D USCT system, as it offers temporally correlated dynamical imaging. 4D imaging is accomplished via a 4D Total variation algorithm in a 3D USCT system.

The chapter is organised as follows: Section 7.2 describes the volumetric USCT system and 4D regularization algorithm. Section 7.3 is dedicated to several static and dynamical experiments, including the crystallisation process. Finally, the conclusions are drawn in section 7.4.

7.2. **Methods**

7.2.1. Tomographic system & Measurements Acquisition

The tomograph is preferably set to transmission mode, which provides a signal acquisition temporal frequency of 4 fps. The tomograph in transmission mode measures signal' travel-time and signal amplitude. The device automatically finds the minimum and maximum values of the signal, based on which it converts the percentage value to the numerical value of the ADC converter. Parameters of the system can be found in Table 6.1. Figure 7.1a shows the ultrasonic tomograph with 32 channels where the travel time data can be collected between two rings of 16 sensors each. Sensors can be used as a transmitters or receivers.

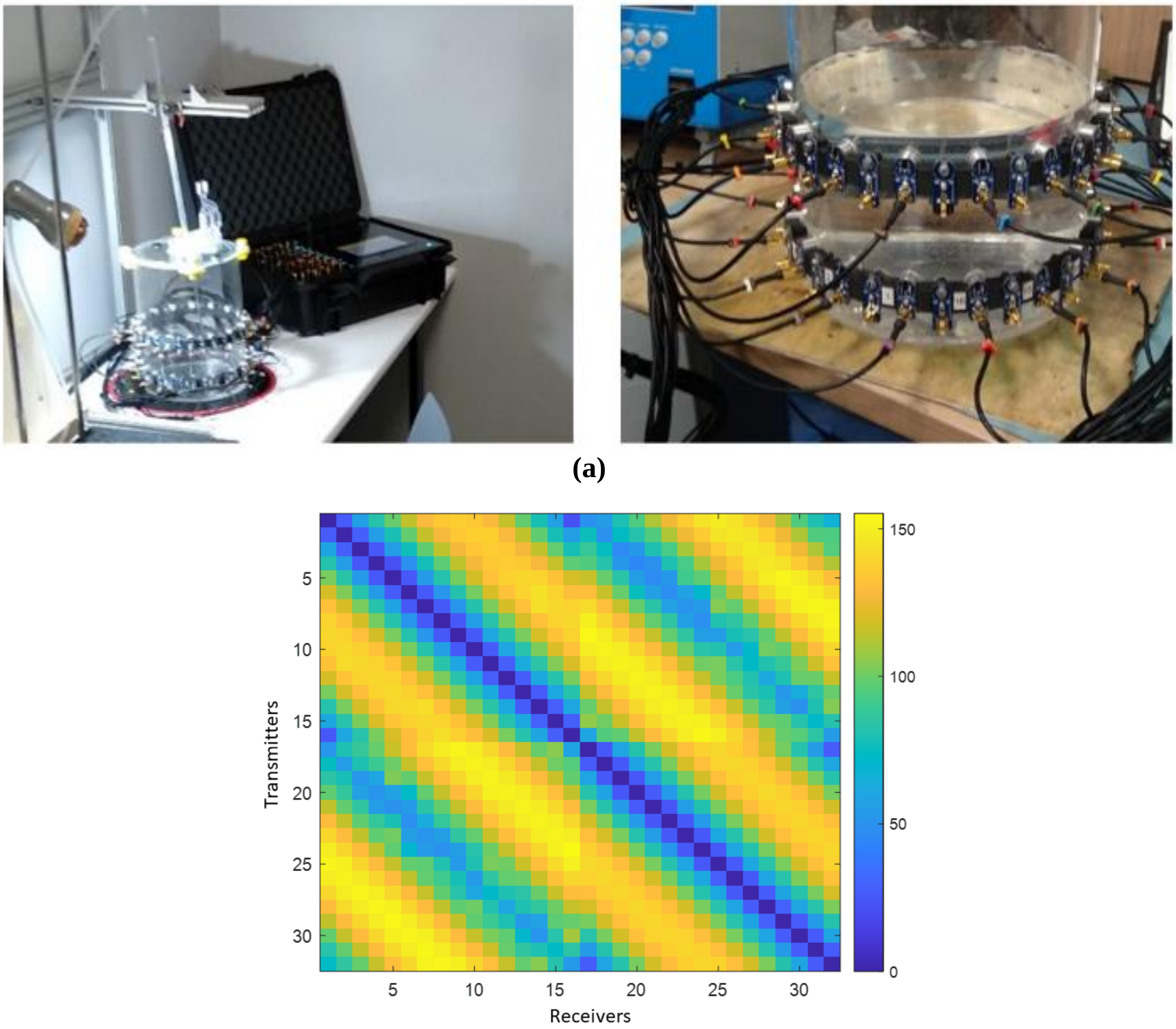

(a)

(b)

Figure 7.1. (a) USCT system and sensors attached in the 20cm tank and a zoomed view of the two layers of the 16 sensors each. (b) TOF measurements resulting from a test of a tank filled with water.

In total 1024 measurements are possible, with the received signal on the exciting sensor to be considered as null (self-measurements). Figure 7.1b shows the TOF data for a homogeneous liquid background, a 1024 TOF data values coming from 32 excitations, with 32 recordings per excitation. The data were displayed in an image form. Every image's row account for a different excitation, while every column for another recording. The zero diagonal line indicates the zero values of the self-measurements, namely, the measurements coming from the same sensor as the excitation sensor. Furthermore, with a closer look at the first 32 recordings which account for the first excitation (first row), it can be noticed that the first 16 values are related to the same plane excitation and the rest 16 to the inter-plane excitation, as the later 16 TOF values seem to be higher. Thus, there is a noticeable pattern on this image that can distinguish between quadrants. This TOF data's pattern exist due to the topology of sensors and the sequence of excitation and can describe the tomographic set-up. The inter-plane data plays an important role in volumetric image reconstruction providing an axial resolution that may not be possible in 2D or 2.5D imaging.

The measurement system presented in this chapter uses MCUSD11A400B11RS ultrasonic sensors with frequency 400kHz +/- 16kHz, diameter 11mm, a material made of aluminium, input voltage 300Vp-p, directivity (-3dB) 7 ° +/- 2 °, operating temperature -20 ° C to 80 ° C. For each transmitter, an excitation of 5 cycles (tone burst) pulse takes place. These sensors are suitable for transmission testing. However, they have a smaller angle of beam compared to 40kHz sensors. The wave period is much smaller, so that the TOF measurement error is almost 10 times smaller. Therefore, 400kHz transmitters are the most accurate and are suitable for transmission measurements. In addition, reference measurements of a single excitation were carried out to measure the width of wave propagation for a 400kHz transducer. For this purpose, 32 measuring points were placed at appropriate intervals around the circumference of the tank (NETRIX S.A.). The acquired measurements are presented in Figure 7.2. A high keying voltage is required to achieve good quality measurements. The amplitude measurements address that the transducer works optimally in the range of +/- 90 degrees. Above that, its signal is much weaker. The TOF data seem to be reliable and measurement errors are minimal.

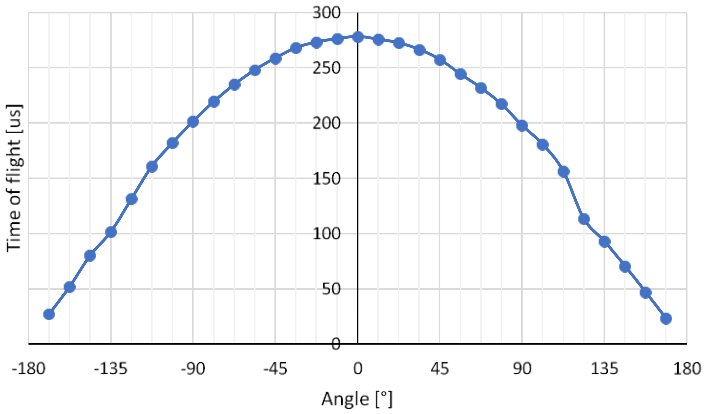

(a)

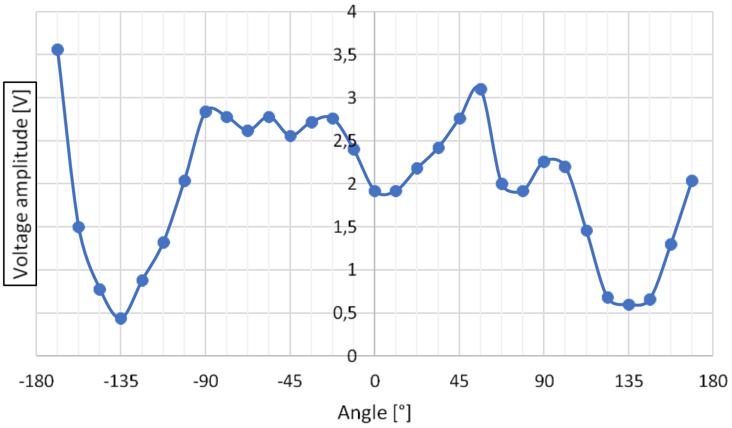

(b)

Figure 7.2. The graphs display 31 measurements from a single excitation of 400 kHz. (a) TOF measurements, (b) amplitude measurements. The analysis has been done by "NETRIX S.A.".

7.2.2. 3D Reconstruction

A 3D ultrasound transmission tomography method was developed and applied to this work, based on the time-of-flight of the first arrival pulse, whose trajectory is assumed as a straight line. The ray trajectories are calculated by solving the vector eq. (3.21) and accounting for high emission frequencies. The proposed tomographic approach uses the transmission sensitivity matrix based on ray-voxel intersection, which is described below. Furthermore, a spatio-temporal Total Variation regularization method was applied in the reconstruction, as described in section 3.4.4.3. In dynamical 3D imaging the image reconstruction process deals with many frames of data and images. Certain information in x, y, z space can be temporally regularized providing 4D imaging. We use a 4D total variation (TV) algorithm proven very successful in various other imaging modalities [186], [250], [252].

Optimised discretization

For solving the 3D forward calculation problem, a domain needs to be addressed. Then, the software for 3D USCT sensitivity matrix computation is based on the ray-voxel intersection algorithms of tray-tracing methods [253], [254], [255]. Thus, by calculating the intersection region, the weighted values can be assigned. In the specific experimental cases the sensor rings have a perimeter of 200-mm and they are positioned in layers of a 70-mm distance. A (32x32) spatial resolution was applied for the cross-sectional planes of a 200-mm edge. For the z-axis a study was followed to compare and provide a well-arranged discretization, following the cross-sectional planes' sensitivity distribution. Figure 7.3 presents the (32x32x8) cubic-voxel and (32x32x4) cuboid-voxel grids. Every green point depicts the centre of each voxel (grid space). The black dots depict sensors' topology. The grey lines represent the voxels.

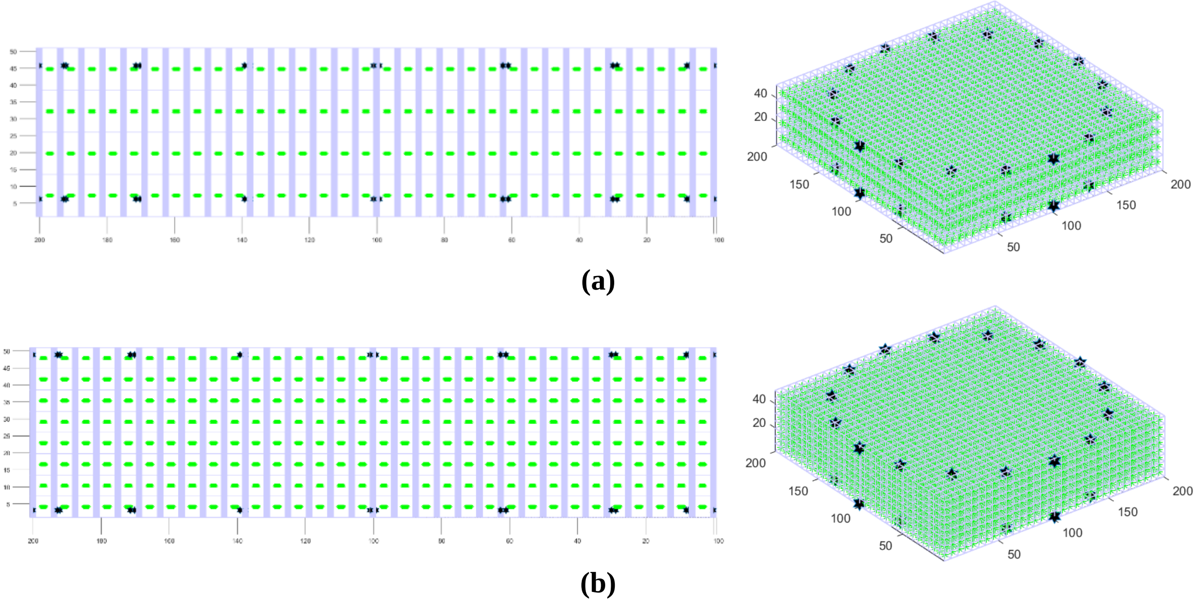

Figure 7.3. Discretization of a (200x200x50) mm ROI by (a) (32x32x4) and (b) (32x32x8) voxel grids.

A grid of (32x32x8) voxels for a (200x200x70) mm cylindrical volume is proportional to the (32x32) pixels grid for a (200x200) mm circular space; accounting for cubic voxels of 6.25 mm diameter. Such a discretization, however, proved to introduce sparsity in sensitivity distribution related to the ray-voxel intersection method. Figure 7.4 shows two sensitivity matrices produced by the same ray-voxel intersection method (described below). The (32x32x8) case displays high sparsity along the z-axis, with the sensitivity distribution displaying a pattern of higher values in the middle planes and blank regions in the 2nd and 7th layers, counting from the top. This effect lies to the combination of the ray width and also to the chosen discretization. To tackle the introduced sparsity in z-axis, one can either increase the ray's width or reduce the resolution. We chose to decrease the resolution as increasing the ray's width can introduce more instability through the cross-sectional and inter-planar layers.

Finally, a (32x32x4) cuboid voxels grid was used. Comparing the sensitivity distributions between different cases of different discretization along z-axis (Figure 7.4), the proposed seems to overcome sparsity and be superior. A ray-based algorithm is computationally efficient in context of linear image reconstruction, especially when it is compared to FWI making it a good candidate for industrial application. The matrix A can be pre-calculated and evaluated before it can be used for the image reconstruction process.

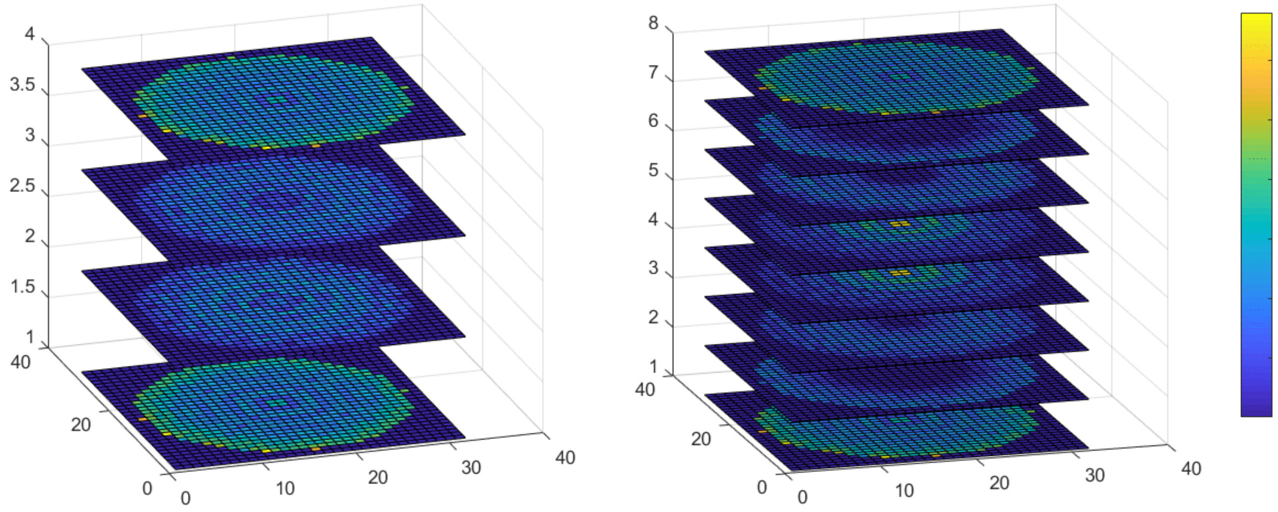

(a) **(b)**

Figure 7.4. Sensitivity distributions of (a) (32x32x4) and (b) (32x32x8) sensitivity matrices. The sparsity introduced in the second case is obvious in the 2nd,3rd,6th and 7th layer, counting from the top.

Ray-voxel intersection

An optimized ray-voxel intersection method was developed for assigning values to the sensitivity matrix. In the pre-developed 2D USCT algorithm the pixel was considered circular instead of square. The inscribed circle of a pixel defines the circular pixel. Thus, the imaging software becomes much faster, which is particularly important in cases where “online” imaging is needed [85]. Regarding this modification, an approximation of this method for 3D models was developed. Prior studies have shown the efficiency of this concept in 3D problems [198]. Furthermore, the voxel has been treated as an inscribed sphere of a voxel rather than as a cube. Thus, the method’s main objective is to compare the distance from the ray to the voxel’s centre, with the voxel’s radius. Subsequently, only one task needs to be executed instead of four complicated ones, leading to less complexity. Therefore, the distance of the ray to the voxel’s centre is computed, as it has been previously presented in eq. (4.7). Then the distance is compared to a fixed value, which usually is the radius, r, of the spherical voxel [199]. By increasing the intersection criterion value, the calculated rays turn to “thick lines” tackling sparsity that might be introduced [86]. To enhance the sensitivity distribution and subsequently the inversion’s outcomes we chose to apply a “thick lines” model. Such a model is more realistic to the real set-up because it accounts for the piezoelectric transducers’ characteristics.

Rymarzyck et al. have presented a method that incorporates smoother sensitivity distribution by using the circumscribed sphere’s radius, instead of using the inscribed spheres’ radius of the voxel [256]. The circumscribed sphere’s radius represents half of the diagonal value of the voxel. The diagonal, dg, is calculated by equation below:

$$dg = \sqrt{(r)^2 + (r)^2} \tag{7.1}$$

Figure 7.5 presents the two different concepts, with the latter offering a better distribution.

In the specific case of a ROI of (200x200x70)-mm using a (32x32x4) resolution, the grid comprises of spheroid voxels. A spheroid has not a unique radius value. Instead, it can be defined by two radii. The longer radius is called the semimajor axis, and the shorter radius is called the semi-minor axis. Therefore 2 radii have been used to calculate the diagonal, dg.

$$r_1 = \frac{vl_1}{2}, \qquad where \quad vl_1 = \frac{200}{32}\,\mathrm{mm} \tag{7.2}$$

$$r_2 = \frac{vl_2}{2}, \qquad where \quad vl_2 = \frac{70}{4}\,\mathrm{mm} \tag{7.3}$$

So, eq. (7.1), in respect of eq. (7.2) and (7.3), becomes:

$$dg = \sqrt{(r_1)^2 + (r_2)^2} \tag{7.4}$$

where dg is the distance that defines the radius of the circumscribed spheroid on cuboid voxel. Finally, for the calculation of dg a radii combination of (r_1, r_1) was used for the rays propagating on a single plane and a radii combination of (r_1, r_2) for inter-planar rays. Values of the sensitivity matrix are produced by the ratio of the radius length to the distance from the ray to the centre of voxel, eq. (7.5).

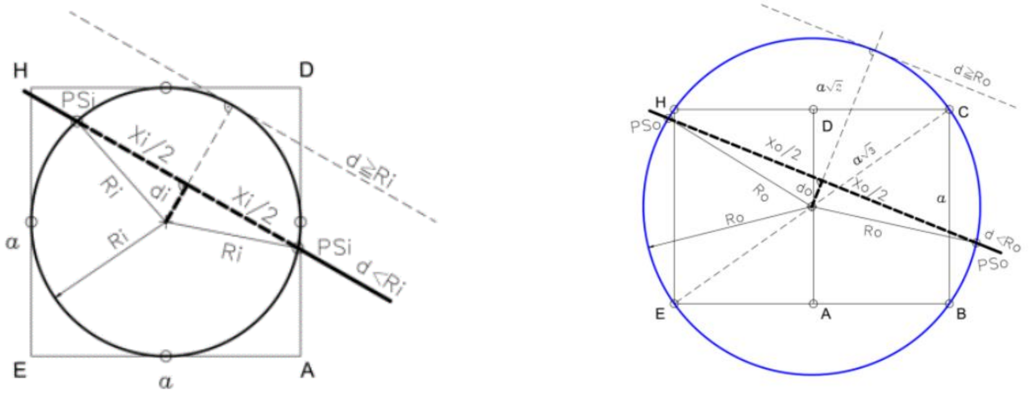

(b) **(c)**

Figure 7.5. Projections of a sphere (a) inscribed in a voxel and (b) circumscribed on a voxel [256]. The proposed method uses the latter form.

$$A_{i,j} = \begin{cases} 0, & for\ d > dg \\ \sqrt{1-\left(\frac{d}{R}\right)^2}, & for\ d \le dg \end{cases} \tag{7.5}$$

Eq. (7.5) includes the distance criterion which defines the ray-voxel intersection. So, for voxels that are not intersected with the ray, zero values are assigned. For the other voxels the assigned value is described as a weighted value proportional to the amount of the ray that intersects the voxel’s area. Thus, the sensitivity matrix contains weighted values which define the regional sensitivity according to the effect of rays on every voxel of the ROI. Moreover, accounting for the excitation pattern of the piezoelectric transducers the software developed in a cone-beam shaped excitation. The angle of beam set at 120^0.

Figure 7.6 presents volumetric representations of sensitivity matrices using different ray-voxel intersection criterion. The volumes include the rays from the 1st to the 9th, 17th and 25th sensors. Figure 7.6(a) displays a matrix that uses the inscribed sphere’s radius, Figure 7.6(b) uses the circumscribed sphere’s radius and at last Figure 7.6(c) uses the proposed method incorporating two radii for the computation of intersection criterion. As it is obvious from the figure, the latter approach provides with the more uniform distribution of the rays. In the first two methods there are gaps along the inter-planar ray’s trajectories, which are corrected in the latter. Also, using the same intersection criterion for rays propagating in a single plane and multiple planes introduces problems, as the ray of 1st – 17th pair of sensors does not affect the pixels. This is also tackled by the proposed method.

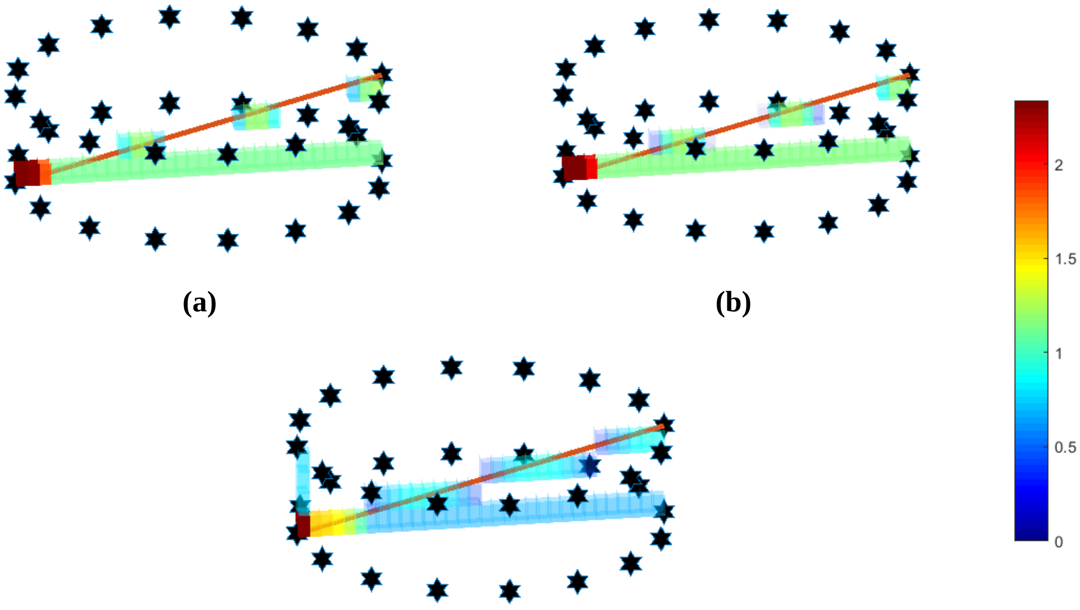

(a) **(b)**

(c)

Figure 7.6. Volumetric presentations of sensitivity matrices using different ray-voxel intersection criterion. The volumes include the rays from the 1st to the 9th, 17th, 25th sensors. (a) the inscribed sphere's radius was used, (b) the circumscribed sphere's radius was used, (c) the proposed two radii method.

Sensitivity Matrix Analysis

To evaluate the performance of each of these approaches to the forward and inverse problem in 3D USCT, an evaluation of forward model and ill-posedness of the inverse problem is considered. Singular Values Decomposition (SVD) provide the means to study the ill-posedness of an inverse problem, by decomposing the sensitivity matrix A. SVD is described in eq. (4.10) of chapter 4. At first, a method which uses for the ray-voxel intersection the inscribed sphere's radius is noted as "SM1"; then a sensitivity matrix that uses the circumscribed sphere's radius is noted as "SM2"; and finally, the sensitivity matrix which incorporates both radii to calculate dg for the interplanar computations is noted as "SM3".

Figure 7.7a presents the 3D sensitivity matrix distributions of the three applied methods described above. The distribution of values seems to be well-balanced across the ROI. However, at the top of Figure 7.7a a few lower intensity spots can be noticed, as a result of the method's sparsity. In Figure 7.7c, such artefacts can barely be seen. Figure 7.7d present a graph of singular values normalized by the first singular value of the sensitivity matrix against singular value number. The rank of the sensitivity matrix corresponds to the independent measurements which is the value of singular number at which the log of the normalized singular values drops suddenly. In our case almost 480, which means that our problem does not seem severely ill-possed, which is good. However, analysing the trend of the curve, the abrupt descending tracking means the smoothing trend of distribution in our sensitivity matrix. Thereafter, the results come with a over-smoothed, blurred trend.

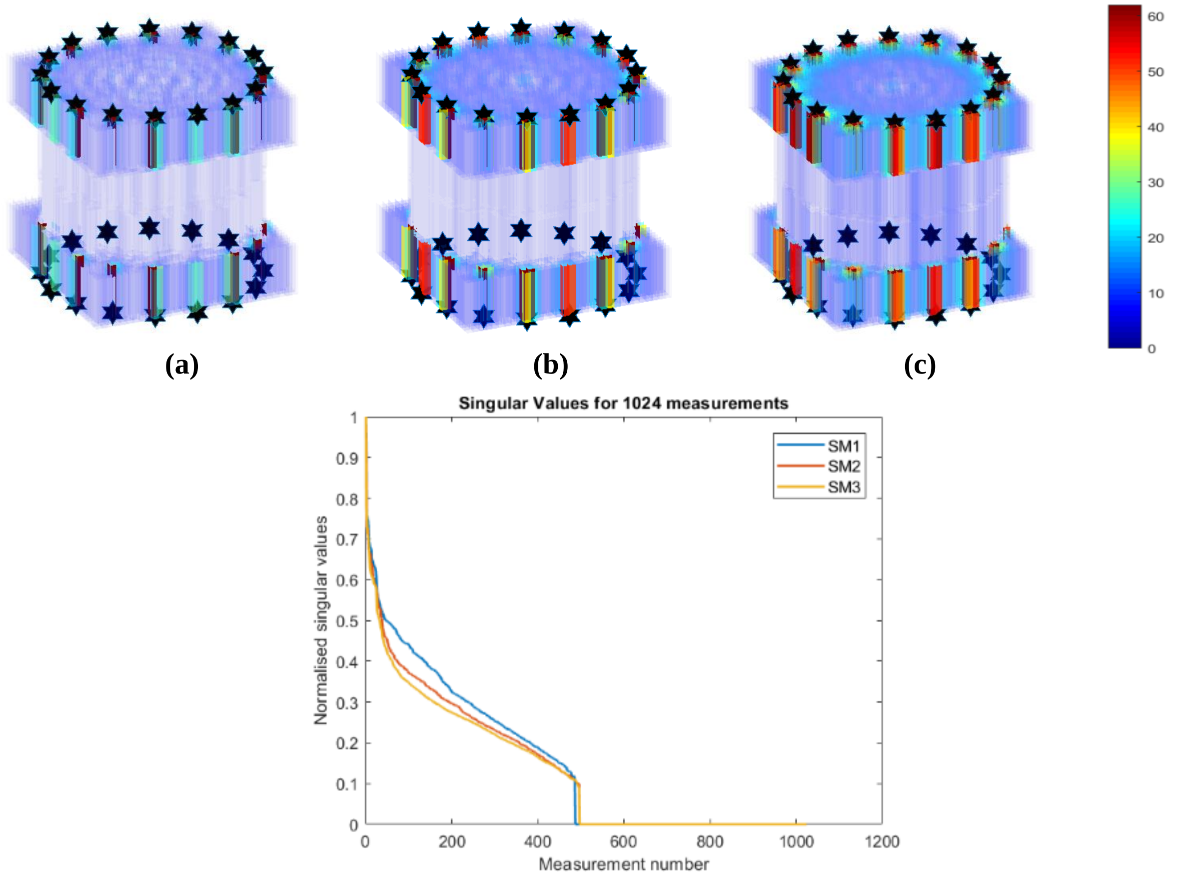

(a) **(b)** **(c)**

(d)

Figure 7.7. (a) Overall Sensitivity distribution of constructed matrices. (b) Singular Values of all the different methods of the sensitivity matrices. It helps to characterize inverse problems according to their ill-posedness.

To evaluate further the proposed methodology, the values of the experimental reference measurement data is compared with the synthetic background data produced by three generated sensitivity matrices based on different methodology, all of them described in the previous chapter.

All three matrices multiplied by a unity vector to produce the so called “synthetic” data. Synthetic data have been produced by solving the forward problem, using a uniform sound speed distribution in the ROI.

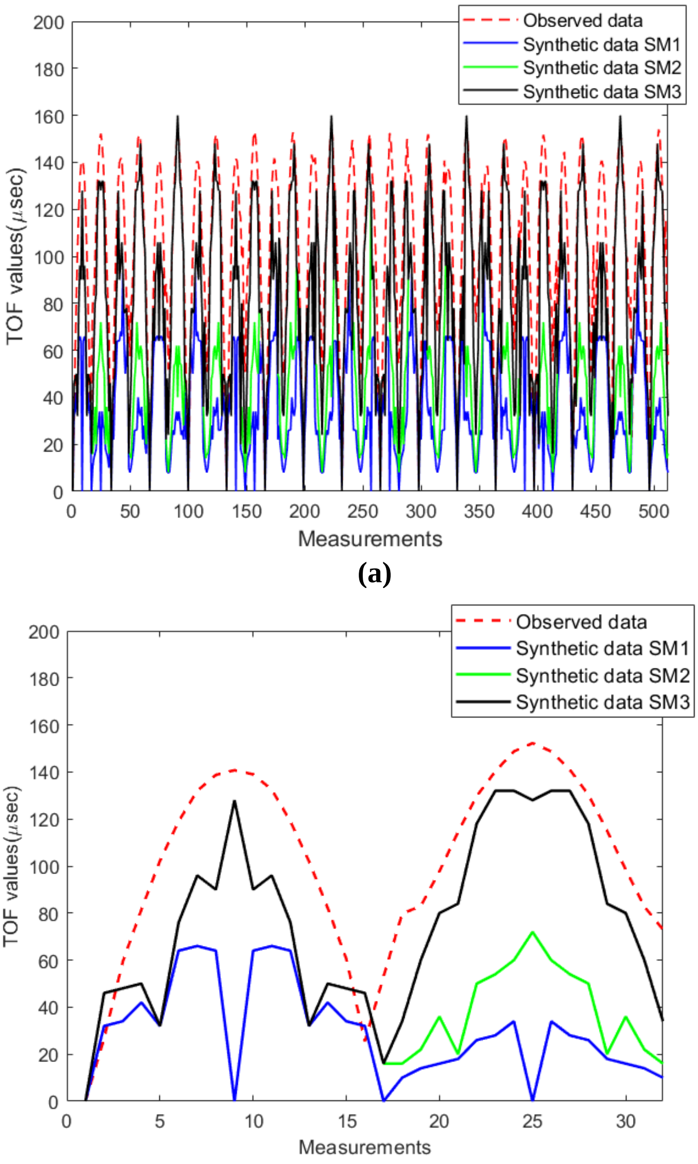

(a)

(b)

Figure 7.8. Acquired and synthetic TOF data plots. (a) Half of the data (512 data), (b) one cycle of data coming from a single excitation (32 data).

The closer these data get to the experimental data; more efficient our sensitivity matrix is. Figure 7.8a shows the half of the acquired and approximated TOF data and Figure 7.8b presents one cycle of the same data (regarding one single excitation) to better visualise the differences. This represents how well each matrix can produce data from a measurement of uniform background (for example water background). The experimental data presented with a red, line curve and all synthetic data, from different sensitivity matrices, in other colours. As it can be seen, the "SM3" provides a better approximation against the real measured data. Sinograms also produced by the acquired reference and synthetic data, as shown in Figure 7.9. It is obvious that "SM3" provides with the closer image to the real data. To quantify the divergence between acquired and approximated data, the Correlation Coefficient (CC) method was used between the 3 synthetic and the real data's sinogram images.

$$CC = \frac{\sum_{n=1}^{N}(\sigma_n - \delta)(\sigma_n^* - \delta^*)}{\sqrt{\sum_{n=1}^{N}(\sigma_n - \delta)^2 \sum_{n=1}^{N}(\sigma_n^* - \delta^*)^2}} \tag{7.6}$$

where σ is the calculated acoustic distribution by the reconstruction algorithms and σ^* is the real one (true image), σ_n and σ_n^* are nth elements of σ and σ^* respectively, δ and δ^* are the mean values of σ and σ_n^* respectively. Table 7.1 shows the CC results, confirming the supremacy of the "SM3" method of sensitivity matrix computation.

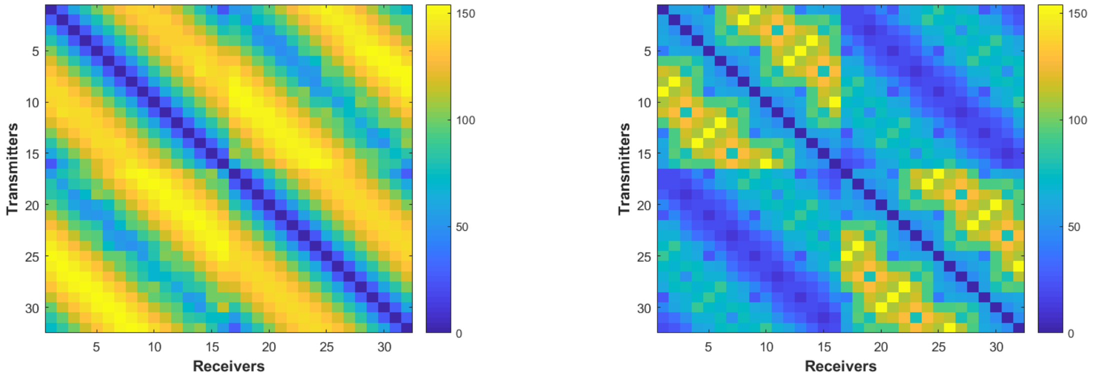

(a) **(b)**

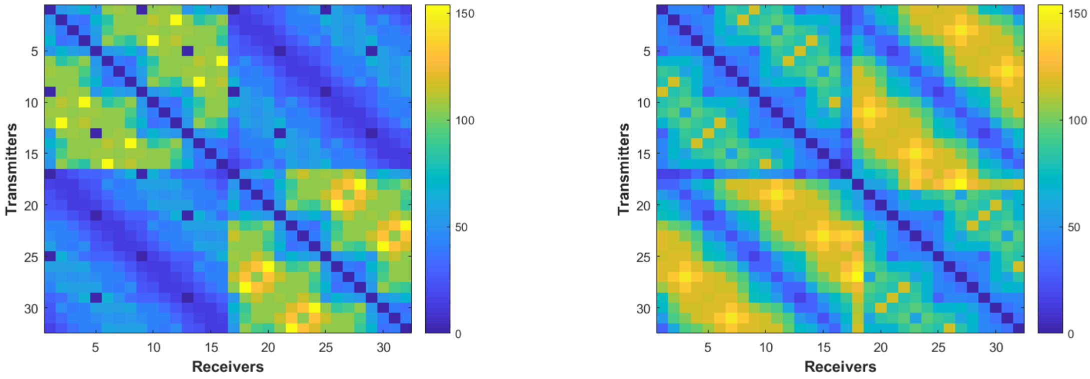

(c) **(d)**

Figure 7.9. Plots of synthetic data produced by all the different methods of sensitivity matrices against the background measurement. (a) Sinogram of reference data. (b) Sinogram of synthetic data corresponding to "SM1". (c) Sinogram of synthetic data corresponding to "SM2". (d) Sinogram of synthetic data corresponding to "SM3".

Table 7.1 CC of the synthetic data's sinograms

Sensitivity Matrices	CC
SM1	0.43
SM2	0.59
SM3	0.83

7.3. Results & Analysis

The imaging performance was tested through various experimental configurations in terms of 3D static and dynamical imaging. This section includes three subsections as "Static experiments" (7.3.1), "Dynamical experiments (4D)" (7.3.2) and "4D Crystallization imaging" (7.3.3). The imaging performance was tested through various experimental configurations in terms of 3D static and dynamical imaging. In section 7.3.1, static experiments took place including plastic objects and sucrose/water solutions. The purpose for these tests is to investigate the spatial and quantitative resolution of the 3D system. Section 7.3.2 presents dynamical cases using manually shifted plastic objects of a 2-cm diameter and aims to demonstrate the results of 4D regularization algorithm over temporal changes. At last, section 7.3.3 presents a crystallization experiment and aims to investigate the 4D imaging on the process with a special interest on the third dimension (height).

7.3.1. *Static experiments*

At first, eight static experimental cases were conducted using cylindrical plastic objects in different combinations and positions with static objects. Objects of 10, 20, and 30-mm diameter have been tested. Any object less than 20-mm was difficult to reconstruct as the sensors could not be sensitive to those. In this work, cases with 20 and 30-mm objects are presented. Various combinations of these objects were tested. Figure 7.10a shows the experimental photographs of all the conducted experiments, Figure 7.10b shows the reconstructed volumetric data by using cross-sectional slices, and figure 7.10c shows the reconstructed volumetric data by isosurfaces, imposing 3-D travel-time tomography. Tests with a single object at the center of ROI were executed, distinguishing well between a 20 and 30-mm object. Items were being positioned at different distances from each other. The variety and amount of different applied topologies offers a great indication of the system's overall spatial resolution and potential in industrial processes.

1

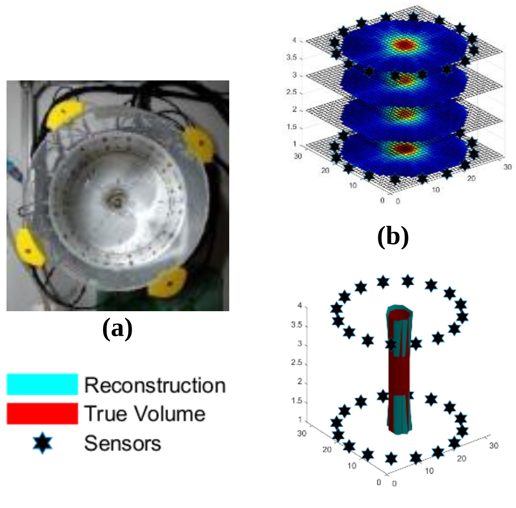

(a) **(b)** **(c)**

2

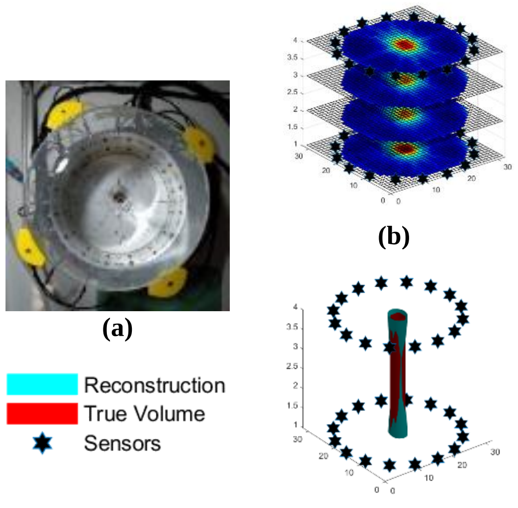

(a) **(b)** **(c)**

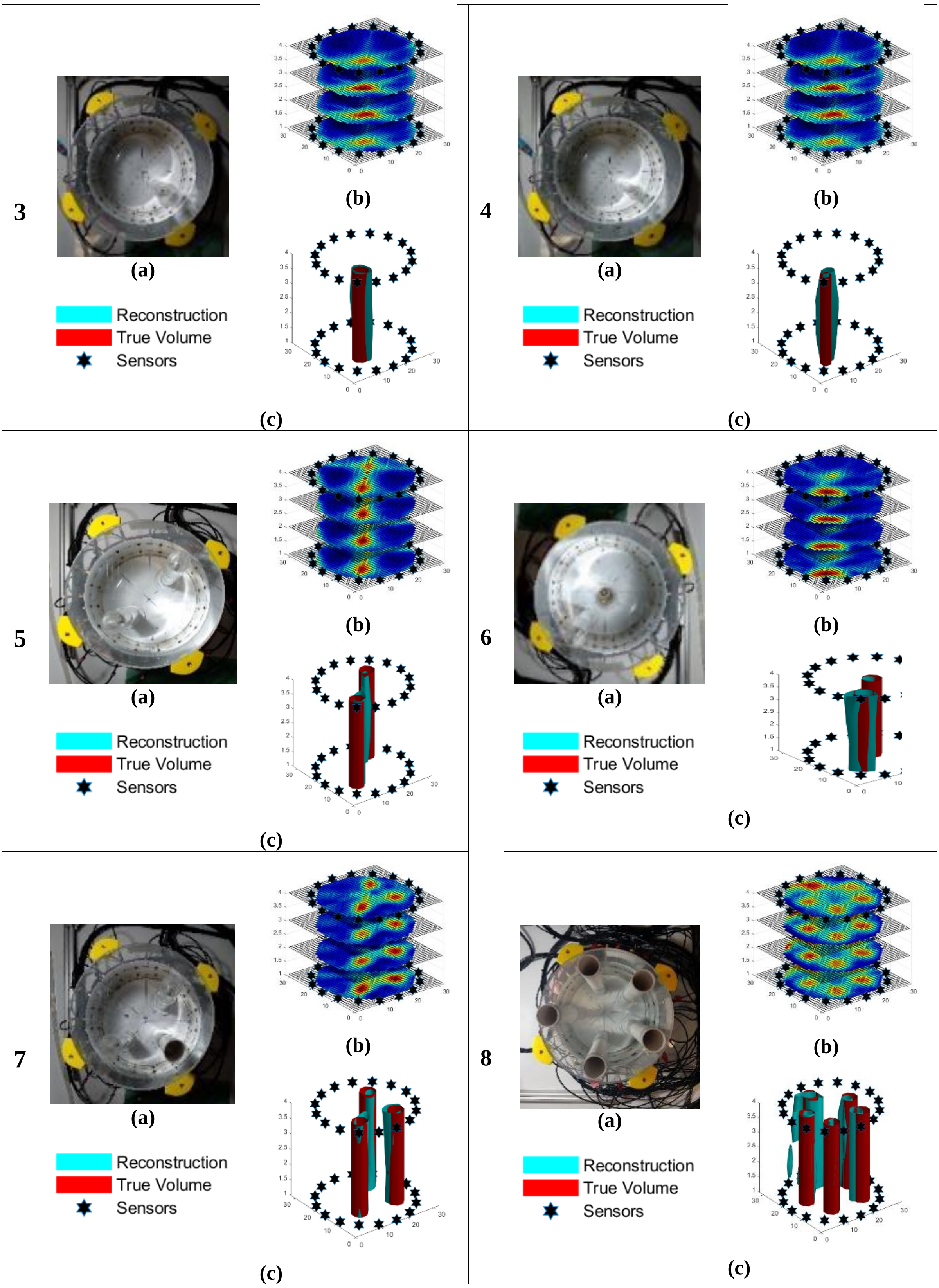

Figure 7.10. Eight positions of single and multiple circular static objects of 30 and 20-mm diameter. (a) True positions, (b) volumetric reconstructions with cross-sectional slices, (c) volumetric reconstructions of isosurfaces.

A version of the structural similarity index (SSIM) based on volumetric data has been used [257] to acquire a quantitative index for the reconstructions. The SSIM is an image quality assessment metric that overall outperforms the error sensitivity-based image quality assessment techniques such as mean squared error (MSE) and peak signal-to-noise ratio (PSNR) [258]. A more advanced form of SSIM, called Multiscale SSIM (MS-SSIM), is conducted over multiple scales through a process of multiple stages of sub-sampling [259]. This image quality metric has been shown equal or better performance than SSIM on different subjective image and video databases. Thus, it is considered a more robust method for image quality assessment. In this work, MS-SSIM was used. MS-SSIM is presented in equation below:

$$MS-SSIM=[l_M(\Delta t_{true},\Delta t_{rec})]^{a_M}\prod_{j=1}^{M}\left[c_j(\Delta t_{true},\Delta t_{rec})\right]^{\beta_j}\left[s_j(\Delta t_{true},\Delta t_{rec})\right]^{\gamma_j} \quad (7.7)$$

where Δt_{true} and Δt_{rec} are the 3D signals to compare, namely the true and the reconstructed volume;a_M , β_j and γ_j are the weighted parameters to define the importance of the three components l accounting for luminance, c accounting for contrast and s accounting for structural similarity. A higher MS-SSIM shows better image quality, with the region of the possible values to be in [0 1]. Figure 7.11 presents MS-SSIM values of the eight experimental cases' reconstructed data. The quality metrics provide consistency to the nature of the experiment. At first, relatively high values result from the first four cases containing single objects as inclusions. Then, in the multiple inclusions case, the MS-SSIM values show a noticeable decay which is expected.

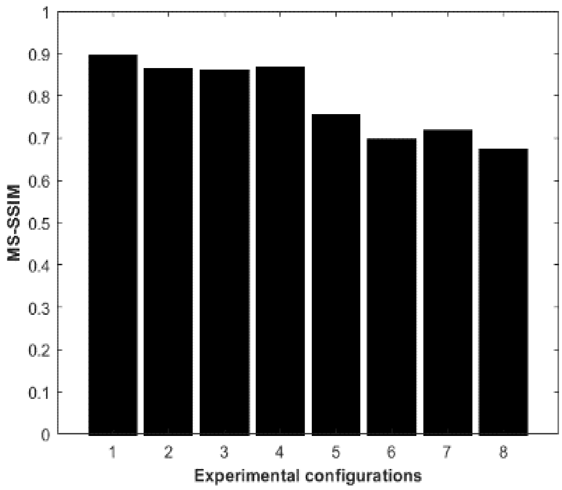

Figure 7.11. MS-SSIM values for all the 8 experimental configurations with static cylindrical objects.

In addition, a test including five cylinders of 2-cm diameter and a test including a cone of 2-cm upper and 5-cm lower diameter, were conducted. Figure 7.12 shows the volumetric reconstruction of two experiments, 5 cylindrical inclusion and a cone shape object. The axial variation on reconstructed images is clear from iso -surface image in cone shape object's case.

Specific experiments based on different concentrations of fine sucrose particles in water were conducted, as well. These experiments aimed to test the quantitative response of the 3D system. Travel-time delays are assumed to remain at a minimum level when the medium is almost homogeneous. On the other hand, delays of sound travel-time are increased if the differences in density and structure of materials within the medium remain significant. TOF delays result from difference imaging, when the subtraction of full data form the background data takes place.. In this case, reference data (background) were collected by scanning the tank filled with water. Single inclusions of 20%, 42% and 70% m/vol mixtures were tested. Figure 7.13a presents photos of the experimental setup with water/sucrose inclusions, and Figure 7.13b shows each case's reconstructed volumetric data. The solutions filled plastic cups of 1-mm wall thickness. The thin wall of the plastic cup ensures ultrasonic wave transmissivity.

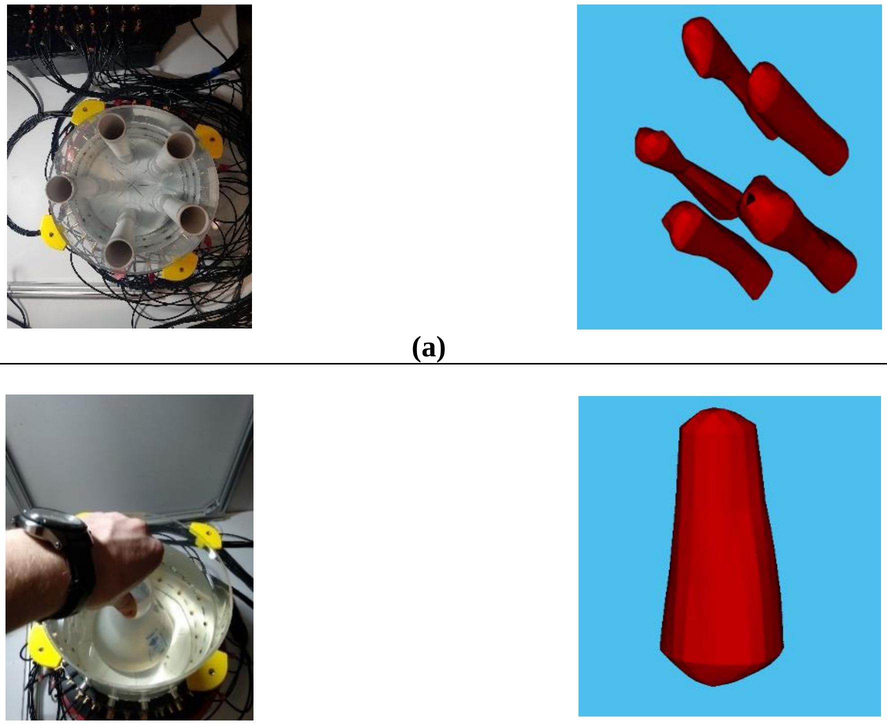
(a)

(b)

Figure 7.12. (a) Multiple inclusions and (b) cone shape inclusion.

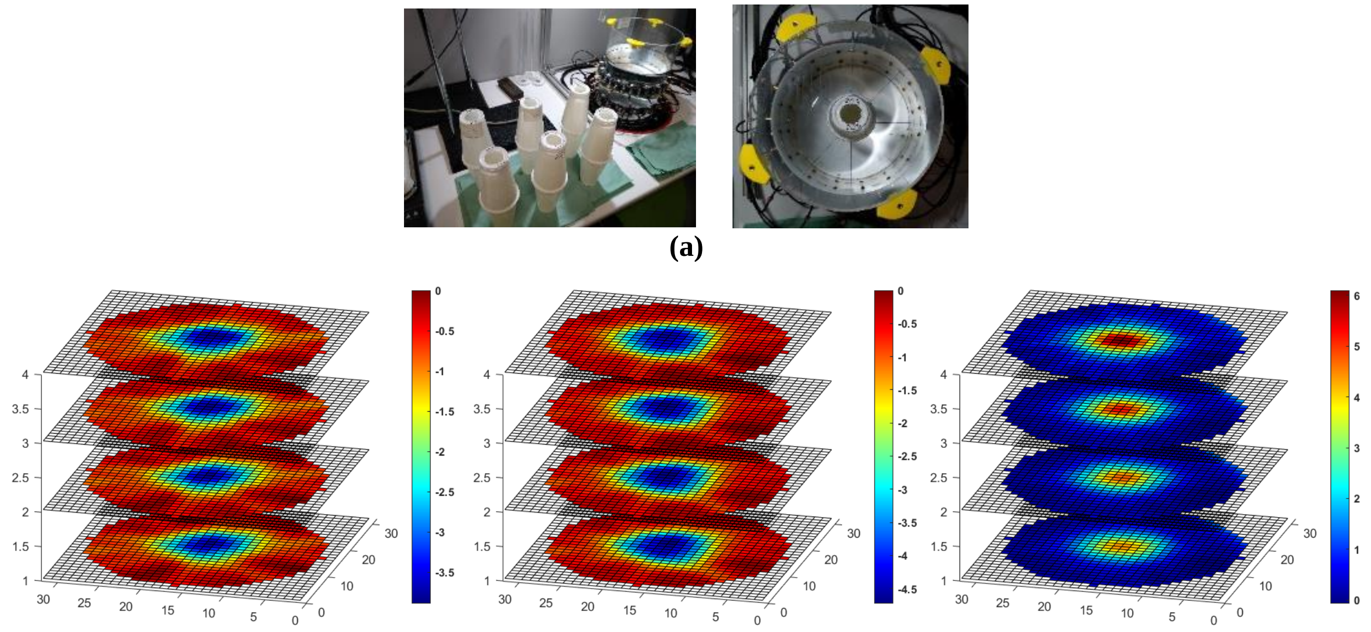

(a)

(b) **(c)** **(d)**

Figure 7.13. (a) Photo of the inclusions filled with sucrose/water solutions (b) 20% (c) 42% (d) 70% m/vol solutions with difference data and reconstructed volumes presented.

In cases of 20% and 42%, the delays are negative as the difference data addresses. The scale of these two reconstructions introduces a quantification indication as the reconstruction scale’s absolute values are increased. The increasing number of negative values defines the ultrasound acceleration within the tested liquid compared to the background. In the case of the 70%, the difference data are positive, and subsequently, the reconstruction includes positive TOF delays. Therefore, an opposite-colour bar reconstructed image than the previous cases were noticed. This effect may come from the floating particles, as the mixture is a saturated solution, with its concentration being close to the saturation point of the mixture (66.7%). Therefore, the sound may be blocked by a significant number of undissolved particles, which will need more time to be dissolved or sediment. Difference data plots provide a good indication of quantification, as differences can be noticed in all three cases. Between the first two cases, the difference in negative data values indicates the inclusion density change, while few positive values come from noise in the measurements. On the other hand, in the third case of 70%, the higher positive values are established, showing the difference in medium’s distributions.

At last, multi-inclusion scenarios with concentrated solutions have been conducted. Four different combinations have been chosen to challenge the system’s quantitative response in more depth. Same as before, the 60.78% case produced positive TOF delays, resulting in higher reconstructed values than the medium (water). However, this was the only case that decreased the sound propagation. The difference between inclusion positioned simultaneously in the tank is evident in all the cases. Thus, the system provides relatively good substance characterization incorporating a robust approach of travel-time imaging. Particular interest can be drawn by Figure 7.14c, where the two inclusions of 42% and 50% concentration have been put very close to each other. In addition to the objects’ location, their concentration is very close, too. Therefore, the case itself makes a special and challenging experiment. Nevertheless, the reconstruction is clear, indicating the concentrated regions of the medium. Moreover, one can notice a clear relation of the total cumulative sucrose concentration to the resulting scalebar of reconstructions amongst all the tests. They result in a clear indication of the quantitative travel-time imaging in concentrated solutions tests.

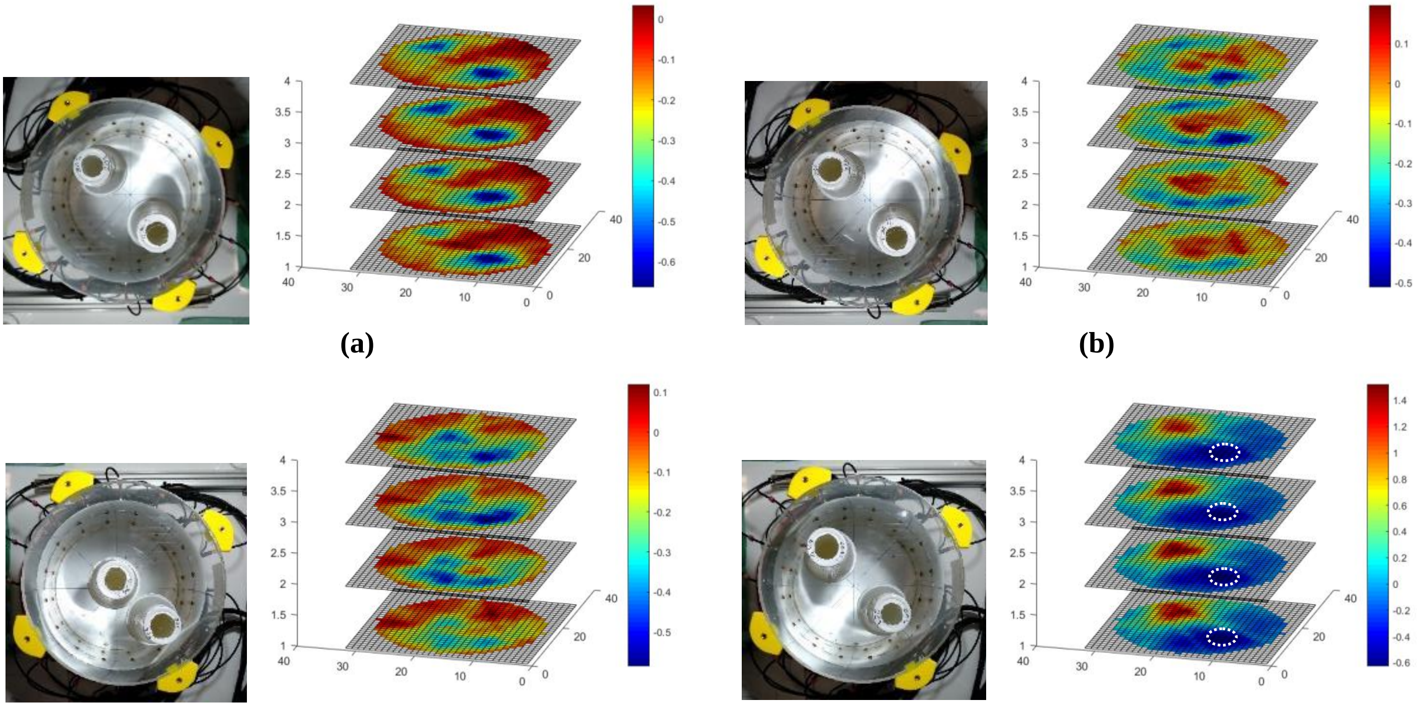

(a) **(b)**

(c) **(d)**

Figure 7.14. Multi-inclusion scenarios of (a) 20%-42% (b) 42%-50% far-positioned (c) 42%-50% near-positioned (d) 70%-20% combinations. Photos and reconstructed volumes presented.

7.3.2. Dynamical experiments (4D)

This section presents results using the pre-described 4D regularization algorithm. Multiple frames have been used in each case. The system was able to provide a high data frame of up to 4 frames per second. The system provides high temporal resolution as its electronic design can filter the waveform data and capture the TOF values of the first-arrival pulse, which saves much time from the data transferring process. Achieving such high temporal resolution regarding a USCT system, we were able to test cases of real-time movement of objects. These tests can offer a first impression of real-time changes leading to a robust system for industrial tanks and pipes. The need of such a system is crucial as ultrasound process tomography gains more attention [260], [261], [31], [122], [262], [263].

Figure 7.15 presents tests using two 20-mm diameter cylindrical objects. The experiment included movement in z-axis to check the sensitivity on the added axis. At first, one object is already positioned in the tank, and the second object is moving in and out of the tank manually.

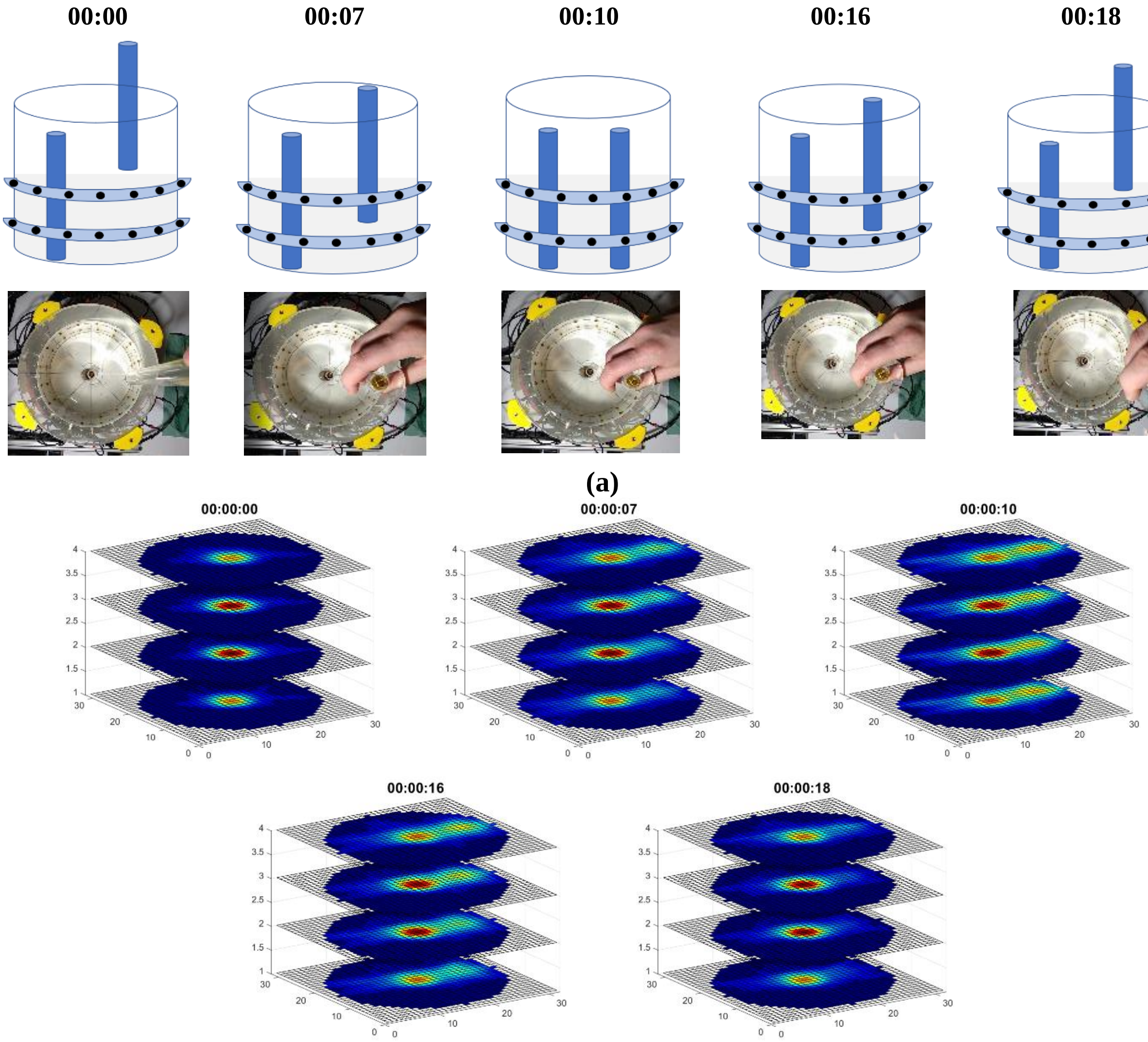

(a)

(b)

Figure 7.15. 4D reconstructed volumes of moving object in a multiple inclusion scenario of two objects positioned small distance. (a) Drawing and real figure of real experiment; (b) reconstructed images

The objects are positioned at a close distance as the test takes place in the same quadrant of the tank (distance between objects is around 4-cm), which makes the case more challenging. Nevertheless, the frame rate provided by the system is adequate to recognize a few steps during the movement, as presented by the resulting volumes. In Figure 7.15a, five steps of the experiment are described with schemes and experimental photos accompanied by the time indication in seconds. In Figure 7.15b, the corresponding reconstructed volumes over the specific time-spots are presented. The main changes, due to the movement, happen in the z-direction as the objects move vertically. It can be noticed through the reconstructed frames, as a few address changes in the z-axis. However, the regularization algorithm still behaves not only accounting for time in the z-axis (where the movement takes place) but also for x-y-z reconstructions, providing good spatial resolution. Figure 7.16 presents the overall mean values of difference TOF data with corresponding reconstructed isosurfaces. At first, non-zero TOF delays exist due to the inhomogeneity of the medium, as the first object is already positioned in the tank. During the experiment, the TOF delays are increased and later decreased due to the movement of the second cylinder in the tank. The peak of the signal in Figure 7.16 displays the moment in the experiment that both objects are fully positioned in the tank.

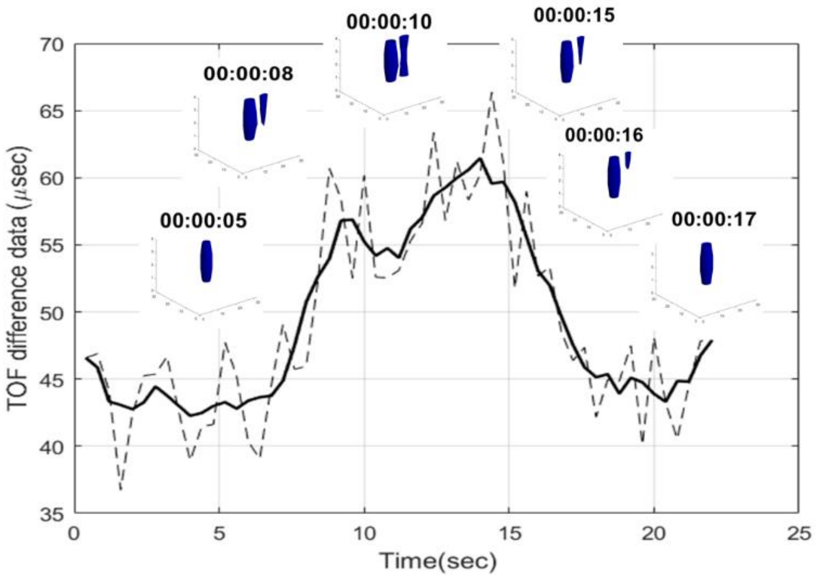

Figure 7.16. Mean values of difference TOF data displayed together with the corresponding reconstructed isosurfaces.

The acquired and reconstructed data seem to be well-correlated to the real-time experimental changes, providing a good temporal and spatial response. Overall, the presented 4D algorithm showed accuracy in all the regularized dimensions of x-y-z time.

In addition, a dynamical test was conducted incorporating a writing technique in 3D. This test aimed to efficiently produce a 3D letter of the English alphabet, tracking the movement amongst the individual generated frames and superimposing it to a unified volume. As a result of the manual movement, this test also aims to examine the response in a physical disturbance situation. A plastic rod of 20 mm in diameter, acting as a writing object, was used. The pen is manually shifted inside the tank to produce the shape of a 3D letter. Figure 7.17a displays a planar and a panoramic scheme describing the experiment. At first, the object is inserted into the tank. Then a motion begins driving the object linearly into 5 different spots of the tank, shaping letter “Y”. Figure 7.17c displays 4D volumetric reconstructions of different frames with the respected times, and finally, Figure 7.17b presents the reconstructed letter “Y”. The reconstructed letter results from the individual superimposed frames into a unified volume. The resulting volume constitutes all the motion of the rod in the tank and defines the engraved letter.

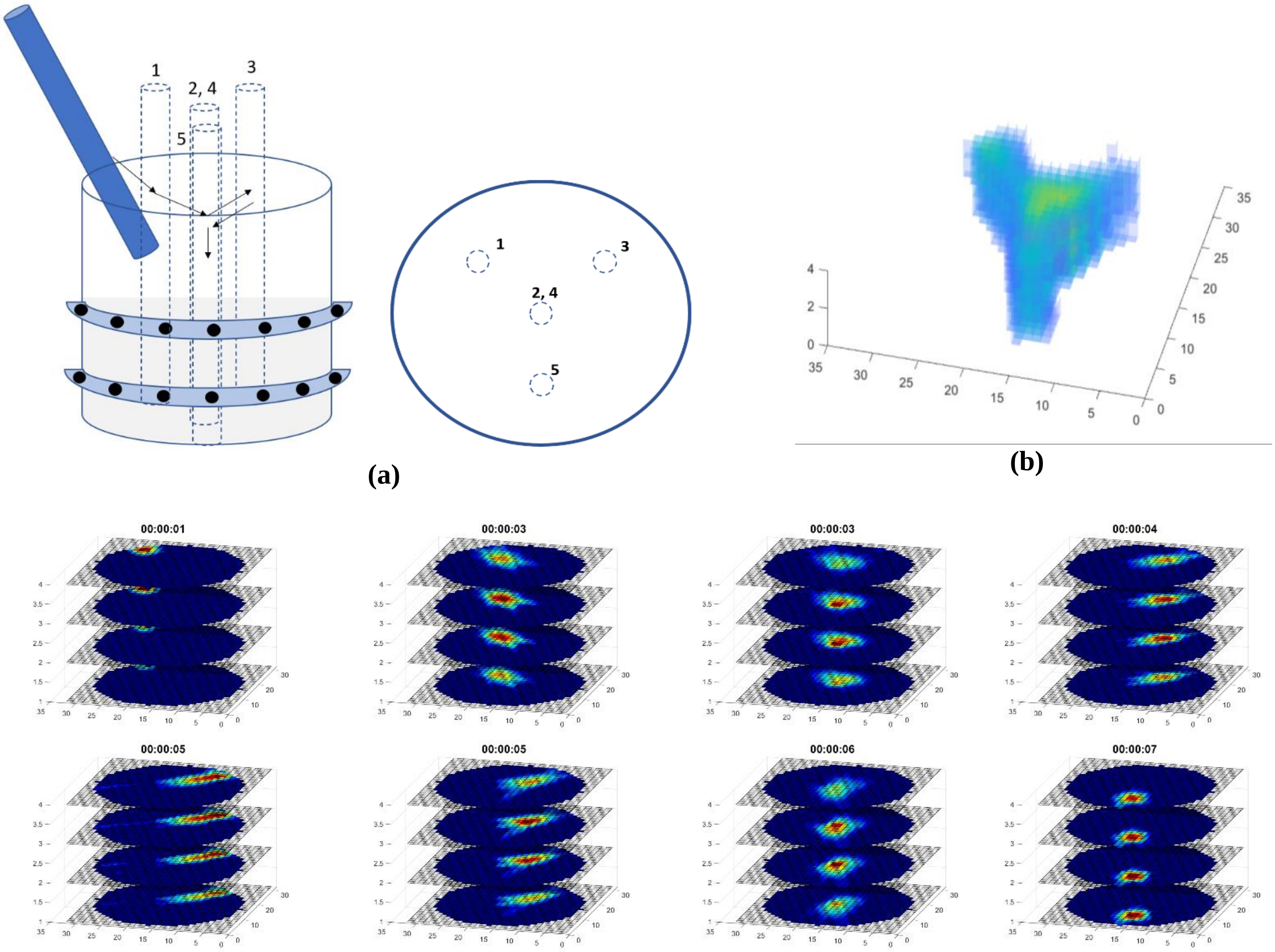

(a)

(b)

(c)

Figure 7.17. Multi-frame 4D reconstruction of a moving plastic rod of 20-mm diameter, drawing the letter “Y”. (a) Scheme describes the overall experiment and, more specifically, the motion of the plastic rod. The rod is inserted at the start of the process, at “00:03” reaches position “2”, at “00:045” reaches position 3, at “00:06” is at position “4” and finally, at “00:07” reaches the last position “5”. (b) Volumetric 4D reconstruction of the super-imposed volume depicting the engraved letter. (c) Individual volumetric frames presented with the respected times.

In Figure 7.18 the mean values of TOF delays have been presented. In contrast to the previous experiment, the TOF data starts from zero values as the tank's medium is homogeneous at the beginning, and after the insertion of the object, the values start increasing. During the small object' movement, a decrease in TOF delays has been recognized. Thus, it seems that the object's movement is not preventing the pulse's transmission as a static object would do. Reconstructed isosurfaces have been displayed in this graph to highlight the rod's insertion frames and the 5 different spots of its movement inside the tank. A 4D approach to image reconstruction captures the 3D frame in their natural dynamical situation, providing a seamless method for motion tracking in tank reactors.

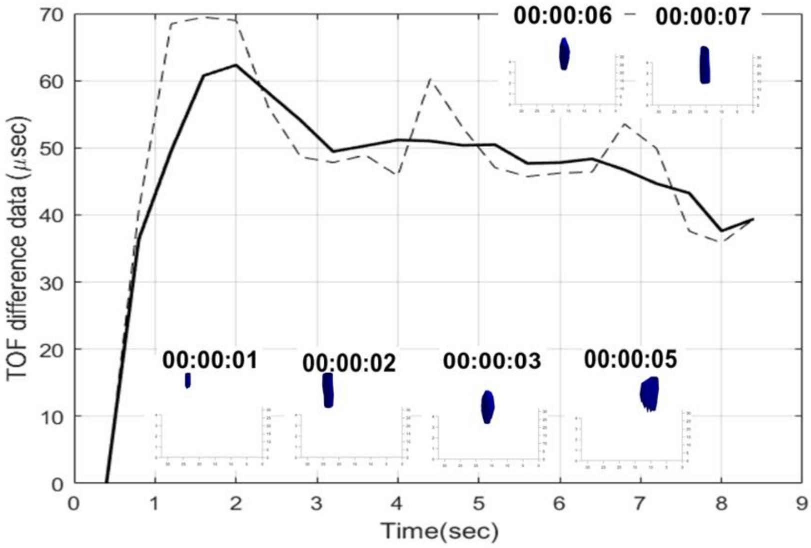

Figure 7.18. Mean values of difference TOF data displayed together with the corresponding reconstructed isosurfaces.

7.3.3. 4D crystallization imaging

A reactive calcium carbonate crystallization is applied in a batch concept. Figure 7.19 shows the entire experimental setup in which the USCT system is utilized to conduct process monitoring. The crystallization reactor is made of plexiglass with an inner diameter of 190 mm. In the micron-sized, liquid-liquid crystallization system, aqueous CO_3^{2-} as the reagent solution flows through an inlet pipe (diameter: 2 mm) into the crystallizer containing calcium chloride. A detailed description of the membrane contactor-based CO2 capture unit and its integration with a calcium carbonate crystallization process is given in [227] and [264], respectively. The chemical reaction governing the crystallization of calcium carbonate is presented in eq. (6.1).

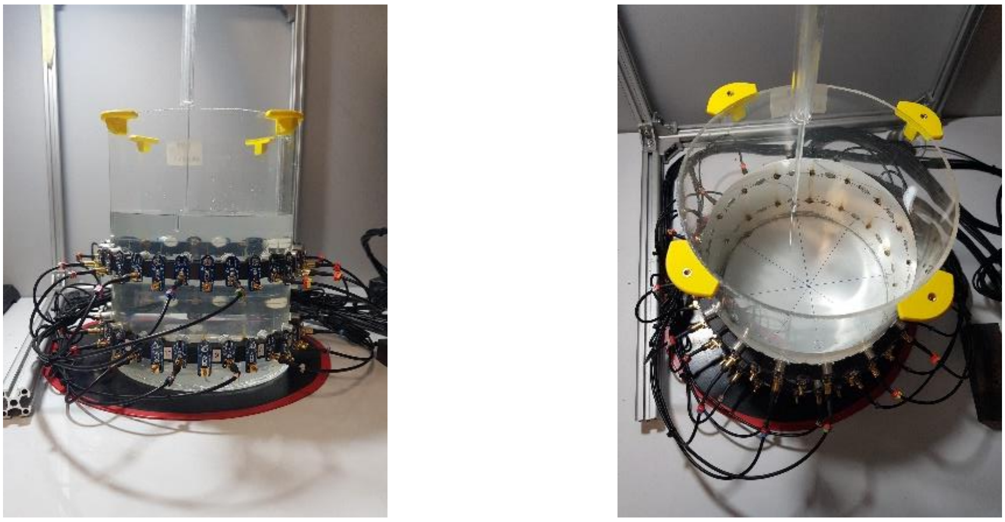

Figure 7.19. Planar and panoramic photos of the non-stirring crystallization experimental apparatus.

Ultrasound-based tomographic measurement is used to detect localized crystals and monitor the reactive crystallization of the calcium carbonate process. In the investigated crystallization experiments, the initial concentration of calcium chloride is 1.6 g /L; the feed flow rate is 27 ml/min. Feed solution composition is NaOH at pH 12.1 ± 0.05 and CO_3^{2-} concentration of 0.14 ± 0.02 mol/L. Due to the fast kinetic nature of the particulate system, the nucleation phenomena are instantaneous, resulting in the formation of micron-sized particles. The ultrasonic excitation of 400kHz is not sensitive enough to react significantly to the onset of inherently stochastic nucleation, which begins at approximately 30 seconds after the first recorded frame of the process. After initiating the feed solution, the formation of amorphous calcium carbonate (ACC) could be an alternative cause of the TOF delay. Due to these delays, the system can display the injection point and the gradual increase of concentration/ suspension density at this specific point.

Figure 7.20 shows photos of the first minute of the process. The photo sequence describes the start of ACC formation and its gradual growth in the time window of approximately one minute. Figure 7.20 presents six reconstructed volumes of the tank during this time window. The USCT images, in that case, depicts the ACC’s formation and propagation in the space, as after a few seconds, its sediments slowly to the bottom of the tank. The white circle points to the injection point. 4D imaging responded well in the z dimension, too, as the layers depicted the axial difference. Nucleation is an important first step in crystallization process. Due to the zero mixing conditions, the compounds' transformation happens slower, and instead of producing clear calcite, a mesostructured calcite product occurs. It is worth noting that the early part of the feed may not be clear in USCT images due to the limited resolution expected by two rings of 16 channel sensors.

Figure 7.21 presents experimental photos of the whole experiment with a few corresponding frames below. The sequence of the photos shows the progress of the medium's phase changes. Reconstructions are also presented in the specific times of the captured experimental photos. Reconstructions show the injection point and the propagation of denser suspension through the medium. Also, the homogeneity of the medium can be noticed from 37th minute and onwards appointed by the reconstructions. However, the injection point could still be visible as injection continuously runs and provide higher concentrations.

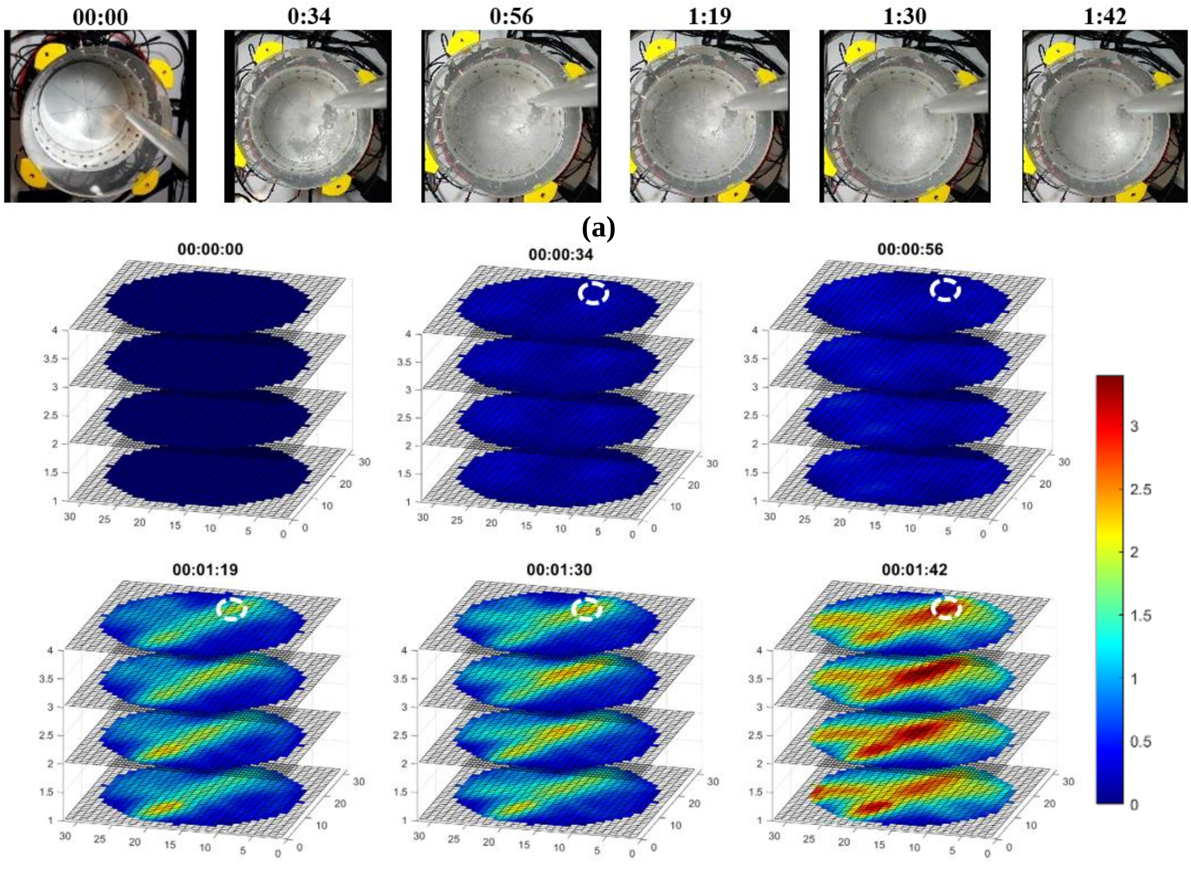

(a)

(b)

Figure 7.20. Experimental photos and reconstructed volumetric UST images for the first minute of the injection.

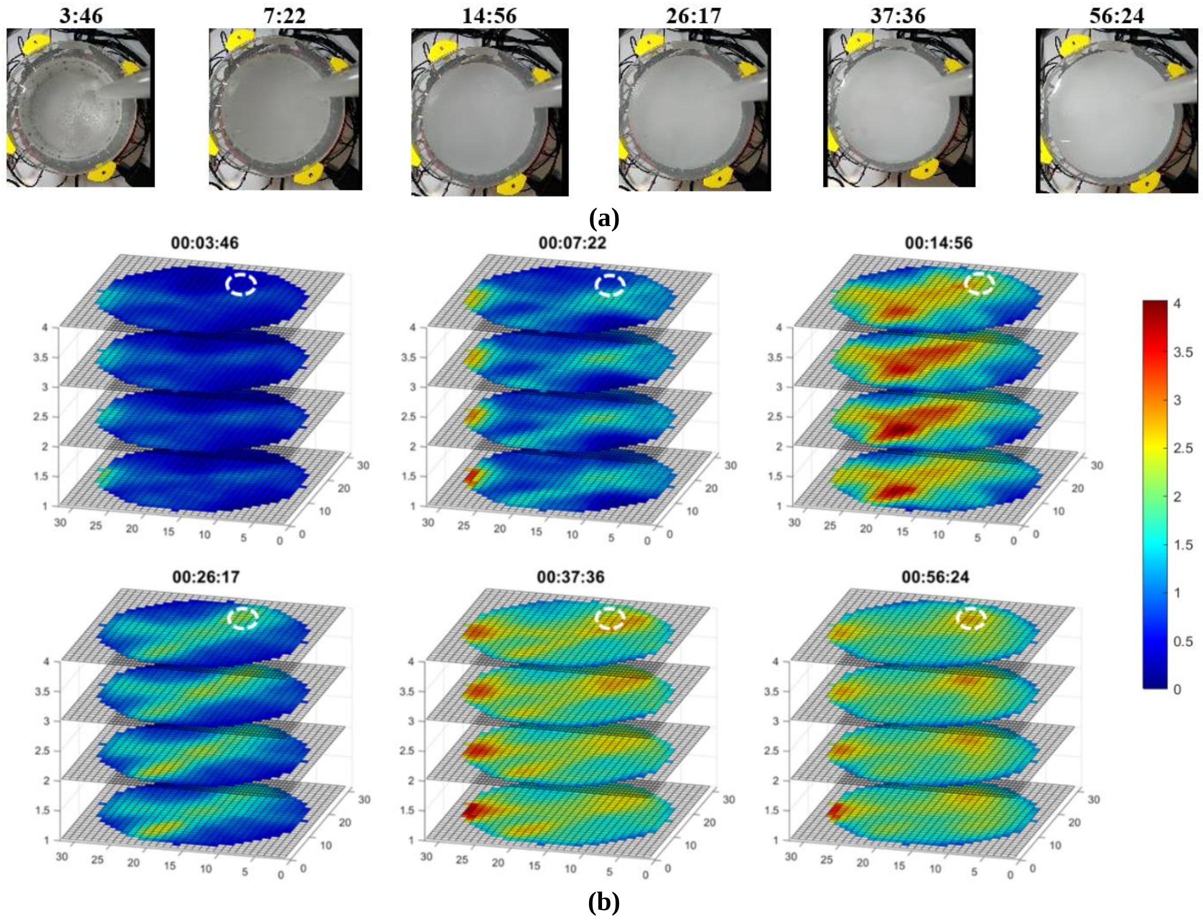

Figure 7.21. Photos and reconstructions of 27ml/min injection rate, non-stirring case.

The following experiment was conducted in which the same 27ml/min feeding rate and stirring using a flat-blade propeller with 100rpm were used. Crystalline forms of vaterite and calcite were produced, depending on the pH of the solution and the mixing conditions [228]. In the current precipitation system, there is a possibility for the following succession of the mechanism to occur [229], [230]: (i) the development and expansion of ACC; (ii) the ACC is the advancement and the surface complexation is occurring that can lead to precipitation of the calcite ;(iii) further calcite expansion from ACC; (iv) More calcite surface complexation is created allowing for further precipitation of calcite. Moreover, due to the nature of the experiment, lower disturbances are expected in the feeding region as stirring quickly dissolves and propagates the forming suspensions. Experimental photos of Figure 7.22a confirm the theoretical background of the process. Compared with the no-stirring case, more clear polymorphs are formed, and the medium’s phase is more dispersed with small micron-sized particles. According to the reconstructions in Figure 7.22b, no localized suspensions in the feeding region were noticed. On the other hand, the reconstructed volumes showed higher disturbances gradually increasing, reaching a peak and then decreasing. These disturbances located at the centre of the tank, around the stirring region. The disturbances define higher concentrations that occurred through the process as after a while start disappearing. Stirring finally dissolves them as depicted in reconstructions. Stirring also might be the reason for the higher concentration to start appearing in the stirring region. The crystalline formations move to the centre and bottom of the ROI and finally, after frame “00:18:39” the TOF delays values start decreasing. The images are produced for every stage of the experiments. The USCT images show the material phase changes during the crystallization process.

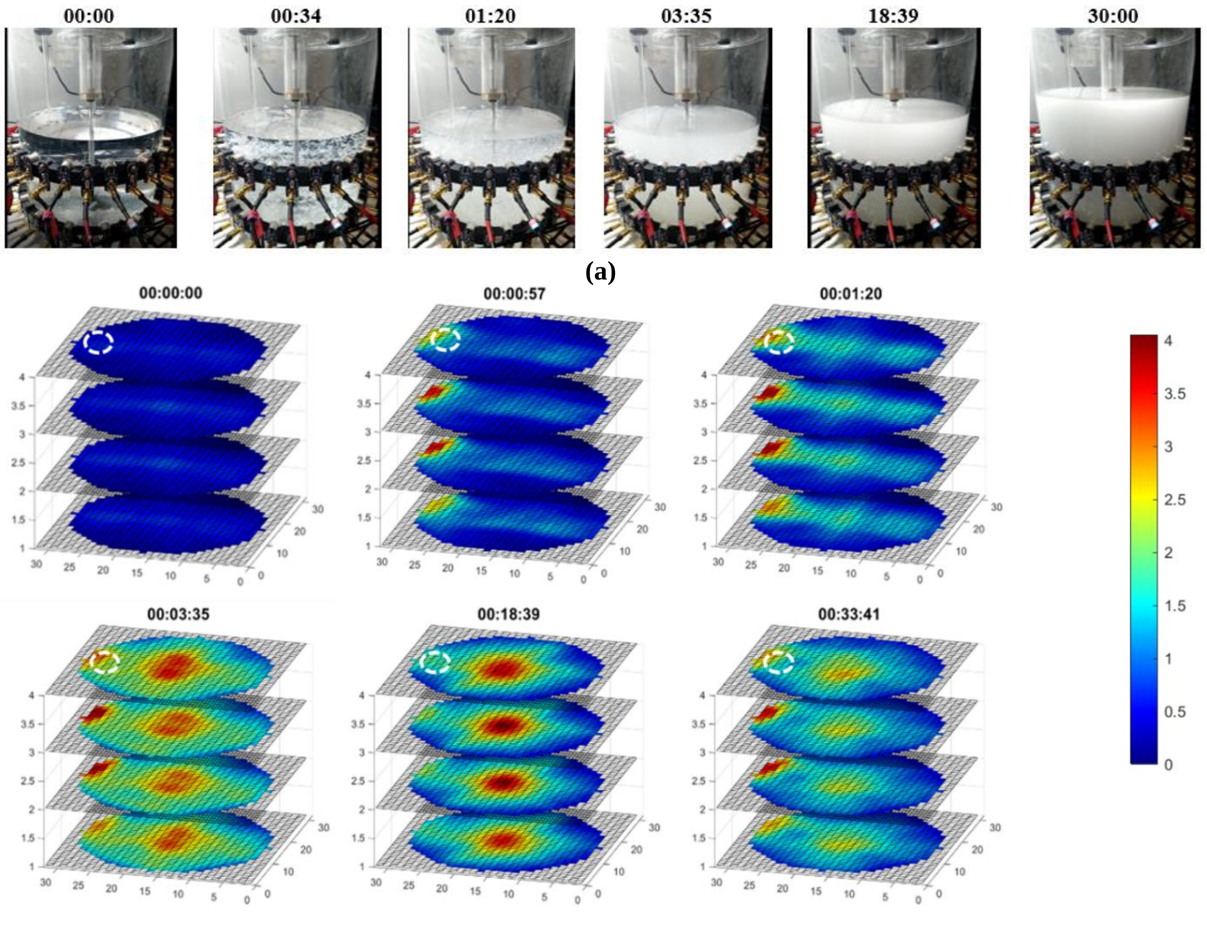

(a)

(b)

Figure 7.22. Photos and reconstructions of 27ml/min injection rate, 100rpm stirring case.

The mean value of TOF data of USCT are considered to show a global picture of the process dynamics. The rate of changes on these mean values will also give further insight into process dynamics. Two additional non-stirring experiments were undertaken using an 18ml/min and 27ml/min injection rate. Figure 7.23 presents the mean value plots for the experimental cases using 18, 27 and 36 ml/min injection rates. In all the three graphs, the same pattern of first increasing and at some point, and after decreasing existence of TOF delays, can be recognized. The ε lines were used to depict the point at which the change of the function direction happened. It is the point for every experiment when all the dense suspensions sediment to the bottom or dissolve to the tank's medium and TOF delays decrease. Comparing the ε_2, ε_3, and $\varepsilon_3$points, one can conclude the difference in the reaction between different injection rates. As higher is the injection rate, the quicker this point appears in the graph. Because of the faster injection the whole chemical reaction forms faster and this point always comes faster in time. Regarding the stirring and no-stirring crystallization case, the ε_1, ε_3 lines are compared. ε_1 comes faster than the ε_3, due to the high dynamics in stirring case. In stirring experiment, the ACC distributes or dissolves faster than in no-stirring cases. This aids to the uniformity of the medium and subsequently to lower TOF delays.

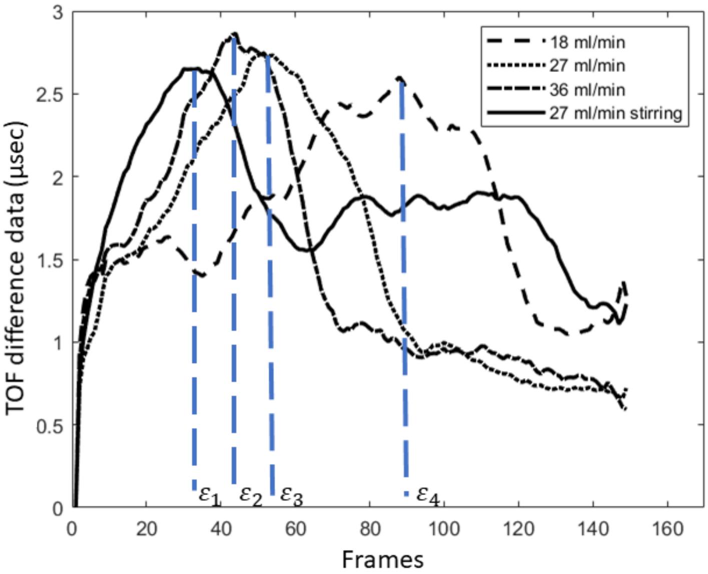

Figure 7.23. Mean value plots of 36ml/min, 27ml/min and 18ml/min injection rate, all non-stirring. The plot of the mean value for the 27ml/min-100 rpm case is presented. A total 150 frames cover 60 minutes of the experiments

7.4. Conclusions

The 3-D and 4-D USCT imaging for static and dynamical imaging are presented. In 3-D imaging mode, the axial varying information can be extracted to provide unique information that is impossible in 2-D. For example, different behaviours in different z-axis positions in the crystallization process are important in describing the process dynamics. Separate two rings of 2D can give useful information on each level in the z-axis, but the 3D imaging by collecting inter-plane data that can also retrieve information for the volume between two rings of sensor giving a fully volumetric picture of the process under investigation.

In addition, the 4D implementation will enhance the 3D imaging results by providing additional stabilities due to time-correlated data and time-correlated image regularization. The proposed method is applicable to the crystallization process, where 4D crystallization monitoring provides real-time information on feed points, mixing process and crystal formation. This holistic time- and space-based information then can be used to optimize the yield and avoid process malfunction.

Chapter 8 Triple-modality USCT based on full-waveform data

USCT is gaining interests in many application areas in industrial processes. The recent scientific research focuses on the possible uses of USCT for varied fields of industry such as flow monitoring in pipes, non-destructive inspection, and monitoring of stirred tanks chemical processes. Until now, most transmission tomography (UTT) and reflection tomography (URT) have been demonstrated individually for these applications. A full waveform USCT contain large amount of information on process under evaluation. The developed approach in this paper is focusing on demonstration of a triple modality USCT. First, an optimised transmission image is formed by fusion of time-of-flight (TOF) and acoustic attenuation (AA) images. Secondly, a reflection image is being optimised by using the information from the transmission image. This triple modality method enables integration of a shape-based approach obtained by URT mode with the quantitative image-based approach UTT mode. A delicate combination of the different information provided by various features of the full-wave signal offers optimal and increased spatial resolution and provides complementary information. Verification tests have been implemented using experimental phantoms of different combinations, sizes, and shapes, to investigate the qualitative imaging features. Moreover, experiments with different concentrations solutions further validate the quantitative traits to benefit from both reflection and transmission modes. This work displays the potential of the full-waveform USCT for industrial applications.

8.1. Introduction

USCT has been studied lately on a broad spectrum of industrial applications with significant success [36], [110], [122], [124], [194], [245], [265]–[268]. Its usage has drawn a special attention notably relating to the imaging of biphasic medium and liquid mixtures in pipe flows and stirred reactors environments [86], [93], [269], [270]. USCT works by analysing the acoustic wave propagation, via sound velocity or pulse amplitude decays of different materials. It aims to the mapping of medium's acoustical properties. It is non-invasive and non-destructive, compatible with high dynamical processes, like oil and gas flow. A better understanding of the measurement process and fast reconstructions algorithms are imperative for the use of USCT within the industry. Moreover, complex stirred tank processes, require sophisticated algorithms, which can provide accurate results. Due to the complex physical behaviour of acoustics propagation, there are multiple reconstruction modes, which use different waveform's properties. The transmission and reflection modes have been traditionally used in ultrasound tomography reconstructions, accounting for transmitted diffracted and reflected waves. Functional features of these reconstruction modes can be complementary. For instance, reflection tomography offers good resolution at the boundary of different media, while the transmission method has better resolution in distinguishing discontinuities along the signals' propagation path. Transmission mode properties, such as acoustic attenuation (AA) or the time-of-flight (TOF), can be used to determine the amplitude and sound-speed profiles of the region of interest (ROI), offering quantitative information. All the AA, TOF, and reflection modes have drawbacks with artefacts under certain biphasic medium distributions. Thus, the performance of single-modality Ultrasonic Process Tomography (UPT) is limited. However, these shortcomings may be compensated with a multi-modality reconstruction. For instance, in a liquid-liquid mixture, the reflected signals will be significantly low, leading to a possible reflection reconstruction failure. However, transmission image should be more meaningful in such scenarios. On the other hand, in a liquid-solid or liquid-gas medium, reflected waves may be exploited. For instance, in many stirred tanks chemical processes like fermentation and crystallization, localised super-saturated suspensions may be formed due to process malfunction e.g., stirrer malfunction. In this case, a drastic structural phase difference may occur. Thereafter, reflection mode might be used as a malfunction detection by detecting the localised high concentrated suspensions. It would be also possible to detect complex dynamic phenomena such as a gas-flow or vortexes coming from a high stirring effect. Although, the use of reflection mode in that direction needs to be further investigated.

The multiple mechanisms (transmission, diffraction, reflection) during ultrasound propagation and the rich information (attenuation, time-delay, distortion) contained in an ultrasonic full signal, establishes the need for a multi-modality method. Therefore, a multi-modality approach, that can facilitate multiple reconstruction methods, is expected to result in more accurate imaging, as it can process measurements coming from different signal's features. Several studies show that dual-modality UPT (transmission/reflection) is superior to single-modality, confirming that multi-modality offers tremendous benefits [271], [272]. As a result, a novel triple-modality image reconstruction method combining AA and TOF transmission as well as TOF reflection is proposed.

In a small circular setup filled with a non-homogeneous medium, significant back-scattering and reflections are expected to happen. Thus, the "noise" levels are higher. Most common issues in ultrasound tomography revolve around the estimation of TOF and AA from the full-waveforms, especially in instruments that are not calibrated or that are characterised by high "noise" levels [239], [273]–[275]. A novel reflection TOF picking method was built to tackle this problem. It exploits a forward reflection solver based on ray acoustics, to optimise the recorded reflected TOF values and subsequently the reflected image. The proposed method fits well in the robust triple-modality proposed approach. The amplitude of the transmitted pulses and time-of-flight of both the transmitted and reflected pulses have been used to produce three different reconstructions (TOF, AA, reflection). Finally, a method of image fusion, using the results of TOF-UTT, AA-UTT and URT methods, was developed and used to generate the final image.

The chapter is organised as follows. Section 8.2 presents the main functionality of the tomographic system and details its specifications; it also includes the description of the proposed reconstruction method. Section 8.3 includes the results' presentation and analysis, and section 8.4 presents the conclusions of this work.

8.2. **Methods**

Figure 8.1 depicts the design of such a triple-modality ultrasound tomographic concept. For a 16-channel transducer system each sensor acts as both transmitter and receiver and complete tomographic data is collected by exciting each sensor in turn. When Tx1 is an excitation transducer Rx1, Rx2,…,Rx15 represent the receivers. The transmission mode uses AA and TOF data for Rx3, Rx4, Rx5,..., Rx13 and for reflection mode Rx1, Rx2, Rx14, Rx15 data are used. The actuated receivers in transmission mode are those that are included in the fan beam of 120-degree angle where the best quality of transmission data is possible. Those sensors, located in the neighbourhood of the transmitter are excluded from transmission mode data but used in reflection mode.

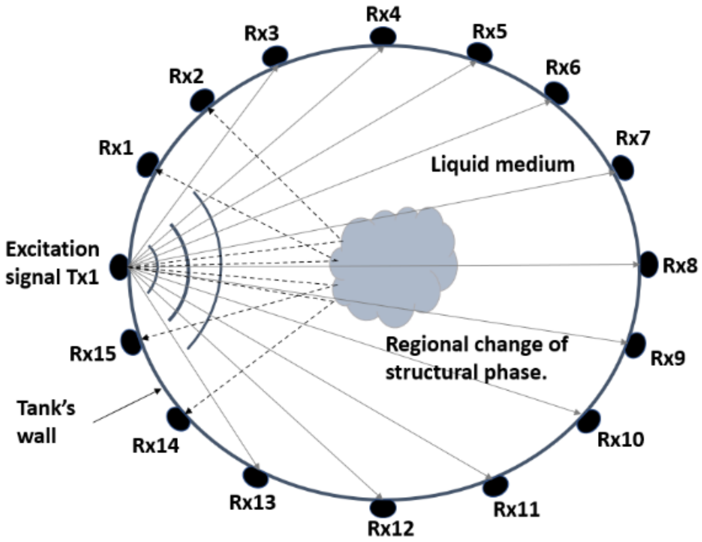

Figure 8.1. Triple-modality ultrasonic tomography (transmission/ reflection). Design of transmitted and reflected signals' paths.

The multi-modality USCT approach utilizes TOF and amplitude information from transmission and reflection waves. These waves come from the interaction of different material phase within the medium. Acoustical properties are dependent on changes in the material phase (i.e., acoustic impedance, velocity). Sound transmission and reflection would, therefore, change within these phases. Acoustic impedance Z affects the propagation and nature of pulse excitation and is dependent on the material's phase. It indicates the intensity of a medium's regions to block the vibrations of the particles in the acoustic field [276]. The ratio of the reflected pulse's amplitude, P_r, to the incident wave's amplitude, P_o, is called the acoustic pressure reflection coefficient R [277], and it is defined in eq. (3.12). By the same way, the acoustic pressure transmission coefficient, T, is defined in eq. (3.13). When a sound wave propagates through a medium, its intensity decreases with the distance travelled, as expressed in eq. (3.8). The two primary mechanisms that cause the attenuation of sound energy are absorption and scattering. Industrial processes usually consist of multiple phase media with a drastic difference in structural phase. Such conditions are favourable for a multi-modality approach in ultrasonic reconstructions, exploiting attenuation, sound-speed and acoustic impedance change within the medium.

The proposed method combines transmission travel-time and AA mapping reconstructions with reflection reconstruction. Transmission reconstructions have been conducted using “fat-ray” method described in section 3.4.2. The Total Variation, described in section 3.4.3.2, regularization was applied in transmission reconstructions, as well. The reflection reconstruction method is based on TOF data of the direct reflected from the object’s boundaries pulse. This method is described in section 3.4.4.

8.2.1. Tomographic system & Measurements Acquisition

USTC3.0 was used in this work. The tomographic system worked on “full-waveform mode” providing full signal recordings. A 16 channel sensor-array in a single plan 2D USCT mode, was used. The bottom layer was used for the data collection. At the same time, a sensor sends an ultrasonic signal of 5 cycles (tone burst), while remaining sensors record. Respectively, receivers measure the full-waveform signal. The sequence repeats until every sensor produces an excitation signal. A central excitation frequency of 400 kHz was used. Figure 8.2 presents the USCT system with the sensor-array attached to the wall of the acrylic tank of 20cm.

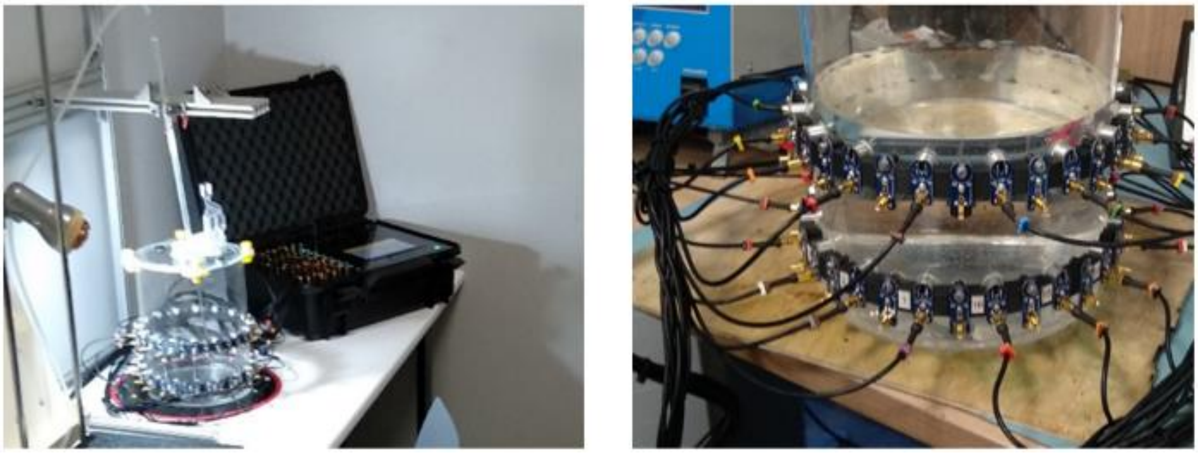

Figure 8.2 Ultrasound tomographic system. (c) tank with sensors.

8.2.2. TOF/ AA picking method for transmission tomography

Transmission signals directly travel from the transmitter to the receivers without any reflection. These signals undergo either diffraction or direct transmission, without significant change of direction. A transmission pulse usually travels faster and transmits at a larger amplitude. Figure 8.3a shows a full-waveform signal and its envelope, recorded by Rx6 upon Tx1 excitation. Moreover, it illustrates signal specific TOF and AA picked points, calculated by the applied method. Figure 8.3b,c present background and full calculated TOF and amplitude data. The picking method of transmitted TOF values is described below.

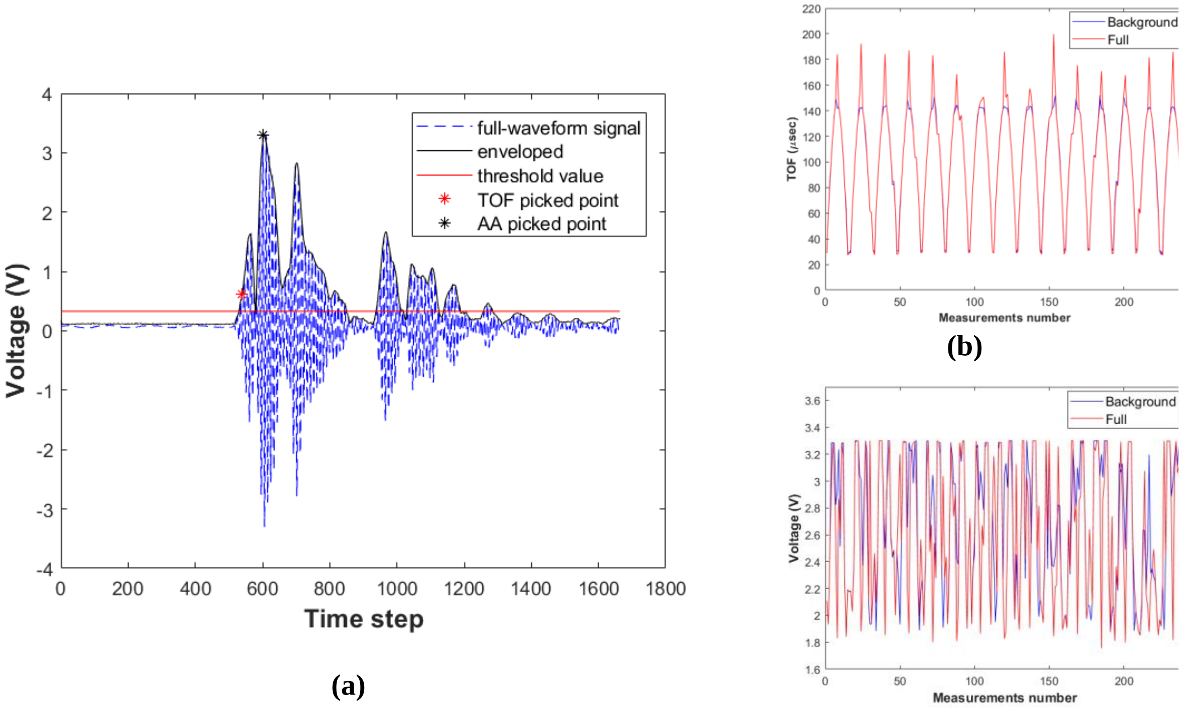

(a)

(b)

(c)

Figure 8.3. (a) Recorded full-waveform signals from Tx1-Rx6 pair, with its envelope. Each timestep is ¼ μs. (b) TOF data computed from the enveloped signals. (c) AA data calculated from the enveloped signals.

First, the analytic envelope of the signal processed using Hilbert transform. Using the envelope, signal oscillation can be removed, facilitating more accurate peak detection. The advantage of using the envelope is to migrate the effect of arbitrariness and to eliminate the effect of phase changes. Then, the enveloped is processed to detect the transmitted pulse and record its x-value, defining the pulse’s travel-time, and y-value, determining the recorded pressure. The method is described in eq. (8.1-8.5), where $v(i)$ represents an enveloped signal, in our experiments the receiving signal contains 1665 samples or time steps. A minimum threshold of 10%, $th,$ is used to cut down the minor pulses caused by back-scattering or equipment-related noise, eq. (8.1). TOF value is determined by the projection of the first signal's point after threshold, th, to the x-axis. According to the sampling frequency, the TOF must be multiplied by 0.25, to be converted in μsec. Eq. (8.2-8.5) describe this in a linearised fashion. Comparatively, the biggest y-value within a 20% signal's window in the transmitted pulse "region" indicates the recorded pulse's amplitude, eq. (8.5).

$$th = 0.1\max\big(v(i)\big), where\ i = \{1,2,\dots,n\}, q = 1665 \tag{8.1}$$

$$v'(i) = \begin{cases} v(i) & for\ v(i) > th \\ 0 & for\ v(i) < th \end{cases} \tag{8.2}$$

$$k_j = i|v'(i) \neq 0, j = \{1,2,\dots,m\}\ where\ m \leq n \tag{8.3}$$

$$TOF = 0.25k_1 \tag{8.4}$$

$$\begin{gathered} AA = \max\,(v'(l)), \\ where\{\ l = k|l = \{i, i+1, \dots, i+0.2q\} \end{gathered} \tag{8.5}$$

All reconstructions are generated by using difference imaging, collecting background data (reference data), $\mathrm{TOF}_{\mathrm{back}}$, and full data (data collected by scanning a non-uniform medium), $\mathrm{TOF}_{\mathrm{full}}$. TOF measurement data, $\mathrm{TOF}_{\mathrm{tr}}$, originates from the subtraction of full data from the background data and define the travel-time delays (μs), eq. (3.15). AA difference measurement data are computed by eq. (3.16) [3].

In both TOF and amplitude data, the "Deleting Outliers" statistical filtering method was used to handle this noise for all the datasets [195]. Specifically, "outlier" TOF values usually are generated from back-scattering or reflected signals. Iterative implementation of the Grubbs Test was used to identify the outlier signals. In any given iteration, the tested value is either the highest or lowest value, represented by the furthest value from the sample mean.

8.2.3. TOF picking method for reflection tomography

The “traditional” picking method of reflected pulses is described in this section. This method makes full use of all the four transducers positioned in pairs, on each side of the emitter. Contrasting full and background measurements, cancels tank-related back-scattering and reflection, as expressed in eq. (8.6). As both background and full data are assumed to present similar tank specific back-scattering and reflection. The recorded maximum pulse peak is assumed as the observed reflected TOF, TOF_{rfl}, as shown in eq. (8.7).

$$p_i = |(v(i)_{back} - v(i)_{full})|, \qquad where\ i = \{1,2,\dots,1665\} \tag{8.6}$$

$$TOF_{rf}^{obs} = \max(p_i)\ , where\ i = \{1,2,\dots,900\} \tag{8.7}$$

Figure 8.4a illustrates the experimental setting. Figure 8.4b represents the plots of full (background and inclusions) and background waveforms and their respective envelopes.

The first peak comes from the transmission pulse and exists in both signals. The two second peaks come from the reflected pulse within the inclusion surface and exist only in Full data. Lastly, the third peak represents tank-related back-scattered signal, existing in both signals as well. Absolute subtraction optimises reflected pulses measurements, reducing overall noise and back-scattered effects. As the reflected pulse remain unchanged, it is easily trackable. Figure 8.4c depicts the absolute subtracted signal.

8.2.4. Novel reflection TOF picking approach

Dual modality ultrasound imaging, fusing transmission and reflection reconstructions, have been recently researched as an optimised ultrasound tomography method [267], [271], [278]. Indeed, combining the two different modalities, which use different full-waveform’s features, can aid reconstructions by combining complementary information.

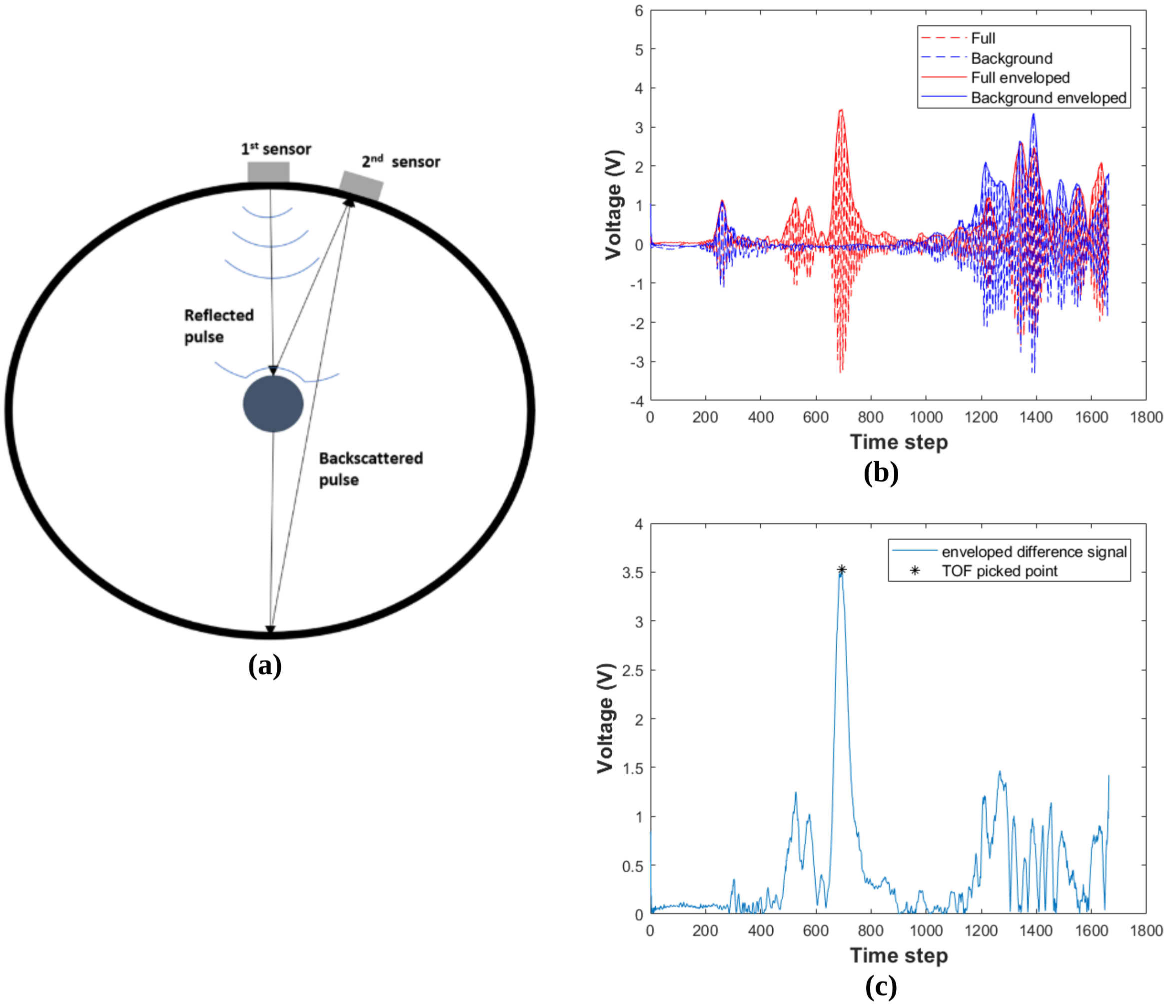

(a)

(b)

(c)

Figure 8.4. (a) Schematic of the setup. (b) Background and Full measurements in full waveforms. (c) Difference data in full waveforms. Each timestep is ¼ µs.

Despite the good performance of transmission imaging, reflection imaging can aid more towards the improvement of outcomes, especially in well-characterizing the domain boundaries. Therefore, a robust algorithm for reflection reconstruction needs to exploit the medium’s boundaries. In practice however, picking algorithms struggle to locate the correct reflection pulse many times, and noise is added to the measurements. This is a common issue of all ultrasonic tomographic instruments, caused by the back-scattering effect [279]. Therefore, a reflection TOF picking method guided by transmission image was developed. The developed method is based on the reflection forward solver to produce better-reflected TOF values than those coming from picking the reflected pulses, described in section 8.2.5.

The reflection forward solver applied in this work is described in section 3.4.4. An acoustic velocity domain of the ROI is created by transmission image and used from the reflection forward solver to produce the simulated reflected data, TOF_{rf}^{sim}. In that case, the fused transmission image is used as described below in Section 8.2.5. A segmentation approach has been developed to define the acoustic distribution on the fused transmission image. First, the global Otsu's thresholding method was used [280]. Then, a labelling method calculates the number of noncontinuous detected regions [7]. For every region, the centre of mass and its boundaries' shape are calculated. The solver uses the regions' information to find the closest region to the corresponding pair of transmitter-receiver, to avoid multiple reflection signals. This aims to improve accuracy, notably considering the impact of more complex distributions on the reflective forward solver.

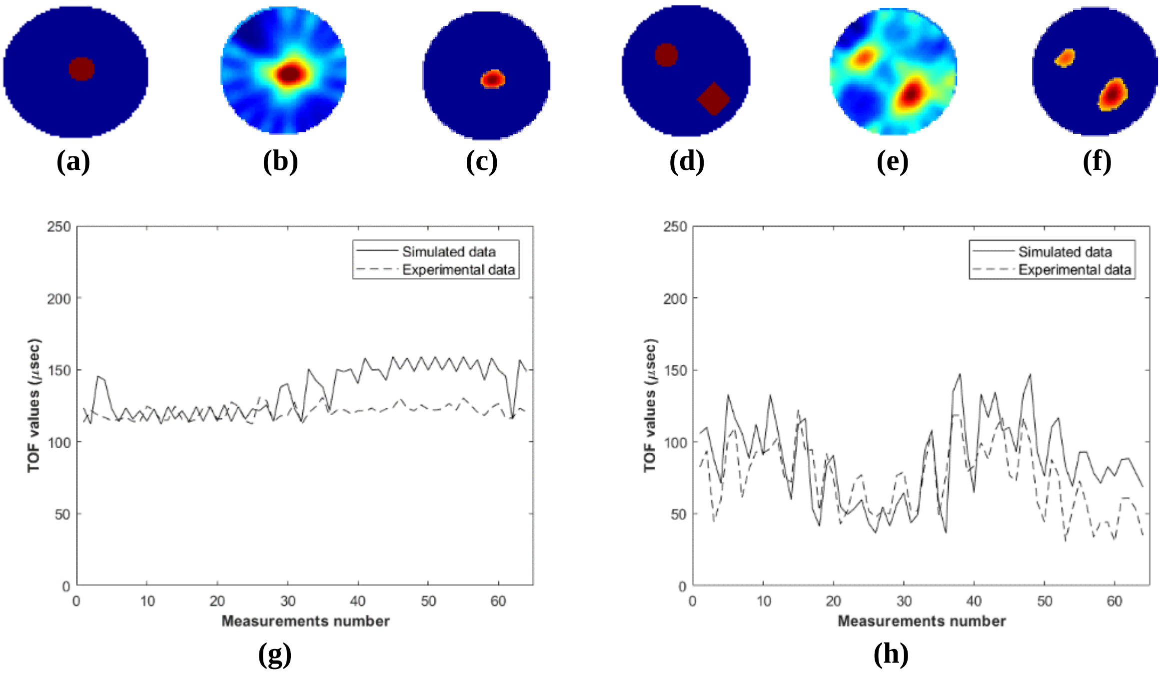

Figure 8.5. (a), (d) True images. (b), (e) Fused transmission images. (c), (f) Segmented Images used as domain in forward reflection solver. (g), (h) Reflection simulated data.

Figure 8.5a-f present the true, transmission reconstructed and segmentation images of two single and double inclusions cases. Figure 8.5g-h present the recorded, TOF_{rf}^{obs}, and the simulated, TOF_{rf}^{sim}, reflection data, using the reflection forward solver.

In the reflected data, there are lower-values region for every positioned object, coming from the time-delays that they introduce. In Figure 8.5g, a single low-values region can be noticed, while Figure 8.5h two of them. Furthermore, a clear resemblance between simulated and observed data can be noticed, showing the good performance of the reflection forward solver. The number of reflection points reduces significantly in multiple inclusions cases, which is clearly a disadvantage of the method. However, a ring setup with more sensors would increase the spatial resolution and the accuracy of the method.

Proposed method for reflection TOF optimization

This method incorporates an optimised travel-time picking method. It picks a signal's value, using as an a priori information the simulated reflection data, TOF_{rf}^{sim}, to optimise the observed data, TOF_{rf}^{obs}. At first, an appropriate threshold was set, and all the potential reflected peaks above that threshold were stored, ($P_{m,n}$). In this way, no peak is being excluded. Then, the algorithm calculates the "closest" peak to the corresponding simulated TOF value, TOF_{rf}^{sim}. The calculated point represents the predicted travel-time value, $TO\mathrm{F}_{\mathrm{rf}}^{\mathrm{pred}}$, eq. (8.8).

$$TO\mathrm{F}_{rf}^{\mathrm{pred}} = P | \min_{n\varepsilon N}(\mathrm{P} - TOF_{rf}^{sim}) \tag{8.8}$$

where P is a $m = [1, \dots, M]$ by $n = [1, \dots, N]$ matrix, containing the peaks of the full-waveforms; M is the number of the measurements and N the number of peaks for each measurement. Usually, the generated $TO\mathrm{F}_{rf}^{\mathrm{pred}}$ data were considered optimised comparing to the observed ones, TOF_{rf}^{obs}. This method ensures a significantly richer dataset than the straightforward way of picking the reflected pulses. This method is named as "minimum distances method".

Nevertheless, the data were occasionally highly affected by the simulated data, leading to overfitting cases. Therefore, a non-linear iterative reflection travel-time method is introduced at this stage, to make use of the forward solver and eventually refine the reflection reconstructions. A convergence criterion of the average percentage of similarity of the observed data, TOF_{rf}^{obs}, and the predicted data, TOF_{rf}^{pred}, was used to investigate the necessity of the non-linear method. Eq. (8.9) describes this criterion. If the similarity percentage is greater or equal than 0.1, then the algorithm proceeds to the optimization.

$$C = \frac{\left|TOF_{rf}^{obs} - TOF_{rf}^{pred}\right|}{TOF_{rf}^{obs}} \tag{8.9}$$

Travel-time reflection tomography attempts to estimate an ellipse model from the time-of-flight measurements that calculated from the received signals. Solution of such problem can be obtained by minimizing the absolute error between the measured data and the simulated data, as studies in travel-time transmission tomography have previously shown [18], [169], [281]–[283]. This process aims to find a solution in the least square function for which the corresponding travel-times are closest to the measured travel-times. The observed data are used to optimise the already predicted data, minimizing the cost function, eq. (8.10-8.11).

$$\varepsilon = \frac{1}{2}\sum_{m=1}^{M}\left[TOF_{rf}^{obs} - TOF_{rf}^{pred}\right]^2 \tag{8.10}$$

$$\xi_{opt} = arg\,min||\varepsilon(\xi)|| \tag{8.11}$$

where ξ represents the acoustical property distribution derived from the reflection "ellipse" reconstruction algorithm, and $\varepsilon(\xi)$ is the error functional. Minimization is achieved by finding a local minimum of a function, in this case the eq. (8.11). These algorithms are iterative and initiate with an initial guess of ξ. In every iteration a ξ is calculated with a sequence of $\xi_1, \xi_2, \ldots, \xi_{opt}$. The algorithm stops when it reaches convergence by finding a local minimum. All the minimization algorithms require the calculation of a direction to move (ideally the direction to the global minimum) and a step size to define how fast in that direction to move. A line-search method was used to solve the non-linear least square problem. The method uses as iterative rule eq. (8.12).

$$\xi_{k+1} = \xi_k - \lambda \, \nabla_{\xi_\kappa} e(\xi_k)^k \tag{8.12}$$

where the gradient $- \nabla_{\xi_\kappa} e(\xi_k)^k$ expresses the direction of the "error curve" and indicates to the algorithm the direction to travel and λ is the step-size for the next iteration.

Specifically, in a tomographic problem the initial guess is a model of acoustical property distribution. Usually, tomographic algorithms that aim to solve the optimization problem between observed and simulated data start with a uniform (background) model of acoustical property distribution. However, the pre-calculated TOF_{rf}^{pred} allows the computation of a relatively good reconstruction to be used as initial guess model. The advantage is that the iterative minimization algorithm may take less to be executed, as it starts with a prior information. Table 8.1 presents the non-linear iterative method for minimizing eq. (8.10) and updating the acoustical property distribution. The inversion is run until the residual between the model and the data (the travel times) no longer changes substantially. For the convergence criterion at step 7 of table 8.1, $\boldsymbol{\varepsilon(\xi)}$ is compared $\boldsymbol{\varepsilon_\tau}$ which represents the value that minimize the error.

Table 8.1 Non-linear reflection reconstruction method minimizing cost function.

1	:	Solve reflection reconstruction for $\boldsymbol{TOF_{rf}^{pred}}$ and estimate reflection image.
2	:	Set as initial guess model $\boldsymbol{\xi_0}$, the reflection image of step 1.
3	:	Solve reflection forward problem using $\boldsymbol{\xi_0}$ and calculate $\boldsymbol{TOF_{rf}^{pred}}{}_{\boldsymbol{1}}$
4	:	Compute $\boldsymbol{\varepsilon(\xi)}$ using $\boldsymbol{TOF_{rf}^{obs}}$ and $\boldsymbol{TOF_{rf}^{pred}}{}_{\boldsymbol{1}}$.
5	:	Update $\boldsymbol{TOF_{rf}^{pred}}{}_1$. $\boldsymbol{TOF_{rf}^{pred}}{}_{\boldsymbol{1}} = \frac{\boldsymbol{TOF_{rf}^{obs} - TOF_{rf}^{pred}}{}_1}{2}$
6	:	Solve reflection ellipse reconstruction method for $\boldsymbol{TOF_{rf}^{pred}}{}_1$ and calculate $\boldsymbol{\xi_1}$.
7	:	Convergence. If $\boldsymbol{\varepsilon(\xi)} \leq \boldsymbol{\varepsilon_\tau}$ stop. Otherwise, $\boldsymbol{\xi_0} = \boldsymbol{\xi_1}$ and move to step 3.

At last, TOF_{rf}^{opt} are generated from the above-mentioned non-linear method, if $C \geq 0.1$ or from the "minimum distances method", if $C < 0.1$. The non-linear reflection reconstruction produces the last reflection data TOF_{rf}^{opt}, which in the most cases is optimised. Figure 8.6a shows the difference data signal, computed by eq. (8.6), and a zoomed window of the reflection pulse. The black dot represents the travel-time of the reflected pulse coming from the straightforward method of section 8.2.2. (TOF_{rf}^{obs}).

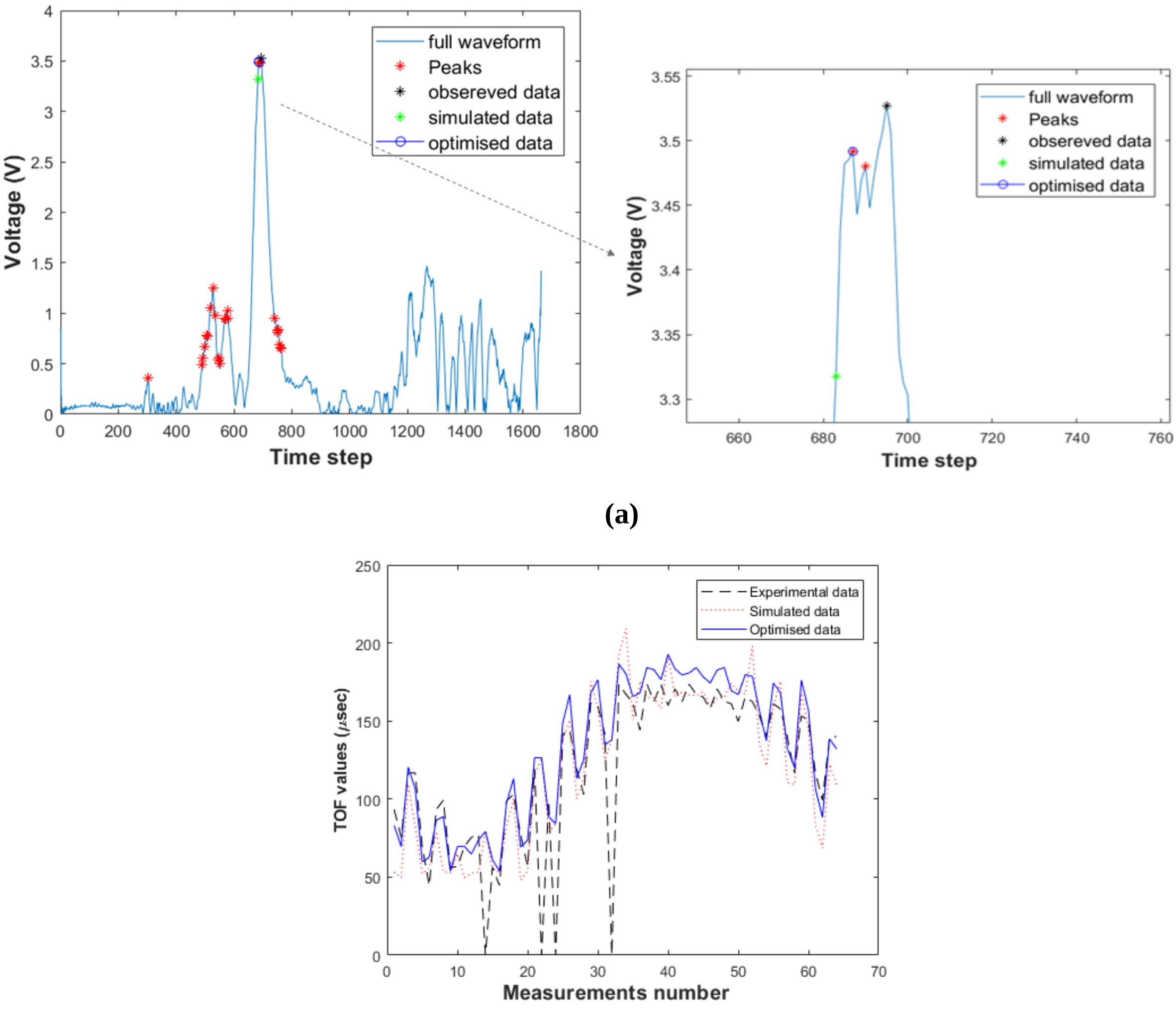

(a)

(b)

Figure 8.6. (a) Subtracted full-waveform signal with Peaks, observed, simulated, optimised data depicted. The corresponding pulse is represented zoomed. (b) The plot of experimental, simulated, and “optimal” data of all waveforms.

The green dot is the simulated travel-time, TOF_{rf}^{sim}. The red dots represent all the captured peaks of the waveform above the threshold value. Finally, the blue circle represents the “optimal” reflected travel-time value that results from the “minimal distances method”, TOF_{rf}^{opt}. The effect of the method is noticeable in Figure 8.6b. The blue function represents the “optimal” data, the red function the simulated data and the black function the recorded data. The black function missed calculating a correct TOF value in few cases, where zeros are observed. However, the zeros have been replaced with estimated values, in the “optimal” data, with the aid of simulated data, concluding in the well-behaviour of the optimization. These travel-time values are assumed to be refined when compared to the observed data.

Figure 8.7 presents the reflection data optimisation process for two single and double inclusions cases. Specifically, Figures 8.7a,d show the true images, while figures 8.7b,e present reflection reconstructions using the TOF_{rf}^{obs} and figures 8.7c,f present reconstructions resulting from the “proposed” reflection TOF picking method.

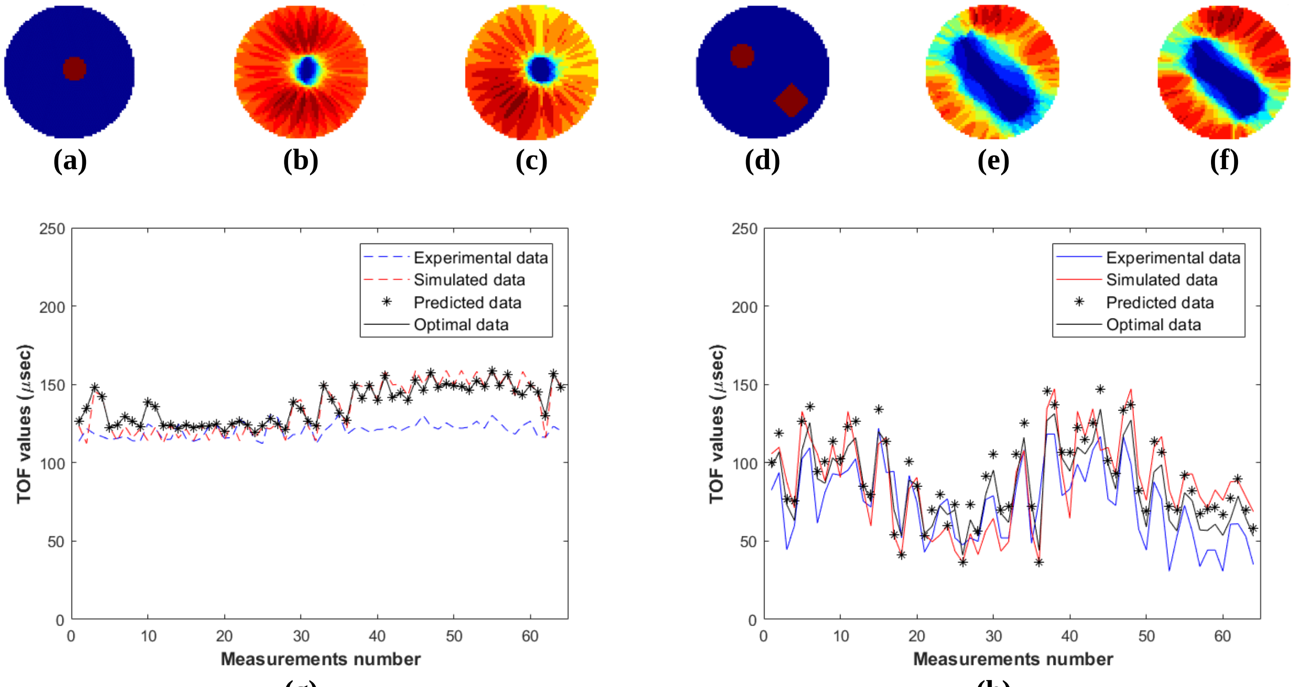
(a) (b) (c) (d) (e) (f)

(g) (h)

Figure 8.7. (a) True images of two tested configurations. (b), (d) Reflection images generated by the “traditional” method. (c), (e) Reflection images generated by the “proposed” method. (f) Plots of observed, simulated and optimal reflection data

Figures 8.7g,h present the observed data (TOF_{rf}^{obs}), the simulated data from the reflection forward solver (TOF_{rf}^{sim}), and the “optimal” data (TOF_{rf}^{opt}) from the “proposed” method. In the first case (single inclusion), the “predicted” and the “optimal” data are the same, which means that the convergence criterion was not valid. On the contrary, in the second case (double inclusions), these data differ, which indicates that the non-linear optimization was executed. In both cases, the effect of the simulated data for the computation of optimal data is pronounced.

The novel reflection data picking algorithm consists of all the previously described methods and aims to provide optimal reflection TOF data and reconstructions. The proposed algorithm fits the “optimal” data to the observed ones with respect to a prior information of the “simulated” data, as shown in Figure 8.6. It can be summarised into the following steps: (i) execution of transmission reconstruction; (ii) segmentation using Otsu’s threshold; (iii) execution of reflection forward solver to produce simulated data (TOF_{rf}^{sim}); (iv) calculation of optimised reflection TOF by “minimum distances” (TOF_{rf}^{pred}), (v) checking the convergence criterion and if true, generate reflection reconstruction minimizing the cost function of eq. (8.10). The methodology is displayed in Table 8.2.

Table 8.2 Novel Reflection signal picking algorithm

```
Compute $\boldsymbol{TOF_{rf}^{obs}}$ by using the “traditional” TOF picking method.
Produce fused AA-TOF transmission image.
Create the acoustic domain by segmentation of fused transmission image.
Compute $\boldsymbol{TOF_{rf}^{sim}}$ by solving the reflection forward problem.
Detect all waveform’s peaks, $\boldsymbol{P}$, above a minimum threshold.
Calculate $\boldsymbol{TOF_{rf}^{pred}}$ by locating the shortest distance peaks from $\boldsymbol{TOF_{rf}^{sim}}$ by using the minimum distance method.
Calculate the average percentage of similarity, $C$.
If ($C \geq 0.05$)
        Minimize cost function ε(ξ). $\boldsymbol{TOF_{rf}^{opt}}$ is the last iteration’s updated data.
else
        $\boldsymbol{TOF_{rf}^{opt} = TOF_{ref}^{pred}}$
end
```

8.2.5. Triple-modality

The developed triple modality approach consists of three sets of information, and the fusing method is described by a specific pipeline which is depicted in Figure 8.8. First, the TOF and AA transmission images are fused using a “wavelet transform method” [284]. This intensity-based method was chosen due to the similarities of the TOF and AA images as they both come from transmission reconstruction. The two images were normalised, before being merged, to have the same scale. The result contains both the information coming from TOF and AA data subsequently proved as an optimised reconstructed image. Then, the transmission image is combined with the reflection image.

Because of the different nature of the transmission and reflection images, a different fusion method was used. The transmission images usually contain high “regions” in the position where the objects are located, due to significantly high TOF-delays and amplitude attenuation due to object introduction.

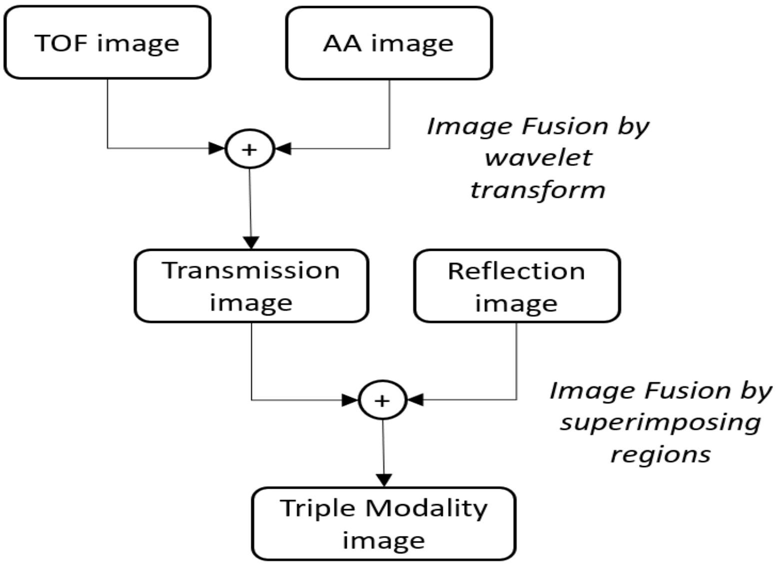

Figure 8.8. Image fusion algorithm for triple modality USCT.

On the other hand, the reflection image has almost zero values to the locations of the objects, as all the reflections are encountered in their boundaries and, according to the ellipse algorithm, no ellipse interaction is happening within the object. Therefore, a method that accounts for these characteristics, by superimposing regions of the images, was applied to fuse the transmission and reflection images. This is described in eq. (8.13).

$$TM_{i,j} = \begin{cases} T_{i,j} & where\ R_{i,j} > 0 \\ 0 & where\ R_{i,j} = 0 \end{cases} \text{ where, } i = [1, \ldots, 32]\ j = [1, \ldots, 32] \tag{8.13}$$

where $T_{i,j}$ is the transmitted image, $R_{i,j}$ is the reflection image and $TM_{i,j}$ is the triple-modality image; i, j represents the rows and columns of the image that is 32 by 32.

Figure 8.9. presents the full framework of the proposed triple modality algorithm for the specific case of a circular inclusion of 20-mm diameter positioned in the centre of the ROI. In the final, triple-modality image, one can clearly distinguish the shape of the inclusion.

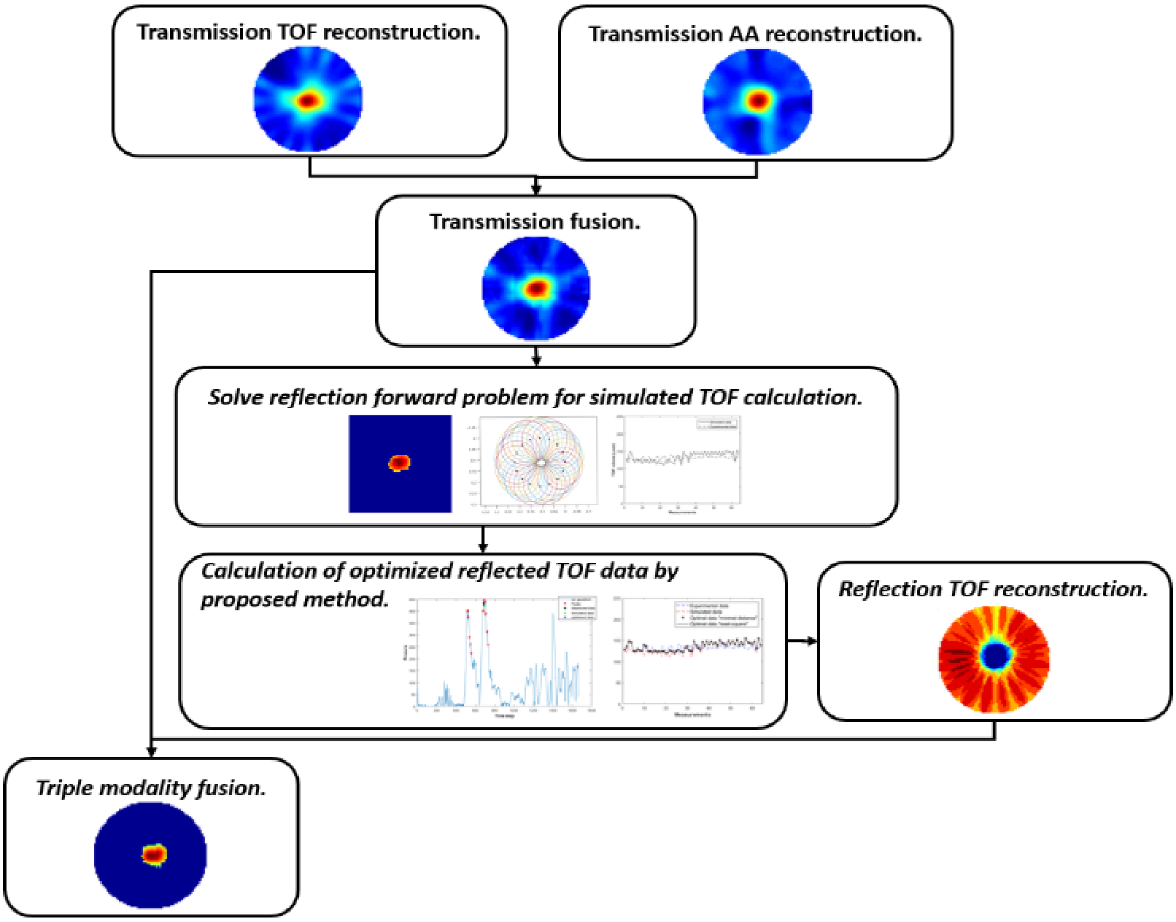

Figure 8.9. Full framework of the proposed triple-modality algorithm for the case of a circular inclusion of 20-mm diameter positioned in the centre of the ROI.

The accuracy of the transmission image in quantitative analysis and the accuracy of reflection image in the qualitative analysis result to a supreme outcome by the combination of them.

8.3. **Results and analysis**

This section has been separated in “Qualitative experiments” (8.3.1) and “Quantitative experiments” (8.3.2) subsections. At first, the system was experimentally validated by applying several single and multiple static inclusions tests with different shapes and sizes.

These tests aimed to simulate dispersed phases of a liquid mixture existing in industrial processes. The change in the structural phase aims to simulate the change happening during a crystallization or fermentation process. All the applied combination of inclusions aimed to prove supremacy in spatial resolution over previous discussed single-modality reconstruction methods. Secondly, to further test the performance of the proposed system and the multi-modality approach, different setups of water/sucrose solutions were used. These experimental scenarios simulated miscible liquids and multi-phase flow in an industrial tank scenario. The tests aimed to prove the supremacy of the quantitative travel-time imaging and the reflection imaging combination.

8.3.1. Qualitative experiments

All the inclusions are made from plastic (PVC) and are not compact; thus, the sound can only be diffracted and reflected. Circular inclusions of 1cm, 2cm and 3cm of diameter, square inclusion of 4cm side-length and an equilateral triangle inclusion of 3cm were used to provide various testing cases. Figure 8.10 presents results using different reconstruction methods of 10 different experimental configurations. Among the reconstructed methods are TOF, AA, fused transmission, “traditional” reflection, “proposed” reflection and triple-modality reconstructions. Regarding the transmission mode, the fused images are more reliable in all cases comparing to the TOF and AA images. More specifically, regarding the configurations 4, 5, 7 and 8, the AA images are better representations of the corresponding experimental topology. This leads to the conclusion of the supremacy of AA reconstructions in the multi-inclusion cases with small distances between inclusions, as TOF reconstruction fails to well represent these cases due to the acoustic behaviour (diffraction). Configuration 8 presents this. Furthermore, it is evident that transmission mode can be used in object localisation as in most cases can offer a good representation of the acoustic properties’ distributions, notably upon multiple inclusions. However, transmission mode struggles to provide a good shape recognition, as the images are more blurred in the regions of the domain’s boundaries. On the other hand, reflection is significantly better in detecting the boundaries of the domain accurately. However, reflection has a clear disadvantage in multi-inclusions cases in which it is unable to reconstruct regions that lie between two objects.

Therefore, the combination of the transmission and reflection reconstructions can be a crucial step enhancing the spatial resolution as they provide complementary information.

To quantify the imaging quality of the proposed reconstruction approach, Correlation Coefficient (CC) and Root Mean Square Error (RMSE) were calculated, eq. (8.14) and eq. (8.15) respectively. The segmentation method described in section IV. Normalisation was applied to all the images to turn them into a uniform form, aiming at quantitative similarities.

$$CC = \frac{\sum_{n=1}^{N}(\sigma_n - \delta)(\sigma_n^* - \delta^*)}{\sqrt{\sum_{n=1}^{N}(\sigma_n - \delta)^2 \sum_{n=1}^{N}(\sigma_n^* - \delta^*)^2}} \tag{8.14}$$

$$RMSE = \sqrt{\frac{\sum_{n=1}^{N}(\sigma - \sigma^*)^2}{N}} \tag{8.15}$$

where σ is the calculated acoustic distribution by the reconstruction algorithms and σ^* is the real one (true image), σ_n and σ_n^* are nth elements of σ and σ^* respectively, δ and δ^* are the mean values of σ and σ_n^* , respectively. Figure 8.11 shows the CC and the RMSE of TOF, AA, fused transmission, “traditional” reflection, “proposed” reflection and triple-modality reconstructions. In almost all the cases, the proposed algorithm proved to be more efficient by acquiring the overall highest CC and lowest RMSE value. CC was higher and RMSE was lower in single inclusion cases comparing with the multiple inclusions’ cases due to the medium’s complexity.

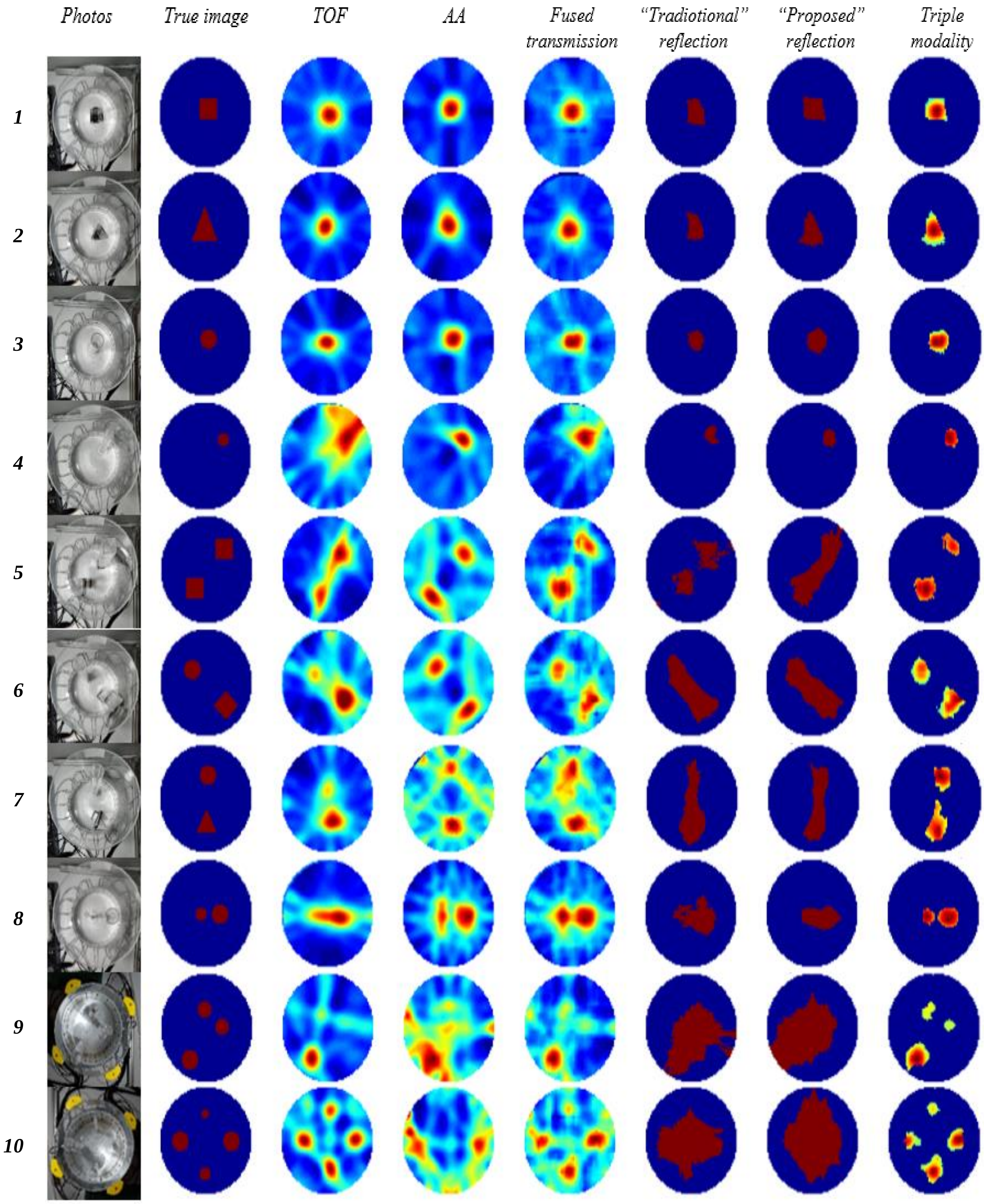

Figure 8.10. Image reconstructions of the Triple-Modality USCT.

Concluding in the supremacy of the proposed reflection algorithm, a triple modality approach was applied using TOF, AA and reflection images. The MRSE of triple-mode images is generally smaller, while CC is more prominent than all the other methods. TOF and AA images converted to binary form using a high threshold to segment the inclusions. Then transmission and reflection images were fused in binary format. Regarding CC, in almost all cases, the final image is closer to the real geometry. The significant aid of the triple modality method can clearly be noticed as, in all cases, the TOF, AA and reflection reconstructions' accuracy differs, but the triple-modality reconstruction is always higher. The qualitative difference can be noticed in multiple inclusions cases, as they consist of more complex nature. The quantitative analysis indicates that the multi-modality method provides more accurate reconstruction on both the area and the location of the objects than a single modality of either transmission or reflection mode.

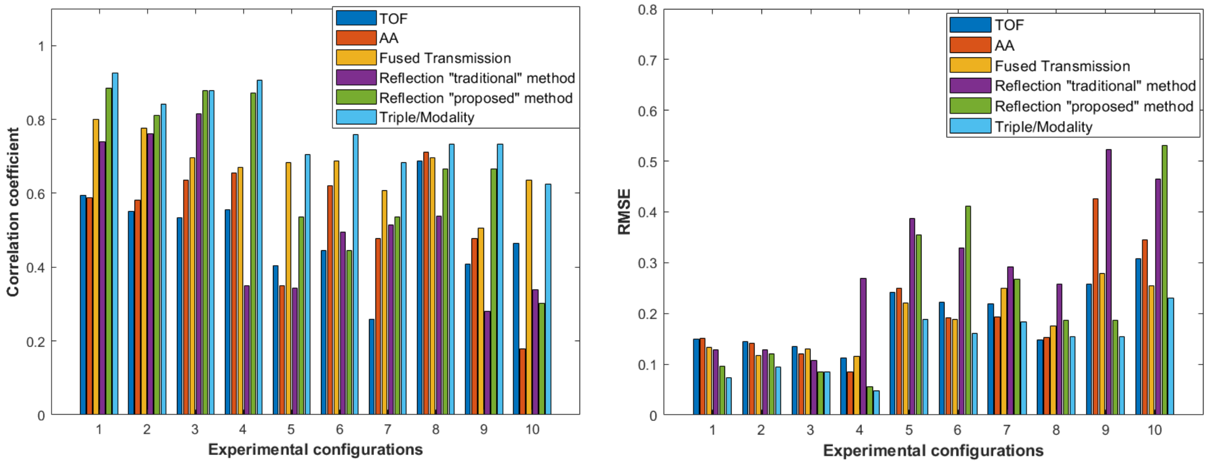

(a) **(b)**

Figure 8.11. (a) CC and (b) RMSE of several different reconstruction methods.

8.3.2. Quantitative experiments

A plastic cup of 1mm length, filled with the solutions, was used as a static inclusion. The cup's sound transmissivity has been tested and approved. The system acquired transmitted signals passed through the water/sucrose solutions and reflected signals came from the cup's surface. Figure 8.12 displays experimental photos and reconstructions of three different water/sucrose cases. Figure 8.12a shows a 60.7% solution positioned in the centre, Figure 8.12b shows a combination of 50% and 42.8%, and Figure 8.12c a combination of 20% and

42.8%. The TOF mapping distinguished well between different concentrations in multiple inclusions experiments. Furthermore, the tests TOF-delays scale follows the overall concentration increase, as shown in igure 8.12b, c. Additionally, six different single inclusions cases with water/sucrose concentrations of 20%, 33%, 42.8%, 50%, 56.7% and 60.7% were reconstructed. Table 8.2 shows the TOF delays caused due to the existence of the solution. The presented TOF-delays, calculated as the object was segmented and its mean value was calculated. Difference imaging was used by subtracting the background from the full TOF measurements. Since the sound velocity of the concentrations is higher than the medium (water in 20^{o}C), the produced difference data were negative.

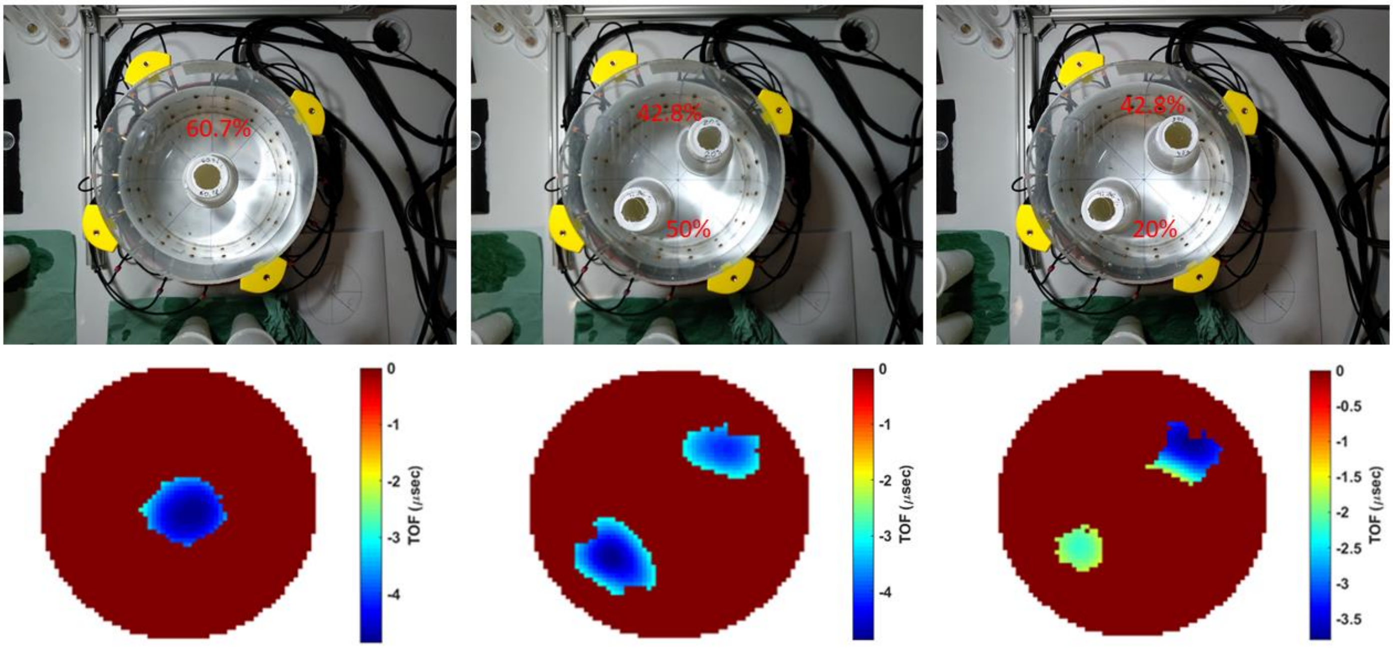

(a) **(b)** **(c)**

Figure 8.12. Experimental photos and reconstructions of water/sucrose solutions of (a) 60.7% in the centre (b) 50% down-left and 42.8% up-right (c) 20% down-left and 42.8% up-right.

Small positive values were caused by noise and therefore were neglected. TOF delays showed good response, as they form an ascending function over the increasing concentration of the solutions. The solutions experiment proved efficient in distinguishing between low changes of concentration, showing the high quantitative resolution that the system can provide.

Table 8.3 TOF delays from the experimental process with water/sucrose solutions.

Mass concentration (mass/volume)	TOF delays
20% m/vol	1.94 μs
33% m/vol	2.85 μs
42.86% m/vol	3.69 μs
50% m/vol	3.96 μs
56.52% m/vol	4.14 μs
60.78% m/vol	4.42 μs

8.4. **Conclusions**

This work presents the advantages of triple-modality ultrasound tomographic imaging for real industrial processes. Accurate results of multiple solid objects and various concentrated solutions could significantly benefit complex industrial processes of two-phase media and multi- phase interactions. Reflection and transmission reconstruction methods can work in a complementary way and provide optimal results. Moreover, acoustic attenuation measurements were proven effective, facilitating the transmission of TOF reconstructions, especially in more inhomogeneous media. So, there is great potential in the combination of two types of transmission mode tomography. This kind of rich full-waveform tomography proved to work well in exploiting full-waveform information. Without introducing heavy computational algorithms, it can benefit from combining different reconstructions and at the same time perform at a high temporal frequency. Therefore, it comprises a potential solution to many industrial processes that need inspection over time and a good temporal resolution.

The developed methods provided good qualitative and quantitative performance regarding the quality image measurements and the correlation of TOF-delays with various solutions. Static experiments showed good system performance in distinguishing objects of different sizes and shapes in single and multiple objects. The solutions used in the experiments showed that the triple-modality imaging could also use the TOF scale to characterise small changes in the density of biphasic media, which is a significant addition to the system. The results of this research show that this rich full-waveform USCT can aid industrial processes and may be used for stirred tanks chemical processes. Given the existence of biphasic media, which include integration of liquid solutions and suspensions, the added value of the multi-modality full-waveform system will become apparent in our future studies. In case of cup with multiple percentage solution both a reflection image due to the cup and a quantitative transmission image due to particle concentration can be produced.

Chapter 9 Conclusions & Future work

9.1. Conclusions

The purpose of this thesis is to present works aiming at the further development of USCT in industrial processes and especially in chemical reactor processes. USCT offers a great potential for visualizations and quantitative analysis when comparing with other IPT modalities. Its low-cost design, non-invasive and non-destructive application combined with its potential for high spatial resolution, that can be achieved using various information from the rich full-waveform signals, makes it a challenging candidate for any industrial process monitoring. An important consideration is the trade-off between spatial and temporal resolution, since chemical reactor processes usually require high temporal resolution imaging due to their fast pace of change. Indeed, USCT can offer significant spatial resolution of the ROI exploiting information of the full-waveform signal. Nevertheless, using full-waveform reconstructions can turn the system into a slow response. On the other hand, higher temporal resolution can be achieved by applying prior analogue signal processing before the data transferring to the host-computer for tomographic reconstructions. In this case, geometrical acoustic reconstruction algorithms are applied which result to a lower spatial resolution. Therefore, this thesis proposes a framework that combines multiple geometric reconstruction methods to maintain a low temporal resolution and at the same time enhance the spatial resolution. Contents of all chapters are progressively demonstrating the procedures of being gradually reach the subjects. Each chapter of this thesis equally contributes to the final target, and methods with valuable results are deeply discussed.

Chapter 1 discusses the general overview of USCT and crystallization process, where there are proposed the problems to be solved as well as the procedures in this thesis.

In **Chapter 2**, the IPT applications and USCT general applications are presented, with special focus on industrial processes and reactors.

Chapter 3 is about USCT principles and presents the basic theory of ultrasonic waves, the two USCT systems that used in the experiments the data-acquisition method and the reconstruction algorithms including forward and inverse problem. Algorithms for solving inverse problem, Hybrid Tikhonov regularization and Split Bregman Total Variation, and also regularizations aiming at temporal imaging, Spatiotemporal Total Variation method, are demonstrated.

Chapter 4 presents the proposed sound-speed imaging for liquid elaborations. It includes experimental procedure in testing the developed quantitative sound-speed reconstruction method in emulsions and immiscible liquids. The tests were conducted in 2D cross-sectional fashion of a 32x32 ring-sensor array of piezoelectric transducers of 40 kHz centre frequency and width of 2cm each one of them. USCT1.0 was used for conducting the experiments. At first the system was tested in static inclusions scenario providing good results regarding spatial resolution up to 2.8 cm. The piezoelectric sensors' width is at 2 cm and the travel-time measurements seem not to sensitive enough for detecting a single cylinder with diameter of 2.8 cm. Moreover, system's performance on multiple inclusion cases was successful. The study showed good qualitative figures. Furthermore, dynamical testing also took place with a manual-moving cylindrical object of 2.8 cm. The system proved a good data acquisition temporal resolution of 4 fps. Except of qualitative resolution, the system proved accuracy in quantitative resolution, as well. Experiments with various concentration of sucrose solutions showed a challenging quantitative system detecting distributions of solutions with a quantitative resolution step of 8 (kg/m^3) in concentrated solutions. Experiments were static and managed to result in a clear correlation between density factor and reconstructed sound-speed profiles.

Chapter 5 displays experimental procedure conducted for investigating the functionality of UTT on process tanks emulsion scenarios and more specifically on reactive precipitation. The same USCT system (USCT1.0) has been used as in Chapter's 4, using a 16x16 ring-sensor array and applying a travel-time reconstruction. The 16x16 array was chosen for better temporal resolution as the studying density distributions permits lower spatial resolution standards. Batch crystallization involves stirring process. Thus, a magnetic stirrer was used to add a certain but low level of dynamics to the tank. As this work was focused on the suspension density on live process experiments, we chose a more simplistic approach using the magnetic stirrer instead of a stirring propeller which would add significant disturbances to the system. The device displayed good response in distinguishing between liquid solutions and crystalline liquid suspensions testing suspensions of various crystalline concentrations. Experiments also included calcium carbonate reactive precipitation. The proposed system proved that can be considered as a challenging alternative by promising potential of travel-time ultrasound tomography not only for monitoring the process by detecting and reconstructing regions with higher crystalline particle concentration but also for quantifying the different forms of crystalline suspensions by utilising the scale of the travel-time delays. Therefore, it was introduced as a potential assurance control tool for batch crystallization.

Chapter 6 presents a study designed to investigate the functionality of batch crystallization aligned with industrial standards. The reactive precipitation of calcium carbonate used, as in Chapter 5. Also, shear mixing was used by utilising flat-blade propeller of 200rpms. The USCT3.0 system was used in this study providing a centre frequency of 400 kHz was used. A high frequency more directive signal could not be affected significantly by stirring noise. The system was set to “transmission mode” which leads to a data acquisition temporal resolution of 4 fps. In this study TOF and AA data were used. Both, the two types of reconstructions offered similar results but AA quantitative plots over live-process experiments were more sensitive than TOF, especially on malfunction detection. Both, of them proved accuracy in distinguishing between different particle concentration levels of floating suspensions. The major events on the process, such as feeding, and switching on and off the pumps and the stirrer, could be seen in the data, making a clear proof of the system’s function as assurance control tool. Furthermore, a clear indication that the USCT tool can be used to monitor batch-wise processes noninvasively was shown.

Chapter 7 presents the extension of 2D travel-time transmission tomography into 3D model. The USCT3.0 system was used with a centre frequency of 400 kHz and a data acquisition temporal resolution of 4 fps. The 3D setup consisted of two ring-sensor arrays of 16 transducers each one of them. Static experiments were tested using different number and shapes of inclusions; successfully reconstructing inclusions of up to 2 cm. Dynamical experiments were also conducted including experiments with manual-shifting objects to test the temporal resolution of the device. The challenging nature of these experiments can reveal the accuracy of the proposed methods. Finally, crystallization experiments conducted aiming at 4D monitoring and a spatial-temporal 3D Total Variation regularization applied as well. The applied algorithm has been priorly applied to tomographic 4D studies with significant advantages. The 3D imaging proved to be more informative than the 2D as it responded well to specific tests that includes variations in the z-axis (height) which was the dimension of extension from the 2D system. Moreover, dynamical experiments were conducted

Chapter 8 presents the proposed multi-modality ultrasound tomography reconstruction framework based on geometrical acoustics. The new developed reconstruction method is based on full-waveform signal acquisition. The USCT3.0 system was used for this study set up to “full-waveform” mode. The method combines multiple signal’s information including transmission amplitude and time-of-flight and reflection time-of-flight. The study uses the USCT.3 system accounting for frequencies of 400 kHz. The test included static reconstruction of multiple objects providing refined results compared to the individual single-modalities reconstruction. The aim was to enhance image quality by combining multiple analytic reconstruction methods rather than developing a full-scale full-waveform reconstruction methods, which would be computationally demanding. Especially industrial processes that are very sensitive to time are in need of fast reconstruction algorithms. In the specific case of crystallization, transmission method showed applicability and reflection method is considered to aid the reconstructions when localised super-saturated suspensions may be formed due to process malfunction e.g., stirrer malfunction. In this case, a drastic material phase difference may occur. Thereafter, reflection mode might be used as a malfunction detection by detecting the localised high concentrated suspensions. It would be also possible to detect complex dynamic phenomena such as a gas-flow or vortexes coming from a high stirring effect.

9.2. **Future work**

In this thesis, USCT for process tanks monitoring and more specifically for batch crystallization was investigated. First the basic framework of quantitative imaging was built and tested in 2D fashion. Then specific experiments were carried out aiming at functionality on crystallization monitoring and forming suspensions detection. As a continuation, the integrated 2D USCT system and algorithm were tested in shear mixing and particle concentrations and in lab-scale batch crystallization apparatus aligned with industrial standards. A 3D travel-time USCT reconstruction was developed and tested in batch crystallization showing similar features with 2D monitoring and expanding the monitoring in axial direction. A novel spatiotemporal 3D TV method was applied. Finally, a triple-modality reconstruction framework was developed and presented in 2D fashion. The proposed reconstruction method showed optimization process and can be a significant tool for further developments in industrial USCT. The main advantage is that by combining multiple geometric acoustics reconstructions, the algorithm's complexity retains to a significant low level comparing to full-waveform reconstruction methods. However, future works are still required for reaching the final target of being a mature technique in practice applications. In addition, this research can also be developed into more potential applications apart from batch crystallization. A list of further works and applications are suggested below:

- Relation with CSD measurements

Avery interesting subject would be the continuation of the tomographic studies in crystallization methods and the specification of the formulas describing the sound velocity and the crystal size distributions. A tomographic method cannot directly monitor crystals, instead the measurements are sensitive in the suspension density factor. Our work has extensively shown the USCT capabilities in characterizing slurries. In that way, future studies could aim in approximating relative CSD measurements by correlating the density suspension or other information.

- Higher frequencies investigation on crystallization

The effect of frequency in the work can be studied further. Higher excitation frequencies own higher level of signal's transmittivity. Higher frequencies studies in medical imaging have been shown better accuracy in distinguishing tiny lesions.

- Expansion of triple-modality algorithm. in 3D fashion.

Further investigation on crystallization phases, malfunctions and ultrasound reflections is to be considered. Furthermore, given the optimization that the 2D triple-modality offered, the expansion into a 3D model would be a significant contribution.

- Multi-modality tomography combining different measurement methods.

A suggested in our work [93] dual-modality tomographic methods can significantly improve the outcomes of single modalities, especially in industrial process applications and other complex processes. The use of USCT combined with other tomographic modalities has to be studied further in crystallization processes. For instance, an ERT application in crystallization can be seen in this work [285]. Our work [73] addresses a simulation study of multimodality USCT-ERT on semi-batch crystallization process control.

- Control with temporal TV algorithm

Tomography-based control system can potential developed in the future. In industrial process, quantitative parameter is important. For example, monitoring of oil-water two phase flow can reflect information relating with, for instance, water disposal or reinjection. For purpose of control, a real-time modality with high time response is required. Based on the discoveries of temporal TV algorithm showing good time response, it could potential be applied to be a real-time visualization technique for exploiting information from the objectives and reflect quantitative factors for purposes of control.

References

[1] S. Siltanen, T. Lokki, and L. Savioja, “Rays or Waves? Understanding the Strengths and Weaknesses of Computational Room Acoustics Modeling Techniques” Proceedings of the International symposium on room acoustics, 2010.

[2] F. Kühn, “Ultrasound medical imaging using 2d viscoacoustic full-waveform inversion”, MSc Thesis, Kalsruhe Institute of Technology, 2018.

[3] M. Pérez-Liva, J. L. Herraiz, J. M. Udías, E. Miller, B. T. Cox, and B. E. Treeby, “Time domain reconstruction of sound speed and attenuation in ultrasound computed tomography using full wave inversion” J. Acoust. Soc. Am., vol. 141, no. 3, pp. 1595–1604, Mar. 2017.

[4] R. Stotzka et al., "Prototype of a new 3D ultrasound computer tomography system: transducer design and data recording", Proc. SPIE 5373, Medical Imaging 2004: Ultrasonic Imaging and Signal Processing, April 2004.

[5] O. Roy, I. Jovanović, A. Hormati, R. Parhizkar, and M. Vetterli, “Sound speed estimation using wave-based ultrasound tomography: theory and GPU implementation” Med. Imaging 2010 Ultrason. Imaging, Tomogr. Ther., vol. 7629, p. 76290J, 2010.

[6] A. Hormati, I. Jovanović, O. Roy, and M. Vetterli, “Robust ultrasound travel-time tomography using the bent ray model,” in Medical Imaging 2010: Ultrasonic Imaging, Tomography, and Therapy, vol. 7629, p. 76290I, 2010.

[7] M. Perez-Liva, J. L. Herraiz, J. M. Udias, B. T. Cox, and B. E. Treeby, “Full-wave attenuation reconstruction in the time domain for ultrasound computed tomography” Proc. - Int. Symp. Biomed. Imaging, vol. 2016-June, pp. 710–713, 2016.

[8] K. Wang, T. Matthews, F. Anis, C. Li, N. Duric, and M. Anastasio, “Waveform inversion with source encoding for breast sound speed reconstruction in ultrasound computed tomography” IEEE Trans. Ultrason. Ferroelectr. Freq. Control, vol. 62, no. 3, pp. 475–493, 2015.

[9] A. Fhager and M. Persson, “Comparison of two image reconstruction algorithms for microwave tomography,” Radio Sci., vol. 40, no. 3, pp. 1–15, 2005.

[10] N. V Ruiter R. Stotzka T. O Muller R. Liu G. Schwarzenberg and H. Gemmeke. "State of The A rt and Challenges in Ultrasound Computer Tomography". The 3rd European Medical and Biological Engineering Conference EMBEC. Nov 20-25 Prague Czech Republic, 2005.

[11] P. Lasaygues, R. Guillermin, J. Lefebvre. "Ultrasonic Computed Tomography." P. Laugier, G. Haiat. Bone Quantitative Ultrasound, Springer, pp.441-459, 2010.

[12] S. Bernard, V. Monteiller, D. Komatitsch, and P. Lasaygues, “Ultrasonic computed tomography based on full-waveform inversion for bone quantitative imaging,” Phys. Med. Biol., vol. 62, no. 17, pp. 7011–7035, Aug. 2017.

[13] M. P. Shortell, M. A. M. Althomali, M. L. Wille, and C. M. Langton, “Combining ultrasound pulse-echo and transmission computed tomography for quantitative imaging the cortical shell of long-bone replicas,” Front. Mater., vol. 4, no. November, pp. 1–8, 2017.

[14] P. Lasaygues, “Assessing the cortical thickness of long bone shafts in children, using two-

dimensional ultrasonic diffraction tomography," Ultrasound Med. Biol., vol. 32, no. 8, pp. 1215–1227, 2006.

[15] E. Ouedraogo, P. Lasaygues, J. P. Lefebvre, M. Gindre, M. Talmant, and P. Laugier, "Contrast and velocity ultrasonic tomography of long bones" Ultrason. Imaging, vol. 24, no. 3, pp. 139–160, 2002.

[16] S. Roecker, B. Baker, and J. McLaughlin, "A finite-difference algorithm for full waveform teleseismic tomography" Geophys. J. Int., vol. 181, no. 2, pp. 1017–1040, 2010.

[17] S. Butzer, "3D elastic time-frequency full-waveform inversion.", PhD Thesis, Kalsruhe Institute of Technology, 2015.

[18] E. Treister and E. Haber, "Full waveform inversion guided by travel time tomography" SIAM J. Sci. Comput., 39(5), S587–S609, 2016.

[19] S. Husen and E. Kissling, "Local earthquake tomography between rays and waves: Fat ray tomography," Phys. Earth Planet. Inter., vol. 125, no. 1–4, pp. 171–191, 2001.

[20] X. Bao and Y. Shen, "Full-Waveform Sensitivity Kernels of Component-Differential Traveltimes and ZH Amplitude Ratios for Velocity and Density Tomography," J. Geophys. Res. Solid Earth, vol. 123, no. 6, pp. 4829–4840, Jun. 2018.

[21] X. Wang and X. Liu, "3-D acoustic wave equation forward modeling with topography." Appl. Geophys., vol. 4, no. 1, pp. 8–15, Mar. 2007.

[22] J. Tromp, C. Tape, and Q. Liu, "Seismic tomography, adjoint methods, time reversal and ppik-doughnut kernels," Geophys. J. Int., vol. 160, no. 1, pp. 195–216, Jan. 2005.

[23] Y. A. Chepurin, "Experiments on underwater acoustic tomography." Acoust. Phys., vol. 53, no. 3, pp. 393–416, 2007.

[24] B. M. Howe, J. Miksis-Olds, E. Rehm, H. Sagen, P. F. Worcester, and G. Haralabus, "Observing the oceans acoustically," Front. Mar. Sci., vol. 6, no. JUL, pp. 1–22, 2019.

[25] A. Goodney and Y. H. Cho, "Acoustic tomography with an underwater sensor network" Sea Technol., vol. 54, no. 7, pp. 33–37, 2013.

[26] V. K. Aatre, "Underwater Acoustic Tomography.," Def. Sci. J., vol. 35, no. 2, pp. 151–161, 198.

[27] N. Li, M. Cao, K. Xu, J. Jia, and H. Du, "Ultrasonic transmission tomography sensor design for bubble identification in gas-liquid bubble column reactors" Sensors (Switzerland), vol. 18, no. 12, 2018.

[28] R. A. Rahim, M. H. F. Rahiman, and M. N. Mohd Taib, "Non-invasive ultrasonic tomography: Liquid/gas flow visualization," 2005 1st Int. Conf. Comput. Commun. Signal Process. with Spec. Track Biomed. Eng. CCSP 2005, pp. 243–247, 2005.

[29] S. Langener, M. Vogt, H. Ermert, and T. Musch, "A real-time ultrasound process tomography system using a reflection-mode reconstruction technique" Flow Meas. Instrum., vol. 53, pp. 107–115, Mar. 2017.

[30] C. Tan, X. Li, H. Liu, and F. Dong, "An Ultrasonic Transmission/Reflection Tomography System for Industrial Multiphase Flow Imaging" IEEE Trans. Ind. Electron., pp. 1–1, Jan. 2019.

[31] T. T. Flow, “Parallel Image Reconstruction in Real-Time Ultrasound Process,” Electr. Eng., vol. 303, no. 1997, pp. 295–303, 1997.

[32] D. L. Núñez, M. Á. Molero-Armenta, M. Á. G. Izquierdo, M. G. Hernández, and J. J. A. Velayos, “Ultrasound transmission tomography for detecting and measuring cylindrical objects embedded in concrete” Sensors (Switzerland), vol. 17, no. 5, May 2017.

[33] M. Schickert, “Progress in ultrasonic imaging of concrete” Mater. Struct. Constr., vol. 38, no. 283, pp. 807–815, 2005.

[34] M. Słoński, K. Schabowicz, and E. Krawczyk, “Detection of flaws in concrete using ultrasonic tomography and convolutional neural networks” Materials (Basel)., vol. 13, no. 7, pp. 1–16, 2020.

[35] J. L. Rose, “Exhibition on Non-Destructive Evaluation Successes and Challenges in Ultrasonic Guided Waves for NDT and SHM” Proc. Natl. Semin. Exhib. Non-Destructive Eval., 2009.

[36] H. I. Schlaberg, F. J. W. Podd, and B. S. Hoyle, “Ultrasound process tomography system for hydrocyclones,” Ultrasonics, vol. 38, no. 1, pp. 813–816, 2000.

[37] A. C. Essed, “Modeling of Membrane Distillation assisted Crystallization", Msc Thesis, Delft University of Technology , 2015.

[38] M. Rushdi, “Process Analytical Technology Based Approaches for the Monitoring and Control of Size and Polymorphic Form in Pharmaceutical Crystallisation Processes” CEUR Workshop Proc., vol. 1542, no. 9, 2010.

[39] J. Ulrich and M. J. Jones, “Industrial Crystallization: Developments in Research and Technology” Chem. Eng. Res. Des., vol. 82, no. 12, pp. 1567–1570, 2004.

[40] Strege, C., On (pseudo) polymorphic phase transformations, Ph. D. Thesis, Martin Luther university Halle-Wittenberg, Germany, 2004.

[41] J. S. Wey and P. H. Karpinski, “Handbook of Industrial Crystallization: Chapter 10- Batch crystallization,” Batch Cryst., vol. 67, no. 110, pp. 231–248, 2002.

[42] J. Ulrich and C. Strege, “Some aspects of the importance of metastable zone width and nucleation in industrial crystallizers” J. Cryst. Growth, vol. 237–239, pp. 2130–2135, 2002.

[43] S. Titiz-Sargut and J. Ulrich, “Application of a protected ultrasound sensor for the determination of the width of the metastable zone,” Chem. Eng. Process. Process Intensif., vol. 42, no. 11, pp. 841–846, 2003.

[44] Mullin, J.W., 2001. "Crystallisation, 4th edition" Organic Process Research & Development, 6 (2), 201–202.

[45] E. Lopez-Quiroga, R. Wang, O. Gouseti, P. J. Fryer, and S. Bakalis, “Crystallisation in concentrated systems: A modelling approach” Food Bioprod. Process., vol. 100, pp. 525–534, 2016.

[46] K. A. Berglund, “4 - Analysis and measurement of crystallization utilizing the population balance” in Handbook of Industrial Crystallization (Second Edition), Second Edi., A. S. Myerson, Ed. Woburn: Butterworth-Heinemann, pp. 101–113, 2002.

[47] R. Lin, S. Y. J. Chen, V. Mor-Avi, J. Bednarz, C. T. Chen, and R. M. Lang, “Three-dimensional

reconstruction of LV endocardial surfaces from echocardiographic images using deformable shell models” Comput. Cardiol., vol. 0, no. 0, pp. 697–700, 1996.

[48] M. Mostafavi, “In-line/on-line measuring techniques in the solution crystallization processes,” PhD Thesis, der Martin-Luther-Universität, 2015.

[49] E. Simone, A. N. Saleemi, and Z. K. Nagy, “In situ monitoring of polymorphic transformations using a composite sensor array of Raman, NIR, and ATR-UV/vis spectroscopy, FBRM, and PVM for an intelligent decision support system” Org. Process Res. Dev., vol. 19, no. 1, pp. 167–177, 2015.

[50] L. Liu, R.F. Li, S. Collins, X.Z. Wang, R. Tweedie, K. Primrose, "Ultrasound spectroscopy and electrical resistance tomography for online characterisation of concentrated emulsions in crossflow membrane emulsifications" Powder Technology, Volume 213, Issues 1–3, pp. 123-131, 2011.

[51] F. Lewiner, G. Févotte, J. P. Klein, and F. Puel, “Improving batch cooling seeded crystallization of an organic weed-killer using on-line ATR FTIR measurement of supersaturation” J. Cryst. Growth, vol. 226, no. 2, pp. 348–362, 2001.

[52] L. L. Simon, Z. K. Nagy, and K. Hungerbuhler, “Comparison of external bulk video imaging with focused beam reflectance measurement and ultra-violet visible spectroscopy for metastable zone identification in food and pharmaceutical crystallization processes” Chem. Eng. Sci., vol. 64, no. 14, pp. 3344–3351, 2009.

[53] J. Cornel and M. Mazzotti, “Calibration-free quantitative application of in situ Raman spectroscopy to a crystallization process” Anal. Chem., vol. 80, no. 23, pp. 9240–9249, 2008.

[54] J. A. Falcon and K. A. Berglund, “Monitoring of Antisolvent Addition Crystallization with Raman Spectroscopy” Cryst. Growth Des., vol. 3, no. 6, pp. 947–952, 2003.

[55] Q. Hu, S. Rohani, D. X. Wang, and A. Jutan, “Optimal control of a batch cooling seeded crystallizer,” Powder Technol., vol. 156, no. 2–3, pp. 170–176, 2005.

[56] G. Févotte, “In situ Raman spectroscopy for in-line control of pharmaceutical crystallization and solids elaboration processes: A review” Chem. Eng. Res. Des., vol. 85, no. 7 A, pp. 906–920, 2007.

[57] T. Stelzer, D. Pertig, and J. Ulrich, “Ultrasonic crystallization monitoring technique for simultaneous in-line measurement of liquid and solid phase,” J. Cryst. Growth, vol. 362, no. 1, pp. 71–76, 2013.

[58] P. Sessiecq, F. Gruy, and M. Cournil, “Study of ammonium chloride crystallization in a mixed vessel,” J. Cryst. Growth, vol. 208, no. 1, pp. 555–568, 2000.

[59] L. Helmdach, M. P. Feth, and J. Ulrich, “Application of ultrasound measurements as pat tools for industrial crystallization process development of pharmaceutical compounds” Org. Process Res. Dev., vol. 19, no. 1, pp. 110–121, 2015.

[60] L. Helmdach, F. Schwartz, and J. Ulrich, “Process Control Using Advanced Particle Analyzing Systems: Applications from Crystallization to Fermentation Processes” Chem. Eng. Technol., vol. 37, no. 2, pp. 213–220, 2014.

[61] A. K. Hipp, B. Walker, M. Mazzotti, and M. Morbidelli, “In-situ monitoring of batch

crystallization by ultrasound spectroscopy" Ind. Eng. Chem. Res., vol. 39, no. 3, pp. 783–789, 2000.

[62] D. Pertig, R. Buchfink, S. Petersen, T. Stelzer, and J. Ulrich, "Inline analyzing of industrial crystallization processes by an innovative ultrasonic probe technique" Chem. Eng. Technol., vol. 34, no. 4, pp. 639–646, 2011.

[63] H. Glade, A. M. Ilyaskarov, and J. Ulrich, "Determination of crystal growth kinetics using ultrasonic technique," Chem. Eng. Technol., vol. 27, no. 7, pp. 736–740, 2004.

[64] Y. Zhao, J. Yao, and M. Wang, "On-line monitoring of the crystallization process: Relationship between crystal size and electrical impedance spectra," Meas. Sci. Technol., vol. 27, no. 7, 2016.

[65] S. D. M. Jacques, K. Pile, P. Barnes, X. Lai, K. J. Roberts, and R. A. Williams, "An in-situ synchrotron X-ray diffraction tomography study of crystallization and preferred crystal orientation in a stirred reactor" Cryst. Growth Des., vol. 5, no. 2, pp. 395–397, 2005.

[66] P. Mougin et al., "On-line monitoring of a crystallization process," AIChE J., vol. 49, no. 2, pp. 373–378, 2003.

[67] T. Marshall, J. S. Tebbutt, and R. E. Challis, "Monitoring the crystallization from solution of a reactive dye by ultrasound," Meas. Sci. Technol., vol. 11, no. 5, pp. 509–517, 2000.

[68] Q. Wang, M. Wang, K. Wei, and C. Qiu, "Visualization of Gas – Oil – Water Flow in Horizontal Pipeline Using Dual-Modality Electrical Tomographic Systems," vol. 17, no. 24, pp. 8146–8156, 2017.

[69] K. Wei, C. H. Qiu, and K. Primrose, "Super-sensing technology: Industrial applications and future challenges of electrical tomography" Philos. Trans. R. Soc. A Math. Phys. Eng. Sci., vol. 374, no. 2070, 2016.

[70] V. Stolojanu and A. Prakash, "Characterization of slurry systems by ultrasonic techniques" Chem. Eng. J., vol. 84, no. 3, pp. 215–222, Dec. 2001.

[71] M. S. Greenwood, "Particle size and density of a slurry from ultrasonic backscattering measurements at a solid interface," Review of Scientific Instruments, vol. 83, no. 9. Sep. 2012.

[72] K. Shikha Ojha, Timothy J. Mason, Colm P. O'Donnell, Joseph P. Kerry, Brijesh K. Tiwari,Ultrasound technology for food fermentation applications, Ultrasonics Sonochemistry, Volume 34, pp. 410-417, 2017.

[73] V. Stolojanu and A. Prakash, "Characterization of slurry systems by ultrasonic techniques," Chem. Eng. J., vol. 84, no. 3, pp. 215–222, 2001.

[74] Silva RC. Experimental Characterization Techniques for Solid-Liquid Slurry Flows in Pipelines: A Review. *Processes*. 10(3):597, 2022.

[75] D. J. Mcclements, "Ultrasonic Measurements in Particle Size Analysis", Encyclopedia of Analytical Chemistry (R.A. Meyers), John Wiley and Sons, pp. 1–8, 2000.

[76] M. J. W. Povey, "Ultrasound particle sizing: A review" Particuology, vol. 11, no. 2, pp. 135–147, 2013.

[77] G. Rao, S. Aghajanian, T. Koiranen, R. Wajman, and L. Jackowska-Strumiłło, "Process

monitoring of antisolvent based crystallization in low conductivity solutions using electrical impedance spectroscopy and 2-D electrical resistance tomography” Appl. Sci., vol. 10, no. 11, 2020.

[78] K. M. Primrose, “Applications of electrical tomography to improve the performance of crystallization, precipitation and mixing processes” J. South. African Inst. Min. Metall., vol. 108, no. 10, pp. 591–596, 2008.

[79] D. V. Gradov, G. González, M. Vauhkonen, A. Laari, and T. Koiranen, “Experimental investigation of reagent feeding point location in a semi-batch precipitation process,” Chem. Eng. Sci., vol. 190, pp. 361–369, 2018.

[80] M. V. Sardeshpande, G. Kumar, T. Aditya, and V. V. Ranade, “Mixing studies in unbaffled stirred tank reactor using electrical resistance tomography” Flow Meas. Instrum., vol. 47, pp. 110–121, 2016.

[81] J. J. Ford, T. J. Heindel, and T. C. Jensen, “Imaging a gas-sparged stirred-tank reactor with X-ray CT,” 2007 Proc. 5th Jt. ASME/JSME Fluids Eng. Summer Conf. FEDSM 2007, vol. 1 SYMPOSIA, no. PART A, pp. 445–452, 2007.

[82] S. Hosseini, D. Patel, F. Ein-Mozaffari, and M. Mehrvar, “Study of solid–liquid mixing in agitated tanks through electrical resistance tomography” Chem. Eng. Sci., vol. 65, no. 4, pp. 1374–1384, Feb. 2010.

[83] D. Patel, F. Ein-Mozaffari, and M. Mehrvar, “Using tomography technique to characterize the continuous-flow mixing of non-newtonian fluids in stirred vessels” Chem. Eng. Trans., vol. 32, no. 2003, pp. 1465–1470, 2013.

[84] G. T. Bolton and K. M. Primrose, “An overview of electrical tomographic measurements in pharmaceutical and related application areas” AAPS PharmSciTech, vol. 6, no. 2, pp. E137–E143, Jan. 2006.

[85] P. Koulountzios, T. Rymarczyk, and M. Soleimani, “Ultrasonic Tomography for automated material inspection in liquid masses” 9th World Congr. Ind. Process Tomogr. WCIPT9, Sep 2018, pp. 693–702, 2018.

[86] P. Koulountzios, T. Rymarczyk, and M. Soleimani, “A quantitative ultrasonic travel-time tomography to investigate liquid elaborations in industrial processes” Sensors (Switzerland), vol. 19, no. 23, 2019.

[87] P. Koulountzios, T. Rymarczyk, and M. Soleimani, “Ultrasonic time-of-flight computed tomography for investigation of batch crystallisation processes” Sensors (Switzerland), vol. 21, no. 2, pp. 1–19, Jan. 2021.

[88] P. Koulountzios, T. Rymarczyk, and M. Soleimani, “Handwriting With Sound-Speed Imaging Using Ultrasound Computed Tomography” IEEE Sensors Lett., vol. 5, no. 10, pp. 1–3, 2021.

[89] P. Koulountzios, S. Aghajanian, T. Rymarczyk, T. Koiranen, M. Soleimani. "An Ultrasound Tomography Method for Monitoring CO2 Capture Process Involving Stirring and CaCO3 Precipitation". Sensors (Switzerland), vol. 21, no. 21:6995, 2021.

[90] P. Koulountzios, T. Rymarczyk and M. Soleimani, "A 4-D Ultrasound Tomography for Industrial Process Reactors Investigation" in IEEE Transactions on Instrumentation and Measurement,

vol. 71, pp. 1-14, 2022, Art no. 4502714.

[91] P. Koulountzios, T. Rymarczyk and M. Soleimani, "A Triple-Modality Ultrasound Computed Tomography Based on Full-Waveform Data for Industrial Processes" in IEEE Sensors Journal, vol. 21, no. 18, pp. 20896-20909, 15 Sept.15, 2021.

[92] S. Aghajanian, G. Rao, P. Koulountzios, L. Jackowska-Strumillo, M. Soleimani, and T. Koiranen, “Towards real-time control of a semibatch crystallization process by electrical and ultrasound tomographic techniques” Chem. Eng. Trans., vol. 86, pp. 307–312, 2021.

[93] X. Duan, P. Koulountzios, and M. Soleimani, “Dual Modality EIT-UTT for Water Dominate Three-Phase Material Imaging,” IEEE Access, vol. 8, pp. 14523–14530, 2020.

[94] M. S. Beck and R. A. Williams, “Process tomography: A European innovation and its applications” Meas. Sci. Technol., vol. 7, no. 3, pp. 215–224, 1996.

[95] N. A. Zulkiflli et al., “Ultrasound Tomography Hardware System for Multiphase Flow Imaging” Proc. 2019 IEEE Int. Conf. Signal Image Process. Appl. ICSIPA 2019, pp. 264–268, 2019.

[96] J. Bond et al., “Industrial monitoring of hydrocyclone operation using electrical resistance tomography” 1st World Congr. Ind. Process Tomogr., vol. 12, no. 10, pp. 102–107, 1999.

[97] T. A. York, J. L. Davidson, L. Mazurkiewich, R. Mann and B. D. Grieve, "Towards process tomography for monitoring pressure filtration" in IEEE Sensors Journal, vol. 5, no. 2, pp. 139-152, April 2005.

[98] T. Dyakowski et al., “Imaging nylon polymerisation processes by applying electrical tomography” 1st World Congr. Ind. Process Tomogr., pp. 383–387, 1999.

[99] M. Gasulla, J. Jordana, and R. Pallás-Areny, “2D and 3D subsurface resistivity imaging using a constrained least-squares algorithm” 1st World Congr. Ind. Process Tomogr., no. January, pp. 20–27, 1999.

[100] M. Wang and J. J. Cilliers, “Detecting non-uniform foam density using electrical resistance tomography” Chem. Eng. Sci., vol. 54, no. 5, pp. 707–712, 1999.

[101] A. Laari, T. Koiranen, M. Vauhkonen, G. González, and D. V. Gradov, “Experimental and Numerical Study of Multiphase Mixing Hydrodynamics in Batch Stirred Tank Applied to Ammoniacal Thiosulphate Leaching of Gold” J. Chem. Eng. Process Technol., vol. 08, no. 03, 2017.

[102] D. M. Scott and O. W. Gutsche, “ECT studies of bead fluidization in vertical mills” 1st World Congr. Ind. Process Tomogr., pp. 90–95, 1999.

[103] A. J. Jaworski and T. Dyakowski, “Application of electrical capacitance tomography for measurement of gas-solids flow characteristics in a pneumatic conveying system,” Meas. Sci. Technol., vol. 12, no. 8, pp. 1109–1119, 2001.

[104] R. Deloughry, M. Young, E. Pickup, and L. Barratt, “Development of a variable density flowmeter for an industrial application,” 1st World Congr. Ind. Process Tomogr., pp. 236–243, 1999.

[105] R. C. Waterfall, R. He, P. Wolanski, and Z. Gut, “Monitoring flame position and stability in combustion cans using ECT” 1st World Congr. Ind. Process Tomogr., pp. 35–38, 1999.

[106] H. Wang and W. Yang, "Application of electrical capacitance tomography in pharmaceutical fluidised beds – A review" Chem. Eng. Sci., vol. 231, p. 116236, 2021.

[107] L. Ma, S. Spagnul, and M. Soleimani, "Metal Solidification Imaging Process by Magnetic Induction Tomography" Sci. Rep., vol. 7, no. 1, pp. 1–11, 2017.

[108] L. De Chiffre, S. Carmignato, J. P. Kruth, R. Schmitt, and A. Weckenmann, "Industrial applications of computed tomography" CIRP Ann. - Manuf. Technol., vol. 63, no. 2, pp. 655–677, 2014.

[109] Z. Du, Y. Hu, N. Ali Buttar, and A. Mahmood, "X-ray computed tomography for quality inspection of agricultural products: A review," Food Sci. Nutr., vol. 7, no. 10, pp. 3146–3160, 2019, doi: 10.1002/fsn3.1179.

[110] R. Seidl, "Full Waveform Inversion for Ultrasonic Nondestructive Testing.", 2018.

[111] P. Ingleby and W. M. D. Wright, "Ultrasonic imaging in air using fan-beam tomography and electrostatic transducers," in Ultrasonics, May 2002, vol. 40, no. 1–8, pp. 507–511.

[112] C. Li, N. Duric, and L. Huang, "Breast imaging using transmission ultrasound: Reconstructing tissue parameters of sound speed and attenuation" Biomed. Eng. Informatics New Dev. Futur. - Proc. 1st Int. Conf. Biomed. Eng. Informatics, BMEI 2008, vol. 2, pp. 708–712, 2008.

[113] J. R. Street, "Breast Imaging Using Transmission Ultrasound: Reconstructing Tissue Parameters of Sound Speed and Attenuation" pp. 1632–1636, 2008.

[114] N. Duric and P. Littrup, "Breast Ultrasound Tomography," Breast Imaging, InTechOpen, 2018.

[115] J. Nebeker and T. R. Nelson, "Breast sound speed tomography from B-mode data" Proc. - IEEE Ultrason. Symp., pp. 2344–2347.

[116] Y. Quan and L. Huang, "Sound-speed tomography using first-arrival transmission ultrasound for a ring array," vol. 6513, no. 650, p. 651306.

[117] K. Wang, T. Matthews, F. Anis, C. Li, N. Duric, and M. Anastasio, "Waveform inversion with source encoding for breast sound speed reconstruction in ultrasound computed tomography" IEEE Trans. Ultrason. Ferroelectr. Freq. Control, vol. 62, no. 3, pp. 475–493, 2015.

[118] D. L. Núñez, M. Á. Molero-Armenta, M. Á. G. Izquierdo, M. G. Hernández, and J. J. A. Velayos, "Ultrasound transmission tomography for detecting and measuring cylindrical objects embedded in concrete" Sensors (Switzerland), vol. 17, no. 5, 2017.

[119] E. F. Oliveira, C. C. Dantas, D. A. A. Vasconcelos, and F. Cadiz, "Comparison Among Tomographic Reconstruction Algorithms With a Limited Data" Int. Nucl. Atl. Conf. - Ina., 2011.

[120] A. Lorenzi, L. A. Reginato, R. B. Fávero, L. Carlos, and S. Filho, "3D Ultrasonic Tomography Technique as a tool to Evaluate Concrete Structures.", e-Journal of Nondestructive Testing (NDT) ISSN 1435-4934, Issue: 2016-10, 2016.

[121] S. Langener, T. Musch, H. Ermert, and M. Vogt, "Simulation of full-angle ultrasound process tomography with two-phase media using a ray-tracing technique" IEEE Int. Ultrason. Symp. IUS, pp. 57–60, 2014.

[122] T. Rymarczyk and J. Sikora, "Applying industrial tomography to control and optimization flow systems" Open Phys., vol. 16, no. 1, pp. 332–345, 2018.

[123] M. H. F. Rahiman, R. A. Rahim, and Z. Zakaria, “Design and modelling of ultrasonic tomography for two-component high-acoustic impedance mixture” Sensors Actuators, A Phys., vol. 147, no. 2, pp. 409–414, Oct. 2008.

[124] M. Yang, H. I. Schlaberg, B. S. Hoyle, M. S. Beck, and C. Lenn, “Parallel Image Reconstruction in Real-Time Ultrasound Process Tomography for Two-phased Flow Measurements” Real-Time Imaging, vol. 3, no. 4, pp. 295–303, Oct. 2002.

[125] F. Wiegand and B. S. Hoyle, “Simulations for Parallel Processing of Ultrasound Reflection-Mode Tomography with Applications to Two-Phase Flow Measurement” IEEE Trans. Ultrason. Ferroelectr. Freq. Control, vol. 36, no. 6, pp. 652–660.

[126] A. Wahab, A. Rahim, F. Rahiman, S. Aw, F. Yunus, C. Goh, H. Rahim, L. Ling, "Non-invasive process tomography in chemical mixtures – A review", Sensors and Actuators B: Chemical, Volume 210, 2015, pp. 602-617, 2015.

[127] B. S. Hoyle, “Process tomography using ultrasonic sensors” Meas. Sci. Technol., vol. 7, no. 3, pp. 272–280, 1996.

[128] T. Rymarczyk and G. Kłosowski, “Innovative methods of neural reconstruction for tomographic images in maintenance of tank industrial reactors” Eksploat. i Niezawodn., vol. 21, no. 2, pp. 261–267, 2019.

[129] R. Mann, S. J. Stanley, D. Vlaev, E. Wabo, and K. Primrose, “Augmented-reality visualization of fluid mixing in stirred chemical reactors using electrical resistance tomography (ERT)” Process Imaging Autom. Control, vol. 4188, no. February 2001, p. 224, 2001.

[130] G. T. Bolton and K. M. Primrose, “An overview of electrical tomographic measurements in pharmaceutical and related application areas” AAPS PharmSciTech, vol. 6, no. 2, 2005.

[131] S. J. Stanley, “Tomographic imaging during reactive precipitation in a stirred vessel: Mixing with chemical reaction” Chem. Eng. Sci., vol. 61, no. 24, pp. 7850–7863, Dec. 2006.

[132] M. Sharifi and B. Young, “Electrical Resistance Tomography (ERT) applications to Chemical Engineering,” Chem. Eng. Res. Des., vol. 91, no. 9, pp. 1625–1645, Sep. 2013.

[133] H. Movafagh, G. Turcotte, and F. Ein-Mozaffari, “Using tomography images to study the mixing of wheat straw slurries” Biofuels, vol. 7, no. 4. pp. 365–375, 2016.

[134] J. A. Bamberger and M. S. Greenwood, “Using ultrasonic attenuation to monitor slurry mixing in real time,” Ultrasonics, vol. 42, no. 1–9, pp. 145–148, 2004.

[135] G. Févotte and N. Gherras, "Acoustic emission: A new in-line and non-intrusive sensor for monitoring batch solution crystallization operations", vol. 8, no. PART 1. IFAC, 2012.

[136] E. Simone, A. N. Saleemi, and Z. K. Nagy, “Application of quantitative Raman spectroscopy for the monitoring of polymorphic transformation in crystallization processes using a good calibration practice procedure” Chem. Eng. Res. Des., vol. 92, no. 4, pp. 594–611, Apr. 2014.

[137] Y. Hu, J. K. Liang, A. S. Myerson, and L. S. Taylor, “Crystallization Monitoring by Raman Spectroscopy: Simultaneous Measurement of Desupersaturation Profile and Polymorphic Form in Flufenamic Acid Systems” Ind. Eng. Chem. Res., vol. 44, no. 5, pp. 1233–1240, Mar. 2005.

[138] P. Frohberg and J. Ulrich, “Single-frequency ultrasonic crystallization monitoring (UCM): Innovative technique for in-line analyzing of industrial crystallization processes” Organic Process Research and Development, vol. 19, no. 1. American Chemical Society, pp. 84–88, Jan. 16, 2015.

[139] P. Frohberg and J. Ulrich, “Single-frequency ultrasonic crystallization monitoring (UCM): Innovative technique for in-line analyzing of industrial crystallization processes” Org. Process Res. Dev., vol. 19, no. 1, pp. 84–88, 2015.

[140] S. Ali and R. Bandyopadhyay, “Use of ultrasound attenuation spectroscopy to determine the size distribution of clay tactoids in aqueous suspensions” Langmuir, vol. 29, no. 41, pp. 12663–12669, 2013.

[141] M. L. Rasche, B. W. Zeiger, K. S. Suslick, and R. D. Braatz, “Mathematical modelling of the evolution of the particle size distribution during ultrasound-induced breakage of aspirin crystals” Chem. Eng. Res. Des., vol. 132, pp. 170–177, Apr. 2018.

[142] R. J. Urick, “A sound velocity method for determining the compressibility of finely divided substances,” J. Appl. Phys., vol. 18, no. 11, pp. 983–987, 1947.

[143] M. Polacci et al., “Crystallisation in basaltic magmas revealed via in situ 4D synchrotron X-ray microtomography” Sci. Rep., vol. 8, no. 1, Dec. 2018.

[144] A. Vancleef, D. Maes, T. Van Gerven, L. C. J. Thomassen, and L. Braeken, “Flow-through microscopy and image analysis for crystallization processes” Chem. Eng. Sci., vol. 248, p. 117067, 2022.

[145] R. Wajman, “The concept of 3D ECT system with increased border area sensitivity for crystallization processes diagnosis” Sens. Rev., vol. 41, no. 1, pp. 35–45, 2021.

[146] J. Szilard, "Ultrasonic Testing: Non-conventional Testing Techniques.", John Wiley and Sons, 1982.

[147] N. M. Tole, H. Ostensen, W. H. O. D. Imaging, and L. T. Team, “Basic physics of ultrasonic imaging / by Nimrod M. Tole ; Editor: Harald Ostensen.” World Health Organization, p. 95 p., 2005.

[148] V. E. Ostashev, "Acoustics in moving inhomogeneous media." London; New York: E & FN Spon, 1997.

[149] M. OK-Ashfaq, “Measuring and signal processing techniques for ultrasound computed tomography,”, Ruhr University of Bochum, 2007.

[150] M. Pérez-Liva, “Time domain image reconstruction methods for transmission ultrasound computed tomography”, PhD Thesis, University of Madrid, 2017.

[151] T. Rymarczyk, M. Golbek, P. Bozek, P. Adamkiewicz, M. Maj, and J. Sikora, “The prototype ultrasound tomography device to analyze the properties of processes” 2018 Appl. Electromagn. Mod. Tech. Med. PTZE 2018, pp. 228–231, 2018.

[152] V. V Krylov, “Geometric acoustics approximation for Rayleigh and Lamb waves,” Ninth Int. Conf. Cond. Monit. Mach. Fail. Prev. Technol., 2012.

[153] L. Savioja and U. P. Svensson, “Overview of geometrical room acoustic modeling techniques,”

J. Acoust. Soc. Am., vol. 138, no. 2, pp. 708–730, 2015.

[154] E. Deines et al., “Comparative visualization for wave-based and geometric acoustics” IEEE Trans. Vis. Comput. Graph., vol. 12, no. 5, pp. 1173–1180, 2006.

[155] R. Dapp, M. Zapf, and N. V. Ruiter, “Geometry-independent speed of sound reconstruction for 3D USCT using apriori information,” IEEE Int. Ultrason. Symp. IUS, pp. 1403–1406, 2011.

[156] A. Hormati, I. Jovanović, O. Roy, and M. Vetterli, “Robust ultrasound travel-time tomography using the bent ray model” Med. Imaging 2010 Ultrason. Imaging, Tomogr. Ther., vol. 7629, no. May 2014, p. 76290I, 2010.

[157] J. R. Jago and T. A. Whittingham, “Experimental studies in transmission ultrasound computed tomography” Phys. Med. Biol., vol. 36, no. 11, pp. 1515–1527, 1991.

[158] Matthias Birk, Robin Dapp, N.V. Ruiter, J. Becker, "GPU-based iterative transmission reconstruction in 3D ultrasound computer tomography", Journal of Parallel and Distributed Computing, Vol 74, Issue 1, Pages 1730-1743, 2014.

[159] C. Li, N. Duric, and L. Huang, “Comparison of ultrasound attenuation tomography methods for breast imaging” Med. Imaging 2008 Ultrason. Imaging Signal Process., vol. 6920, no. March 2008, p. 692015, 2008.

[160] A. C. Kak and Malcolm Slaney, "Principles of Computerized Tomographic Imaging", IEEE Press, 1988.

[161] Y. Levakhina, Three-dimensional digital tomosynthesis: Iterative reconstruction, artifact reduction and alternative acquisition geometry. 2014.

[162] P. M. Joseph, “An Improved Algorithm for Reprojecting Rays Through Pixel Images” IEEE Trans. Med. Imaging, vol. 1, no. 3, pp. 192–196, 1982.

[163] R. L. Siddon, “Fast calculation of the exact radiological path for a three-dimensional CT array.” Med. Phys., vol. 12, no. 2, pp. 252–255, 1985.

[164] S. B. Lo, “Strip and line path integrals with a square pixel matrix: a unified theory for computational CT projections.,” IEEE Trans. Med. Imaging, vol. 7, no. 4, pp. 355–363, 1988.

[165] H. Turbell, "Cone-Beam Reconstruction Using Filtered Backprojection.", PhD Thesis, University of Linköpings, 2001.

[166] F. Xu and K. Mueller, “A comparative study of popular interpolation and integration methods for use in computed tomography” 2006 3rd IEEE Int. Symp. Biomed. Imaging From Nano to Macro - Proc., vol. 2006, pp. 1252–1255, 2006.

[167] Kravtsov, Yury A. and Yu. I. Orlov., “Geometrical optics of inhomogeneous media.” *Geometrical Optics of Weakly Anisotropic Media* , 2019.

[168] M. Perez-Liva et al., “Ultrasound computed tomography for quantitative breast imaging,” 2016 Glob. Med. Eng. Phys. Exch. Am. Heal. Care Exch. GMEPE/PAHCE 2016, pp. 2–7, 2016.

[169] E. Miller, B. T. Cox, J. L. Herraiz, J. M. Udías, M. Pérez-Liva, and B. E. Treeby, “Time domain reconstruction of sound speed and attenuation in ultrasound computed tomography using full wave inversion” J. Acoust. Soc. Am., vol. 141, no. 3, pp. 1595–1604, 2017.

[170] F. A. Dahlen, G. Nolet, and S.-H. Hung, “Frechet kernels for finite- ´ frequency traveltimes - I. Theory,” Geophysical Journal International, vol. 141, no. 1, pp. 157–174, 04 2000.

[171] D. W. Vasco, J. E. Peterson, and E. L. Majer, “Beyond ray tomography; wavepaths and Fresnel volumes,” Geophysics, vol. 60, no. 6, pp. 1790–1804, Dec. 1995.

[172] M. L. Buursink, T. C. Johnson, P. S. Routh, and M. D. Knoll, “Crosshole radar velocity tomography with finite-frequency Fresnel volume sensitivities,” Geophys. J. Int., vol. 172, no. 1, pp. 1–17, Jan. 2008.

[173] J. M. Jensen, B. H. Jacobsen, and J. Christensen-Dalsgaard, “Sensitivity kernels for time-distance inversion,” Sol. Phys., vol. 192, no. 1–2, pp. 231–239, 2000.

[174] T. M. Hansen, K. S. Cordua, M. C. Looms, and K. Mosegaard, “SIPPI: A Matlab toolbox for sampling the solution to inverse problems with complex prior information: Part 2-Application to crosshole GPR tomography,” Comput. Geosci., vol. 52, pp. 481–492, Mar. 2013.

[175] F. Santos and M. Vogelius, “A backprojection algorithm for electrical impedance imaging,” Siam J. Appl. Math., vol. 50, pp. 216–243, 1990.

[176] R. A. Rahim, M. H. F. Rahiman, and M. N. Mohd Taib, “Non-invasive ultrasonic tomography: Liquid/gas flow visualization,” 2005 1st Int. Conf. Comput. Commun. Signal Process. with Spec. Track Biomed. Eng. CCSP 2005, pp. 243–247, 2005.

[177] L. Jing, S. Liu, L. Zhihong, and S. Meng, “An image reconstruction algorithm based on the extended Tikhonov regularization method for electrical capacitance tomography,” Meas. J. Int. Meas. Confed., vol. 42, no. 3, pp. 368–376, 2009.

[178] I. Peterlík, R. Jiřík, N. Ruiter, and J. Jan, “Regularized image reconstruction for ultrasound attenuation transmission tomography,” Radioengineering, vol. 17, no. 2, pp. 125–132, 2008.

[179] M. Cheney, D. Isaacson, J. C. Newell, S. Simske, and C. Goble, “NOSER: An algorithm for solving the inverse conductivity.pdf,” Int. J. Imaging Syst. Technol., vol. 2, no. 1990, pp. 66–75, 1990.

[180] L. I. Rudin, S. Osher, and E. Fatemi, “Nonlinear total variation noise removal algorithm,” Phys. D Nonlinear Phenom., vol. 60, no. 1–4, pp. 259–268, 1992.

[181] F. Li, J. F. P. J. Abascal, M. Desco, and M. Soleimani, “Total Variation Regularization with Split Bregman-Based Method in Magnetic Induction Tomography Using Experimental Data,” IEEE Sens. J., vol. 17, no. 4, pp. 976–985, 2017.

[182] J. F. P. J. Abascal et al., “Fluorescence diffuse optical tomography using the split Bregman method,” Med. Phys., vol. 38, no. 11, pp. 6275–6284, 2011.

[183] T. Goldstein and S. Osher, “The split Bregman method for L1-regularized problems” SIAM J. Imaging Sci., vol. 2, no. 2, pp. 323–343, 2009.

[184] J. Xiang, Y. Dong, and Y. Yang, “Multi-Frequency Electromagnetic Tomography for Acute Stroke Detection Using Frequency-Constrained Sparse Bayesian Learning,” IEEE Trans. Med. Imaging, vol. 39, no. 12, pp. 4102–4112, 2020.

[185] F. Li, M. Soleimani, and J. Abascal, “Planar array magnetic induction tomography further improvement” Sens. Rev., 2018.

[186] B. Chen, J. F. P. J. Abascal, and M. Soleimani, “Electrical resistance tomography for visualization of moving objects using a spatiotemporal total variation regularization algorithm” Sensors (Switzerland), vol. 18, no. 6, 2018.

[187] K. Liu, B. Wu, C. He, N. Li, and K. Xu, “A Novel Sensitivity Matrix Construction Method for Ultrasonic Tomography Based on Simulation Studies” IEEE Trans. Instrum. Meas., vol. PP, pp. 1–15, 2019.

[188] L. Yang, C. Xu, and X. Guo, “Ring-shaped array ultrasound imaging using ellipse algorithm,” Comput. Model. New Technol., vol. 18, pp. 315–320, 2014.

[189] J. Tu and B. Yang, “The Research of Ellipse Parameter Fitting Algorithm of Ultrasonic Imaging Logging in the Casing Hole,” Appl. Math., vol. 5, no. May, pp. 1317–1321, 2014.

[190] L. Yang, Q. Pan, C. Xu, X. Guo, and K. Peng, “Immersion ultrasonic reflection tomography by annular array system,” in FENDT 2013 - Proceedings of 2013 Far East Forum on Nondestructive Evaluation/Testing: New Technology and Application, 2013, pp. 82–89.

[191] Yu Yan, “Ultrasound tomography image reconstruction reflection mode" BEng Thesis, University of Bath, 2014.

[192] L. Yang, Q. Pan, C. Xu, X. Guo, and K. Peng, “Immersion ultrasonic reflection tomography by annular array system” FENDT 2013 - Proc. 2013 Far East Forum Nondestruct. Eval. New Technol. Appl., pp. 82–89, 2013.

[193] S. J. Stanley, R. Mann, and K. Primrose, “Tomographic imaging of fluid mixing in three dimensions for single-feed semi-batch operation of a stirred vessel” Chem. Eng. Res. Des., vol. 80, no. 8, pp. 903–909, 2002.

[194] T. Rymarczyk, E. Kozłowski, G. Kłosowski, and K. Niderla, “Logistic Regression for Machine Learning in Process Tomography” Sensors, vol. 19, no. 15, p. 3400, 2019.

[195] Alle, “Procedures for detecting outlying observations in samples” Technometrics, vol. 11, no. 1, pp. 1–21, 1969.

[196] F. E. Grubbs, “Procedures for Detecting Outlying Observations in Samples,” Technometrics, vol. 11, no. 1, pp. 1–21, Feb. 1969.

[197] T. Rymarczyk, P. Adamkiewicz, J. Sikora, and K. Polakowski, “Image reconstruction methods in radio and ultrasound tomography,” 2018 Int. Interdiscip. PhD Work. IIPhDW 2018, pp. 165–168, 2018.

[198] T. Rymarczyk, J. Sikora, P. Adamkiewicz, and K. Polakowski, “Effective ultrasound and radio tomography imaging algorithm for three-dimensional problems,” 2018 Appl. Electromagn. Mod. Tech. Med. PTZE 2018, pp. 232–235, 2018.

[199] T. Rymarczyk, K. Kania, M. Gołąbek, J. Sikora, M. Maj, and P. Adamkiewicz, “Image reconstruction by solving the inverse problem in ultrasonic transmission tomography system,” COMPEL - Int. J. Comput. Math. Electr. Electron. Eng., vol. 40, no. 2, pp. 238–266, 2020.

[200] N. Li, K. Xu, K. Liu, C. He, and B. Wu, “A Novel Sensitivity Matrix Construction Method for Ultrasonic Tomography Based on Simulation Studies,” IEEE Trans. Instrum. Meas., pp. 1–15, 2019.

[201] M. H. Fazalul Rahiman, R. Abdul, H. Abdul, and N. M. Nor Ayob, “Design and Development of Ultrasonic Process Tomography,” in Ultrasonic Waves, InTechOpen, 2012.

[202] R. P. Agarwal, D. O’Regan, and R. Precup, “Nonuniform nonresonance for nonlinear boundary value problems with y′ dependence,” Dyn. Syst. Appl., vol. 16, no. 3, pp. 587–594, 2007.

[203] W. Tobler, “Measuring spatial resolution,” Proc. L. Resour. Inf. Syst. Conf., vol. 48, no. July, pp. 12–16, 1987.

[204] B. Chen, J. F. P. J. Abascal, and M. Soleimani, “Extended joint sparsity reconstruction for spatial and temporal ERT imaging,” Sensors (Switzerland), vol. 18, no. 11, 2018.

[205] P. Resa, L. Elvira, F. Montero De Espinosa, and Y. Gómez-Ullate, “Ultrasonic velocity in water-ethanol-sucrose mixtures during alcoholic fermentation,” Ultrasonics, vol. 43, no. 4, pp. 247–252, 2005.

[206] G. Natta and M. Baccaredda, “Ultrasonic velocity in macromolecular substances,” J. Polym. Sci., vol. 4, no. 4, pp. 533–537, 1949.

[207] N. S. Tavare, "Inudstrial Crystallization: Process Simulations Analysis and Design.", in the Plenum chemical engineering series Includes bibliographical references and index.

[208] M. Torbacke and Å. C. Rasmuson, “Mesomixing in semi-batch reaction crystallization and influence of reactor size,” AIChE J., vol. 50, no. 12, pp. 3107–3119, Dec. 2004.

[209] M. Barrett, D. O’Grady, E. Casey, and B. Glennon, “The role of meso-mixing in anti-solvent crystallization processes,” Chem. Eng. Sci., vol. 66, no. 12, pp. 2523–2534, Jun. 2011.

[210] M. Porru and L. Özkan, “Monitoring of Batch Industrial Crystallization with Growth, Nucleation, and Agglomeration. Part 2: Structure Design for State Estimation with Secondary Measurements” Ind. Eng. Chem. Res., vol. 56, no. 34, pp. 9578–9592, 2017.

[211] Hamine A., Faiz B., Moudden A., Menou A., Benallo A., Izbaim D., Maze G. and Decultot D. "Ultrasonic Attenuation Measurement Method for Characterization of Clay Particles Mass Fraction in Dilute Suspension." High Temperature Materials and Processes, vol. 28, no. 6, pp. 369-378, 2009.

[212] G. Févotte and N. Gherras, “Acoustic emission: A new in-line and non-intrusive sensor for monitoring batch solution crystallization operations” in IFAC Proceedings Volumes (IFAC-PapersOnline), vol. 8, no. PART 1, pp. 178–185, 2012.

[213] P. J. Holden, M. Wang, R. Mann, F. J. Dickin, and R. B. Edwards, “Imaging Stirred-Vessel Macromixing Using Electrical Resistance Tomography” AIChE J., vol. 44, no. 4, pp. 780–790, 1998.

[214] S. Žáček, J. Nývlt, J. Garside, and A. W. Nienow, “A stirred tank for continuous crystallization studies,” Chem. Eng. J., vol. 23, no. 1, pp. 111–113, 1982.

[215] S. Aghajanian and T. Koiranen, “Dynamic modeling and semibatch reactive crystallization of calcium carbonate through CO2 capture in highly alkaline water,” J. CO2 Util., vol. 38, no. February, pp. 366–374, 2020.

[216] M. Bohlin and Å. C. Rasmuson, “Importance of Macromixing in Batch Cooling Crystallization,” AIChE J., vol. 42, no. 3, pp. 691–699, 1996.

[217] M. V. Sardeshpande, G. Kumar, T. Aditya, and V. V. Ranade, “Mixing studies in unbaffled stirred tank reactor using electrical resistance tomography,” Flow Meas. Instrum., vol. 47, pp. 110–121, Mar. 2016.

[218] Bohlin, M. and Rasmuson, Å.C., Importance of macromixing in batch cooling crystallization. AIChE J., 42: 691-699, 1996.

[219] Sholl, D., Lively, R., "Seven chemical separations to change the world." Nature 532, 435–437 2016.

[220] W. S. Kim and J. M. Tarbell, “Micromixing effects on barium sulfate precipitation in an MSMPR reactor,” Chem. Eng. Commun., vol. 146, pp. 33–56, 1996.

[221] M. Öner, F. C. C. Montes, T. Ståhlberg, S. M. Stocks, J. E. Bajtner, and G. Sin, “Comprehensive evaluation of a data driven control strategy: Experimental application to a pharmaceutical crystallization process,” Chem. Eng. Res. Des., vol. 163, pp. 248–261, 2020.

[222] R. M. Cuéllar-Franca and A. Azapagic, “Carbon capture, storage and utilisation technologies: A critical analysis and comparison of their life cycle environmental impacts,” J. CO2 Util., vol. 9, pp. 82–102, 2015.

[223] N. Duric and P. Littrup, “Breast Ultrasound Tomography,” in Breast Imaging, InTechOpen, 2018.

[224] M. V. de Hoop and R. D. van der Hilst, “On sensitivity kernels for ‘wave-equation’ transmission tomography,” Geophys. J. Int., vol. 160, no. 2, pp. 621–633, 2005.

[225] S. Wöckel, U. Hempel, R. Weser, B. Wessely, and J. Auge, “Particle characterization in highly concentrated suspensions by ultrasound scattering m hod,” Procedia Eng., vol. 47, pp. 582–585, 2012.

[226] S. Ali and R. Bandyopadhyay, “Use of ultrasound attenuation spectroscopy to determine the size distribution of clay tactoids in aqueous suspensions,” Langmuir, vol. 29, no. 41, pp. 12663–12669, Oct. 2013, doi: 10.1021/la402478h.

[227] S. Aghajanian, H. Nieminen, A. Laari, and T. Koiranen, “Integration of a calcium carbonate crystallization process and membrane contactor–based CO2 capture” Sep. Purif. Technol., vol. 274, no. May, 2021..

[228] Q. Shen et al., “Properties of amorphous calcium carbonate and the template action of vaterite spheres” J. Phys. Chem. B, vol. 110, no. 7, pp. 2994–3000, 2006.

[229] A. Lassin et al., “Dynamics of calcium carbonate formation: Geochemical modeling of a two-step mechanism,” Geochim. Cosmochim. Acta, vol. 240, pp. 236–254, 2018.

[230] D. Gebauer, A. Völkel, and H. Cölfen, “Stable prenucleation calcium carbonate clusters” Science (80-.)., vol. 322, no. 5909, pp. 1819–1822, 2008.

[231] M. Soleimani, H. Wang, Y. Li, and W. Yang, “A Comparative Study of 3D Electrical Capacitance Tomography” Int. J. Inf. Syst. Sci, vol. 3, no. 2, pp. 292–306, 2007.

[232] A. Biguri, M. Dosanjh, S. Hancock, and M. Soleimani, “TIGRE: A MATLAB-GPU toolbox for CBCT image reconstruction,” Biomed. Phys. Eng. Express, vol. 2, no. 5, 2016.

[233] P. Babin et al., “Fast X-ray tomography analysis of bubble growth and foam setting during

breadmaking," J. Cereal Sci., vol. 43, no. 3, pp. 393–397, 2006.

[234] Wiskin, J., Malik, B., Borup, D. et al." Full wave 3D inverse scattering transmission ultrasound tomography in the presence of high contrast." Sci Rep 10, 20166 (2020).

[235] C. Liu, C. Xue, B. Zhang, G. Zhang, and C. He, "The application of an ultrasound tomography algorithm in a novel ring 3D ultrasound imaging system," Sensors (Switzerland), vol. 18, no. 5, May 2018.

[236] M. Birk, E. Kretzek, P. Figuli, M. Weber, J. Becker, and N. V. Ruiter, "High-Speed Medical Imaging in 3D Ultrasound Computer Tomography," IEEE Trans. Parallel Distrib. Syst., vol. 27, no. 2, pp. 455–467, Feb. 2016.

[237] H. Gemmeke and N. V. Ruiter, "3D ultrasound computer tomography for medical imaging," Nucl. Instruments Methods Phys. Res. Sect. A Accel. Spectrometers, Detect. Assoc. Equip., vol. 580, no. 2, pp. 1057–1065, 2007.

[238] J. Wiskin, D. T. Borup, S. A. Johnson, and M. Berggren, "Non-linear inverse scattering: High resolution quantitative breast tissue tomography," J. Acoust. Soc. Am., vol. 131, no. 5, pp. 3802–3813, May 2012.

[239] C. Li, L. Huang, N. Duric, H. Zhang, and C. Rowe, "An improved automatic time-of-flight picker for medical ultrasound tomography," Ultrasonics, vol. 49, no. 1, pp. 61–72, Jan. 2009.

[240] C. Li, G. S. Sandhu, O. Roy, N. Duric, V. Allada, and S. Schmidt, "Toward a practical ultrasound waveform tomography algorithm for improving breast imaging," Med. Imaging 2014 Ultrason. Imaging Tomogr., vol. 9040, no. January 2015, p. 90401P, 2014.

[241] A. Javaherian, F. Lucka, and B. T. Cox, "Refraction-corrected ray-based inversion for three-dimensional ultrasound tomography of the breast," Inverse Probl., vol. 36, no. 12, 2020.

[242] A. Stanziola, S. R. Arridge, B. T. Cox, and B. E. Treeby, "A Helmholtz equation solver using unsupervised learning: Application to transcranial ultrasound," J. Comput. Phys., vol. 441, p. 110430, 2021.

[243] N. Li, L. Wang, J. Jia, and Y. Yang, "A Novel Method for the Image Quality Improvement of Ultrasonic Tomography," IEEE Trans. Instrum. Meas., vol. 70, 2021.

[244] M. Wang, C. Tan, F. Dong and Y. Bao, "Quantitative Sound Velocity Reconstruction Based on Ultrasonic Tomography," 2021 IEEE International Instrumentation and Measurement Technology Conference (I2MTC), pp. 1-5, 2021.

[245] C. Tan, X. Li, H. Liu, and F. Dong, "An ultrasonic transmission/reflection tomography system for industrial multiphase flow imaging," IEEE Trans. Ind. Electron., vol. 66, no. 12, pp. 9539–9548, Dec. 2019.

[246] S. Roux, L. Desbat, A. Koenig, and P. Grangeat, "Exact reconstruction in 2D dynamic {CT}: compensation of time-dependent affine deformations," Phys. Med. Biol., vol. 49, no. 11, pp. 2169–2182, May 2004.

[247] U. Schmitt and A. K. Louis, "Efficient algorithms for the regularization of dynamic inverse problems: I. Theory" Inverse Probl., vol. 18, no. 3, pp. 645–658, 2002.

[248] Kazantsev D, Guo E, Kaestner A, Lionheart WR, Bent J, Withers PJ, Lee PD. "Temporal sparsity

exploiting nonlocal regularization for 4D computed tomography reconstruction." J Xray Sci Technol., 2016.

[249] M. Soleimani, C. N. Mitchell, R. Banasiak, R. Wajman, and A. Adler, “Four-Dimensional electrical capacitance tomography imaging using experimental data” Prog. Electromagn. Res., vol. 90, pp. 171–186, 2009.

[250] G. Ma and M. Soleimani, “A versatile 4D capacitive imaging array: a touchless skin and an obstacle-avoidance sensor for robotic applications”, Scientific Reports, vol. 10, no. 1. 2020.

[251] V. Vishnevskiy, T. Gass, G. Szekely, C. Tanner, and O. Goksel, “Isotropic Total Variation Regularization of Displacements in Parametric Image Registration”, IEEE Trans. Med. Imaging, vol. 36, no. 2, pp. 385–395, 2017.

[252] M. Soleimani, C. N. Mitchell, R. Banasiak, R. Wajman, and A. Adler, “Four-Dimensional electrical capacitance tomography imaging using experimental data”, Prog. Electromagn. Res., vol. 90, no. January, pp. 171–186, 2009.

[253] G. Marmitt, A. Kleer, I. Wald, H. Friedrich, and P. Slusallek, “Fast and accurate ray-voxel intersection techniques for iso-surface ray tracing”, Vision, Model. Vis. 2004, VMV 2004 - Proc., no. January, pp. 429–435, 2004.

[254] J. Amanatides and A. Woo, “A Fast Voxel Traversal Algorithm for Ray Tracing” Eurographics, vol. 87, no. 3, pp. 3–10, 1987.

[255] A. Majercik, C. Crassin, P. Shirley, and M. Mcguire, “A Ray-Box Intersection Algorithm and Efficient Dynamic Voxel Rendering,” J. Comput. Graph. Tech. A Ray-Box Intersect. Algorithm, vol. 7, no. 3, pp. 66–81, 2018.

[256] T. Rymarczyk, K. Polakowski, and J. Sikora, “A New Concept of Discretization Model for Imaging Improving in Ultrasound Transmission Tomography” Inform. Autom. Pomiary w Gospod. i Ochr. Środowiska, vol. 9, no. 4, pp. 48–51, 2019.

[257] E. P. Simoncelli, H. R. Sheikh, A. C. Bovik, and Z. Wang, “Image quality assessment: From error visibility to structural similarity” IEEE Trans. image Process., vol. 13, no. 4, pp. 600–612, 2004.

[258] C. L. Goh, R. A. Rahim, H. F. Rahiman, T. Zhen Cong, and Y. A. Wahad, “Simulation and experimental study of the sensor emitting frequency for ultrasonic tomography system in a conducting pipe” Flow Meas. Instrum., vol. 54, pp. 158–171, Apr. 2017.

[259] Z. Wang, E. P. Simoncelli and A. C. Bovik, "Multiscale structural similarity for image quality assessment" The Thrity-Seventh Asilomar Conference on Signals, Systems & Computers, pp. 1398-1402 Vol.2, 2003.

[260] T. Rymarczyk, G. Kłosowski, K. Kania, P. Rymarczyk, and M. Mazurek, “Tomographic ultrasonic sensors in industrial applications” Prz. Elektrotechniczny, vol. 97, no. 1, pp. 166–169, 2020.

[261] W. Li and B. S. Hoyle, “Ultrasonic process tomography using multiple active sensors for maximum real-time performance” Chem. Eng. Sci., vol. 52, no. 13, pp. 2161–2170, 1997.

[262] H. I. Schlaberg, M. S. Beck, B. S. Hoyle, C. Lenn, and Ming Yang, “Real-time ultrasound process tomography for two-phase flow imaging using a reduced number of transducers,” IEEE Trans. Ultrason. Ferroelectr. Freq. Control, vol. 46, no. 3, pp. 492–501, 2002.

[263] Liu H, Tan C, Dong F. "Continuous-wave ultrasonic tomography for oil/water two-phase flow imaging using regularized weighted least square framework." Transactions of the Institute of Measurement and Control. 2020.

[264] H. Nieminen, L. Järvinen, V. Ruuskanen, A. Laari, T. Koiranen, and J. Ahola, "Insights into a membrane contactor based demonstration unit for CO2 capture" Sep. Purif. Technol., vol. 231, no. August 2019, p. 115951, 2020.

[265] L. Xu, Y. Han, L. Xu, J. Yang, "Application of ultrasonic tomography to monitoring gas/liquid flow" Chemical Engineering Science, Volume 52, Issue 13, 1997, pp. 2171-2183.

[266] N. N. Kishore, I. Sridhar, and N. G. R. Iyengar, "Finite element modelling of the scattering of ultrasonic waves by isolated flaws," NDT E Int., vol. 33, no. 5, pp. 297–305, 2000.

[267] J. Gu, H. Yang, F. Fan, and M. Su, "A transmission and reflection coupled ultrasonic process tomography based on cylindrical miniaturized transducers using PVDF films," J. Instrum., vol. 12, no. 12, Dec. 2017.

[268] Q. Su, C. Tan, and F. Dong, "Measurement of Oil-Water Two-Phase Flow Phase Fraction with Ultrasound Attenuation," IEEE Sens. J., vol. 18, no. 3, pp. 1150–1159, 2018.

[269] Yang M, Schlaberg HI, Hoyle BS, Beck MS, Lenn C. Real-time ultrasound process tomography for two-phase flow imaging using a reduced number of transducers. IEEE Trans Ultrason Ferroelectr Freq Control. 1999

[270] H. Liu, C. Tan, S. Zhao, and F. Dong, "Nonlinear ultrasonic transmissive tomography for low-contrast biphasic medium imaging using continuous-wave excitation" IEEE Trans. Ind. Electron., vol. 67, no. 10, pp. 8878–8888, Oct. 2020.

[271] L. Huang et al., "Breast ultrasound tomography with two parallel transducer arrays" in Medical Imaging 2016: Physics of Medical Imaging, Mar. 2016, vol. 9783, p. 97830C.

[272] G. Liang, S. Ren, and F. Dong, "Ultrasound guided electrical impedance tomography for 2D free-interface reconstruction" Meas. Sci. Technol., vol. 28, no. 7, 2017.

[273] B. Jiang, W. Zhao, and W. Wang, "Improved Ultrasonic Computerized Tomography Method for STS (Steel Tube Slab) Structure Based on Compressive Sampling Algorithm" Appl. Sci., vol. 7, no. 5, p. 432, Apr. 2017.

[274] L. Espinosa, J. Bacca, F. Prieto, P. Lasaygues, and L. Brancheriau, "Accuracy on the time-of-flight estimation for ultrasonic waves applied to non-destructive evaluation of standing trees: A comparative experimental study" Acta Acust. united with Acust., vol. 104, no. 3, pp. 429–439, 2018.

[275] Y. S. Huang, Y. P. Huang, K. N. Huang, and M. S. Young, "An accurate air temperature measurement system based on an envelope pulsed ultrasonic time-of-flight technique" Rev. Sci. Instrum., vol. 78, no. 11, 2007.

[276] H. I. Schlaberg, M. Yang, and B. S. Hoyle, "Ultrasound reflection tomography for industrial processes" Ultrasonics, vol. 36, no. 1–5, pp. 297–303, 1998.

[277] A. Macchi, H. Bi, J. R. Grace, C. A. McKnight, and L. Hackman, "Effect of gas density on the hydrodynamics of bubble columns and three-phase fluidized beds" Can. J. Chem. Eng., vol. 81, no. 3–4, pp. 846–852, 2003.

[278] M. Williamson et al., “Breast ultrasound waveform tomography: using both transmission and reflection data, and numerical virtual point sources,” Med. Imaging 2014 Ultrason. Imaging Tomogr., vol. 9040, p. 90400T, 2014.

[279] L. Brancheriau, P. Lasaygues, E. Debieu, and J. P. Lefebvre, “Ultrasonic tomography of green wood using a non-parametric imaging algorithm with reflected waves,” Ann. For. Sci., vol. 65, no. 7, 2008.

[280] N. Otsu, “A Threshold Selection Method from Gray-Level Histograms,” IEEE Trans. Syst. Man. Cybern., vol. 9, no. 1, pp. 62–66, 1979.

[281] T. Alkhalifah and Y. Choi, “From tomography to full-waveform inversion with a single objective function,” Geophysics, vol. 79, no. 2, pp. R55–R61, 2014.

[282] R. Djebbi and T. Alkhalifah, “Traveltime sensitivity kernels for wave equation tomography using the unwrapped phase,” Geophys. J. Int., vol. 197, no. 2, pp. 975–986, 2014.

[283] P. Lasaygues, J. Rouyer, S. Mensah, E Franceschini, G Rabau, et al. "Non-linear Ultrasonic Computed Tomography (USCT) for soft and hard tissue imaging." International Workshop on Medical Ultrasound Tomography, Speyer, Germany, Nov 2017.

[284] H. Li and B. s. Manjunath, “Multisensor-Image-Fusion-Using-the-Wavelet-Transform_1995_Graphical-Models-and-Image-Processing.pdf,” Graphical models and image processing, vol. 57, no. 3. pp. 235–245, 1995.

[285] S. Aghajanian, G. Rao, V. Ruuskanen, R. Wajman, L. Jackowska-Strumillo, and T. Koiranen, “Real-Time Fault Detection and Diagnosis of CaCO3 Reactive Crystallization Process by Electrical Resistance Tomography Measurements,” Sensors, vol. 21, no. 21, 2021.